

# Electrochemical Conversion of Biomass-derived Chemical: Benzaldehyde

Li Gong



Aquesta tesi doctoral està subjecta a la llicència <u>Reconeixement- NoComercial – SenseObraDerivada 4.0. Espanya de Creative Commons.</u>

Esta tesis doctoral está sujeta a la licencia <u>Reconocimiento - NoComercial – SinObraDerivada</u> **4.0.** España de Creative Commons.

This doctoral thesis is licensed under the <u>Creative Commons Attribution-NonCommercial-NoDerivs 4.0. Spain License.</u>



## Electrochemical Conversion of Biomassderived Chemical: Benzaldehyde

Li GONG

# Document signat digitalment per: LI GONG

#### **Doctoral Program**

#### **Electrochemistry. Science and Technology**

## Electrochemical Conversion of Biomass-derived Chemical: Benzaldehyde

#### Author

#### Li GONG

#### **Directors**

Andreu Cabot Codina and Paulina R. Martínez-Alanis
(Catalonia Institute for Energy Research of University of Barcelona)

#### **Tutor**

#### Elvira Gómez Valentín

(Department of Materials Science and Physical Chemistry of Faculty of Chemistry of University of Barcelona)

## Table of contents

Acknowledgement	1		
Preface	3		
Results	4		
Resultados			
Acronyms	12		
1. Introduction	17		
1.1 Background	17		
1.2 Electrochemistry	21		
1.3 Electrocatalytic reduction reaction mechanism of BZH	24		
1.4 Thermodynamics and kinetics of electrocatalytic reduction of BZH	29		
1.4.1 Thermodynamics of electrocatalytic reduction of BZH	29		
1.4.2 Kinetics of electrocatalytic reduction of BZH	30		
1.5 Electrode materials for electrocatalytic reduction of BZH	36		
1.5.1 Electrode materials for ECH of BZH into BA	36		
1.5.2 Electrode materials for self-coupling reaction of BZH into HDB	41		
1.6 Fundamental studies of electrooxidization of BZH	43		
1.7 References	44		
2. Objectives	54		
3. Experimental sections	58		
3.1 Chemicals or raw materials used in experiments.	60		
3.2 Material preparation method	61		
3.2.1 Solvothermal method	61		
3.2.2 Reflux method	62		
3.2.3 Colloidal method	63		
3.2.4 Deposition-precipitation method	64		
3.2.5 Heat treatment process	64		
3.3 Material characterizations.	65		
3.3.1 X-ray diffraction (XRD)	65		
3.3.2 Scanning electron microscopy (SEM) and energy dispersive x-ra	VS		

	spectroscopy (EDS)	66
	3.3.3 Transmission electron microscopy (TEM) and electron energy los	SS
	spectroscopy (EELS)	69
	3.3.4 X-ray photoelectron spectroscopy (XPS)	69
	3.3.5 Ultraviolet–visible spectroscopy (UV-vis)	71
	3.3.6 Gas absorption/desorption	72
	3.3.7 Fourier-transform infrared spectroscopy (FTIR)	72
	3.3.8 High-performance liquid chromatography (HPLC)	73
	3.3.9 Electron Paramagnetic Resonance Spectroscopy (EPR)	73
3.4	Electrochemistry techniques and parameters for catalyst performation	
	3.4.1 Preparation before the electrochemical tests	74
	3.4.2 Cyclic voltammetry and linear sweep voltammetry	75
	3.4.3 Electrochemical Impedance Spectroscopy (EIS)	77
	3.4.4 Potentiostatic method	78
3.5	References	79
	ectrochemical Hydrogenation of benzaldehyde into benzyl alcohol @Ni-MOF	
Art	icle included in chapter 4	85
	ectrochemical Reduction of benzaldehyde into Hydrobenzoin miconductor Materials	
Ar	ticle included in chapter 5	.118
	ectrochemical Reduction of benzaldehyde into Hydrobenzoin on Opped Cu <sub>2</sub> S	
Ar	ticle included in chapter 6	.147
	ctrochemical Oxidization of Benzaldehyde into Benzoic Acid on Au-	
Art	icle included in chapter 7	.167
8. Con	clusion and further work	.183
Curric	ulum Vitae	.190

#### Acknowledgement

First and foremost, I would like to sincerely thank my main supervisor Prof. Andreu Cabot who gave me the strength and courage to complete this thesis. Thanks for his invaluable help of suggestions throughout the thesis work and academic and administrated roles to make sure I finish strong on time. It has been a great honor and pleasure to have him as my main supervisor.

I would sincerely like to thank my supervisor Dr. Paulina R. Martínez-Alanis for her guidance, understanding, and patience, and most importantly, she has provided positive encouragement and a warm spirit for me to finish this thesis.

I would like to thank the cooperators; I have worked with them on some projects, and I am grateful for the help and knowledge that I got.

I would like to express my appreciation to the Functional Nanomaterials Group members for their kindness and moral support during my study. Thanks for the friendship and memories with Ting Zhang, Xu Han, Chaoqi Zhang, Ruifeng Du, Mengyao Li, Xinag Wang, Junshan Li, Ke Xiao, Guillem, Alberto, Jesus, Xueqiang Qi, Juguo Dai, Guifang Zeng, Qin Sun, Bingfei Nan, Ren He, Linlin Yang, Chaoyue Zhang, Xuan Lu, Karol, Cristhyan, Nicolas, Xingqi Chang, Canhuang Li, Chen Huang, Jing Yu, Ao Yu, Jiali Chai, Shengnan Zhang, Xingyuan Lu, Yuchuan Ren, Xiaoyu Bi, Xuede Qi, Qian Xue. I would like to express my appreciation to the administrative and technical staff of the Catalonia Institute for Energy Research for their support and kindness.

The precious opportunity for me to study abroad is supported by the China Scholarship Council (No. 202106180029), providing me with all the financial support during the last several years that made it possible for me to pursue my PhD degree study.

Last but not least, my deepest gratitude goes to my beloved parents, elder sister and elder brother for their support and encouragement throughout my study. I must thank

my wonderful friends Min Zhu, Tursungul, Yaling Hui, Ji Yang, as without their support throughout my PhD I may never have completed this thesis.

Li GONG

17/05/2024

#### **Preface**

The chapters included in this PhD thesis cover the work developed by the PhD candidate Li GONG at the Catalonia Institute for Energy Research (IREC) in Sant Adrià de Besòs, Barcelona from 2021.09 supported by China Scholarship Council (No. 202106180029). The thesis is particularly focused on the electrocatalysts preparation and their application in electrocatalytic reactions.

This thesis consists of eight chapters. The first chapter mainly introduces history of electrochemistry, fundamental concepts and applied electrode materials of electrochemical conversion of benzaldehyde. Chapter 2 claimed the objectives of this thesis. Chapter 3 introduced experiments parts. The following explorations were undertaken from chapter 4-7: (1) Optimization of electrocatalysts to enhance the efficiency of converting BZH to BA. (2) Investigation of the reaction pathways for converting BZH to HDB and the properties of the electrocatalysts required for this process. (3) Examination of the specific influencing factors on the different reaction pathways for converting BZH to BA or HDB. (4) Replacing high energy consumption oxygen reduction reaction (OER) with BZH electrooxidization reaction and obtaining high value-added chemical by employing electrode material Au-TiO<sub>2</sub>-P25.

#### **Results**

Developing advanced and efficient electrocatalytic energy conversion systems is of great and practical significance for propelling the efficient development of clean energy for the construction of new low-carbon power systems. Among them, electrocatalytic reduction reactions driven by renewable electricity to transform biomass-derived chemicals into biofuels and high value-added chemicals provide an effective way to improve the H/C ratio of biomass-derived chemicals and the stabilizations of bio-oil systems. However, the electrocatalytic reduction of organic compounds is more intricate compared to the electrocatalytic reduction of water molecules. It involves the adsorption of various organic functional groups, multi-step electron transfer, and the generation of organic intermediates. Meanwhile, organic electrocatalytic reduction calls for designing efficient, highly selective, and cost-effective electrocatalysts.

During a series conversion process of raw biomass, aldehydes are believed to be particularly troublesome for the aldol condensation and polymerization reactions. To avoid them, hydrogenation processes are necessary. As an alternative to traditional high-pressure and -temperature processing, we choose electrochemistry that can operate in ambient conditions for the conversion of benzaldehyde (BZH), which was chosen as a typical biomass-derived chemical. Another reason for choosing BZH is that the hydrogenation products benzyl alcohol (BA) and hydrobenzoin (HDB) are important industrial chemicals.

Based on the mentioned above, this work seeks to design highly efficient and high selective catalysts for the electrocatalytic conversion of the carbonyl group of BZH into BA, HDB or benzoic acid (BZA) in aqueous solution at pH > 5 (avoiding the deoxygenation product toluene). Additionally, this work screens the optimal reaction conditions for various products and speculates their most probable reaction pathways.

Chapter 4 focused on the electrocatalytic reduction of BZH into BA. Pd nanoparticles supported on a nickel metal-organic framework (MOF), Ni-MOF-74, are prepared and

their activity towards the ECH of BZH in a 3M sodium acetate-acetic acid (pH 5.2) aqueous electrolyte is explored. An outstanding ECH rate up to 283 µmol cm<sup>-2</sup> h<sup>-1</sup> with a Faradic efficiency (FE) of 76% is reached. Besides, higher FEs of up to 96% are achieved using a step-function voltage. Materials studio and density functional theory calculations show these outstanding performances to be associated with the Ni-MOF support that promotes H-bond formation, facilitates water desorption, and induces a favorable tilted BZH adsorption on the surface of the Pd nanoparticles. In this configuration, BZH is bonded to the Pd surface by the carbonyl group rather than through the aromatic ring, thus reducing the energy barriers of the elemental reaction steps and increasing the overall reaction efficiency.

Chapter 5 focused on the electrochemical reduction of self-coupling of BZH to HDB using semiconductor electrocatalysts with nanosheet morphologies. The effects of electrode potential and electrolyte pH on BZH self-coupling reaction were comprehensively studied on several semiconductor electrocatalysts. A correlation is observed between their band gap and the electrochemical potential necessary to maximize selectivity towards HDB in alkaline medium, which we associate with the charge accumulation at the semiconductor surface. N-type CuInS<sub>2</sub> provides the highest conversion rate at 0.3 mmol cm<sup>-2</sup> h<sup>-1</sup> with a selectivity of 98.5% at -1.3 V vs. Hg/HgO in aqueous alkaline solution pH=14. Additional density functional theory calculations demonstrate a lower kinetic energy barrier at the CuInS<sub>2</sub> surface compared with graphitic carbon, proving its catalytic role in the self-coupling reaction of BZH.

Based on the previous two works, we realize that even when selecting materials with poor HER performance, different voltages and pH values have a significant impact on the selectivity of HDB. This drives us towards the rational design of electrocatalysts for these two different reaction pathways. Chapter 6 employed material with exposed active sites Cu<sub>2</sub>S and the material Cu<sub>2</sub>S-OAm with ligands capped to catalyze the electrocatalytic reduction reaction of the biomass platform molecule BZH convert into BA and HDB. Cu<sub>2</sub>S particles are used as electrocatalysts for the BZH electrochemical

conversion. We particularly analyze the effect of surface ligands, oleylamine (OAm), on the selective conversion of BZH to BA or HDB. The effect of the electrode potential, electrolyte pH, and temperature are studied. Results indicate that bare Cu<sub>2</sub>S exhibits higher selectivity towards BA, while OAm-capped Cu<sub>2</sub>S promotes HDB formation. This difference is explained by the competing adsorption of protons and BZH. During the BZH electrochemical conversion, electrons first transfer to the C in the C=O group to form a ketyl radical. Then the radical either couples with surrounding H<sup>+</sup> to form BA or self-couple to produce HDB, depending on the available H<sup>+</sup> that is in turn affected by the electrocatalyst surface properties. The presence of OAm inhibits the H adsorption on the electrode surface therefore reducing the formation of high-energy state H<sub>ad</sub> and its combination with ketyl radicals to form BA instead promotes the outer sphere reaction for obtaining HDB.

Finally, we turn our attention to the anodic reaction in chapter 7. The electrooxidation of organic compounds offers a promising strategy for producing value-added chemicals through environmentally sustainable processes. A key challenge in this field is the development of electrocatalysts that are both effective and durable. In this study, we grow gold nanoparticles (Au NPs) on the surface of various phases of titanium dioxide (TiO<sub>2</sub>) as highly effective electrooxidation catalysts. Subsequently, the samples are tested for the oxidation of BZH to BZA coupled with a hydrogen evolution reaction (HER). We observe the support containing a combination of rutile and anatase phases to provide the highest activity. The excellent electrooxidation performance of this Au-TiO<sub>2</sub> sample is correlated with its mixed-phase composition, large surface area, high oxygen vacancy content, and the presence of Lewis acid active sites on its surface. This catalyst demonstrates an overpotential of 0.467 V at 10 mA cm<sup>-2</sup> in a 1 M KOH solution containing 20 mM BZH, and 0.387 V in 100 mM BZH, well below the oxygen evolution reaction (OER) overpotential. The electrooxidation of BZH not only serves as OER alternative in applications such as electrochemical hydrogen evolution, enhancing energy efficiency, but simultaneously allows the generation of high-value byproducts such as BZA.

#### Resultados

Desarrollar sistemas de conversión de energía electrocatalítica avanzados y eficientes es de gran importancia práctica para impulsar el desarrollo eficiente de energía limpia para la construcción de un nuevo sistema de energía baja en carbono. Entre ellos, la reacción de reducción electrocatalítica impulsada por electricidad renovable para transformar productos químicos derivados de la biomasa en biocombustibles y productos químicos de alto valor agregado proporciona una forma efectiva de mejorar la relación H/C de los productos químicos derivados de la biomasa y la estabilización del sistema de aceites biológicos. Sin embargo, la reducción electrocatalítica de compuestos orgánicos es más compleja en comparación con la reducción electrocatalítica de moléculas de agua. Implica la adsorción de varios grupos funcionales orgánicos, transferencia de electrones en múltiples etapas y la generación de intermediarios orgánicos. Mientras tanto, la reducción electrocatalítica orgánica requiere el diseño de electrocatalizadores eficientes, altamente selectivos y rentables. Durante un proceso de conversión de biomasa cruda, se cree que los aldehídos son particularmente problemáticos para las reacciones de condensación aldólica y polimerización, para evitar los cuales es necesario el proceso de hidrogenación. Como alternativa al procesamiento tradicional de alta presión y temperatura, estamos eligiendo la electroquímica que puede operar en condiciones ambientales para la conversión de benzaldehído (BZH), que es un producto químico típico derivado de la biomasa. Otra razón para elegir BZH es que los productos de hidrogenación alcohol bencílico (BA) e hidrobencoina (HDB) son productos químicos importantes para la industria.

Basándonos en lo mencionado anteriormente, este trabajo busca diseñar catalizadores altamente eficientes y selectivos para la conversión electrocatalítica del grupo carbonilo de BZH en el producto objetivo BA, HDB o ácido benzoico (BZA) en solución acuosa con pH>5 (evitando el producto de desoxigenación tolueno). Además, este trabajo

intentó seleccionar las condiciones de reacción óptimas para varios productos y especular sus vías de reacción más probables.

El Capítulo 4 se centró en la reducción electrocatalítica de BZH en BA. Se preparan nanopartículas de Pd soportadas en un marco metal-orgánico de níquel (MOF), Ni-MOF-74, y se explora su actividad hacia la ECH de BZH en un electrolito acuoso de acetato de sodio-ácido acético 3M (pH 5,2). Se alcanza una tasa de ECH sobresaliente de hasta 283 µmol cm<sup>-2</sup> h<sup>-1</sup> con una eficiencia faradaica (FE) del 76%. Además, se logran FEs más altos de hasta el 96% utilizando un voltaje de función escalonada. Los cálculos del estudio de materiales y de la teoría del funcional de la densidad muestran que estas actuaciones sobresalientes están asociadas con el soporte Ni-MOF que promueve la formación de enlaces de hidrógeno, facilita la desorción de agua e induce una adsorción inclinada favorable de BZH en la superficie de las nanopartículas de Pd. En esta configuración, BZH está unido a la superficie de Pd por el grupo carbonilo en lugar de a través del anillo aromático, reduciendo así las barreras energéticas de los pasos de reacción elemental y aumentando la eficiencia general de la reacción.

El Capítulo 5 se centró en la reducción electroquímica del acoplamiento automático de BZH a HDB utilizando electrocatalizadores semiconductores con morfologías de nanoplacas. Los efectos del potencial del electrodo y el pH del electrolito en la reacción de autocoplamiento de BZH se estudiaron exhaustivamente en varios electrocatalizadores semiconductores. Se observa una correlación entre su brecha de banda y el potencial electroquímico necesario para maximizar la selectividad hacia HDB en medio alcalino, que asociamos con la acumulación de carga en la superficie del semiconductor. CuInS2 de tipo N proporciona la mayor tasa de conversión a 0.3 mmol cm<sup>-2</sup> h<sup>-1</sup> con una selectividad del 98.5% a -1.3 V vs. Hg/HgO en solución alcalina acuosa pH=14. Cálculos adicionales de la teoría del funcional de la densidad demuestran una barrera de energía cinética más baja en la superficie de CuInS2 en comparación con el carbono grafítico, demostrando su papel catalítico en la reacción de autocoplamiento de BZH.

Basándonos en los dos trabajos anteriores, nos damos cuenta de que incluso al seleccionar materiales con un rendimiento HER pobre, diferentes voltajes y valores de pH tienen un impacto significativo en la selectividad de HDB. Esto nos lleva hacia el diseño racional de electrocatalizadores para estas dos vías de reacción diferentes. El Capítulo 6 empleó material con sitios activos expuestos Cu<sub>2</sub>S y el material Cu<sub>2</sub>S-OAm con ligandos tapados para catalizar la reacción de reducción electrocatalítica de la molécula de plataforma de biomasa BZH convertida en BA y HDB. Se utilizan partículas de Cu<sub>2</sub>S como electrocatalizadores para la conversión electroquímica de BZH. Analizamos especialmente el efecto de los ligandos superficiales, oleylamine (OAm), en la conversión selectiva de BZH a BA o HDB. Se estudia el efecto del potencial del electrodo, el pH del electrolito y la temperatura. Los resultados indican que Cu<sub>2</sub>S desnudo exhibe una mayor selectividad hacia BA, mientras que Cu<sub>2</sub>S con OAm promueve la formación de HDB. Esta diferencia se explica por la adsorción competitiva de protones y BZH. Durante la conversión electroquímica de BZH, los electrones primero se transfieren al C en el grupo C=O para formar un radical cetilo. Luego, el radical se acopla con H<sup>+</sup> circundantes para formar BA o se acopla por sí mismo para producir HDB, dependiendo del H<sup>+</sup> disponible que a su vez es afectado por las propiedades superficiales del electrocatalizador. La presencia de OAm inhibe la adsorción de H en la superficie del electrodo, reduciendo así la formación de Had en estado de alta energía y su combinación con radicales cetilos para formar BA, promoviendo en cambio la reacción de esfera exterior para obtener HDB.

Finalmente, dirigimos nuestra atención hacia la reacción anódica en el capítulo 7. La electrooxidación de compuestos orgánicos ofrece una estrategia prometedora para producir productos químicos de valor añadido a través de procesos ambientalmente sostenibles. Un desafío clave en este campo es el desarrollo de electrocatalizadores que sean tanto efectivos como duraderos. En este estudio, cultivamos nanopartículas de oro (Au NPs) en la superficie de diversas fases de dióxido de titanio (TiO<sub>2</sub>) como catalizadores de electrooxidación altamente efectivos. Posteriormente, se prueban las

muestras para la oxidación de benzaldehído (BZH) a ácido benzoico (BZA) acoplado con una reacción de evolución de hidrógeno (HER). Observamos que el soporte que contiene una combinación de fases de rutilo y anatasa proporciona la mayor actividad. El excelente rendimiento de electrooxidación de esta muestra de Au-TiO2 está correlacionado con su composición de fases mixtas, gran área superficial, alto contenido de vacancias de oxígeno y la presencia de sitios activos de ácido de Lewis en su superficie. Este catalizador demuestra una sobretensión de 0.467 V a 10 mA cm<sup>-2</sup> en una solución de KOH 1 M que contiene 20 mM de BZH, y 0.387 V en 100 mM de BZH, muy por debajo de la sobretensión de la reacción de evolución de oxígeno (OER). La electrooxidación de BZH no solo sirve como alternativa a OER en aplicaciones como la evolución electroquímica de hidrógeno, mejorando la eficiencia energética, sino que simultáneamente permite la generación de subproductos de alto valor como BZA.

## Acronyms

Average reaction rate (ARR)
Benzaldehyde (BZH)
Butler-Volmer equation (B-V equation)
Benzyl alcohol (BA)
Carbon cloth (CC)
Carbon felt (CF)
CuInS <sub>2</sub> (CIS)
Cu <sub>1.8</sub> S (CS)
Cyclic voltammetry (CV)
Density functional theory (DFT)
Electrocatalytic hydrogenation (ECH)
Electrical double layer (EDL)
Electrochemical impedance spectroscopy (EIS)
Electrochemical reduction (ECR)
Electron energy loss spectroscopy (EELS )
Electrooxidation of organic compounds (EOO)
Electron Paramagnetic Resonance Spectroscopy (EPR)
Energy-dispersive X-ray spectroscopy (EDX)
Faraday efficiency (FE)
Fourier-transformed infrared (FT-IR)
2,5-Furandicarboxylic acid (FDCA)
High-angle annular dark-field (HAADF)

High performance liquid chromatography (HPLC) High-resolution TEM (HRTEM) H<sub>2</sub>-temperature-programmed reduction (H<sub>2</sub>-TPR) Hydrobenzoin (HDB) Hydrofuroin (HDF) Hydrogen Evolution Reaction (HER) 5-Hydroxymethylfurfural (HMF) Inductively coupled plasma mass spectrometry (ICP-MS) In<sub>2.77</sub>S<sub>4</sub> (IS) Langmuir-Hinshelwood mechanism (LH mechanism) Linear scanning voltammetry (LSV) Metal-organic frameworks (MOFs) Nanoparticles (NPs) Noble-metals (NMs) Open-circuit voltage (OCV) Oxygen evolution reaction (OER) Pd supported on carbon (Pd/C) Proton-Coupled Electron Transfer (PCET) Rate-determining step (RDS) Scanning electron microscopy (SEM) Scanning TEM (STEM) Solid polymer electrolyte (SPE) Space charge layer (SCL)

Terephthalic acid (BDC)

Transmission electron microscopy (TEM)

Turnover frequency (TOF)

Two-dimensional (2D)

Ultraviolet-visible spectroscopy (UV-vis)

Vienna ab initio simulation package (VASP)

X-ray diffraction (XRD)

X-ray photoelectron spectroscopy (XPS)

Zero-point energy (ZPE)

ZnIn<sub>2</sub>S<sub>4</sub> (ZIS)

 $Zn_{0.5}Cd_{0.5}S$  (ZCS)

# **Chapter 1**

## Introduction

#### 1. Introduction

#### 1.1 Background

Natural variations in solar activity or large volcanic eruptions have historically affected the Earth's temperature and weather. However, over the past 200 years, human activities, primarily the combustion of fossil fuels such as coal, oil, and natural gas, have been the main drivers of climate change, not natural reasons. <sup>1-3</sup>

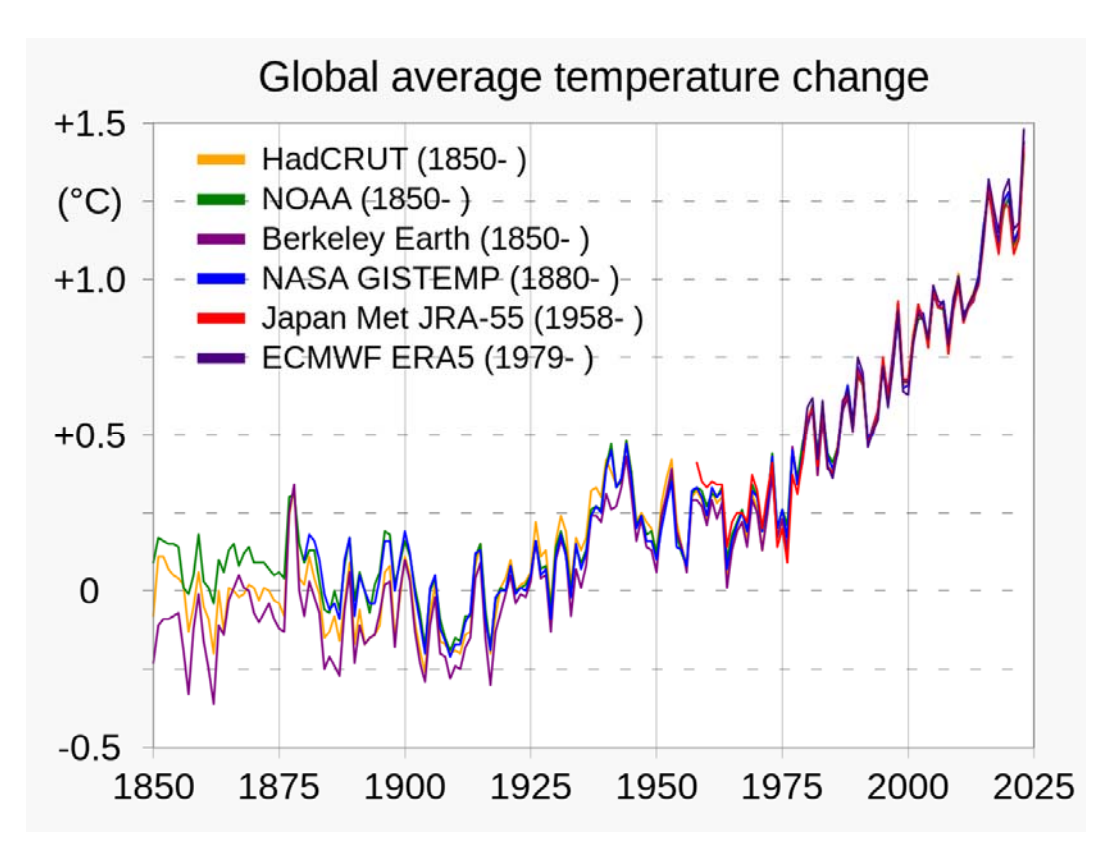


**Figure 1-1.** Measured global average surface temperature data from several scientific organizations is highly correlated. (In this chart, the "0" value is the average temperature from 1850 to 1900, which is considered the "pre-industrial" temperature level. Annual global mean temperatures expressed as a difference from pre-industrial conditions. Four different data sets are shown - HadCRUT, NOAAGlobalTemp, GISTEMP, and Berkeley Earth - as well as two reanalysis - ERA5 and JRA-55. <sup>4</sup>

Burning fossil fuels generates a pollutant layer that traps the sun's heat on Earth, leading to a rise in global temperatures. Global warming subsequently results in other consequences, such as droughts, water scarcity, severe wildfires, rising sea levels,

floods, polar glacier melting, intense storms, and a reduction in biodiversity. <sup>5, 6</sup> The more accumulations of pollutants like nitrogen oxides (NO<sub>x</sub>), carbon dioxide (CO<sub>2</sub>), and organic/inorganic sulfides in the atmosphere, the warmer our earth becomes. There is a close relationship between the cumulative emissions of carbon dioxide and the increase in global surface temperatures (Figure 1-1). <sup>7-9</sup>

Since the Industrial Revolution, machinery fueled by coal, oil, and natural gas has replaced manual labor, causing an unprecedented rapid increase in atmospheric carbon dioxide levels. Today, the concentration of carbon dioxide in the atmosphere is approximately 50% higher than in 1750, far exceeding natural variations over at least the past 800,000 years.

The need for cooling in a warming climate is growing, leading to a significant increase in energy demand. This is compounded by the rising global population, increased production and consumption of goods, more frequent travel, higher food consumption, and greater use of electronic devices. All these factors contribute to the escalating energy requirements and environmental impact. Global energy demand grew by 2.9% in 2018 and in a business-as-usual scenario, by 2040 global energy consumption will reach 740 million terajoules - equivalent to an additional 30 percent growth. The world must completely transform the global energy system. The most important strategies for reducing CO<sub>2</sub> emissions from energy in the Net Zero Emissions by 2050 scenario include expanding the use of renewable energy sources such as wind, solar, and hydro to replace fossil fuels; (Figure 1-2).10, 11 enhancing energy efficiency in buildings, industries, and transportation; increasing the adoption of electric vehicles and developing charging infrastructure; implementing carbon capture, utilization, and storage (CCUS) technologies; promoting low-carbon fuels like biofuels, hydrogen, and synthetic fuels for hard-to-electrify sectors; decarbonizing heavy industries through cleaner production processes; encouraging behavioral changes and demand management; and investing in innovation and technology development to support the transition to a low-carbon economy. <sup>12, 13</sup> Electricity is the fastest-growing clean energy carrier. Renewable energy sources generate electricity that needs to be transported and stored. Using electricity, particularly in energy-intensive industries like chemical manufacturing, is crucial for advancing societal electrification efforts.

The production of chemicals from fossil fuels is equally important, as these chemicals are integral to a wide range of industries, including pharmaceuticals, plastics, and agriculture. Transitioning to more sustainable methods for chemical production is crucial to reducing the environmental impact. This involves developing and adopting alternative feedstocks, such as biomass and recycled materials, as well as improving energy efficiency and implementing carbon capture and utilization technologies. Innovation in green chemistry and process optimization can also play a significant role in minimizing emissions and resource consumption, thereby supporting the broader goal of achieving net zero emissions by 2050.

As an abundant renewable carbon-based resource, biomass is expected to replace traditional fossil resources such as oil and coal for the production of fuels and chemicals to alleviate problems of energy depletion and the greenhouse effect. Around the world, there is a significant amount of biomass fuel used for small-scale heating and cooking. Highly inefficient combustion of biomass fuel could cause severe pollution. Utilizing renewable biomass fuel in this manner poses a challenge for sustainable development.

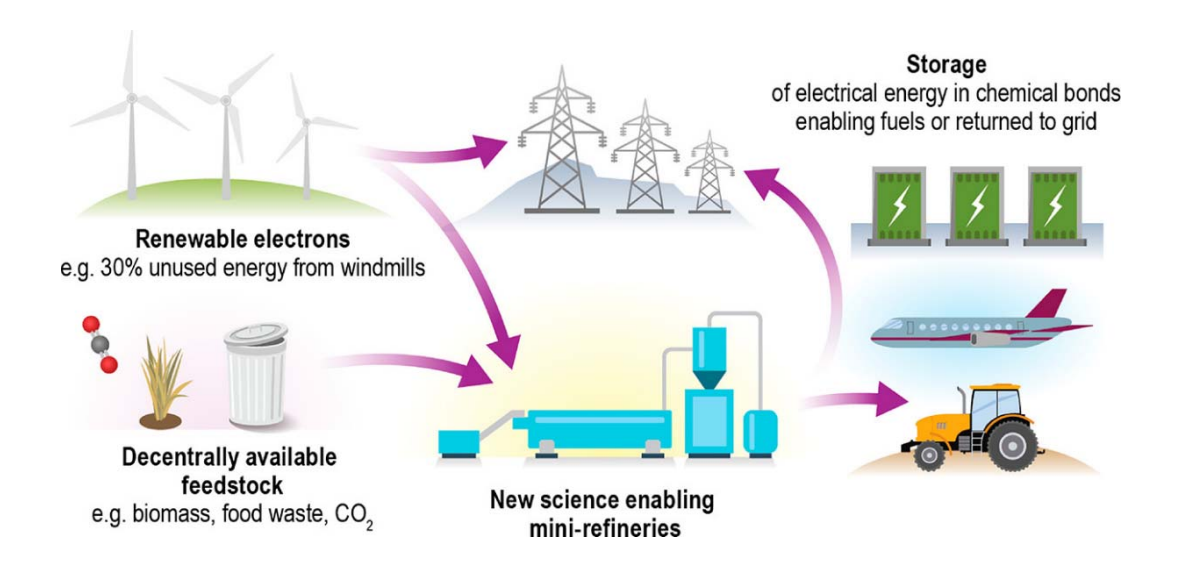


**Figure 1-2.** Schematic representation of decentralized conversion of dispersed, underutilized carbon resources into chemicals and/or fuels biomass valorization.<sup>14</sup>

Biomass valorization is the process of adding value to different types of plants and organic residues. Food crops tend to be avoided, as they are intended for human and animal use, particularly given the expected increase of the world population to more than 9 billion people by 2050. <sup>15</sup>

Waste biomass can be converted to green fuels and value-added products via thermochemical, electrochemical, photocatalytic and biological conversion processes. <sup>16-18</sup> The electrochemical conversion of biomass-derived chemicals represents a promising frontier in sustainable chemistry, offering innovative pathways to transform renewable resources into valuable compounds. Firstly, biomass must be converted to liquid form through pyrolysis or hydrothermal liquefaction. Then through another process to obtain derived high value-added products including the gaseous fuels (mostly H<sub>2</sub> and syngas), liquid hydrocarbon fuels (bio-oils, carboxylic, carbonyl, phenolic, aromatic, olefinic, ethereal, alcoholic, and aliphatic carbons) as alternative transportation fuels to petroleum-derived diesel and other fine chemicals such as phenol, benzaldehyde (BZH), 5-hydroxymethylfurfural (HMF) and so on. <sup>19-21</sup> One thing that should be pointed out is that biomass feeds are oxygen-rich and hydrogen-poor, yet high-energy fuels are oxygen-poor and hydrogen-rich. The amount of oxygen that can

be tolerated depends on the fuel or power application but invariably the oxygen content of raw biomass must be reduced to be viable. Therefore, multistep and integrated processes that deconstruct, liquefy, deoxygenate, and increase the hydrogen content are central to successful biomass utilization for energy purposes. <sup>22-25</sup> Combining biomass valorization and the electrification process of industrial production could be a great strategy for developing a sustainable future. <sup>26-28</sup>

#### 1.2 Electrochemistry

In 1821, Thomas Johann Seebeck discovered electrical current flowing through two interconnected, disparate metal plates when a temperature difference was applied across the junction, leading to the conversion of heat energy into electrical energy. Since then, extensive efforts have been made to study various techniques for converting electrical energy and other forms of energy, including the development of batteries, electrolysis for hydrogen production, and electrocatalytic synthesis of various high-value chemicals, enabling the conversion of electrical energy into chemical energy for storage. <sup>29, 30</sup>

In the early 19th century, researchers conducted simple electrochemical reduction reactions of organic compounds using inert cathodes (such as Hg, Pb, C) in single cells. Under an applied voltage, electrons flowed from the anode to the cathode, and organic compounds at the cathode surface gained electrons and were reduced. <sup>31</sup> These non-catalytic electron transfer reactions were often accompanied by rearrangement or coupling of organic radicals. Ludwig Gattermann worked with nitro compounds and summarized the ratio and yields of these products. He attributed the reduction activity to the primary hydrogen generated on the cathode, although it couldn't explain the differences in activity. <sup>32</sup>

In 1898, Fritz Haber and Bredig Leipzig studied the steps of electrochemical reduction of nitrobenzene at different potentials by using a reference electrode. They proposed that the electrode potential was the determining factor for redox reactions. Those works laid the foundation for further studies of organic electrochemical processes. <sup>33</sup> During

the same period, Kolbe electrolyzed highly concentrated carboxylic acids using platinum as the cathode under neutral or weakly acidic conditions and obtained the alkanes. <sup>34</sup> Tafel and Naumann later discovered 1,3,7-trimethylxanthine was more easily reduced on Hg electrode than succinimide under acidic conditions. The situation was the opposite on a Pb electrode. This led them to recognize different adsorption properties of organic substances on electrodes. Those are the fundamental understanding of organic electrocatalysis.

In 1905, Tafel conducted organic compound reduction experiments on different metal electrodes. He observed the highest activity of quinoline on Au electrodes with lower hydrogen overpotential. Tafel then explored various metals such as Pt, Hg, Ni, Cu, Au, Bi, and Sn for HER. In this process, he proposed the famous Tafel equation indicating that the logarithm of the current is linearly related to the electrode potential. This formula provides a quantitative description of the electrode kinetics. <sup>35</sup> Frank Popp later observed only electron transfer is involved on the inert electrode (e.g., Hg, Pb), while specific functional groups could be reduced on Ni, Pt, Pd electrodes. Thus, he concluded potential regulation and catalytic effects need to be considered simultaneously for electrochemical reduction of organic compounds. However, due to the rapid development of thermodynamic theories in the 1930s, organic thermal catalysis gradually took over the dominant position and achieved large-scale industrial application. Electrocatalysis was left behind in the laboratory.

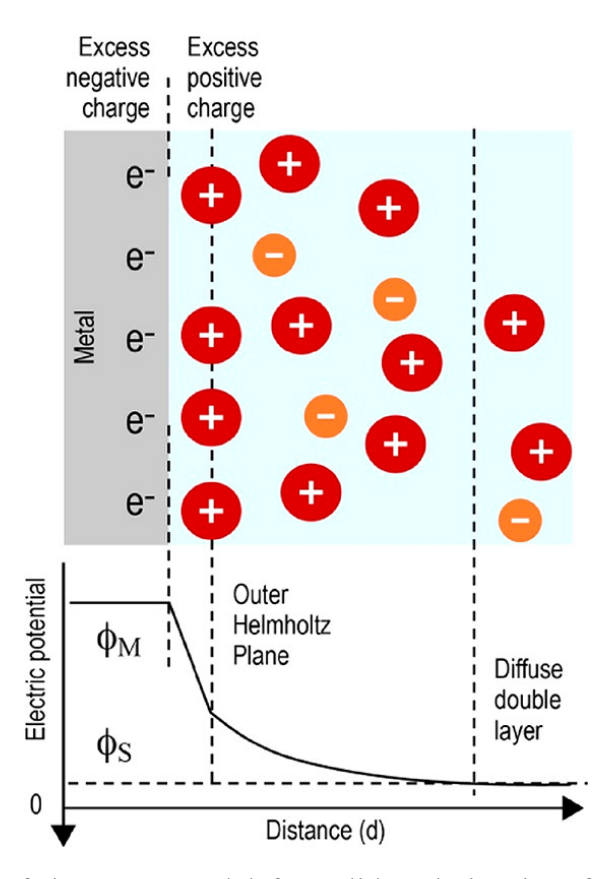


**Figure 1-3.** Structure of the Stern model for solid—solution interfaces and electric potential distribution. The metal surface has excess negative charge; thus, it attracts and enriches cations to the surface, forming a tightly packed layer of cations. This plane is called the Helmholtz plane. From this plane to the bulk solution, cation concentration decreases gradually to the level of the bulk solution while the anion concentration increases, forming a diffuse layer. The electric potential changes gradually from the metal surface to the bulk solution. The potential difference between the metal surface and the bulk solution is the electrode potential ( $\phi_{\text{electrode}} = \phi_{\text{M}} - \phi_{\text{S}}$ ).

In the mid-20th century, Butler and Volmer derived the Butler-Volmer equation (B-V equation) based on transition state theory and the Nernst equation. which is one of the most fundamental relationships in electrochemical kinetics and well explains the Tafel equation. <sup>36, 37</sup> Subsequently, modern electrochemical theories turned towards the electrode/electrolyte solution interface. Then various double-layer models to explain electrode processes, including the early Helmholtz model and Gouy-Chapman model, as well as the later more sophisticated Gouy-Chapman-Stern model were developed (Figure 1-3).<sup>38</sup> Theories about electron transfer at the solid-liquid interface also developed rapidly such as Franck-Condon principles of tunneling transitions and

Gurney Bockris' molecular theories. In 1956, Rudolph A. Marcus investigated the effect of solvent solvation on outer-sphere electron transfer using the continuous electrolyte theory and double-sphere model and developed the Marcus theory. With the rapid development of these fundamental electrochemical theories, the industrial application of electrocatalytic organic synthesis began to emerge. In 1961, M. Baizer from the Monsanto Company achieved industrialization of the electrolysis of acrylonitrile to produce adiponitrile for the first time.

As electrocatalysis theory flourished, electrolysis equipment underwent upgrades. In a single electrolysis cell, reduced organics products that diffuse from the cathode towards the anode and then are oxidized lower the yield. Therefore, baffles were required in the middle of the electrolysis cell in some cases. Initially, a glass sand core partition was applied to separate the cathode chamber and the anode chamber, which could not absolutely prevent the migration of organic substrates. In 1962, corporation DuPont invented the perfluorosulfonic acid (Nafion) membrane with the ability to only allow cations to pass through and good conductivity. Thus reducing the diffusion of organic compounds. Current electrolysis systems often use H-cell reactors separated with Nafion membranes for electrocatalytic reduction reactions. These H-type cells can flexibly perform different electrocatalytic reactions on the cathode and anode. Industrial electrolysis cells have also evolved. <sup>39, 40</sup> In practical applications, traditional box-type single electrolysis cells or electrolysis cells with enhanced mass transfer can be equipped based on the organic electrocatalytic characteristics. Solid polymer electrolyte (SPE) electrochemical reactors are smaller and more flexible where the electrodes and membrane are tightly pressed together, which can significantly reduce the resentence between electrodes. 41, 42 Depending on the reaction conditions required for organic reactions, alkaline membranes or bipolar membranes can be selected based on catalysts and organic substrates, thereby realizing versatile electrocatalytic transformations.

#### 1.3 Electrocatalytic reduction reaction mechanism of BZH

While during a series conversion process of raw biomass, Aldehydes are believed to be

particularly troublesome for the aldol condensation and polymerization reactions, to avoid which, a hydrogenation process is necessary. Meanwhile, the BZH hydrogenation product, BA, is a chemical commodity used as a solvent in the fields of printing and coating, and as an additive in the fragrance industry. 43 Another important carbonyl electroreduction process is dimerization, which shows potential for the production of fuels, 44 such as hydrofuroin (HDF) and hydrobenzoin (HDB). HDB is also an important industrial chemical as a structural motif in antiepileptic drugs and photo-initiators.<sup>45</sup> BZH has a simple aromatic structure with a benzene ring and a formyl group (CHO) attached to one of the carbons in the ring. Its molecular formula is C7H6O. Electrocatalytic reduction of BZH reaction possesses a dual nature involving both heterogeneous catalysis and electrochemical processes (Figure 1-4). During the reaction, the target functional group of the organic compound first chemically adsorbs onto the active sites of the catalyst. Subsequently, under the influence of an external circuit, charge transfer occurs, leading to the formation or cleavage of the targeted chemical bonds. The selectivity of the obtained products varies drastically under different electrolyte compositions. BZH can be electrochemically reduced to the corresponding methylated product toluene. Another electrocatalytic reduction reaction of BZH includes electrocatalytic hydrogenation (ECH) for obtaining benzyl alcohol

(BA) and dimerization for hydrobenzoin (HDB).

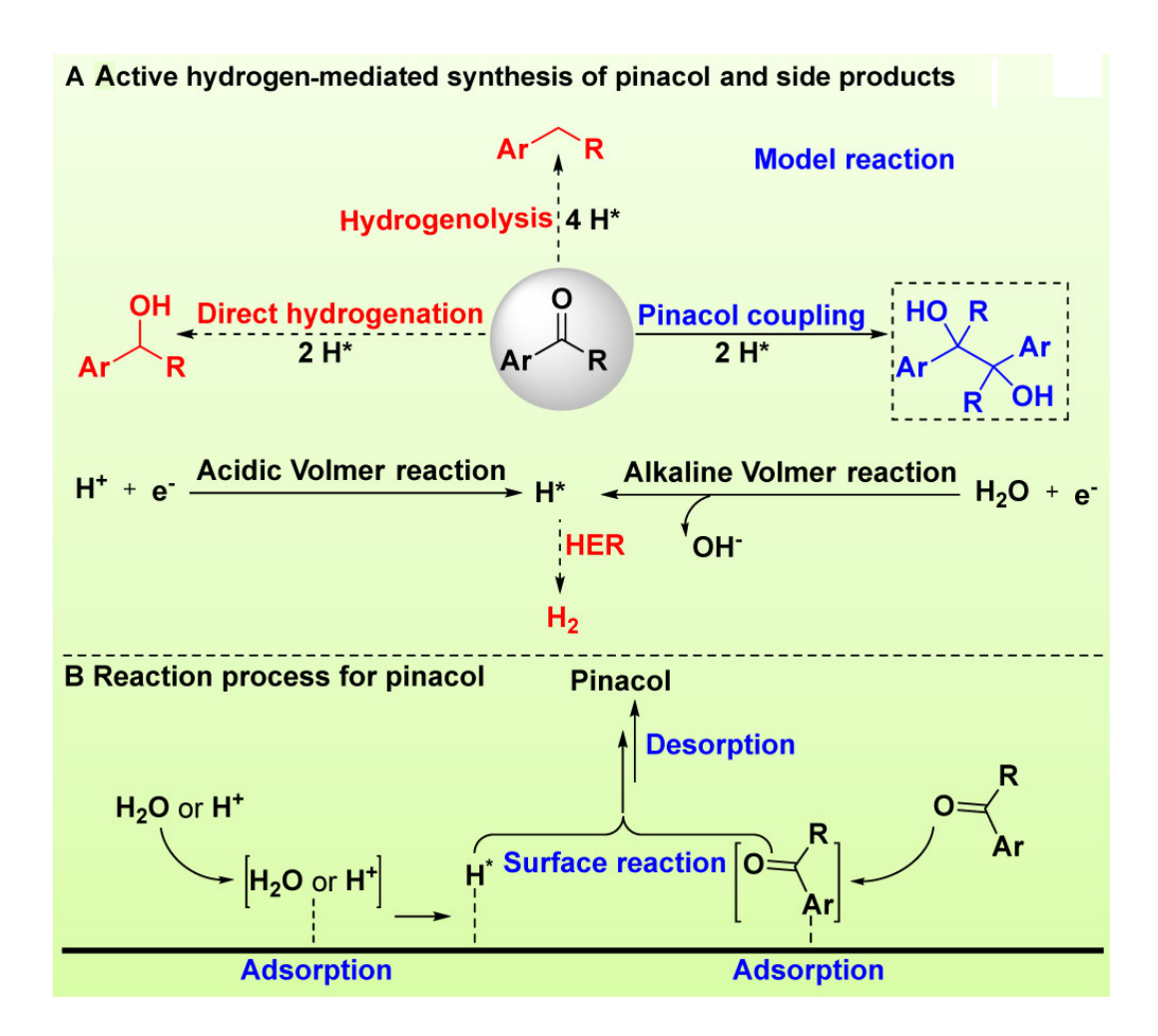


**Figure 1-4.** (a) Active hydrogen (H\*)-mediated synthesis of pinacol and byproducts in an aqueous solution; (b) proposed ideal electrode material to optimize H\* production, adsorption, surface reaction, and desorption during pinacol synthesis. <sup>46</sup>

The mechanism of the BZH ECH reaction can be primarily categorized into two types: one involves the reduction reaction of protons or proton donors with electrons on the surface of the cathode catalyst, followed by the generation of adsorbed hydrogen (Had). This hydrogen then undergoes the next step of reduction with organic substrates also adsorbed on the surface of the cathode. This type of reaction conforms to the Langmuir-Hinshelwood mechanism (LH mechanism). The LH mechanism emphasizes that the rate-determining step (RDS) of the reaction is the intermolecular reaction of molecules adsorbed on the catalyst surface, while the adsorption and desorption processes of reactants and products are in equilibrium. <sup>47</sup>

The second mechanism type of ECH reaction follows the Proton-Coupled Electron

Transfer (PCET) theory. In this case, the adsorbed organic material directly undergoes reduction reactions with protons (from the solution) or proton donors, along with electrons from the surface of the catalyst. PCET involves only a single transition state, avoiding the formation of high-energy intermediates in elemental steps. This optimization eliminates the need for high-energy intermediates and reaches the optimal thermodynamic driving force for the reaction.<sup>48</sup>

The elementary reaction steps for the LH mechanism and the PCET mechanism, as well as the competitive reaction steps involving Hydrogen Evolution Reaction (HER) and free radical dimerization reaction process, are as follows: 45, 49-55

1. LH mechanism: the ECH reaction consists of two steps. The first step involves the adsorption of organic species A and the formation of H<sub>ad</sub>, generated through the electrochemical Volmer reaction. The specific process is outlined below, where AH represents the intermediate product of A and a single electron and H, M denotes the catalytic active sites, and \* represents the adsorption sites:

Organic substrate A adsorption step:

$$A + M = M - A * \tag{1-1}$$

Volmer step:

$$H_3 O^+ + e^- + M = M - H * + H_2 O \text{ (acid)}$$
 (1-2)

$$H_2O + e^- + M \rightarrow M - H * + OH^-(base)$$
 (1-3)

The second step involves the non-electrochemical reaction between the adsorbed organic species M-A\* and adsorbed hydrogen M-H\*, known as the LH step, along with the subsequent desorption of product:

LH step:

$$M - A * + M - H * = M - AH * \tag{1-4}$$

Organic product desorption:

$$M - AH * = M + AH \tag{1-5}$$

2. PCET mechanism: The first step involves the adsorption of organic species B. The second step includes the reduction reaction between the adsorbed organic species M-B\*, protons (or other proton donors), and electrons, along with the subsequent desorption of the organic product.

Organic substrate B adsorption step:

$$B + M = M - B * \tag{1-6}$$

PCET step:

$$M - B * + H_3 O^+ + e^- = M - BH * + H_2 O$$
 (1-7)

Organic product desorption:

$$M - BH * = M + BH \tag{1-8}$$

3. HER Reaction: the HER side reaction often occurs, involving the desorption step of H<sub>ad</sub>. This process is divided into Heyrovsky and Tafel processes, where the Heyrovsky process is electrochemical desorption, and the Tafel process is chemical desorption.

Heyrovsky step:

$$M - H * + H_3 O^+ + e^- = + H_2 + H_2 O + M \text{ (acid)}$$
 (1-9)

$$M - H * + H_2O + e^- = H_2 + OH^- + M(base)$$
 (1-10)

Tafel step:

$$M - H * + M - H * = H_2 + 2M$$
 (1-11)

4. Dimerization or oligomerization: The dimerization reaction is typically considered an outer-sphere electron process. In this case, organic species C does not undergo adsorption but directly gains electrons from the cathode, forming radical C·. The radical then undergoes dimerization or oligomerization to generate the polymer C-C, which diffuses to the solution system or covers the electrode surface.

Dimerization step:

$$C + H_3 O^+ + e^- \leftrightharpoons C \cdot + H_2 O(\text{acid}) \tag{1-12}$$

$$C + H_2O + e^- = C \cdot + OH^-(base) \tag{1-13}$$

$$C \cdot + C := C - C \tag{1-14}$$

Typically, a reaction may produce various products, and the elementary steps leading to the formation of these products may involve different mechanisms. By systematically elucidating the mechanism, clarifying the pathways for product formation, and understanding the various elementary steps, it becomes possible to selectively control and mitigate side reactions This targeted approach allows for the adjustment of reaction conditions, thereby achieving high selectivity and efficiency for obtaining desired product.

# 1.4 Thermodynamics and kinetics of electrocatalytic reduction of BZH

#### 1.4.1 Thermodynamics of electrocatalytic reduction of BZH

For the ECH reaction, reactant A<sup>+</sup> obtained one electron:

$$A_{(aq)}^+ + e^- \to A_{(aq)}$$
 (1-15)

For which the chemical potential relationships is: <sup>56</sup>

$$\mu_{A^{+}} = \mu_{A^{+}}^{\circ} + RT \ln \alpha_{A^{+}} + F \emptyset_{A^{+}}$$
(1-16)

$$\mu_A = \mu_A^{\circ} + RT \ln \alpha_A \tag{1-17}$$

$$\mu_{e^-} = -F \phi_{e^-} \tag{1-18}$$

According to the definition of IUPAC (International Union of Pure and Applied Chemistry), the chemical potential of electrons in a solid is its Fermi level. At equilibrium, the electrochemical potential of the reactants is equal to the electrochemical potential of the products:

$$\mu_{A^{+}} + \mu_{e^{-}} = \mu_{A} \tag{1-19}$$

The potential difference  $\Delta \emptyset$  between the electrode and the electrolyte is:

$$\Delta \emptyset = \emptyset_{e^{-}} - \emptyset_{A^{+}} = \frac{\mu_{A^{+}}^{\circ} - \mu_{A}^{\circ}}{F} + \frac{RT}{F} \ln \left( \frac{\alpha_{A^{+}}}{\alpha_{A}} \right)$$
 (1-20)

 $\Delta \emptyset$  corresponds to the electrode potential, at standard conditions of 25°C, 1 M concentration and 1 atm pressure,  $\alpha_{A^+} = \alpha_A = 1$ , (1-20) can be simplified as:

$$\Delta \phi^{\circ} = \frac{\mu_{A^{+}}^{\circ} - \mu_{A}^{\circ}}{F} \tag{1-21}$$

 $\Delta \emptyset^{\circ}$  is the standard electrode potential of reaction (1-15).

For HER and its  $\Delta \emptyset_{RHE}$ :

$$H_{(aq)}^+ + e^- \to \frac{1}{2} H_2(g)$$
 (1-22)

$$\Delta \phi_{RHE} = \Delta \phi_{SHE} + \frac{RT}{F} \ln \left( \frac{\alpha_{H^+}}{\sqrt{P_{H_2}}} \right)$$
 (1-23)

$$\Delta \emptyset_{SHE} = \frac{\mu_{H^+}^{\circ} - \frac{1}{2}\mu_{H_2}^{\circ}}{F} \tag{1-24}$$

 $\Delta \phi_{SHE}$  is the standard hydrogen electrode (SHE) potential defined as 0 V and is commonly used as the reference potential.  $\Delta \phi_{RHE}$  is the reversible hydrogen electrode (RHE) potential. According to the Nernst equation, under standard conditions, the Nernst potential of HER relative to the general hydrogen electrode (NHE) is zero (EheR = 0 V vs. RHE). Similarly, the standard thermodynamic redox potential for organic reduction reaction can be calculated. For BZH convert into BA,  $C_6 S_5 CHO + 2e^- + 2H^+ \rightarrow C_6 S_5 CH_2 OH$ , EECH = 0.19 V vs. RHE <sup>51</sup> Typically, the ECH process for these organics is thermodynamically more favorable than that of HER. However, in the actual reaction process, the ECH reaction requires a larger applied potential than the HER to overcome the kinetic obstacles caused by high activation energy and low energy efficiency. While for radical self-coupling reaction, normally E is located at around 0 V vs. RHE.<sup>57</sup>

#### 1.4.2 Kinetics of electrocatalytic reduction of BZH

Reaction kinetics deduction can be achieved by altering reaction parameters such as organic substrate concentration, proton concentration, potential, current density, and temperature. Then analyze their influence on the rate of formation of the desired product to take deep insights into the reaction kinetics.<sup>58, 59</sup>

Next, we will discuss the impact of applying voltage on the reaction rate. For species A<sup>+</sup> receiving electrons to generate intermediate products equation (1-15), we can assume that the electron transfer occurs via a transition state to the product (Figure 1-5).

$$A_{(aa)}^+ + e^- \Leftrightarrow [TS] \to A_{(aa)}$$
 (1-25)

Then we can get:

$$\mu_{TS} = \mu_{TS}^{\circ} + RT \ln[TS] - F \phi_{TS} \tag{1-26}$$

where [TS] is the analytical concentration of the transition state. Using transition state theory, we also assume a quasi-equilibrium between the transition state and reactants.

$$\mu_{A^+} + \mu_{e^-} = \mu_{TS} \tag{1-27}$$

Therefore, the concentration of the transition state [TS] is expressed as:

$$[TS]_{aq} = \alpha_{A} + exp \left[ -\frac{\left(\mu_{TS}^{\circ} - \mu_{A}^{\circ} + \right) + F(\phi_{e} - \phi_{A} + - \phi_{TS})}{RT} \right]$$
 (1-28)

The term  $(\emptyset_{e^-} - \emptyset_{A^+})$  is the equilibrium electrode potential, and [TS]<sub>eq</sub> is the analyte concentration at equilibrium. Although the value of  $\emptyset_{TS}$  is unknown, we know it must be within the interval between  $\emptyset_{e^-}$  and  $\emptyset_{A^+}$ . A dimensionless charge transfer coefficient  $\alpha$  is proposed to evaluate  $\emptyset_{TS}$ :

$$\phi_{TS} = \phi_{e^{-}} - \alpha(\phi_{e^{-}} - \phi_{A^{+}}) \tag{1-29}$$

Here,  $\alpha \in [0, 1]$ , When  $\alpha = 1$ , the transition state is very close to the solution and  $\emptyset_{TS}$  is close to  $\emptyset_{A^+}$ ; when  $\alpha = 0$ , the transition state is very close to the electrode surface and  $\emptyset_{TS}$  is close to  $\emptyset_{e^-}$ . Equation 1-28 can then be expressed as:

$$[TS]_{aq} = \alpha_{A^{+}} exp \left[ -\frac{\left(\mu_{TS}^{\circ} - \mu_{A^{+}}^{\circ}\right) + F(\alpha(\phi_{e^{-}} - \phi_{A^{+}}) - \phi_{A^{+}})}{RT} \right]$$
(1-30)

To drive an electrode reaction, an overpotential  $(\eta)$  should be added to the electrode to break the balance of the forward and reverse reactions. The concentration of transition states under such an overpotential  $[TS]_{\eta}$  is then expressed as:

$$[TS]_{\eta} = \alpha_{A} + exp \left[ -\frac{\left(\mu_{TS}^{\circ} - \mu_{A}^{\circ} +\right) + F(\alpha(\emptyset_{e}^{-}, eq + \eta - \emptyset_{A}^{+}, eq)^{-} \emptyset_{A}^{+}, eq^{})}{RT} \right]$$

$$= [TS]_{eq} exp \left( -\frac{\alpha F \eta}{RT} \right)$$
(1-31)

The subscript "eq" indicates that the associated value is under equilibrium. Because the reaction rate is proportional to [TS], the forward reaction rate  $R_f$  is expressed as a function of overpotential  $\eta$ :

$$R_f(\eta) = R_f(0)exp(-\frac{\alpha F\eta}{RT})$$
 (1-32)

where  $R_f(0)$  is the rate at zero overpotential, which is also the rate at electrode equilibrium. The current across the electrode at  $R_f(0)$  is also known as the exchange current. In the same way, the reverse reaction rate  $R_r(\eta)$  is:

$$R_r(\eta) = R_r(0)exp(-\frac{(1-\alpha)F\eta}{RT})$$
(1-33)

Equations 1-32 and 1-33 show that a positive overpotential ( $\eta > 0$ ) increases the oxidation reaction rate, while a negative overpotential ( $\eta < 0$ ) increases the reduction reaction rate. Reactions such as an HER and ECH will have a high rate at a negative overpotential.

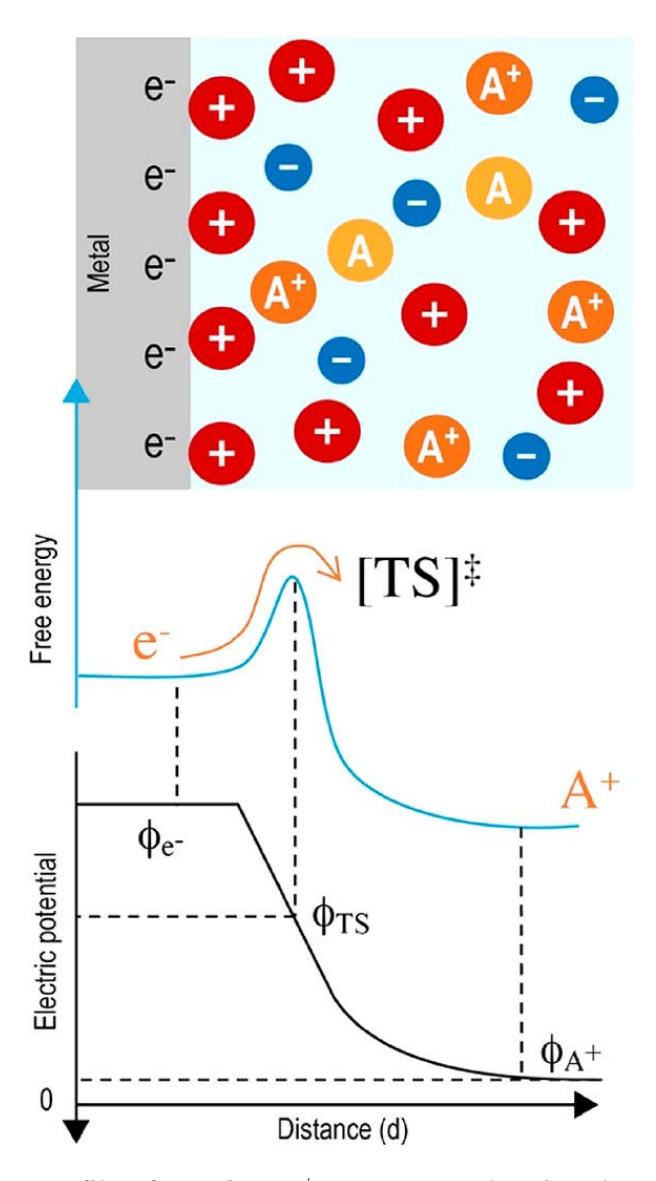


**Figure 1-5.** Energy profile of reaction A  $^+$  + e  $^ \rightarrow$  A, showing the electric potential at the transition state.  $^{51}$ 

In heterogeneous catalysis, the reaction rate is typically associated with the coverage of reactants on the catalyst surface. Coverage refers to the proportion of the catalyst surface occupied by the reactants. The derivation process for the relationship between reaction rate and coverage  $\theta$  is as follows:

In an acidic solution, the first step of ECH is the adsorption of substrate BZH, which we assume is equilibrated. This is followed by consecutive hydrogen addition steps. We surmise that the RDS is an LH or PCET step. The desorption of the product is kinetically irrelevant.

For the LH step, A represents an organic molecule, and H represents a hydrogen atom. There are two different scenarios one is competitive adsorption between A and H at a specific active site (competitive site, \*), and secondly, A does not compete with H for adsorption (for example, H adsorbed at a separate active site, ^). Herein, for equation (1-4):

Competitive LH:

$$M - A * + H * \stackrel{K_{LH,c}}{\Longleftrightarrow} M - AH + 2 * \tag{1-34}$$

Non-competitive LH:

$$M - A * + H^{\wedge} \stackrel{K_{LH,nc}}{\longleftrightarrow} M - AH + * +^{\wedge}$$
 (1-35)

Here we define  $\theta_A(E)$  as the coverage of organic A and  $\theta_H(E)$  as the coverage of organic  $H_{ad}$ , thus the rate equation for the ECH is:

$$r_{LH}(E) = K_{LH} \,\theta_A(E) \,\theta_H(E) \tag{1-36}$$

 $\theta_A(E)$  and  $\theta_H(E)$  are potentially relevant;  $k_{LH}$  is the rate constant for reaction (1-4) and is potentially irrelevant. When reaching adsorption equilibrium:

$$\theta_A(E) + \theta_H(E) + \theta *= 1 \tag{1-37}$$

$$v_{ads,A}(E) = K_{ads,A}[A] \theta *= K_{ads,A}[A] (1 - \theta_A(E) - \theta_H(E))$$
 (1-38)

$$v_{des,A}(E) = K_{des,A}[A] \theta_H(E) \tag{1-39}$$

Where  $v_{ads,A}(E)$ ,  $K_{ads,A}$ , [A],  $v_{des,A}(E)$ ,  $K_{des,A}$  are the adsorption rate, adsorption equilibrium constant, concentration, desorption rate, and the desorption equilibrium constant of intermediate A, respectively.

When reach equilibrium:

$$v_{ads,A}(E) = v_{des,A}(E) \tag{1-40}$$

$$K_{ads,A}[A](1 - \theta_A(E) - \theta_H(E)) = K_{ads,A}[A] \theta_H(E)$$
(1-41)

Giving considering that the adsorption equilibrium constant  $K_A$  for the ECH intermediate A as the ratio of the rate constants for adsorption and desorption, we can further derive the equation.

$$K_A = \frac{\theta_A(E)}{[A] (1 - \theta_A(E) - \theta_H(E))} \tag{1-42}$$

After rearrangement:

$$\theta_A(E) = \frac{K_A[A](1 - \theta_H(E))}{(1 + K_A[A])} \tag{1-43}$$

Similar like  $\theta_A(E)$ ,  $\theta_H(E)$  can be described, the adsorption equilibrium constant of  $H_{ad}$  is  $K_{volmer}(1-2)$ .  $[H_3O^+]$  is the proton concentration.

$$K_{volmer}(E) = \frac{\theta_H(E)}{[H_3O^+]\theta^*}$$
 (1-44)

$$K_{volmer}(E) = \frac{\theta_A(E)}{[H_3O^+](1 - \theta_A(E) - \theta_H(E))}$$

$$(1-45)$$

$$\theta_H(E) = \frac{K_{volmer}(E)[H_3O^+]}{1 + K_A[A] + K_{volmer}(E)[H_3O^+]}$$
(1-46)

Combined with (1-34):

$$\theta_A(E) = \frac{K_A[A]}{1 + K_A[A] + K_{volmer}(E)[H_3O^+]}$$
 (1-47)

For competitive LH:

$$r_{LH,c} = K_{LH,c} \frac{K_A[A]}{1 + K_A[A] + K_{volmer}(E)[H_3O^+]} \frac{K_{volmer}(E)[H_3O^+]}{1 + K_A[A] + K_{volmer}(E)[H_3O^+]}$$

$$= K_{LH,c} \frac{K_A [A] K_{volmer} (E) [H_3 O^+]}{(1 + K_A [A] + K_{volmer} (E) [H_3 O^+])^2}$$
(1-48)

For non-competitive LH:

$$K_{volmer}(E) = \frac{\theta_H(E)}{[H_3O^+]\theta^{\wedge}}$$
 (1-49)

$$1 = \theta_A(E) + \theta * \tag{1-50}$$

$$1 = \theta_H(E) + \theta^{\wedge} \tag{1-51}$$

$$K_A = \frac{\theta_A(E)}{[A] (1 - \theta_A(E))} \tag{1-52}$$

$$\theta_A(E) = \frac{K_A[A]}{1 + K_A[A]} \tag{1-53}$$

$$\theta_H(E) = \frac{K_{volmer}(E)[H_3O^+]}{1 + K_{volmer}(E)[H_3O^+]}$$
(1-54)

$$r_{LH,nc} = K_{LH,nc} \frac{K_A[A]K_{volmer}(E)[H_3O^+]}{(1+K_A[A])(1+K_{volmer}(E)[H_3O^+])}$$
(1-55)

For the competitive adsorption PCET step, since the hydrogenation step does not involve H<sub>ad</sub>, proton can be directly captured from the electrolyte, so there is:

$$r_{PCET} = K_{PCET}\theta_A(E)[H_3O^+] \tag{1-56}$$

$$r_{PCET} = K_{PCET} \left[ H_3 O^+ \right] \frac{K_A [A]}{1 + K_A [A] + K_{volmer} (E) [H_3 O^+]}$$
(1-57)

For the non-competitive adsorption PCET step:

$$r_{PCET} = K_{PCET} \left[ H_3 O^+ \right] \frac{K_A[A]}{1 + K_A[A]} \tag{1-58}$$

## 1.5 Electrode materials for electrocatalytic reduction of BZH

#### 1.5.1 Electrode materials for ECH of BZH into BA

Massive efforts towards the identification of different reaction pathways and the selection of electrode materials have been dedicated. <sup>43, 60-64</sup> Jamie D. Holladay's group explored rates of BZH ECH and HER over C-supported noble-metals (NMs, Pd, Pt) and base-metals (BMs, Cu, Co, Ni, and Zn) and the bare CF (Figure 1-6a-d). The only organic product on NMs was BA. In addition to this alcohol, the BMs produced HDB. Pd showed the highest ECH rates followed by Ru and Rh, whereas on Pd and Ru, the ECH rates increased linearly with negative half-cell potential and the ECH activity of Rh remained unaltered in the same potential range. HER activities of the NMs followed an activity trend opposite to that of their ECH activity. That is, Rh had the highest HER

activity followed by Ru, and Pd had the lowest HER activity. Cu had the highest HER activity among BMs followed by Ni, Co, and Zn. They also analyzed how the binding energies (BEs) relate to the measured ECH activity and exhibit the maximum for Pd at -3.16 eV (Figure 1-6e-f). BZH binds on Cu weakly (-0.70 eV), while it binds on Ru strongly (-4.84 eV), i.e., they show the same ECH activity, but they sit at opposite sides of the ECH volcano plot. In contrast, Pd has an optimum BE with BZH (-3.16 eV), which helps explain why it is consistently found to be the most active and selective metal for ECH of this model compound. At the extremes but different sides of the ECH volcano plot lie Zn, Rh, and Co, which exhibit negligible ECH rates. Ni is the only metal that significantly deviates from its expected performance based on the predicted BE with BZH.

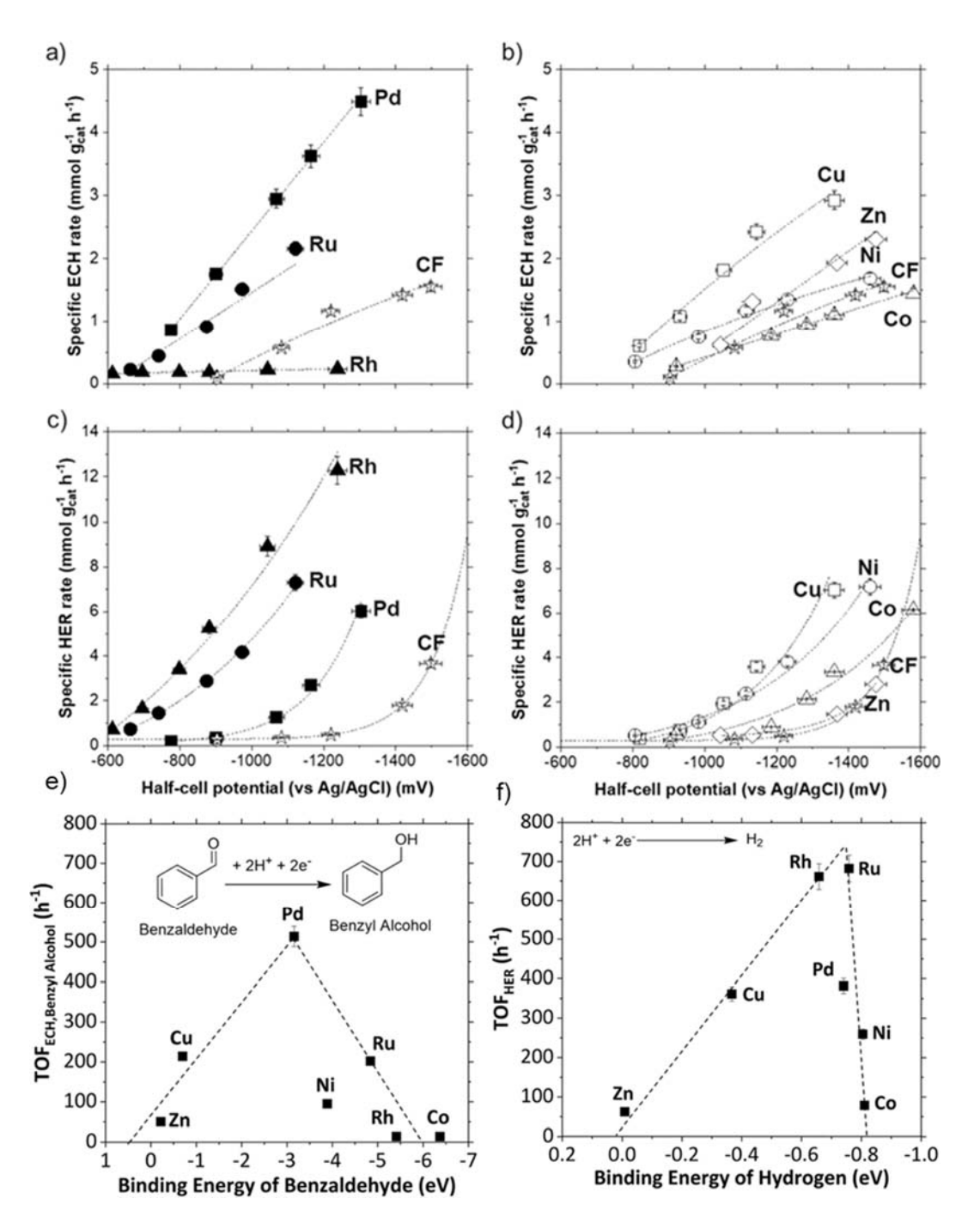


**Figure 1-6**. Rates of ECH of benzaldehyde as a function of half-cell potentials on (a) noble metals (NM) and (b) base metals (BM) with the corresponding H<sub>2</sub> evolution reaction (HER) rates on (c) NM and (d) BM. The symbols represent the different catalysts tested, where ■ is Pd, ● is Ru, ▲ is Rh, □ is Cu, ♦ is Zn,  $\circ$  is Ni,  $\Delta$  is Co, and  $\Rightarrow$  is blank carbon felt (CF). The experiments were carried out galvanostatically at atmospheric pressure and room temperature. The dotted lines are linear, and exponential trendlines fitted to the data for illustrative purposes. The catholyte was 80 mM benzaldehyde in an electrolyte composed of 47.5 wt % isopropanol, 47.5 wt % DI water,

and 5 wt % acetic acid. The anolyte was 1 M KOH in an electrolyte composed of 50 wt % DI water and 50 wt % methanol. Volcano plots combining the experimentally measured intrinsic rates of ECH of BZH to BA with the computed binding energies (BEs) of benzaldehyde (e) and the experimentally measured intrinsic rates of HER in the presence of BZH with the computed BEs of hydrogen (f). All rates were obtained at applied potentials of -1150 mV vs Ag/AgCl at atmospheric pressure and room temperature. The dotted lines are for illustrative purposes only. The catholyte was composed of 80 mM benzaldehyde in an electrolyte composed of 47.5 wt % isopropanol, 47.5 wt % H<sub>2</sub>O, and 5 wt % acetic acid. The computed BEs were obtained for a surface charge of -0.01 e<sup>-</sup>/surface atoms. So

In addition to screening active components of electrode materials, the regulation of ECH environment is also a crucial aspect. Based on the different reaction mechanisms of ECH, highly efficient ECH reactions can be achieved by modifying the microenvironment of the catalyst support to the proton concentration or organic compound concentration in the catalytic environment. <sup>66, 67</sup>

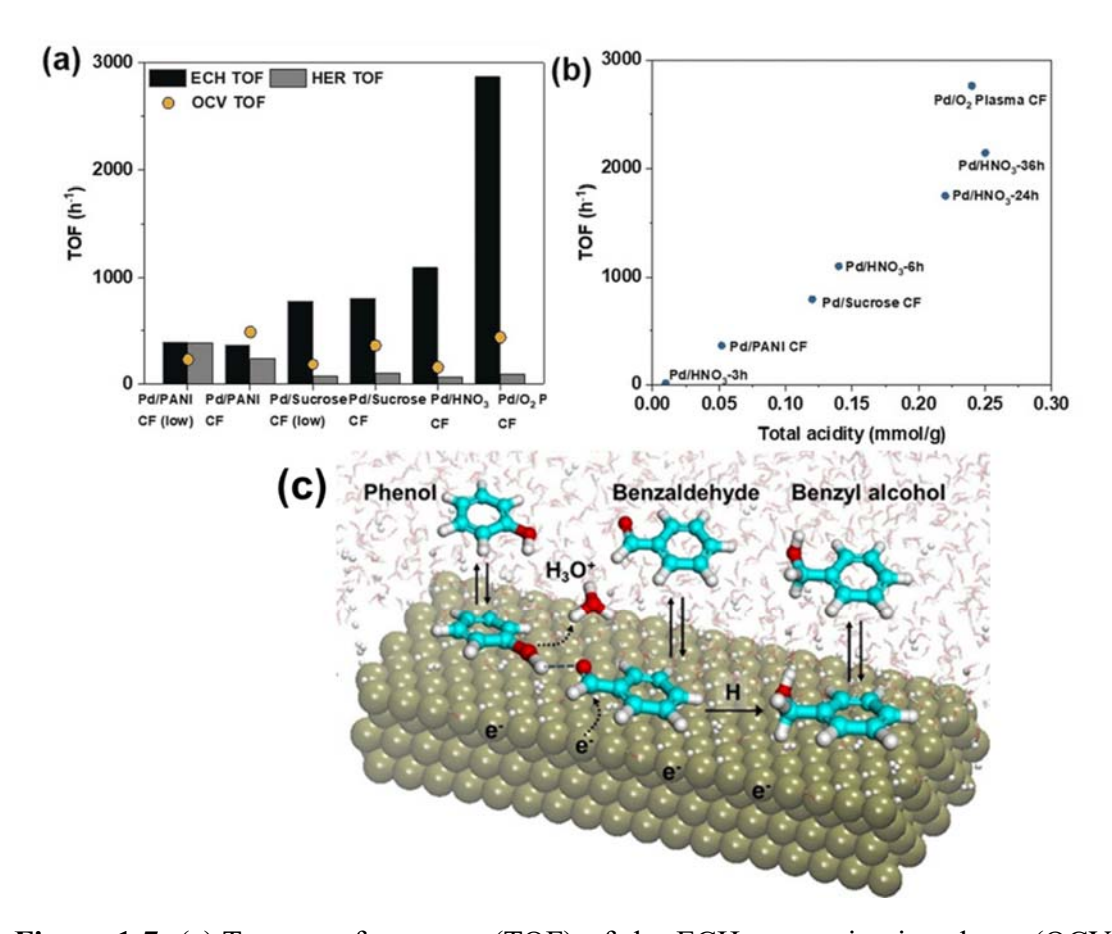


**Figure 1-7.** (a) Turnover frequency (TOF) of the ECH, open-circuit voltage (OCV) reactions, and H<sub>2</sub> evolution (HER) observed during the ECH of benzaldehyde on Pd supported on functionalized felts. (b) TOFs of the ECH of benzaldehyde vs. the concentration of acid sites in the Pd catalysts. Electrochemical tests were performed with solutions containing 20 mm benzaldehyde in an acetate buffer (pH 5.2) at -0.1 V vs. RHE. OCV experiments were performed with 1 bar H<sub>2</sub> instead of an external potential. (c) Schematic diagram of the electrocatalytic hydrogenation of the H-bonded complex formed upon adsorption of benzaldehyde and phenol. The double arrows denote adsorption and the dashed arrows illustrate the flow of electrons accompanying the deprotonation of the hydronium ion and the reduction of the carbonyl group.

Due to the strong adsorption energy of BZH on Pd and the possibility of hydrogenation reaction under acidic conditions through PCET mechanism, increasing the concentration of protons around the catalyst can increase the ECH reaction rate.<sup>68</sup> Lercher's group achieved a significant improvement in the efficiency of BZH ECH to BA by functionalizing the material of Pd supported on carbon (Pd/C), which is that to increase the concentration of Brønsted acid sites around the Pd active sites. <sup>69</sup> Figure 1-

7 show that introducing heteroatoms into the carbon support (via nitrogen functionalization using polyaniline, and oxygen functionalization through nitric acid treatment and oxygen plasma treatment) resulted in a FE for ECH in the range of 40% to 50% of nitrogen-functionalized Pd/C catalysts, while oxygen-functionalized catalysts exhibited FE as high as 80% to 95%. The Turnover Frequency (TOF) of the ECH reaction is directly proportional to the concentration of Brønsted acid sites, confirming the involvement of the PCET mechanism. To elucidate the mechanism, the authors employed a thermal catalytic LH mechanism using H<sub>2</sub> as a reductant and found that the thermal catalytic hydrogenation rate was not affected by the acid-groups functionalization of the support. Therefore, the hydrogenation step was determined as first taking place the simultaneous adsorption of protons and BZH on acid sites formed near Pd particles, followed by electron transfer from the Pd active sites. This effect is enhanced as the ion concentration decreases in the solution. Lercher's group also achieved a higher reaction rate by adding phenol into the BZH ECH system. <sup>70</sup> They attribute this enhancement to the polarization of the carbonyl group in BZH by hydrogen bonding interactions with phenol and a more facile proton-coupled electron transfer pathway enabled by a transition state stabilized by phenol.

## 1.5.2 Electrode materials for self-coupling reaction of BZH into HDB

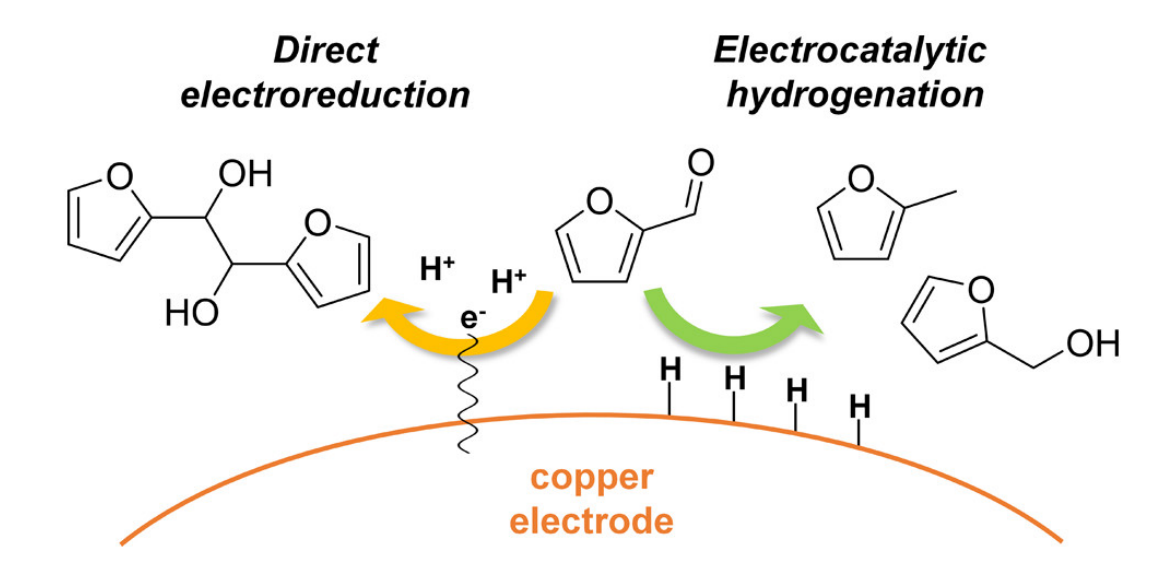


**Figure 1-8.** Illustration of electrochemical reduction pathways of carbonyl compounds in acidic electrolytes. <sup>71</sup>

The mechanisms of ECH and dimerization are illustrated in Figure 1-8. On a Cu electrode, the ECH process for furfural involves a reaction between Hads and the adsorbed furfural molecules. However, dimerization occurs via the electrochemical reduction (ECR) pathway, where furfural participates in electron transfer at the electrode. In the ECR pathway, the carbonyl group undergoes protonation in the solution and then reacts with electrons from the electrode to generate a radical intermediate (·C-OH). This intermediate can either dimerize through C-C coupling with another radical or undergo further transformation with another H<sup>+</sup>/e<sup>-</sup> to generate furfuryl alcohol. Commonly believed that the self-coupling reaction of BZH into HDB follows the electrochemical reduction step, not a catalytic process, which means there is no adsorption-desorption step of substrate and intermediate.  $^{44,46,71,72}$  This means that the rate of electrocatalytic self-coupling reactions of BZH to HDB is independent of the electrode material and is only dependent on the voltage. As the standard thermodynamic redox potential of the self-coupling reaction is very close to that of the BZH ECH and HER, the selection of electrode materials emphasizes suppressing the selectivity of these latter two reactions. One strategy involves selecting electrode materials (C, Pb, Zn, Cd etc.) with a high overpotential for the HER, 46, 73 while another

strategy focuses on suppressing the adsorption of substrates on the catalyst surface.<sup>74</sup> For example, Lam's group explored the use of MoS<sub>2</sub> in the electrocatalytic hydrogenation and dimerization of furfural.<sup>54</sup> They found that the octahedral MoS<sub>2</sub> structure (1T phase), exhibiting metallic properties, promotes the production of monoalcohols, while the semiconducting hexagonal MoS<sub>2</sub> structure (2H phase) showed higher selectivity towards dimer formation.

### 1.6 Fundamental studies of electrooxidization of BZH

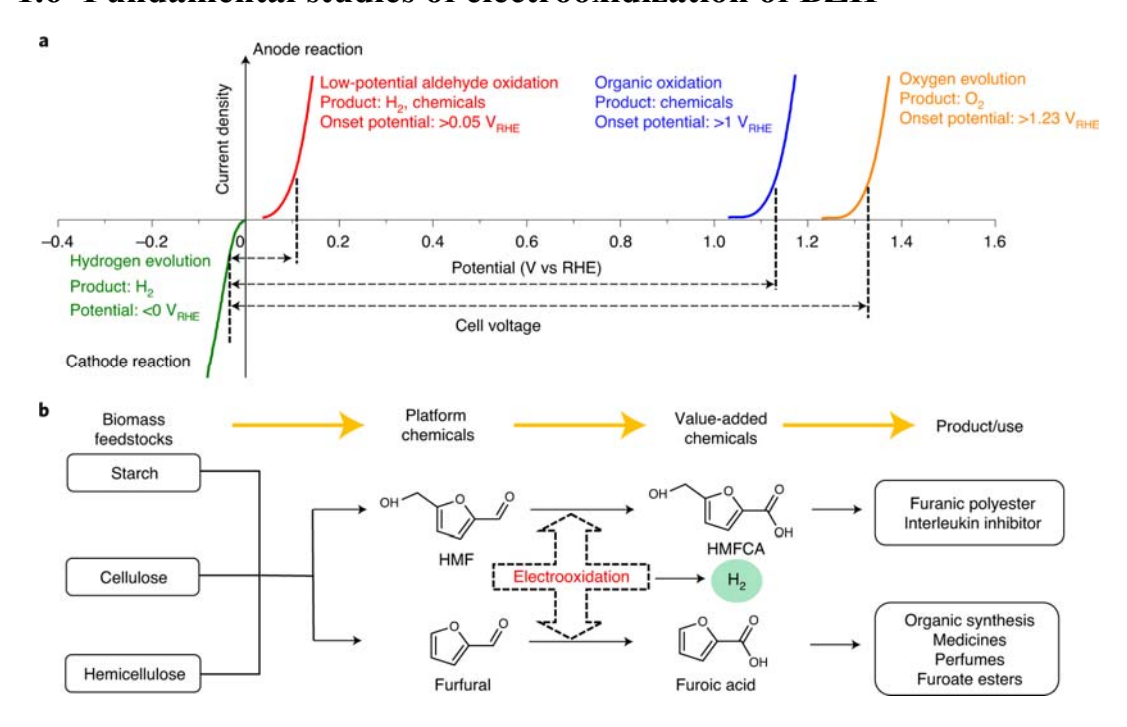


**Figure 1-9.** (a) Comparison of various anode reactions for water electrolysis; (b) Electrochemistry-involved conversion path from biomass feedstock into value-added chemicals. <sup>78</sup>

Electrocatalytic water splitting is widely acknowledged as the most sustainable and environmentally friendly method for producing H<sub>2</sub>. However, its efficiency is significantly hindered by the sluggish kinetics of the oxygen evolution reaction (OER) occurring at the anode. In contrast, electrooxidation of organic compounds (EOO) is more favorable both thermodynamically and kinetically compared to OER. Consequently, the combination of EOO with the HER has emerged as a promising alternative pathway, as it can greatly enhance the catalytic efficiency for H<sub>2</sub> production.

Moreover, this coupling enables the generation of value-added organic compounds on the anode through electrooxidation upgrading simultaneously. Various electrocatalysts have been developed for aldehydes oxidization. Alloys like PdAu, oxides like NiO, NiCo<sub>3</sub>O<sub>4</sub>, hydroxide-based materials like Ni/Co/Fe-OOH, sulfides, phosphides, selenides and with various morphologies such as layered double hydroxides, nanoparticles, nanosheets, and nanowires are all being designed and explored. <sup>75</sup> In 2017, Sun's group has explored the significant meaning of electrocatalysis of furfural oxidation coupled with H<sub>2</sub> evolution. <sup>76</sup> In 2021, Wang et al. successfully realized the low-potential electrooxidation of FUR and HMF at about 0.1 V RHE on a Cu catalyst. In contrast to traditional aldehyde electrooxidation, when coupled with the HER, the assembled electrolyzer produced H<sub>2</sub> on both the cathode and the anode. The energy input was about 0.35 kWh for 1 m <sup>3</sup> H<sub>2</sub> production, much lower than the 5 kWh for H<sub>2</sub> generation from conventional water electrolysis. <sup>77</sup>

### 1.7 References

- 1. Yue, X.-L.; Gao, Q.-X., Contributions of natural systems and human activity to greenhouse gas emissions. *Adv Clim Change Res.* **2018**, 9 (4), 243-252.
- 2. Kumar, V.; Ranjan, D.; Verma, K., 9 Global climate change: the loop between cause and impact. In Global Climate Change, Singh, S.; Singh, P.; Rangabhashiyam, S.; Srivastava, K. K., *Eds. Elsevier:* **2021**; pp 187-211.
- 3. Das, A. K.; Sharma, A., Chapter 1 Climate change and the energy sector. In Advancement in Oxygenated Fuels for Sustainable Development, Kumar, N.; Mathiyazhagan, K.; Sreedharan, V. R.; Kalam, M. A., *Eds. Elsevier:* **2023**; pp 1-6.
- 4. Wikipedia: Scientific consensus on climate change. https://en.wikipedia.org/wiki/Scientific\_consensus\_on\_climate\_change
- 5. Kumar, S.; Chatterjee, U.; David Raj, A.; Sooryamol, K. R., Global Warming and Climate Crisis/Extreme Events. In Climate Crisis: Adaptive Approaches and Sustainability, Chatterjee, U.; Shaw, R.; Kumar, S.; Raj, A. D.; Das, S., Eds. Springer Nature Switzerland: *Cham*, **2023**; pp 3-18.
- 6. Subramanian, A.; Nagarajan, A. M.; Vinod, S.; Chakraborty, S.; Sivagami, K.; Theodore, T.; Sathyanarayanan, S. S.; Tamizhdurai, P.; Mangesh, V. L., Long-

- term impacts of climate change on coastal and transitional eco-systems in India: an overview of its current status, future projections, solutions, and policies. *RSCAdv.* **2023**, 13 (18), 12204-12228.
- 7. Mishra, R. K.; Dubey, S. C., Solar Activity Cause and Effect of Climate Variability and Their Various Impacts. *British Journal of Multidisciplinary and Advanced Studies* **2023**, 4 (2), 21-38.
- 8. Kabir, M.; Habiba, U.; Iqbal, M. Z.; Shafiq, M.; Farooqi, Z. R.; Shah, A.; Khan, W., Impacts of anthropogenic activities & Earth and Environment in 21st Century; A Critical Review. *IOP Conference Series: Earth and Environmental Science* **2023**, 1194 (1), 012010.
- 9. Cronan, C. S., Atmospheric Influences, Global Warming, and Climate Change. In Ecology and Ecosystems Analysis, Cronan, C. S., *Ed. Springer Nature Switzerland: Cham,* **2023**; pp 223-240.
- 10. Paraschiv, L. S.; Paraschiv, S., Contribution of renewable energy (hydro, wind, solar and biomass) to decarbonization and transformation of the electricity generation sector for sustainable development. *Energy Rep.* **2023**, 9, 535-544.
- 11. Osman, A. I.; Chen, L.; Yang, M.; Msigwa, G.; Farghali, M.; Fawzy, S.; Rooney, D. W.; Yap, P.-S., Cost, environmental impact, and resilience of renewable energy<sup>†</sup> under a changing climate: a review. *Environ. Chem. Lett.* **2023**, 21 (2), 741-764.
- 12. Islam, M. A.; Che, H. S.; Hasanuzzaman, M.; Rahim, N. A., Chapter 5 Energy demand forecasting. In Energy for Sustainable Development, Hasanuzzaman, M. D.; Rahim, N. A., *Eds. Academic Press*: **2020**; pp 105-123.
- 13. Smil, V., Energy Transitions: Global and National Perspectives. **2017**.
- 14. Akhade, S. A.; Singh, N.; Gutierrez, O. Y.; Lopez-Ruiz, J.; Wang, H.; Holladay, J. D.; Liu, Y.; Karkamkar, A.; Weber, R. S.; Padmaperuma, A. B.; Lee, M. S.; Whyatt, G. A.; Elliott, M.; Holladay, J. E.; Male, J. L.; Lercher, J. A.; Rousseau, R.; Glezakou, V. A., Electrocatalytic Hydrogenation of Biomass-Derived Organics: A *Review. Chem. Rev.* **2020**, 120 (20), 11370-11419.
- 15. Pfab, E.; Filiciotto, L.; Luque, R., The Dark Side of Biomass Valorization: A Laboratory Experiment To Understand Humin Formation, Catalysis, and Green Chemistry. *J. Chem. Educ.* **2019**, 96 (12), 3030-3037.

- 16. Velvizhi, G.; Jacqueline, P. J.; Shetti, N. P.; K, L.; Mohanakrishna, G.; Aminabhavi, T. M., Emerging trends and advances in valorization of lignocellulosic biomass to biofuels. *J. Environ. Manage.* **2023**, 345, 118527.
- 17. Ambaye, T. G.; Djellabi, R.; Vaccari, M.; Prasad, S.; M Aminabhavi, T.; Rtimi, S., Emerging technologies and sustainable strategies for municipal solid waste valorization: Challenges of circular economy implementation. *J. Clean. Prod.* **2023**, 423, 138708.
- 18. Naveen, S.; Aravind, S.; Yamini, B.; Vasudhareni, R.; Gopinath, K. P.; Arun, J.; Pugazhendhi, A., A review on solar energy intensified biomass valorization and value-added products production: Practicability, challenges, techno economic and lifecycle assessment. *J. Clean. Prod.* **2023**, 405, 137028.
- 19. Zou Jun, C. Y., Yang Haiping, Chen Hanping, Review on high value utilization of biomass. *J. Huazhong Univ. Sci. Technol. Med. Sci.* **2022**, 07, 79-88.
- 20. He, J.; Qiang, Q.; Bai, L.; Su, W.; Yu, H.; Liu, S.; Li, C., Acetalization strategy in biomass valorization: a review. *Industrial Chemistry & Materials* **2024**.
- 21. Yangin-Gomec, C.; Sárvári Horváth, I.; Martín, C., Energy Production from Biomass Valorization. *Energies* **2023**, 16 (11).
- 22. Lucas, F. W. S.; Grim, R. G.; Tacey, S. A.; Downes, C. A.; Hasse, J.; Roman, A. M.; Farberow, C. A.; Schaidle, J. A.; Holewinski, A., Electrochemical Routes for the Valorization of Biomass-Derived Feedstocks: From Chemistry to Application. *ACS Energy Lett.* **2021**, 6 (4), 1205-1270.
- 23. Matthessen, R.; Fransaer, J.; Binnemans, K.; De Vos, D. E., Electrocarboxylation: towards sustainable and efficient synthesis of valuable carboxylic acids. *Beilstein J. Org. Chem.* **2014**, 10, 2484-2500.
- 24. Liu, Y.; Li, G.; Hu, Y.; Wang, A.; Lu, F.; Zou, J.-J.; Cong, Y.; Li, N.; Zhang, T., Integrated Conversion of Cellulose to High-Density Aviation Fuel. *Joule* **2019**, 3 (4), 1028-1036.
- 25. Davis, R. E.; Grundl, N. J.; Tao, L.; Biddy, M. J.; Tan, E. C.; Beckham, G. T.; Humbird, D.; Thompson, D. N.; Roni, M. S. Process Design and Economics for the Conversion of Lignocellulosic Biomass to Hydrocarbon Fuels and Coproducts: 2018 Biochemical Design Case Update; Biochemical Deconstruction and Conversion of Biomass to Fuels and Products via Integrated Biorefinery Pathways; United States, 2018-11-19, **2018**.

- 26. Schotten, C.; Nicholls, T. P.; Bourne, R. A.; Kapur, N.; Nguyen, B. N.; Willans, C. E., Making electrochemistry easily accessible to the synthetic chemist. *Green Chem.* **2020**, 22 (11), 3358-3375.
- 27. Jayan, K.; Thadathil, D. A.; Varghese, A., Electrochemical Hydrogenation of Organic Compounds: A Sustainable Approach. *Asian J. Org. Chem.* **2023**, 12 (10), e202300309.
- 28. Kleinhaus, J. T.; Wolf, J.; Pellumbi, K.; Wickert, L.; Viswanathan, S. C.; junge Puring, K.; Siegmund, D.; Apfel, U.-P., Developing electrochemical hydrogenation towards industrial application. *Chem. Soc. Rev.* **2023**, 52 (21), 7305-7332.
- 29. Yan, Z.; Hitt, J. L.; Turner, J. A.; Mallouk, T. E., Renewable electricity storage using electrolysis. *Proc. Natl. Acad. Sci. U.S.A.* **2020**, 117 (23), 12558-12563.
- 30. Lv, J.; Xie, J.; Mohamed, A. G. A.; Zhang, X.; Wang, Y., Photoelectrochemical energy storage materials: design principles and functional devices towards direct solar to electrochemical energy storage. *Chem. Soc. Rev.* **2022**, 51 (4), 1511-1528.
- 31. Shukla, A.; Prem Kumar, T., Electrochemistry: Retrospect and Prospects. *Isr. J. Chem.* **2021**, 61 (1-2), 120-151.
- 32. KIKUCHI, Y., Practice and Experiment: Analysis, Synthesis, and Paper Tools. *A Cultural History of Chemistry in the Nineteenth Century* **2023**, 67.
- 33. Yount, J.; Piercey, D. G., Electrochemical Synthesis of High-Nitrogen Materials and Energetic Materials. *Chem. Rev.* **2022**, 122 (9), 8809-8840.
- 34. Brachi, M.; El Housseini, W.; Beaver, K.; Jadhav, R.; Dantanarayana, A.; Boucher, D. G.; Minteer, S. D., Advanced Electroanalysis for Electrosynthesis. *ACS Organic & Inorganic Au* **2023**.
- 35. Fang, Y.-H.; Liu, Z.-P., Tafel Kinetics of Electrocatalytic Reactions: From Experiment to First-Principles. *ACS Catal.* **2014**, 4 (12), 4364-4376.
- 36. Dickinson, E. J. F.; Wain, A. J., The Butler-Volmer equation in electrochemical theory: Origins, value, and practical application. *J. Electroanal. Chem.* **2020**, 872, 114145.
- 37. Dreyer, W.; Guhlke, C.; Müller, R., A new perspective on the electron transfer: recovering the Butler-Volmer equation in non-equilibrium thermodynamics. *Phys.*

- Chem. Chem. Phys. 2016, 18 (36), 24966-24983.
- 38. Damaskin, B. B.; Petrii, O. A., Historical development of theories of the electrochemical double layer. *J Solid State Electrochem.* **2011**, 15 (7), 1317-1334.
- 39. Chen, M.; Kitiphatpiboon, N.; Feng, C.; Abudula, A.; Ma, Y.; Guan, G., Recent progress in transition-metal-oxide-based electrocatalysts for the oxygen evolution reaction in natural seawater splitting: A critical review. *eScience* **2023**, 3 (2), 100111.
- 40. Chen, F.-Y.; Wu, Z.-Y.; Adler, Z.; Wang, H., Stability challenges of electrocatalytic oxygen evolution reaction: From mechanistic understanding to reactor design. *Joule* **2021**, 5 (7), 1704-1731.
- 41. Green, S. K.; Tompsett, G. A.; Kim, H. J.; Kim, W. B.; Huber, G. W., Electrocatalytic Reduction of Acetone in a Proton-Exchange-Membrane Reactor: A Model Reaction for the Electrocatalytic Reduction of Biomass. *ChemSusChem* **2012**, 5 (12), 2410-2420.
- 42. Hui, H.; Wang, H.; Mo, Y.; Yin, Z.; Li, J., Optimal design and evaluation of electrocatalytic reactors with nano-MnOx/Ti membrane electrode for wastewater treatment. *J. Chem. Eng.* **2019**, 376, 120190.
- 43. Bhanushali, J. T.; Kainthla, I.; Keri, R. S.; Nagaraja, B. M., Catalytic Hydrogenation of Benzaldehyde for Selective Synthesis of Benzyl Alcohol: A Review. *ChemistrySelect* **2016**, 1 (13), 3839-3853.
- 44. Bender, M. T.; Yuan, X.; Goetz, M. K.; Choi, K.-S., Electrochemical Hydrogenation, Hydrogenolysis, and Dehydrogenation for Reductive and Oxidative Biomass Upgrading Using 5-Hydroxymethylfurfural as a Model System. *ACS Catal.* **2022**, 12 (19), 12349-12368.
- 45. Yu, J.; Zhang, P.; Li, L.; Li, K.; Zhang, G.; Liu, J.; Wang, T.; Zhao, Z.-J.; Gong, J., Electroreductive coupling of benzaldehyde by balancing the formation and dimerization of the ketyl intermediate. *Nat. Commun.* **2022**, 13 (1), 7909.
- 46. Liu, C.; Li, R.; Zhou, W.; Liang, Y.; Shi, Y.; Li, R.-L.; Ling, Y.; Yu, Y.; Li, J.; Zhang, B., Selectivity Origin of Organic Electrosynthesis Controlled by Electrode Materials: A Case Study on Pinacols. *ACS Catal.* **2021**, 11 (14), 8958-8967.
- 47. Liu, C.; Wu, Y.; Zhao, B.; Zhang, B., Designed Nanomaterials for Electrocatalytic Organic Hydrogenation Using Water as the Hydrogen Source. *Acc.*

- Chem. Res. 2023, 56 (13), 1872-1883.
- 48. Costentin, C., Electrochemical Approach to the Mechanistic Study of Proton-Coupled Electron Transfer. *Chem. Rev.* **2008**, 108 (7), 2145-2179.
- 49. Liu, L.; Liu, H.; Huang, W.; He, Y.; Zhang, W.; Wang, C.; Lin, H., Mechanism and kinetics of the electrocatalytic hydrogenation of furfural to furfuryl alcohol. *J. Electroanal. Chem.* **2017**, 804, 248-253.
- 50. Cantu, D. C.; Padmaperuma, A. B.; Nguyen, M.-T.; Akhade, S. A.; Yoon, Y.; Wang, Y.-G.; Lee, M.-S.; Glezakou, V.-A.; Rousseau, R.; Lilga, M. A., A Combined Experimental and Theoretical Study on the Activity and Selectivity of the Electrocatalytic Hydrogenation of Aldehydes. *ACS Catal.* **2018**, 8 (8), 7645-7658.
- 51. Akhade, S. A.; Singh, N.; Gutiérrez, O. Y.; Lopez-Ruiz, J.; Wang, H.; Holladay, J. D.; Liu, Y.; Karkamkar, A.; Weber, R. S.; Padmaperuma, A. B.; Lee, M.-S.; Whyatt, G. A.; Elliott, M.; Holladay, J. E.; Male, J. L.; Lercher, J. A.; Rousseau, R.; Glezakou, V.-A., Electrocatalytic Hydrogenation of Biomass-Derived Organics: A Review. *Chem. Rev.* **2020**, 120 (20), 11370-11419.
- 52. Cleghorn, S. J. C.; Pletcher, D., The mechanism of electrocatalytic hydrogenation of organic molecules at palladium black cathodes. *Electrochimica Acta* **1993**, 38 (2), 425-430.
- 53. Ji, K.; Xu, M.; Xu, S.-M.; Wang, Y.; Ge, R.; Hu, X.; Sun, X.; Duan, H., Electrocatalytic Hydrogenation of 5-Hydroxymethylfurfural Promoted by a Ru1Cu Single-Atom Alloy Catalyst. *Angew. Chem., Int. Ed. Engl.* **2022**, 61 (37), e202209849.
- 54. Huang, S.; Gong, B.; Jin, Y.; Sit, P. H. L.; Lam, J. C.-H., The Structural Phase Effect of MoS2 in Controlling the Reaction Selectivity between Electrocatalytic Hydrogenation and Dimerization of Furfural. *ACS Catal.* **2022**, 12 (18), 11340-11354.
- 55. Meyer, L. C.; Sanyal, U.; Stoerzinger, K. A.; Koh, K.; Fulton, J. L.; Camaioni, D. M.; Gutiérrez, O. Y.; Lercher, J. A., Influence of the Molecular Structure on the Electrocatalytic Hydrogenation of Carbonyl Groups and H2 Evolution on Pd. *ACS Catal.* **2022**, 12 (19), 11910-11917.
- 56. Boettcher, S. W.; Oener, S. Z.; Lonergan, M. C.; Surendranath, Y.; Ardo, S.; Brozek, C.; Kempler, P. A., Potentially Confusing: Potentials in Electrochemistry. *ACS Energy Lett.* **2021**, 6 (1), 261-266.
- 57. Andrieux, C. P.; Pinson, J., The Standard Redox Potential of the Phenyl

- Radical/Anion Couple. J. Am. Chem. Soc. 2003, 125 (48), 14801-14806.
- 58. Lopez-Ruiz, J. A.; Sanyal, U.; Egbert, J.; Gutierrez, O. Y.; Holladay, J., Kinetic Investigation of the Sustainable Electrocatalytic Hydrogenation of Benzaldehyde on Pd/C: Effect of Electrolyte Composition and Half-Cell Potentials. *ACS Sustain. Chem. Eng.* **2018**, 6 (12), 16073-16085.
- 59. Calderón-Cárdenas, A.; Paredes-Salazar, E. A.; Varela, H., Apparent Activation Energy in Electrochemical Multistep Reactions: A Description via Sensitivities and Degrees of Rate Control. *ACS Catal.* **2020**, 10 (16), 9336-9345.
- 60. Song, Y.; Sanyal, U.; Pangotra, D.; Holladay, J. D.; Camaioni, D. M.; Gutierrez, O. Y.; Lercher, J. A., Hydrogenation of benzaldehyde via electrocatalysis and thermal catalysis on carbon-supported metals. *J. Catal.* **2018**, 359, 68-75.
- 61. Singh, N.; Sanyal, U.; Ruehl, G.; Stoerzinger, K. A.; Gutierrez, O. Y.; Camaioni, D. M.; Fulton, J. L.; Lercher, J. A.; Campbell, C. T., Aqueous phase catalytic and electrocatalytic hydrogenation of phenol and benzaldehyde over platinum group metals. *J. Catal.* **2020**, 382, 372-384.
- 62. Cheng, G.; Zhai, Z.; Sun, J.; Ran, Y.; Yang, W.; Tan, F.; Zhang, Z., Elucidating role of alloying in electrocatalytic hydrogenation of benzaldehyde over nanoporous NiPd catalysts. *J. Chem. Eng.* **2023**, 474, 145631.
- 63. Sanyal, U.; Lopez-Ruiz, J.; Padmaperuma, A. B.; Holladay, J.; Gutierrez, O. Y., Electrocatalytic Hydrogenation of Oxygenated Compounds in Aqueous Phase. *Org Process Res Dev.* **2018**, 22 (12), 1590-1598.
- 64. Yuk, S. F.; Lee, M.-S.; Akhade, S. A.; Nguyen, M.-T.; Glezakou, V.-A.; Rousseau, R., First-principle investigation on catalytic hydrogenation of benzaldehyde over Pt-group metals. *Catal. Today* **2022**, 388-389, 208-215.
- 65. Andrews, E.; Lopez-Ruiz, J. A.; Egbert, J. D.; Koh, K.; Sanyal, U.; Song, M.; Li, D.; Karkamkar, A. J.; Derewinski, M. A.; Holladay, J.; Gutiérrez, O. Y.; Holladay, J. D., Performance of Base and Noble Metals for Electrocatalytic Hydrogenation of Bio-Oil-Derived Oxygenated Compounds. *ACS Sustain. Chem. Eng.* **2020**, 8 (11), 4407-4418.
- 66. Yang, Q.; Ge, B.; Yuan, P.; Luo, S.; Zhang, H.; Zhao, Z.; Zhang, J.; Wang, S.; Bao, X.; Yao, X., Amine Coordinated Electron-Rich Palladium Nanoparticles for Electrochemical Hydrogenation of Benzaldehyde. *Adv. Funct. Mater.* **2023**, 33 (25), 2214588.

- 67. Wu, Y.; Guo, Z.; Sun, C.; Ren, X.; Li, Q., High-efficiency electrochemical hydrogenation of biomass-derived benzaldehyde compounds via a durable and versatile dendritic-like Pd/Cu-CF electrocatalyst. *Fuel Process. Technol.* **2022**, 237, 107436.
- 68. Akhade, S. A.; Lee, M.-S.; Meyer, L. C.; Yuk, S. F.; Nguyen, M.-T.; Sanyal, U.; Egbert, J. D.; Gutierrez, O. Y.; Glezakou, V.-A.; Rousseau, R., Impact of functional groups on the electrocatalytic hydrogenation of aromatic carbonyls to alcohols. *Catal. Today* **2022**, 397-399, 63-68.
- 69. Koh, K.; Sanyal, U.; Lee, M.-S.; Cheng, G.; Song, M.; Glezakou, V.-A.; Liu, Y.; Li, D.; Rousseau, R.; Gutierrez, O. Y.; Karkamkar, A.; Derewinski, M.; Lercher, J. A., Electrochemically Tunable Proton-Coupled Electron Transfer in Pd-Catalyzed Benzaldehyde Hydrogenation. *Angew. Chem., Int. Ed. Engl.* **2020**, 59 (4), 1501-1505.
- 70. Sanyal, U.; Yuk, S. F.; Koh, K.; Lee, M.-S.; Stoerzinger, K.; Zhang, D.; Meyer, L. C.; Lopez-Ruiz, J. A.; Karkamkar, A.; Holladay, J. D.; Camaioni, D. M.; Nguyen, M.-T.; Glezakou, V.-A.; Rousseau, R.; Gutierrez, O. Y.; Lercher, J. A., Hydrogen Bonding Enhances the Electrochemical Hydrogenation of Benzaldehyde in the Aqueous Phase. *Angew. Chem., Int. Ed. Engl.* **2021**, 60 (1), 290-296.
- 71. Chadderdon, X. H.; Chadderdon, D. J.; Matthiesen, J. E.; Qiu, Y.; Carraher, J. M.; Tessonnier, J.-P.; Li, W., Mechanisms of Furfural Reduction on Metal Electrodes: Distinguishing Pathways for Selective Hydrogenation of Bioderived Oxygenates. *J. Am. Chem. Soc.* **2017**, 139 (40), 14120-14128.
- 72. Liu, H.; Patel, D. M.; Chen, Y.; Lee, J.; Lee, T.-H.; Cady, S. D.; Cochran, E. W.; Roling, L. T.; Li, W., Unraveling Electroreductive Mechanisms of Biomass-Derived Aldehydes via Tailoring Interfacial Environments. *ACS Catal.* **2022**, 12 (22), 14072-14085.
- 73. Anibal, J.; Malkani, A.; Xu, B., Stability of the ketyl radical as a descriptor in the electrochemical coupling of benzaldehyde. *Catal. Sci. Technol.* **2020**, 10 (10), 3181-3194.
- 74. Anibal, J.; Xu, B., Electroreductive C-C Coupling of Furfural and Benzaldehyde on Cu and Pb Surfaces. *ACS Catal.* **2020**, 10 (19), 11643-11653.
- 75. Chen, G.; Li, X.; Feng, X., Upgrading Organic Compounds through the Coupling of Electrooxidation with Hydrogen Evolution. *Angew Chem Int Ed Engl* **2022**, 61 (42), e202209014.

76. Jiang, N.; Liu, X.; Dong, J.; You, B.; Liu, X.; Sun, Y., Electrocatalysis of Furfural Oxidation Coupled with H<sub>2</sub> Evolution via Nickel-Based Electrocatalysts in Water. *ChemNanoMat* **2017**, 3 (7), 491-495.

77. Wang, T.; Tao, L.; Zhu, X.; Chen, C.; Chen, W.; Du, S.; Zhou, Y.; Zhou, B.; Wang, D.; Xie, C.; Long, P.; Li, W.; Wang, Y.; Chen, R.; Zou, Y.; Fu, X.-Z.; Li, Y.; Duan, X.; Wang, S., Combined anodic and cathodic hydrogen production from aldehyde oxidation and hydrogen evolution reaction. *Nat. Catal.* **2022**, 5 (1), 66-73.

# Chapter 2

# **Objectives**

# 2. Objectives

The objective of this thesis is to develop an electrocatalytic conversion technology to valorizate benzaldehyde into biofuels and added value chemical with high faraday efficiency, yield and selectivity. I will develop and test of electrocatalysts for the reduction and oxidation of biomass-derived product benzaldehyde and an electrochemical prototype system to couple two such reactions and where the technological and economic viability of this strategy can be demonstrated.

The specific objectives of the project are the following:

- Gain fundamental knowledge and experience in related electrocatalytic properties and devices. Provide feedback to optimize catalysts and to define the technical viability of different valorization schemes.
- Design and engineering of electrocatalysts using scalable synthesis routes and taking into account the cost of elements, potential environmental and health impact, performance in terms of activity and selectivity, and stability under reaction conditions.
- Evaluate the electrocatalyst performance in terms of activity toward electrocatalytic oxidation (ECO) and electrocatalytic hydrogenation (ECH), its selectivity to targeted value added chemicals, and its stability under reaction conditions.
- Take deep insight into the reaction mechanism using modelling.
- Select the best suited candidate as electrocatalyst for paired electrolysis of specific reactions.
- Develop a prototype electrochemical system where an oxidation and a reduction reaction are coupled and which allow the valorization of benzaldehyde.
- Demonstrate electrochemistry to be a cost-effective strategy for the valorization of biomass by proving the technical viability of a few valorization schemes.

• To demonstrate that biomass can be an excellent precursor to generate high added value and commodity chemicals, including fuels.

The work presented in this thesis was carried out in the Functional Nanomaterials group of the Catalonia Institute for Energy Research of the Unoversity of Barcelona. Andreu Cabot and Paulina R. Martínez-Alanis guided these projects and strongly participated in all these processes.

# Chapter 3

# **Experimental Sections**

# 3. Experimental sections

This chapter covers the experimental section of the thesis, focusing primarily on the material preparation procedures, the characterization procedures, the methods and technologies for the performance testing of materials as electrocatalysts. I will provide tables listing the chemicals used, as well as the instruments and equipment employed. Additionally, I will give a detailed introduction of the material preparation methods, characterization techniques, and the electrochemical methods used to study electrochemical reactions.

## 3.1 Chemicals or raw materials used in experiments.

The chemicals or raw materials used in the experiment are shown in Table 3-1.

**Table 3-1.** List of chemicals and materials used in the experiments.

Chemical Name	Molecular Formula/Purity	Manufacturer
Palladium(II) acetate	Pd(OAc)2, 98%	Sigma Aldrich
Terephthalic acid	C <sub>6</sub> H <sub>4</sub> -1,4-(CO <sub>2</sub> H) <sub>2</sub> , 98%	Sigma Aldrich
Nickel(II) chloride hexahydrate	NiCl <sub>2</sub> ·6 H <sub>2</sub> O, 99.9%	Sigma Aldrich
Acetonitrile	HPLC, ≥99.9%	Sigma Aldrich
N,N-dimethylformamide	DMF, ≥99.8%	Sigma Aldrich
Triethanolamine	(HOCH <sub>2</sub> CH <sub>2</sub> ) <sub>3</sub> N, 97%	Thermo Scientifi
Ethanol	CH <sub>3</sub> CH <sub>2</sub> OH, 96%	Letslab
Benzaldehyde	C <sub>7</sub> H <sub>6</sub> O, 98%	Sigma Aldrich
Acetone	(CH <sub>3</sub> ) <sub>2</sub> CO	Letslab
Hydrochloric acid	HCl, 37%	Thermo Scientifi
Nickel foam	Ni, 99.9%	Kejing
Copper(I) chloride	CuCl	Sigma Aldrich
Indium(III) chloride	InCl <sub>3</sub>	Sigma Aldrich

Zinc acetate	Zn(CH <sub>3</sub> COO) <sub>2</sub>	Sigma Aldrich
Thiourea	CH <sub>4</sub> N <sub>2</sub> S	Sigma Aldrich
Ethylene glycol	(CH <sub>2</sub> OH) <sub>2</sub>	Thermo Scientifi
Cadmium acetate	Cd(CH <sub>3</sub> COO) <sub>2</sub>	Sigma Aldrich
Ammonia solution	$NH_3 \cdot H_2O$ , 25% $\sim$ 28%	Sigma Aldrich
Copper(II) acetylacetonate	Cu(acac)2, 97%	Sigma Aldrich
Oleylamine	$C_{18}H_{37}N, 70\%$	Aladdin Reagent
Dodecanethiol	C <sub>12</sub> H <sub>26</sub> S, 98%	Sigma Aldrich
Methanol	СН₃ОН 98%	Letslab
Benzyl alcohol	C7H8O 99.8%	Sigma Aldrich
Benzoic acid	C <sub>6</sub> H <sub>5</sub> COOH 99.5%	Sigma Aldrich
Hydrobenzoin	C <sub>6</sub> H <sub>5</sub> CH(OH)CH(OH)C <sub>6</sub> H <sub>5</sub>	Sigma Aldrich
Titanium dioxide-P25	TiO <sub>2</sub> -P25	Evonik
Anatase titanium dioxide	TiO <sub>2</sub> -A	Evonik
Rutile titanium dioxide	TiO <sub>2</sub> -R	Evonik
Chloroauric acid tetrahydrate	HAuCl <sub>4</sub> ·4 H <sub>2</sub> O	Sigma Aldrich
Sodium hydroxide	NaOH, 97%	Sigma Aldrich
Potassium chloride	≥99.0%	Sigma Aldrich
Ag/AgCl electrode	Ag/AgCl	Tianjin Ada Hengsheng
Glassy carbon electrode	C	Tianjin Ada Hengsheng
Pt mesh electrode	Pt	GaossUnion
Nafion™ N-117 membrane	C <sub>9</sub> HF <sub>17</sub> O <sub>5</sub> S	DuPont

# 3.2 Material preparation method

I will introduce the methods and process used to prepare the materials in the thesis

and share the precautions I encountered during experiments.

#### 3.2.1 Solvothermal method

In the experiments detailed in chapters 4 and 5 of our thesis, we utilized the solvothermal method to prepare the materials. This is a versatile and widely used technique for the synthesis of a variety of materials, including nanomaterials, crystals, and composites. This method involves dissolving the desired precursors in a solvent in a Teflon-lined stainless steel autoclave (Figure 3-1), which was heated in an incubator at temperatures above the boiling point of the solvent. The elevated temperature and pressure conditions facilitate the formation of the desired materials through various chemical reactions and physical processes. During use, it is crucial to ensure that the apparatus has good air tightness and is equipped with a pressure relief valve. The solvent should fill 60-80% of the liner's volume. Before the reaction, tighten the lid, and after the reaction, wait until the stainless steel shell has completely cooled to room temperature before proceeding with subsequent experiments.



Figure 3-1. Teflon liner (left) and stainless steel autoclave (right).

#### 3.2.2 Reflux method

The reflux method is a technique used to synthesize inorganic materials by heating a mixture of precursors in a solvent that continuously evaporates and condenses back into the reaction flask. It is widely applied in the synthesis of nanoparticles, catalyst preparation, material functionalization, and the creation of coordination compounds.

In chapter 5, we used this method to prepare sulfide. Water was used as the solvent, and the reaction temperature was controlled at 80 °C, resulting in the synthesis of materials with regular morphology. This method is energy-efficient, safe, and convenient.

#### 3.2.3 Colloidal method

Colloidal method is a traditional method of synthesizing inorganic nanocrystals, including semiconductors and metals. The composition, morphology, and particle size for the material are highly controllable. The colloidal method typically employs solvents with high boiling points such as ethylene glycol and oleylamine (OAm). These solvents have the ability to dissolve salts or substances that are insoluble in water or sensitive to water and air. This means that the method allows for the synthesis of materials under anhydrous and oxygen-free conditions. A schematic diagram of the reaction equipment is shown in Figure 3-2. Prior to the reaction, it is essential to purge the apparatus and solvent of water and air. During the reaction, noble gas can be introduced from the bottom or top of the system as needed to maintain an inert atmosphere in the apparatus and prevent the occurrence of highpressure hazardous situations. The reaction process involves the dissolution of salts, nucleation, and subsequent crystal growth and incubation. Crystals prepared using this method typically exhibit high surface energy and are coated with a layer of organic ligands. This layer can be removed through specific ligand exchange methods or by annealing in an inert atmosphere.

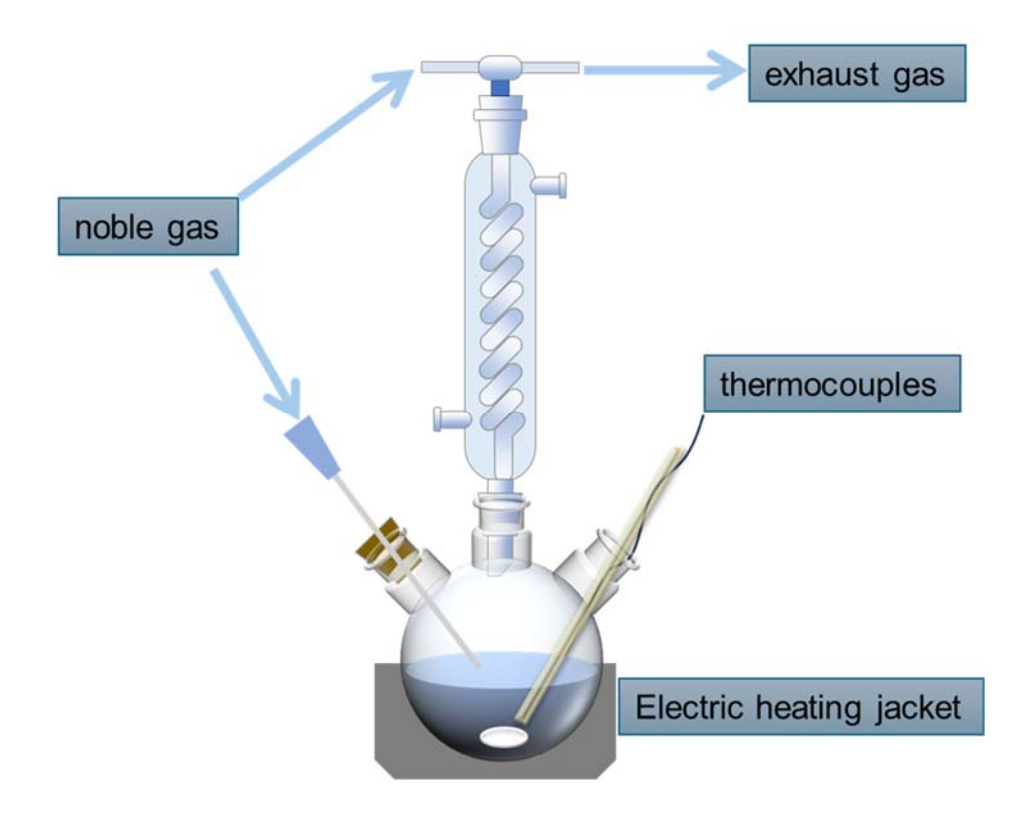


Figure 3-2. Illustration of colloidal method equipment.

### 3.2.4 Deposition-precipitation method

Deposition-precipitation (DP) method involves adding a solution of the desired metal (usually a noble metal) to a suspension of the support (typically metal oxide particles), forming a homogeneous mixture. Under vigorous stirring, at controlled temperature and pH, the desired metal deposits onto the surface of the support. Subsequently, filtration, washing, drying, and heat treatment processes are carried out to obtain a catalyst loaded with the desired metal. This method finds widespread commercial applications, with negligible loss of noble metals during the preparation process.

#### 3.2.5 Heat treatment process

Heat treatment involves heating the material to a specific temperature, holding it at that temperature for a certain duration, and then cooling it down to room temperature or lower at a controlled rate. This process aims to improve the material's microstructure, resulting in superior performance. In both chapters 6 and 7, we utilized a heat treatment process during the material preparation. In chapter 6, we controlled the heat treatment temperature to be higher than the boiling point of OAm, aiming to remove the ligands OAm on the surface of the material prepared by colloidal method using OAm as a solvent. In chapter 7, the purpose of the heating

treatment was to incubate the material, promoting a tighter bonding between the catalytic active components and the substrate.

### 3.3 Material characterizations

### 3.3.1 X-ray diffraction (XRD)

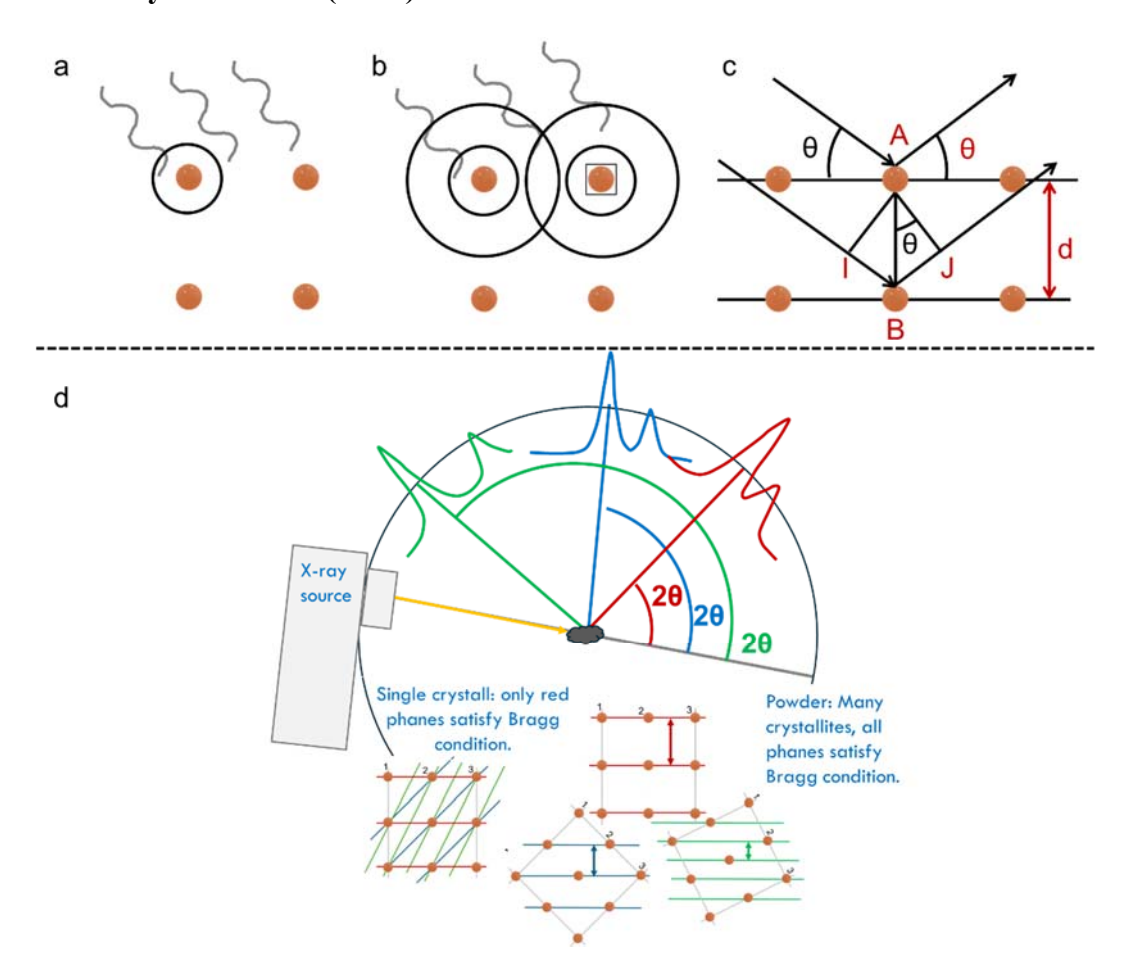


**Figure 3-3.** (a-b) Interaction of X-rays with atoms in crystal; (c) Bragg diffraction illustration; (d) schematic diagram of obtaining XRD pattern.

Bragg's law is a fundamental principle in physics that explains how X-rays can be used to determine the structure of crystals. It explains how the superposition of wave fronts scattered by lattice planes establishes a precise relationship between the wavelength and the scattering angle. <sup>1,2</sup>

Figures 3-3a-b illustrate the interaction of X-rays with the atoms in a crystal. When X-rays are incident on the crystal structure, they are absorbed by the constituent atoms, causing oscillations in the surrounding electron clouds. These oscillations induce the re-emission of X-rays in certain directions based on Rayleigh scattering. For simplicity, X-ray beams can be considered to reflect off the crystal planes formed by the regular arrangement of atoms. These reflected X-rays can be constructive

destructive interferences. Constructive interference occurs when this length is equal to an integer multiple of the wavelength of the radiation. This can be explained using Bragg's law. The derivation process was showed below.

In Figure 3-3c is the illustration of Bragg diffraction. When two beams of X-ray light shine onto the crystal surface and reflect, the paths traveled differ due to the parallel crystal planes. the lower beam traverses an extra length of IB + BJ = 2IB. AB=d (lattice spacing, also d spacing). Therefore:

$$\sin(\theta) = \frac{IB}{d} \tag{3-1}$$

$$IB = d * \sin(\theta) \tag{3-2}$$

$$2IB = 2d * \sin(\theta) \tag{3-3}$$

Generalizing to all parallel crystal planes, the mathematical formulation of Bragg's law is given by:

$$n\lambda = 2 d * \sin(\theta) \tag{3-4}$$

where:

- n is the diffraction order, n=1,2,3...
- d is the distance between the crystal planes,
- $\theta$  is the angle of incidence (and reflection).

Figure 3-3 (d) is the schematic diagram of XRD experiment process and tells apart the similarities and difference between single crystal and powder XRD. A single crystal has only one orientation, and the crystal planes are arranged in a single manner. Therefore, depending on the orientation of the sample, diffraction peaks and their higher-order peaks can only be observed in a specific direction such as (0 0 1) (0 0 2) (0 0 3)···. Powder XRD can provide information about crystal planes with different orientation. Different materials and crystal phases will exhibit distinct diffraction patterns. This method provides detailed and precise insights into the molecular and crystal structure of samples.

# 3.3.2 Scanning electron microscopy (SEM) and energy dispersive x-rays spectroscopy (EDS)

A scanning electron microscopy (SEM) uses a type of electron microscope that produces images of a sample by scanning the surface with a focused beam of electrons. The incident electrons interact with atom resulting in various scattering phenomena. This interaction generates a variety of signals that can characterize certain physical or chemical properties of the solid surface. As shown in Figure 3-4.<sup>3</sup> Collecting secondary electrons and backscattered electrons to obtain the surface morphology of sample. I addition to imaging, surface composition analysis is most performed using characteristic X-rays also known as the EDS technology. Limitation is that the electron beam can only penetrate a very shallow layer of the sample's surface. This method is fast but not highly accurate. <sup>4</sup>

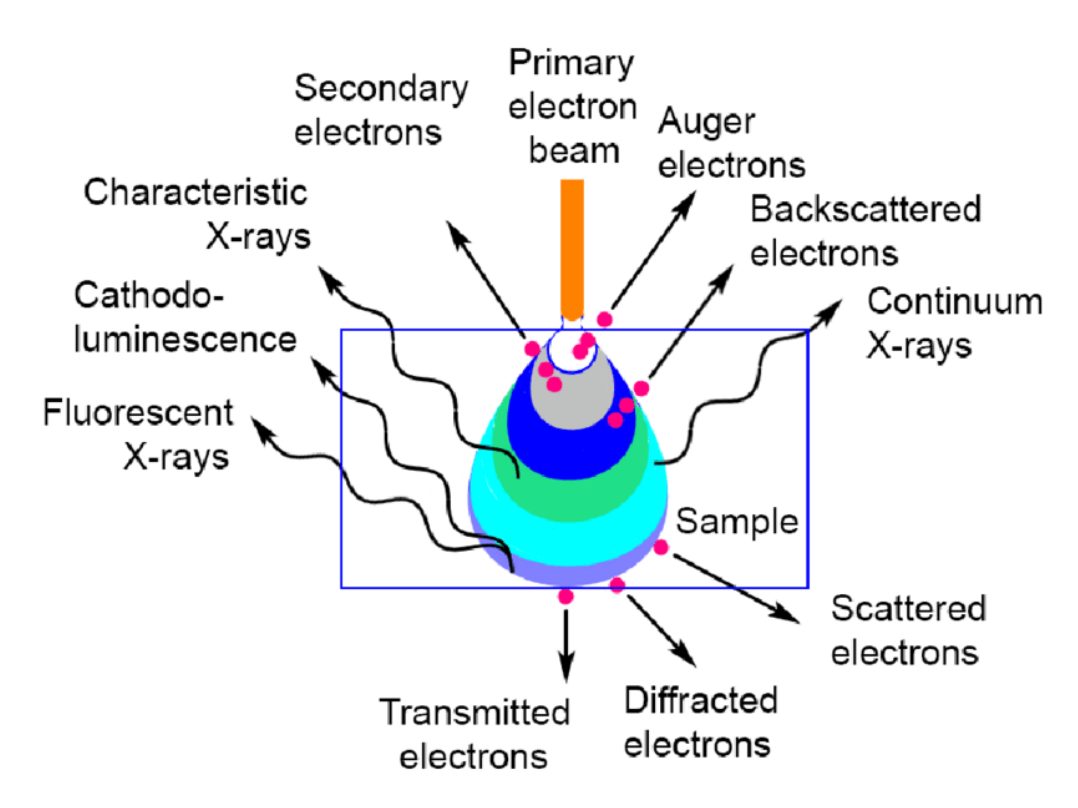


**Figure 3-4.** Working principle of SEM. Sample characteristics from different sample depth can be detected by collecting different sources of information, such as secondary electrons, backscattered electrons, and characteristic X-rays. <sup>5</sup>

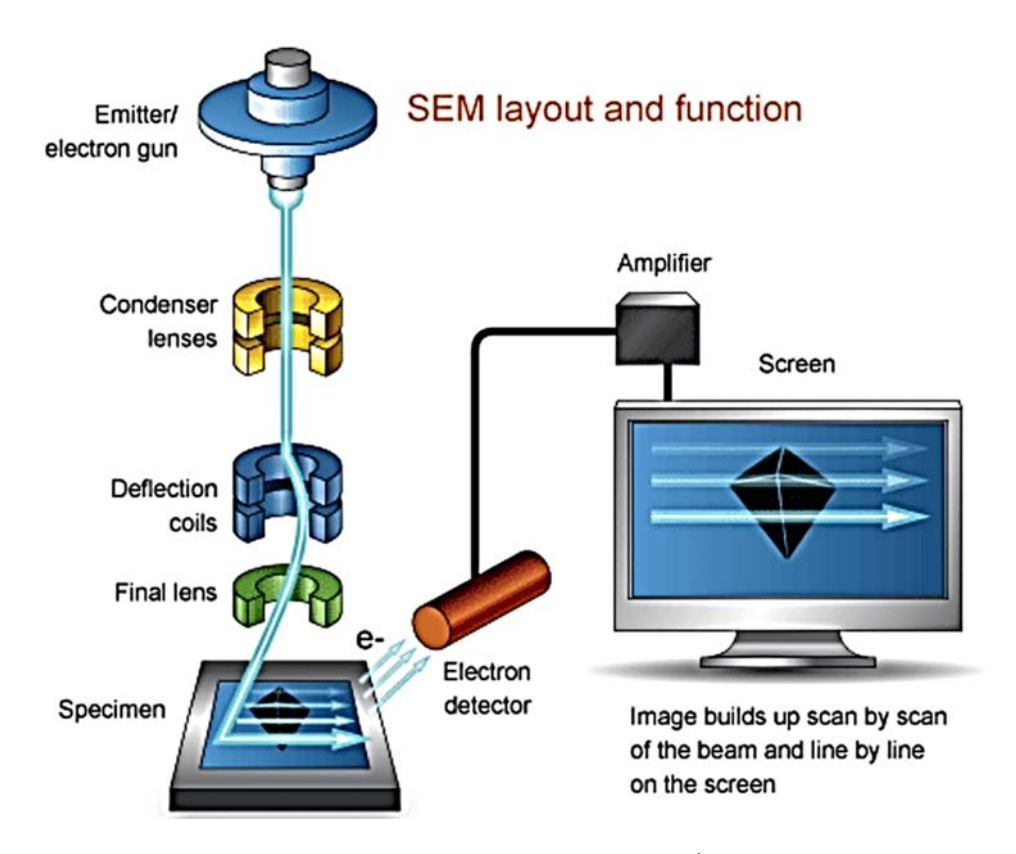


Figure 3-5. All SEM components. <sup>6</sup>

As shown in Figure 3-5, the SEM machine consists of the following components:

- 1. A source to generate electrons of high energy. The electron beam emitted by the electron gun.
- 2. Column down for travelling the electrons through several electromagnetic lenses. The electron beam focused by electromagnetic lenses and accelerated by electromagnetic lenses
- 3. Deflection system consists of scan coils. The specimen image is created point by point as the scan coils move, directing the electron beam to discrete locations in straight lines. For higher magnification, the scan coils deflect the beam across a smaller area. The working distance, the distance from the final lens to the specimen surface, also affects magnification.
- 4. A chamber for the sample.
- 5. Electron detector for backscattered and secondary electron. The electron detector detects emitted electrons (signals) from the scanned sample and is used to create images of the sample.
- 6. Computer system consists of viewing screen to display the scanned images and keyboard to control the electron beam.

## 3.3.3 Transmission electron microscopy (TEM) and electron energy loss spectroscopy (EELS)

Transmission electron microscopy (TEM) is a microscopy technique in which a beam of electrons is transmitted through a specimen to form an image. The similarity between SEM and TEM lies in their use of electron beams. The primary difference is that SEM is used to observe surface structural features of sample, whereas TEM is used to observe the internal fine structure of sample. A high-resolution (HRTEM) is a specialized imaging mode of TEM that directly images the atomic structure of sample.

EELS is also a method for detecting elements and their concentrations. When an electron beam with known kinetic energy is directed at a test material, some electrons undergo inelastic scattering upon interacting with atoms. During this process, these electrons lose a portion of their energy and experience random small deviations in their travel path. The magnitude of energy loss in this process can be measured by an electron energy spectrometer and analyzed to provide insights and explanations.

## 3.3.4 X-ray photoelectron spectroscopy (XPS)

Combining the characterization techniques mentioned above allows for precise determination of material composition, crystal atomic arrangement, and approximate element content. XPS (X-ray Photoelectron Spectroscopy) technology, on the other hand, provides detailed analysis of surface elemental states and their chemical environments.

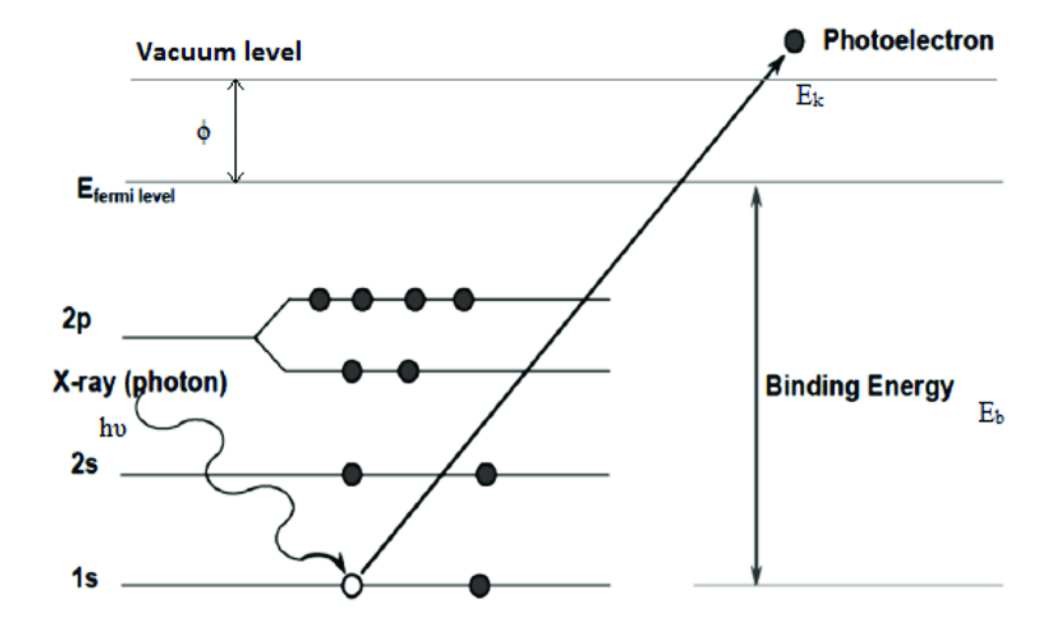


**Figure 3-6.** The principle of photoelectron generation.

When an X-ray of known energy (hv, Al K $\alpha$  at 1486.7 eV or Mg K $\alpha$  at 1253.6 eV) interacts with an atom, a photoelectron can be emitted via the photoelectric effect (Figure 3-6). The emitted electron's kinetic energy (E<sub>k</sub>) can be measured and the atomic core level binding energy (E<sub>b</sub>) relative to the Fermi level (E<sub>F</sub>) of the sample can be determined using the following equation:

$$E_b = h\nu - E_K - \Phi_{sp} \tag{3-5}$$

where  $\Phi_{sp}$  is the work function of the spectrometer (typically 4 to 5 eV). The various core level binding energies observed in a spectrum can be used to identify all the elements of the periodic table except for H and He. Binding energies are sensitive to the chemical environment of the atom. The atom of higher electrons density surrounded will decrease binding energies. Conversely, increased binding energies will be measured for core electrons of atoms that withdraw electrons from their neighboring atoms. Essentially, binding energy will generally increase as chemical state number increases. As shown in Figure 3-7, the main components of an XPS system are an ultra-high vacuum (UHV) chamber with mu-metal magnetic shielding, an Ar ion gun commonly used for source of X-rays, an electron collection lens, an electron energy analyzer, an electron detector system.

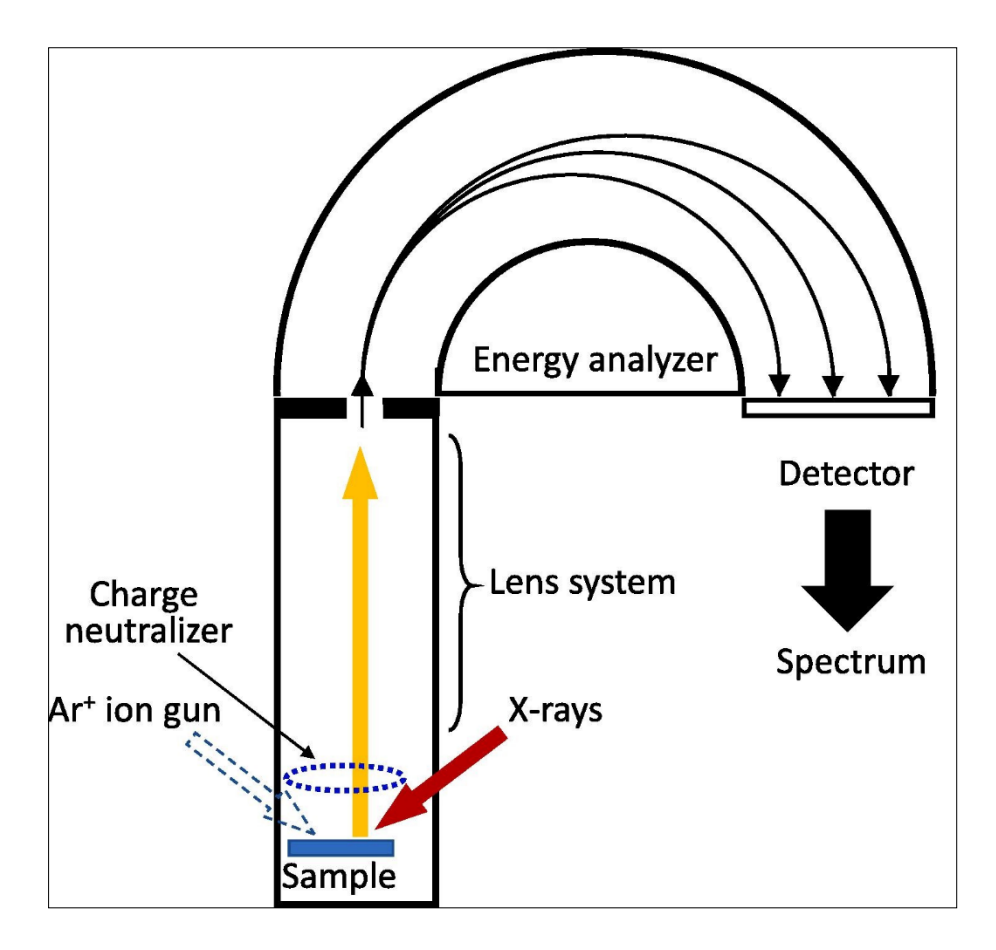


**Figure 3-7.** The schematic view of the photoelectron spectrometer with a hemispherical electron energy analyzer. <sup>8</sup>

## 3.3.5 Ultraviolet-visible spectroscopy (UV-vis)

In chapter 5, the solid ultraviolet–visible spectroscopy (UV-vis) method was used to obtain the band gap of semiconductor materials. The band gap is a crucial parameter for assessing the conductivity of semiconductor materials. The experiment and data processing are as follows: first, obtain the absorbance at different wavelengths through solid UV-vis testing, then set the x-axis  $h\nu$  using the following formula.

$$h\nu = \frac{1240}{\lambda_m} \tag{3-5}$$

Where h is the Planck constant, v is the frequency. Based on Tauc plot method, we set y-axis as  $(\alpha hv)^{1/n}$ 

$$(\alpha h \nu)^{1/n} = B \left( h \nu - E_g \right) \tag{3-6}$$

Where B is a constant number,  $\alpha$  is absorbance coefficient, can be replaced with absorbance. Eg is the band gap for semiconductor. The exponent n is directly related to the type of semiconductor: for a direct band gap, n = 1/2; for an indirect band gap,

n = 2. Then we get a plot:  $(\alpha h \nu)^{1/n} = (h \nu - E_g)$ . The optical direct/ indirect band gap of the semiconductor can be obtained by extending the tangent line of the reverse curve to intersect with the x-axis.

## 3.3.6 Gas absorption/desorption

## 3.3.6.1 N<sub>2</sub> adsorption/desorption

The surface area and pore structure of solid catalysts are crucial parameters for characterizing catalyst performance. Heterogeneous catalytic reactions occur on the surface of solid catalysts. To achieve the highest reaction activity, most catalysts are made porous to increase their surface area. The porous structure and pore size distribution within the catalyst significantly affect the catalyst's activity and selectivity.

The surface area and pore structure of material can be studied N<sub>2</sub> adsorption/desorption isotherm. N<sub>2</sub> adsorption on the surface of solid material is physical adsorption, forming a complete monomolecular adsorption layer on the solid surface. The amount of adsorption is related only to the temperature and the equilibrium pressure of the gas. Based on this, the temperature is set as a constant to obtain the adsorption/desorption isotherm, which is then processed according to the Brunauer-Emmett-Teller (BET) theory. This technology was utilized in both chapter 4 and chapter 7.

## 3.3.6.2 H<sub>2</sub>-temperature-programmed reduction (H<sub>2</sub>-TPR)

H<sub>2</sub> undergoes chemisorption and chemical reactions with the metal/support on the solid catalyst surface. H<sub>2</sub>-temperature-programmed reduction (H<sub>2</sub>-TPR) is technique widely used for catalyst characterization, providing information about active sites of the catalyst. This experiment uses a reducing gas (Ar/H<sub>2</sub> or N<sub>2</sub>/H<sub>2</sub>) under a programmed temperature increase condition. By analyzing and calculating the H<sub>2</sub> consumption amount to qualitatively and quantitatively characterize the active sites. This technology was also utilized in both chapter 4 and chapter 7.

## 3.3.7 Fourier-transform infrared spectroscopy (FTIR)

FTIR is a molecular absorption spectroscopy technique. Different functional groups and chemical bonds absorb infrared light at different wavenumbers due to their vibrations or rotations. Based on this, the presence or changes of specific functional groups or chemical bonds in the sample can be determined, which is useful for

qualitative and quantitative analysis, as well as studying reaction processes. I primarily use FTIR for the identification of organic compounds. It was used in chapter 4 to identify the organic functional groups exist in the Ni-MOF material. In chapter 6, it was employed to verify the surface organic ligands of the material. In chapter 7, FTIR was utilized to detect the adsorption state of pyridine on the active sites of material surface.

## 3.3.8 High-performance liquid chromatography (HPLC)

High Performance Liquid Chromatography (HPLC) is an analytical chemistry technique used for separating, identifying, and quantifying semi-volatile and non-volatile compounds in liquid samples. After sample injection, the mobile phase flows through a chromatographic column packed with a stationary phase under pressure. The mobile phase carries liquid samples through the column to the detector, where compounds or analytes separate based on their varying interactions with the stationary phase. In this thesis, a UV-Vis detector was used.

The condition of the HPLC column has a significant impact on the results. To maintain optimal condition of the HPLC column, several considerations are essential:

- 1. Sample and mobile phase filtration: Both the sample and the mobile phase should be filtered prior to use. This ensures that particulates or impurities do not clog the column, which could affect chromatographic separation and peak resolution.
- 2. Environmental requirements for column usage: The column should be operated within specified environmental conditions, adhering to temperature, pressure, and other manufacturer-recommended parameters. Deviating from these conditions can affect chromatographic performance.
- 3. Storage of columns: If the column is not used for an extended period, it should be stored in a specific solution environment recommended by the manufacturer. This prevents drying out or degradation of the stationary phase, maintaining its integrity and performance.
- 4. Impact of different mobile phases: Different samples require specific mobile phases, which can affect retention times and peak shapes. For aqueous mobile phases, ultrapure water is typically required, while chromatographic-grade solvents are required for organic mobile phases.

By adhering to these practices, the HPLC column can maintain optimal performance, ensuring reliable and reproducible chromatographic results.

## 3.3.9 Electron Paramagnetic Resonance Spectroscopy (EPR)

Electron Paramagnetic Resonance (EPR) is an analytical technique based on electron spin resonance. In an EPR experiment, free electrons in the sample are affected by an applied magnetic field, causing them to undergo spin resonance. When the magnitude of the applied magnetic field matches the energy difference of the free electron spins in the sample, the free electrons absorb the energy of the applied magnetic field, producing a resonance signal. This resonance signal can be analyzed by detecting the microwave signal absorbed by the sample to determine its physical and chemical properties.

## EPR can detect:

- 1. Free Radicals: Substances with one unpaired electron in their molecules, such as diphenylpicrylhydrazyl (DPPH) and triphenylmethyl, each have one unpaired electron.
- 2. Biradicals or Polyradicals: Compounds containing two or more unpaired electrons in one molecule, where the unpaired electrons are far apart and interact weakly with each other.
- 3. Triplet Molecules: Compounds with two unpaired electrons in close proximity within a molecular orbital, resulting in strong interaction, such as oxygen molecules. These can be in the ground state or an excited state.
- 4. Transition Metal Ions and Rare Earth Ions: Molecules with unpaired electrons in atomic orbitals, such as common transition metal ions like  $Ti^{3+}$  (3d<sup>1</sup>) and  $V^{3+}$  (3d<sup>7</sup>).
- 5. Lattice Defects in Solids: Substances with one or more electrons or holes trapped in or near defects, forming materials with single electrons, such as face-centered and body-centered structures.
- 6. Atoms with an Odd Number of Electrons: Atoms such as hydrogen, nitrogen, and alkali metal atoms.

Electron Paramagnetic Resonance is a very useful analytical technique widely used in material science, biomedicine, chemistry, and environmental science.

## 3.4 Electrochemistry techniques and parameters for catalyst performance evaluation

## 3.4.1 Preparation before the electrochemical tests.

The tests were all conducted in a three-electrode system in H-cell reactors divided with Nafion 117 membrane, as shown in the Figure 3-8. In this setup, the working electrode and reference electrode should be kept in one chamber, while the counter

electrode is placed in another chamber. To address the issue of high cell voltage between the reference electrode and the counter electrode, the counter electrode area should be maximized as much as possible. The jacket of the reactor can circulate water to control the reaction temperature, and the system can be purged with the desired gas.

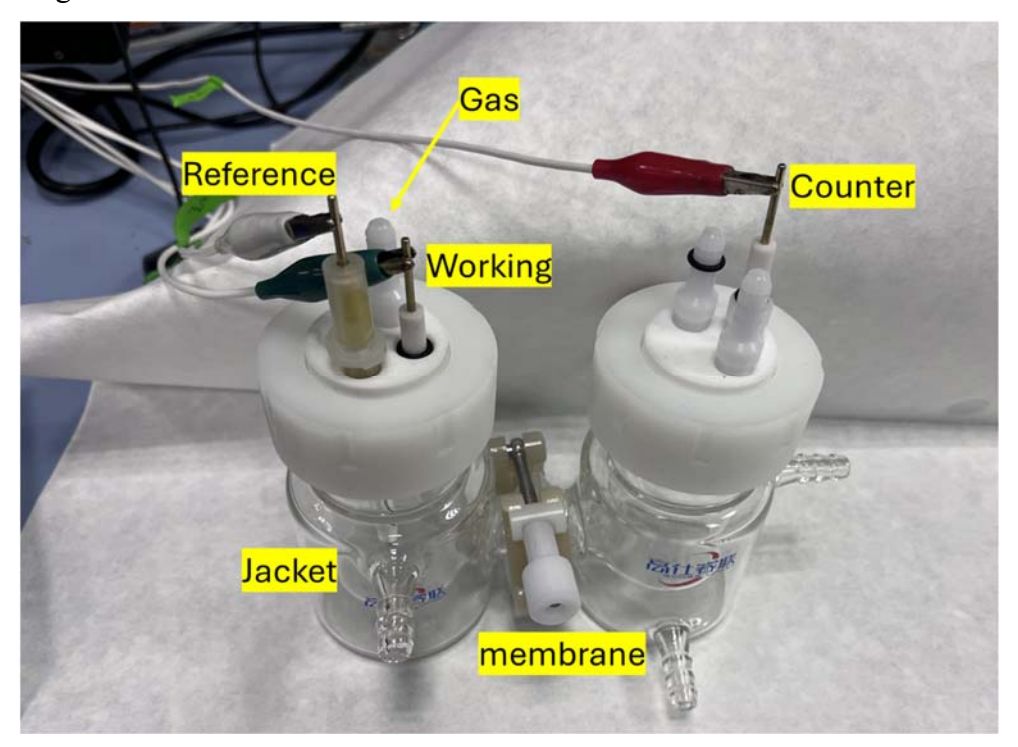


Figure 3-8. Electrochemical testing setup.

When catalyst supported on glassy carbon electrode (GDE, diameter = 0.3 cm) as working electrode, the electrode needs to be polished on a wet polishing cloth containing polishing powder before.

Catalyst prepared by ink: Add 6-8 mg of catalyst to 1 mL of a solution containing 500  $\mu$ L ethanol, 430  $\mu$ L deionized water, and 70  $\mu$ L 0.5 wt% Nafion solution, then disperse thoroughly using ultrasound. Use a pipette to transfer 6-8  $\mu$ L of the middle portion of the suspension, drop it onto the glassy carbon (GDE, diameter = 0.3 cm), allow it dry naturally. Catalyst supported on carbon cloth electrode also employed as working electrode. In this paper, the carbon cloth profoundly influences product selectivity, and we strive to ensure high loading when using it.

## 3.4.2 Cyclic voltammetry and linear sweep voltammetry.

Cyclic voltammetry (CV) and linear scanning voltammetry (LSV) techniques are both transient potential techniques. They involve applying a continuously varying potential over time to the working electrode, causing electroactive species in the solution to

undergo oxidation or reduction reactions at the electrode. The observed current changes ascribe to the applied potential (also substance adsorption) and the capacitive current arising from electronic double-layer charging.

These two methods are highly sensitive, capable of detecting significant changes in response to minor environmental variations which is particularly noticeable in cases where trace reactants are added to the electrolyte, as described in the thesis. Generally, high scan rate and a large working electrode area correspond to large response currents.

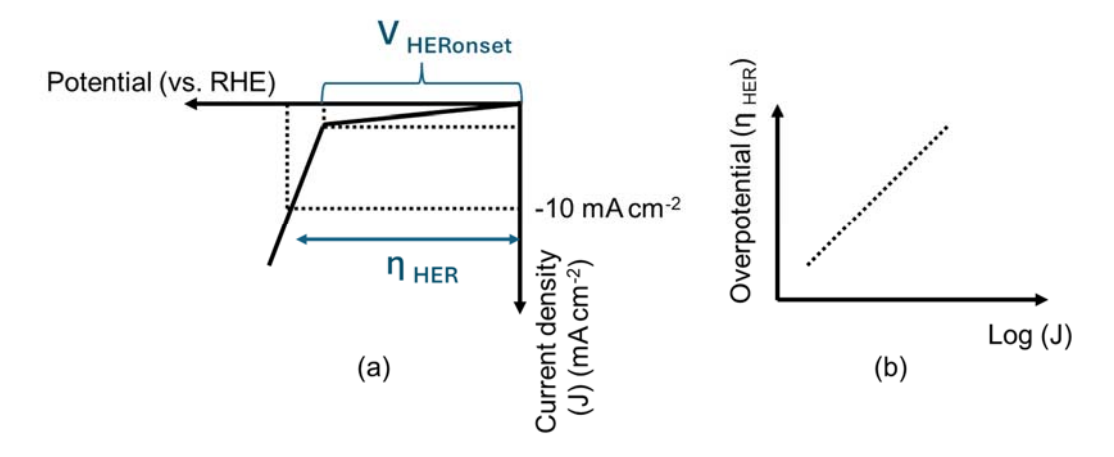


**Figure 3-9.** (a) Voltammogram obtained through linear scanning voltammetry (LSV) measurements and (b) Fitted Tafel plot for a HER electrocatalyst. <sup>9</sup>

For this thesis, when a negative potential was applied to the cathode in the absence of organics, the current density (j) shows a constant negligible value, and no bubbles are seen indicating that the HER process has not begun. The onset voltage ( $V_{HER}$  onset) is the minimum negative potential to be applied at the cathode for HER to initiate. This voltage is measured just as (j) starts increasing (in the negative direction) and becomes more than zero. Physically, we may see bubbles just starting to appear at the cathode at this voltage. Based on the well-known Nernst equation, HER should occur at 0 V (vs. RHE). But for practical electrocatalysts, HER requires an additional negative potential (vs. RHE) at the cathode which is called the overpotential ( $\eta_{HER}$ ). In scientific literature, ( $\eta_{HER}$ ) is reported at current density (j) at the cathode as (-10 or -100) mA cm<sup>-2</sup>. Lower ( $\eta_{HER}$ ) implies less electrochemical energy barrier for HER at the catalyst surface.

However, In the presence of organic compounds in aqueous solutions, CV or LSV tests provide a combined signal for various reactions (including ECH along with HER and dimerization, etc.). Therefore, Therefore, assessing the catalytic performance of

one target reaction cannot be simply determined by comparing reaction overpotentials. Tafel slope and Exchange current density can also obtained. Here, the increase of cathodic current is correlated with a change in overpotential ( $\eta_{HER}$ ) according to the well-known Tafel relation given as:

$$\eta = a + b \log|j| \tag{3-7}$$

where b is the Tafel slope in mV  $dec^{-1}$  and a is a constant representing the x-intercept of  $\eta$  versus  $\log |j|$  plot. A lower value of b and a higher value of a indicate very high charge transfer and high electrocatalytic performance. A good electrocatalyst exhibits a very low  $\eta$  and b. The value of b also corresponds to different reaction mechanisms.

## 3.4.3 Electrochemical Impedance Spectroscopy (EIS)

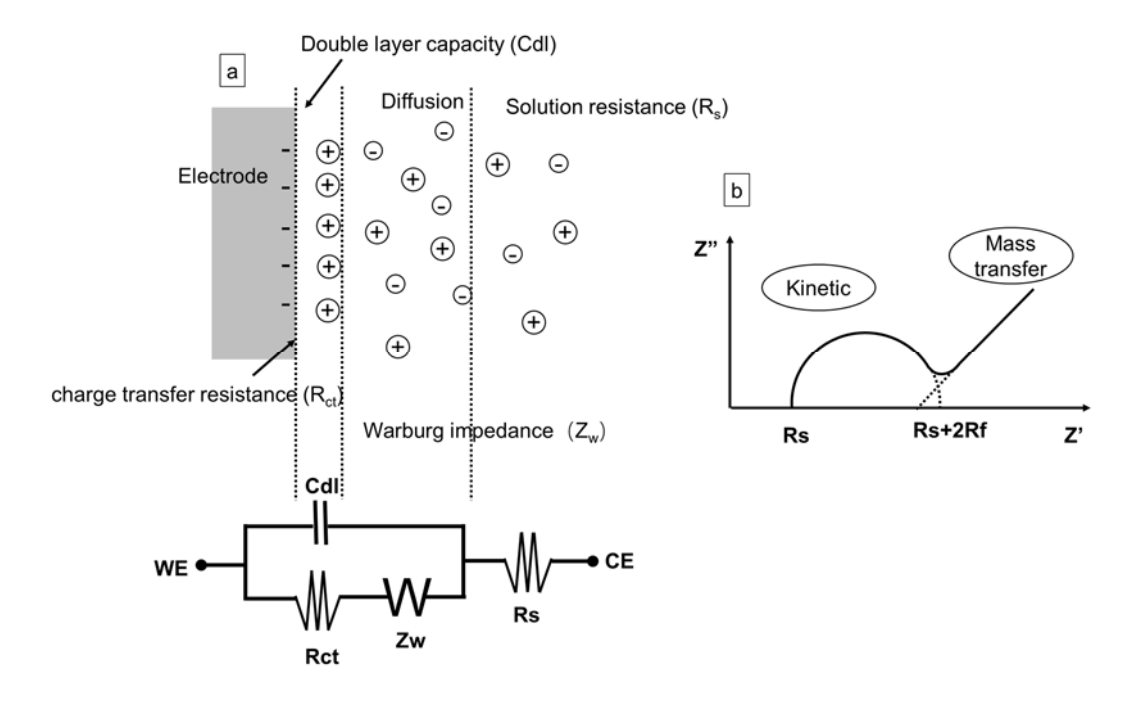


**Figure 3-10.** (a) Model of a typical electrochemistry reaction process and parallel RC circuit, (b) Theoretical Nyquist plot for the simple parallel RC circuit.

The electrochemical impedance spectroscopy (EIS) is to apply a perturbation electrical signal to an electrochemical system and then observe the system's response. EIS perturbation signal applied to the electrochemical system is a small amplitude AC sinusoidal voltage wave with varying frequencies. The measured response signal, which is the ratio of the AC voltage to the current signal, is commonly referred to as the impedance of the system. When analyzing the response signal, the electrochemical system is regarded as an equivalent circuit, consisting of basic components such as capacitors C and resistors R arranged in series or parallel combinations. Through EIS, the values of these components can be quantitatively determined. By interpreting the

electrochemical significance of these components, the structure of the electrochemical system and the nature of the electrode processes can be analyzed. <sup>10, 11</sup>

As shown is Figure 3-10 (a), The total impedance of a typical electrochemical process can be abstracted into three types of electrical components:

- 1. The Cdl comes from the nonactive ions from the electrolyte, there is no chemical reaction happened, only changes the distribution of the electric charge.
- 2. The faradaic impedance  $(Z_f)$  comes from the active ions from the electrolyte there is a chemical reaction happened (Reduction-oxidation reaction) which also called faradaic process.  $Z_f$  is combination of Warburg impedance  $(Z_w)$  and charge transfer resistance  $(R_{ct})$ .
- 3. The internal resistance (R<sub>s</sub>), directly from the electrode and electrolyte.

In practice, the complexity of the circuit is far higher than this. The choice of frequency range deeply affects the results. Figure 3-10b only reflects one simple situation. In thesis only R<sub>ct</sub> was emphasized from high frequencies area to evaluate the resistance of the charge exchange process between the electrode and the solution. The smaller the semicircle, the faster the charge transfer.

## 3.4.4 Potentiostatic method

Applying a constant and stable electrode potential in an electrochemical system, typically at a potential where Faraday reactions can occur, and then recording the current versus time curve (often referred to as the I-t curve), allows continuous electrochemical reactions to take place. This process is used to assess catalyst performance.

1. Faraday efficiency (FE): FE describes the efficiency with which electrons is transferred in a system facilitating an electrochemical reaction. In a constant current or constant potential electrocatalytic reduction reaction, FE is defined as the ratio of the actual number of electrons consumed for the reduction product to the theoretical electron transfer quantity. After product quantification through chromatography, the FE for specific products can be calculated:

$$FE\% = \frac{Electrons\ consumed\ by\ organic\ compounds \times 100\%}{Total\ electrons\ passed}$$
(3-8)

Reaction rate and conversion frequency: Average reaction rate (ARR) can be defined as:

$$ARR[\mu mol cm^{-2} h^{-1}] = \frac{moles \ of \ substrate \ consumed}{area \ of \ working \ electrode * time}$$
(3-9)

2. Conversion and selectivity: conversion refers to the percentage of a specific reactant converted into a particular product in a chemical reaction. In general, we want to achieve the maximum yield of the target organic product. The proportion of the target product in the total products is referred to as selectivity.

$$Conversion\% = \frac{Moles\ of\ reactant\ consumed}{Initial\ moles\ of\ reactant} \times 100\% \tag{3-10}$$

$$Selectivity\% = \frac{Moles\ of\ target\ product}{Moles\ of\ reactant\ consumed} \times 100\% \tag{3-11}$$

3. Stability: stability is another crucial parameter for assessing the practical applicability of catalysts. By conducting several long-lasting times electrolysis reactions with constant current or constant potential on one electrode material. Collecting and quantifying products after each test for calculating FE%, conversion and selectivity, whose numerical constancy indicates good stability.

## 3.5 References

- 1. Shih, K., *X-Ray Diffraction: Structure, Principles and Applications*. Nova Science Publishers, Inc.: New York, 2013; p 1.
- 2. Ali, A.; Chiang, Y. W.; Santos, R. M. X-ray Diffraction Techniques for Mineral Characterization: A Review for Engineers of the Fundamentals, Applications, and Research Directions *Minerals* [Online], 2022.
- 3. Fedorova, I. Alloy development for high Cr martensitic steel. Technical University of Denmark, Fedorova, Irina, 2018.
- 4. Zhou, W.; Apkarian, R.; Wang, Z. L.; Joy, D., Fundamentals of Scanning Electron Microscopy (SEM). In *Scanning Microscopy for Nanotechnology: Techniques and Applications*, Zhou, W.; Wang, Z. L., Eds. Springer New York: New York, NY, 2007; pp 1-40.
- 5. Sharga, B.; Pylypiv, D.; Feketa, V., MEDICAL BIOLOGY PRACTICALS. CYTOLOGY. Practical 2. Electron microscopy. 2021; pp 18-34.
- 6. Mohammed, A.; Abdullah, A. In Scanning electron microscopy (SEM): A review.
- 7. Sharma, V., Spectroscopic ellipsometry for the in-situ investigation of atomic layer depositions. 2014.
- 8. Greczynski, G.; Hultman, L., X-ray photoelectron spectroscopy: Towards reliable binding energy referencing. *Prog. Mater. Sci.* **2020**, *107*, 100591.
- 9. Maitra, S.; Mitra, R.; Nath, T. K., Chapter 9 Metal organic framework-based nanomaterials as suitable electrocatalysts for evolution of hydrogen. In *Metal-Organic Framework-Based Nanomaterials for Energy Conversion and Storage*, Gupta, R. K.; Nguyen, T. A.; Yasin, G., Eds. Elsevier: 2022; pp 185-203.
- 10. Lazanas, A. C.; Prodromidis, M. I., Electrochemical Impedance Spectroscopy-A Tutorial. *ACS meas. sci. au* **2023**, *3* (3), 162-193.
- 11. Yupeng, T.; Bao, J.; Zhang, P.; Zhao, T., Influence of Internal Chloride and Cracking on the Corrosion Behavior of Steel in Mortar. *Int. J. Electrochem. Sci.* **2022**,

17 (8), 220853.

## **Chapter 4**

# Electrochemical Hydrogenation of benzaldehyde into benzyl alcohol on Pd@Ni-MOF

## 4. Electrochemical Hydrogenation of benzaldehyde into benzyl alcohol on Pd@Ni-MOF

The work presented in this chapter aims to explore and enhance the electrocatalytic ECH of BZH to BA using Pd NPs supported on a metal-organic framework (Ni-MOF). The study focuses on achieving a high reaction rate and FE under ambient conditions, addressing the need for efficient and sustainable hydrogenation processes. Findings are listed below.

- 1. Pd nanoparticles were uniformly dispersed on Ni-MOF and were grouthed on nickel foam (NF), resulting in a three-dimensional architecture that facilitates reactant adsorption, diffusion, and charge transport.
- 2. The Pd@Ni-MOF catalyst achieved an ECH rate of up to 283 μmol cm<sup>-2</sup> h<sup>-1</sup> with a FE of 76%, which could be increased to 96% using a step-function voltage.
- 3. Density functional theory (DFT) calculations and materials studio simulations indicated that the Ni-MOF support promotes hydrogen bond formation and favorable adsorption configurations, reducing energy barriers and enhancing reaction efficiency. Specifically, the BZH adsorbs through its carbonyl group rather than the aromatic ring, which is more efficient for the hydrogenation process.
- 4. The ECH method offers significant benefits over traditional thermal hydrogenation, including mild reaction conditions, lower energy requirements, and compatibility with renewable energy sources.

The study successfully demonstrates that Pd@Ni-MOF is a highly effective catalyst for the ECH of BZH to BA. The findings highlight the critical role of the support material in improving catalyst performance by modifying adsorption configurations and reaction pathways. This approach presents a promising, energy-efficient, and environmentally friendly alternative to conventional hydrogenation methods.

When I initially decided to focus on the high-value utilization of BZH for my Ph.D. project, I found that many studies had explored the intrinsic catalytic activities of various elements, identifying Pd as the best catalyst compounts. Therefore I set Pd as the active component. For the support material, I initially considered nitrogen-doped graphite carbon materials, as graphite carbon can form  $\pi$ - $\pi$  conjugation with BZH, and the lone pair of electrons of nitrogen can facilitate substrate adsorption by  $\sigma$ - $\pi$  conjugation combining with aromatic ring. However, after preparing the corresponding materials, I found the catalytic performance was unsatisfactory.

I then read two papers {Angew. Chem. Int. Ed. 2021, 60, 290; Angew. Chem. 2020, 132, 1517–1521} that explored Pd supported on NH<sub>3</sub>-treated carbon cloth, which also showed poor performance. The materials that performed well all had oxygen-rich surfaces, or additives that promoted this effect with oxygen, indicating that BZH binds to the catalyst surface with C=O through H<sup>+</sup>. This led us to consider whether oxygen-rich MOFs could be used as catalyst supports, which subsequently resulted in the development of this work.

During the experiment, as we used the hydrothermal method to grow the catalyst on NF, we found that the pretreatment process of the NF significantly affected the morphology of the catalyst. It is necessary to wash away organic substances with acetone, remove the oxide layer with acid, and then wash multiple times with water. If the NF surface is acidic, the catalyst will form a particle-like structure instead of a sheet-like structure.

I also attempted using non-precious metal catalysts, but found that the HER is difficult to suppress under acidic conditions. In fact, I suspect that on the Pd surface, Pd-H fromation interacts with BZH to produce BA, which is highly likely that both hydrogenation steps follow the L-H mechanism. In contrast, on the surfaces of Co and Ni, at least one step of the reaction likely follows the PCET mechanism.

There are two points that need to be acknowledged: first, the stability of the catalyst under acidic conditions requires further improvement. Second, during our simulation, we did not consider the impact of voltage. When the voltage increases, electron accumulation on the catalyst surface can alter the adsorption behavior of organic molecules.

In this work, I prepared the materials, performed XRD, SEM, and FTIR characterization, and processed the corresponding data. Additionally, I handled the XPS data processing, conducted the electrochemical tests, and identified the products using HPLC along with processing the resulting data. The initial draft of the paper was written by me under the guidance and supervision of Pro. Dr. Andreu Cabot and Dr. Paulina R. Martínez-Alanis. Some tests and characterizations were completed by other collaborators.



www.acsami.org Research Article

## Enhanced Electrochemical Hydrogenation of Benzaldehyde to Benzyl Alcohol on Pd@Ni-MOF by Modifying the Adsorption Configuration

Li Gong, Chao Yue Zhang,\* Junshan Li, Guillem Montaña-Mora, Marc Botifoll, Tiezhu Guo, Jordi Arbiol, Jin Yuan Zhou, Tanja Kallio, Paulina R. Martínez-Alanis,\* and Andreu Cabot\*



Cite This: ACS Appl. Mater. Interfaces 2024, 16, 6948–6957



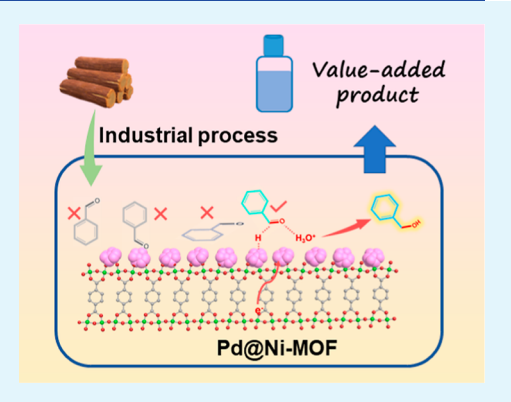
**ACCESS** I

III Metrics & More

Article Recommendations

Supporting Information

ABSTRACT: Electrocatalytic hydrogenation (ECH) approaches under ambient temperature and pressure offer significant potential advantages over thermal hydrogenation processes but require highly active and efficient hydrogenation electrocatalysts. The performance of such hydrogenation electrocatalysts strongly depends not only on the active phase but also on the architecture and surface chemistry of the support material. Herein, Pd nanoparticles supported on a nickel metal—organic framework (MOF), Ni-MOF-74, are prepared, and their activity toward the ECH of benzaldehyde (BZH) in a 3 M acetate (pH 5.2) aqueous electrolyte is explored. An outstanding ECH rate up to 283  $\mu$ mol cm<sup>-2</sup> h<sup>-1</sup> with a Faradaic efficiency (FE) of 76% is reached. Besides, higher FEs of up to 96% are achieved using a step-function voltage. Materials Studio and density functional theory calculations show these outstanding performances to be associated with the Ni-MOF support that promotes H-bond formation, facilitates water desorption, and



induces favorable tilted BZH adsorption on the surface of the Pd nanoparticles. In this configuration, BZH is bonded to the Pd surface by the carbonyl group rather than through the aromatic ring, thus reducing the energy barriers of the elemental reaction steps and increasing the overall reaction efficiency.

KEYWORDS: electrochemical hydrogenation, metal—organic-framework-supported palladium, tilted adsorption configuration, benzaldehyde, benzyl alcohol

## ■ INTRODUCTION

Biomass is a convenient precursor for the carbon-negative production of chemical commodities and fuels. Thus, the development of valorization strategies for the efficient and cost-effective conversion of biomass feedstocks has become a research priority. <sup>1-3</sup> Biomass valorization schemes generally involve several steps, including feedstock deconstruction, conversion of solid biomass into a liquid bio-oil for convenient transportation and postprocessing, and multiple deoxygenation and hydrogenation reactions to upgrade the oxygen-rich and hydrogen-poor biomass derivate into higher-value chemicals, particularly fuels. Usually, several thermocatalytic steps and highly pressurized hydrogen are required in this process, which limits its cost-effectiveness, especially within a small-scale distributed scenario that reflects and adapts to the distributed nature of biomass.<sup>3</sup>

Alternative electrocatalytic approaches, taking advantage of protons within the electrolyte instead of highly pressurized hydrogen, are particularly advantageous in terms of energy efficiency, mild reaction conditions including relatively low temperatures  $\leq 80$  °C, cost, and feasibility of combining with clean electricity provided by renewable energy sources such as

wind and photovoltaics.<sup>4–11</sup> These advantages also make electrocatalytic hydrogenation (ECH) schemes suitable for distributed processing.<sup>3,12</sup>

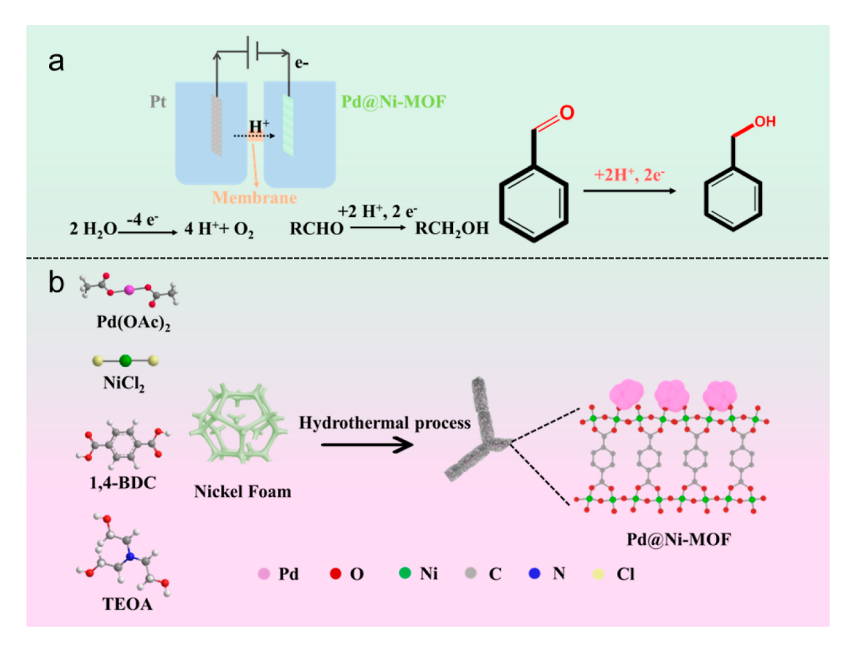
Benzyl alcohol (BA) is a chemical commodity used as a solvent in the fields of printing and coatings, as a desiccant of polymers such as nylon, as a precursor for the preparation of esters, and as an additive in the fragrance industry. The conventional industrial methods for producing BA is the toluene chlorination to benzyne chloride and subsequent hydrolysis. This route produces chlorine residues that are harmful to the environment. Thus, the production of BA from the selective catalytic reduction of benzaldehyde (BZH), which can be obtained from lignin depolymerization, so is considered a convenient green alternative.

Received: September 17, 2023 Revised: January 16, 2024 Accepted: January 23, 2024 Published: February 2, 2024





Scheme 1. (a) Illustration of the ECH of BZH to BA; (b) Scheme of the Preparation Process of the Electrocatalyst Pd@Ni-MOF\*



<sup>a</sup>Hydrogen atoms (white) were deleted from the Pd@Ni-MOF supramolecular structure for clarity.

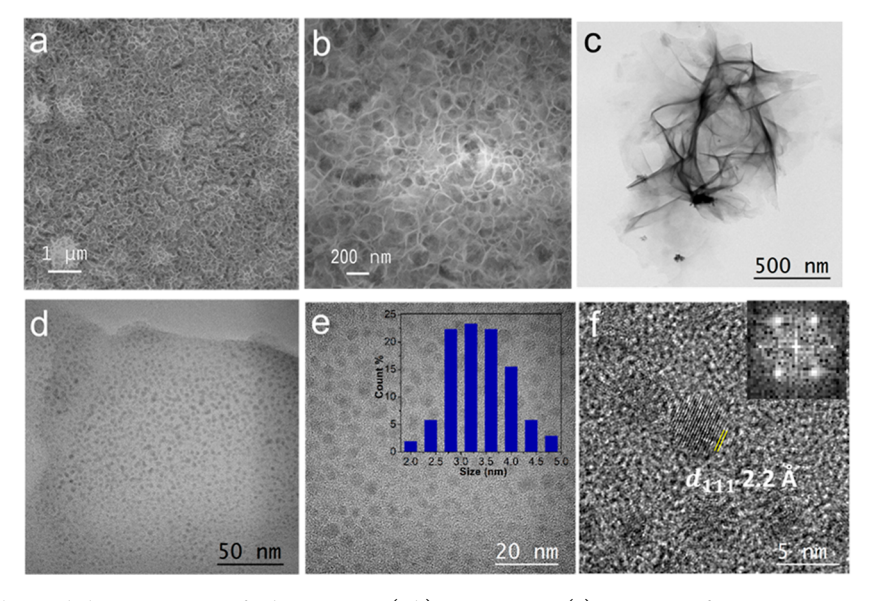


Figure 1. Structural and chemical characterization of Pd@Ni-MOF. (a,b) SEM images. (c) Low-magnification TEM image. (d) High-magnification TEM image; (e,f) HRTEM images and histogram with the size distribution of the Pd nanoparticles.

Due to the benefits of ECH schemes over conventional catalytic hydrogenation approaches, the reaction mechanism and the performance of several transition metals toward the ECH of BZH to BA have been explored both experimentally and theoretically.  $^{3,17-21}$  Among the transition metal electrocatalysts tested for this reaction, Pd is considered the most active because of its optimum interaction strength with BZH, with a computed binding of -3.16 eV.  $^{20,22}$ 

Beyond the active phase, the support also plays a fundamental role in ECH reactions. <sup>23</sup> Large-surface-area-supports are needed to enable a high dispersion of the active phase. In this direction, the large surface area and tunable structure of metal—organic frameworks (MOFs) offer an ideal architecture to support catalytic active centers. <sup>24–28</sup> Moreover,

the metal nodes and aromatic linkers of MOFs can modify electronic energy levels through synergistic interaction between the different elements and  $\pi-\pi$  forces,  $^{29-31}$  thereby potentially enhancing the stability and activity of the active centers. Besides dispersing the active phase, supports play a strong role in binding the reactant molecule or its intermediates. In ECH processes, Langmuir—Hinshelwood (LH) and proton-coupled electron transfer (PCET) mechanisms have been proposed. Both pathways require the concentration of H proton and organic substrate on the electric double layer near the cathode surface. Thus, beyond selecting a proper active phase and having it highly dispersed on a high surface area support, the support composition, transport properties, and surface chemistry are

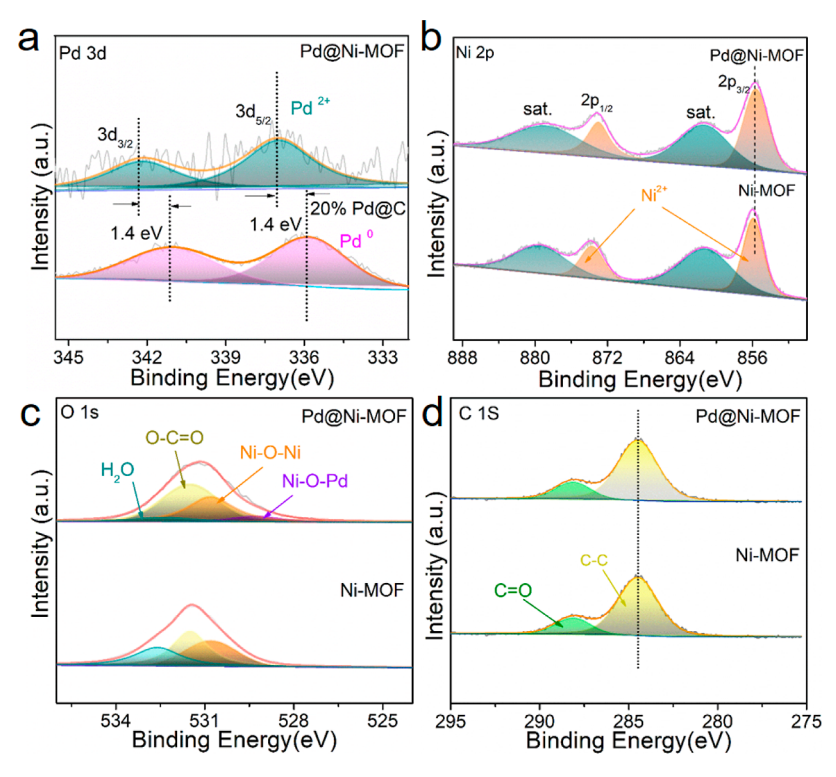


Figure 2. High-resolution XPS spectra of Pd@Ni-MOF, 20% Pd@C, and Ni-MOF, as indicated in each panel: (a) Pd 3d; (b) Ni 2p; (c) O 1s; and (d) C 1s.

fundamental parameters to be optimized to maximize the catalyst performance.<sup>3</sup> As an example, Zou's group reported a UIO-66 MOF modified with terminal sulfonic groups that provided stronger Lewis acidic—basic and Brønsted acidic sites that contribute to the ECH of furfural to furfuryl alcohol.<sup>36</sup> Besides, Lercher's group proved acid functionalization of carbon supports promotes the ECH of BZH to BA.<sup>37</sup> They also proved that adding phenol into the reaction system promoted the reaction rate due to additional hydrogen bond formation.<sup>18</sup>

Herein, we propose a high-performance electrocatalyst for the BZH to BA hydrogenation reaction based on Pd nanoparticles supported on an oxygen-rich Ni-MOF (Scheme 1). The system is studied both experimentally and using theoretical calculations. We particularly analyze the role of the support in the excellent performance obtained, affecting the adsorption/desorption of hydrogen, water, and BZH, and promoting its reaction.

## ■ RESULTS AND DISCUSSION

Pd nanoparticles supported on Ni-MOF-74 (Pd@Ni-MOF) were prepared by a one-step solvothermal process as shown in Scheme 1b (details in the Experimental Section). In this process, terephthalic acid (BDC), nickel(II) chloride hexahydrate, and palladium(II) acetate were used as the source of Ni-MOF and Pd. Nickel foam (NF) was used as the conducting support. A small amount of triethanolamine (TEOA) was used as a morphology control agent to guarantee a good dispersion of Pd

The Pd@Ni-MOF exhibits a three-dimensional architecture formed by intersecting nanosheets (Figure 1a-c) that offer a large surface area for reactant adsorption and diffusion, ample pores for effective electrolyte diffusion, and a suitable solid network for fast charge transport. While in the absence of

TEOA, Pd strongly agglomerates (Figure S1 and Table S1), the addition of a small amount of TEOA results in a homogeneous dispersion of Pd particles with an average diameter of 3 nm across the Ni-MOF surface, as observed by transmission electron microscopy (TEM) characterization (Figure 1d,e). High-resolution TEM (HRTEM) micrographs of Pd and the related fast Fourier transform analysis showed the Pd(111) plane with a 2.2 Å lattice spacing (Figure 1f). Scanning TEM (STEM)-high-angle annular dark-field (HAADF) image and associated energy-dispersive spectrometry (EDS) compositional maps of Pd@Ni-MOF confirmed the excellent dispersion of the different elements. Additionally, EDS analysis showed the Pd/Ni ratio within Pd@Ni-MOF to be 0.28 (Figure S2a and Table S2).

The X-ray diffraction (XRD) patterns of Pd@Ni-MOF and Ni-MOF show peaks at 8.6, 14.9, 15.9, and 17.1°, consistent with literature calculations of the Ni-MOF-74 crystal phase (Figure S2b).<sup>38</sup> On the other hand, the XRD peaks at 40.2 and 46.8°, only present in the Pd@Ni-MOF sample, are assigned to the metallic Pd phase.

The specific surface areas of Pd@Ni-MOF and Ni-MOF were quantified at 30.3 and 31.6 m²·g⁻¹, respectively (Figure S4). Thus, the presence of Pd did not significantly modify the surface area of the Ni-MOF. The organic framework of the material was characterized using FTIR. The IR absorption peaks at 1575 and 1357 cm⁻¹ are associated with the benzene ring skeleton stretching vibration splitting peaks, indicating the presence of an aromatic ring structure in the organic framework (Figure S5). The absorption peaks at 1636 and 1422 cm⁻¹ are related to the antisymmetric and symmetric stretching vibration peaks of carboxylate (COO), respectively. The difference  $\Delta$  [ $\nu_{\rm as}$  –  $\nu_{\rm s}$ ] is about 214 cm⁻¹, indicating that the carboxyl group of 1,4-BDC and the Ni ion form a bond through bridge coordination.  $^{17,39,40}$ 

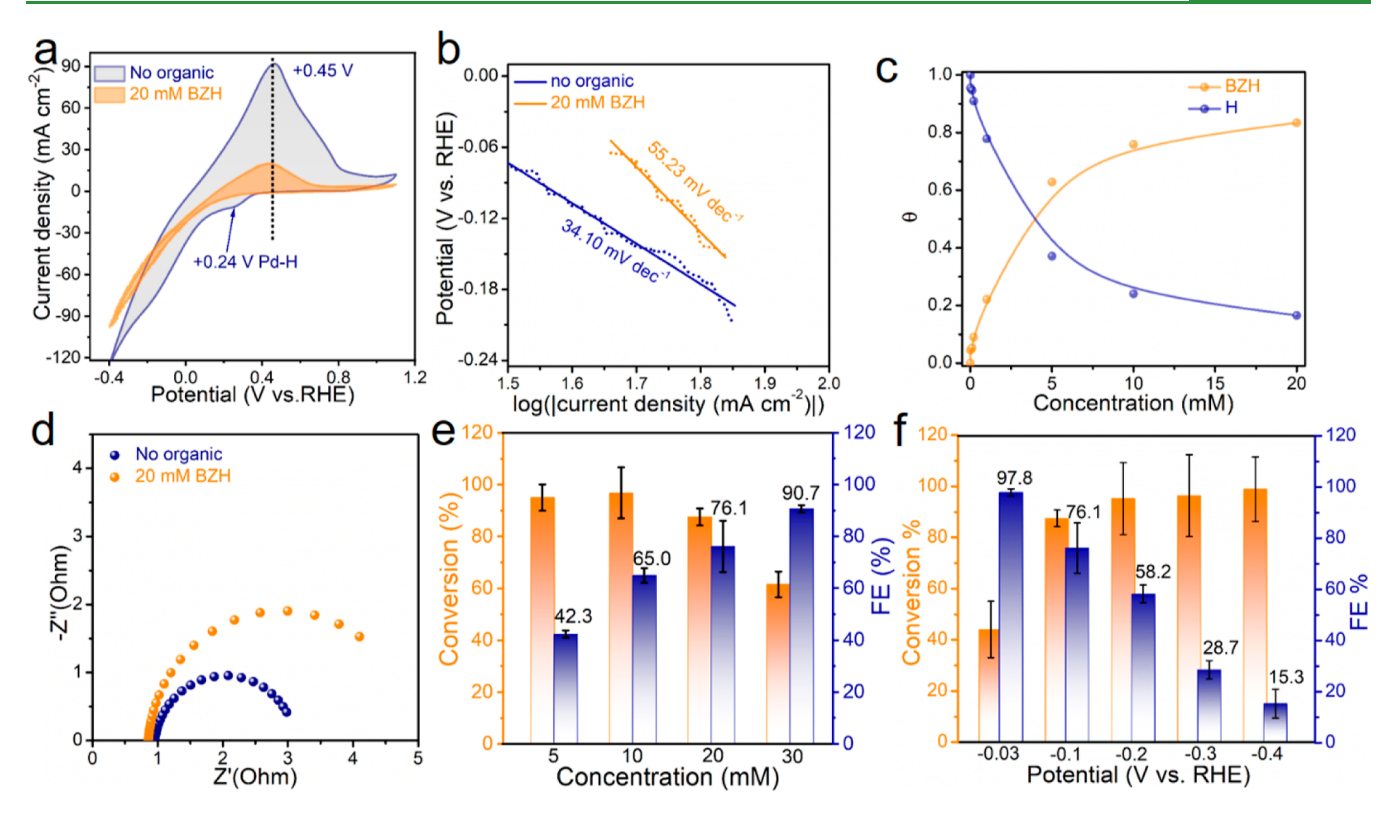


Figure 3. (a) CV curves of Pd@Ni-MOF in the presence and absence of 20 mM BZH. (b) Tafel plot. (c) H and BZH surface coverage. (d) Nyquist plot of the EIS spectra in the presence and absence of 20 mM BZH. (e) BZH-to-BA conversion and FE as a function of the BZH concentration at constant voltage -0.1 V vs RHE; (f) BZH-to-BA conversion and FE as a function of the voltages with 20 mM BZH in sodium acetate—acetic acid (3 M) buffer (pH 5.2) electrolyte, room temperature, 1 bar N<sub>2</sub> flow.

Figure 2 shows the high-resolution Pd 3d, Ni 2p, O 1s, and C 1s XPS spectra of Pd@Ni-MOF, Ni-MOF, and a reference 20% Pd@C sample. The Pd 3d spectrum of Pd@Ni-MOF shows a doublet at 342.4 eV (Pd 3d<sub>3/2</sub>) and 337.1 eV (Pd 3d<sub>5/2</sub>) assigned to a Pd-O chemical environment. In the reference 20% Pd@C sample, the peaks located at 341.1 eV (Pd  $3d_{3/2}$ ) and 335.8 eV (Pd  $3d_{5/2}$ ) are assigned to Pd<sup>0</sup>. Besides the satellite peaks, the Ni 2p XPS spectrum of Pd@Ni-MOF also shows one doublet at 873.0 eV (Ni  $2p_{1/2}$ ) and 855.6 eV (Ni 2p<sub>3/2</sub>) assigned to a Ni<sup>2+</sup> chemical environment.<sup>41</sup> A very similar spectrum was obtained for the Ni-MOF sample. The O 1s spectrum shows several contributions tentatively assigned to Ni-O-Pd (529.1 eV), Ni-O-Ni (530.8 eV) of MOF, O=C-O (531.6 eV) of the linker in MOF, and  $H_2O$ (532.6 eV). The C 1s spectrum of Pd@Ni-MOF and Ni-MOF shows two main contributions that we associate with the C-C bond used as a reference (284.6 eV) and with the C=O chemical environment within the Ni-MOF (288.1 eV).

Electrochemical Performances of Pd@Ni-MOF. Cyclic voltammetry (CV) curves in 3 M pH 5.2 sodium acetate—acetic acid buffer solution electrolyte are shown in Figure 3a (blue line). In the reverse scan, the CV curve shows a shoulder at +0.24 V vs reversible hydrogen electrode (RHE), overlapping with the hydrogen evolution reaction (HER) taking place at a lower potential. This shoulder, usually termed the hydrogen underpotential deposition (H<sub>upd</sub>) region, is assigned to the hydrogen adsorption and the formation of Pd hydride (Pd–H). In the forward scan, the large peak at +0.45 V vs RHE is assigned to the hydrogen desorption.

When BZH was added into the electrolyte, in the forward scan, the hydrogen desorption peak massively shrank. In

parallel, in the reverse scan, the shoulder disappeared, and the step increase related to HER decreased. This is associated with the onset potential of BZH hydrogenation being comparable with that of HER but the kinetics of the BZH hydrogenation reaction being slower than that of HER. This slower BZH hydrogenation kinetics is also reflected in the much larger Tafel slope in the presence of BZH, 55.2 mV dec<sup>-1</sup>, than in its absence (34.1 mV dec<sup>-1</sup>, Figure 3b).

The reversible adsorption of hydrogen,  $H_{upd} \rightleftharpoons H^+(aq) + e^-$ + \*, dominating the CV curve in an acid electrolyte, is commonly used to estimate the number of adsorption sites. Because H<sub>upd</sub> overlaps with the HER, the hydrogen desorption peak in the forward scan is generally used for this estimation. As shown in the CV curves in Figure S6, the presence of larger amounts of BZH progressively inhibits hydrogen deposition, which translates into the area of the hydrogen desorption peak S<sub>H</sub> decreasing with the introduction of increasing amounts of the organic molecule. Figure S6b shows the H<sub>upd</sub> deposition/ desorption region of the CV for Pd@Ni-MOF in acetate buffer (pH 5.2) and with different concentrations of BZH. Under the assumption that only BZH and hydrogen adsorb on the surface active sites of the electrocatalyst, 42-44 that both species occupy all the active sites, with hydrogen atoms occupying the complete active sites in the pure electrolyte, 42 while disregarding the effect of the double-layer capacitance, 45 and that the desorption of BZH does not affect the H desorption peak area, 46 it is possible to determine the hydrogen coverage  $(\theta_{\rm H})$  and BZH coverage  $(\theta_{\rm BZH})$  through

$$\theta_{\rm H} = {{
m area~of~the~H~desorption~region}\over {{
m area~of~H~desorption~region~in~pure~electrolyte}}}$$
 (1)

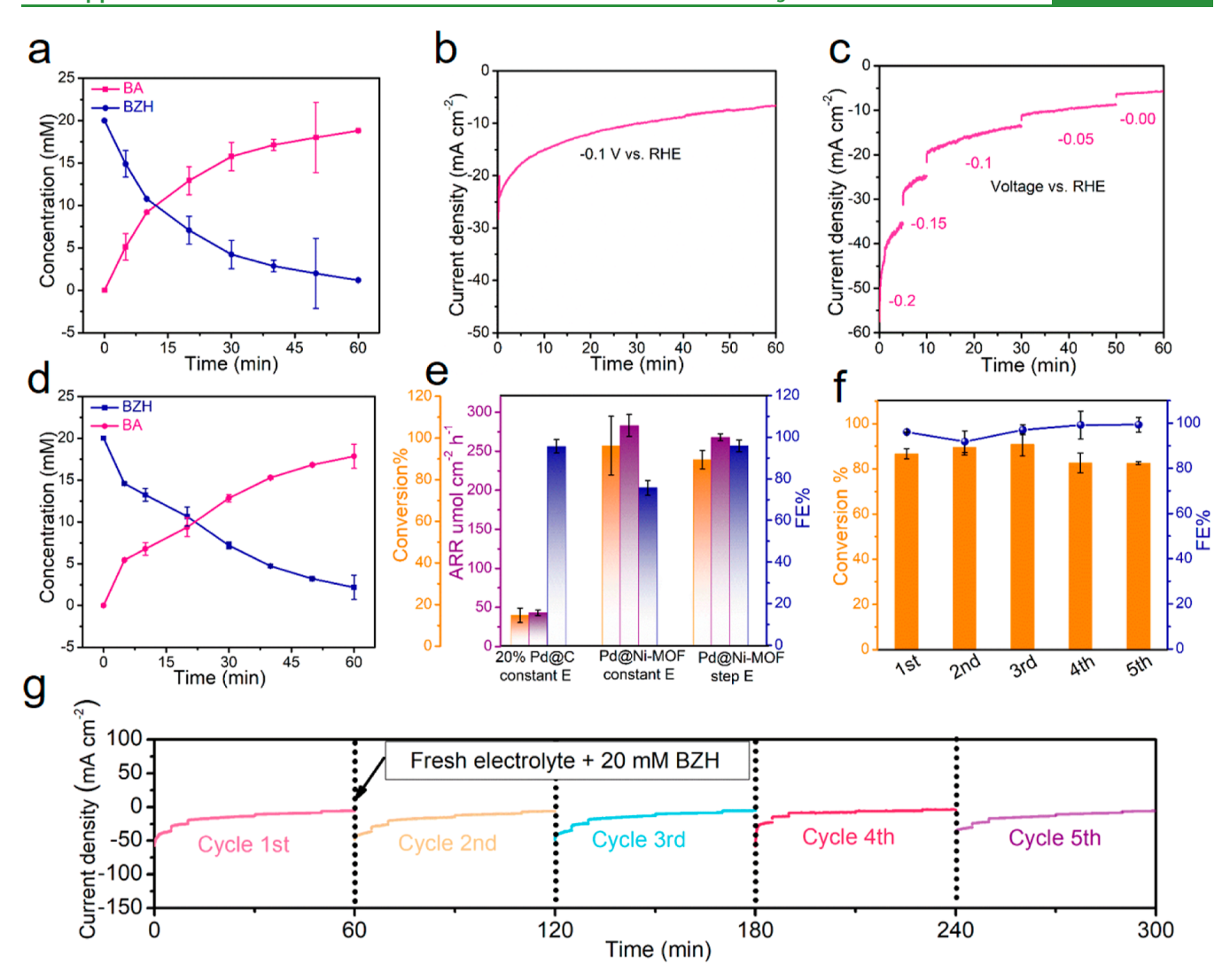


Figure 4. Time-dependent conversion of BZH to BA over Pd@Ni-MOF. (a) BZH conversion and BA production at a constant voltage of -0.1 vs RHE. (b) I-t curve at -0.1 vs RHE. (c) I-t profile under a progressively decreasing voltage. (d) BZH conversion and BA production using the voltage steps displayed in panel c. (e) Comparison of the conversion, FE, and average reaction rate (ARR, eq S2) of different catalysts and strategies; (f) BZH-to-BA conversion and FE for 5 cycles with a stepped voltage. (g) I-t profile of the BZH-to-BA conversion for 5 cycles with a step voltage within 1 h in sodium acetate—acetic acid (3 M) buffer (pH 5.2) electrolyte, room temperature, 1 bar N<sub>2</sub> flow.

$$\theta_{\rm BZH} = 1 - \theta_{\rm H} \tag{2}$$

Adding 20 mM of BZH into the electrolyte, S<sub>H</sub> strongly decreased, from 18.7 to 7.0 mA·V, and  $\theta_{\mathrm{Hydrogen}}$  declined from 1 in the pure electrolyte to 0.38. In contrast, the  $S_H$  of commercial 20% Pd@C (Figure S7a and Table S3) was not substantially affected by the introduction of BZH, from 0.20 to 0.22 mA·V, with  $\theta_{\mathrm{Hydrogen}}$  maintained at almost 1. On the other hand, the TEOA-free Pd@Ni-MOF (Figure S7b and Table S3) also underwent a notable S<sub>H</sub> change, from 17.9 to 7.6 mA·V, reaching a  $\theta_{\mathrm{Hydrogen}}$  of 0.42. In addition, the Ni-MOF showed a notable  $S_H$  change from 5.0 to 3.5 mA·V and a  $\theta_{Hydrogen}$ reduction to 0.72, which indicate that the Ni-MOF plays a role in the adsorption of BZH (Figure S7c and Table S3). These experimental results demonstrate that Pd@Ni-MOF electrodes are much more prone to adsorb BZH than the commercial 20% Pd@C catalyst. To investigate the materials' reducibility, H2-temperature-programmed reduction (H2-TPR) was conducted on Pd@Ni-MOF and compared with that of 20% Pd/C (Figure S8 and Table S4). The Pd@Ni-MOF displayed sharp peaks at 334.8 °C and a weak broad peak at 456.7 °C with a

total area of 171.1 cm<sup>3</sup> g<sup>-1</sup> STP, significantly larger than 20% Pd@C with weak broad peak of 54.5 cm<sup>3</sup> g<sup>-1</sup> STP at 564.5 °C. This implies the superior reducibility of Pd@Ni-MOF owing to the O-rich surface and the presence of Pd<sup>2+</sup>. Besides, as reflected by the dependence of  $S_H$  on the BZH concentration (Figure 3c), at all BZH concentrations, hydrogen adsorption still takes place; thus, both species are simultaneously adsorbed, which is key for the BZH hydrogenation to take place.

Figure 3d displays the Nyquist plot of the electrochemical impedance spectroscopy (EIS) spectra of the Pd@Ni-MOF electrode in the blank electrolyte and the presence of BZH. Comparing the different materials (Figure S7), we observe the charge transfer resistance without BZH to be the lowest for Pd@Ni-MOF ( $\sim$ 2  $\Omega$ ), well below that of Pd@C ( $\sim$ 48  $\Omega$ ) and TEOA-free Pd@Ni-MOF ( $\sim$ 4  $\Omega$ ). As expected, a larger semicircle is obtained in the presence of BZH, associated with the inhibition of the HER and the related higher charge transfer resistance at the electrolyte/electrode interphase. In contrast, the Ni-MOF shows a much larger resistance (>1000

 $\Omega$ ) which is not significantly affected by the presence of BZH, demonstrating its role just as a support of the active component. The performance of the different materials toward the ECH of BZH to BA was evaluated at -0.1 V vs RHE for 1 h in sodium acetate—acetic acid (3 M) buffer (pH 5.2) electrolyte, as shown in Figure S9 and Table S4, confirming the superior performance of Pd@Ni-MOF over that of other materials.

The Faradaic efficiencies (FEs) of the ECH of BZH over Pd@Ni-MOF were determined after 1 h of reaction at a constant voltage of -0.1 V vs RHE using different substrate concentrations (Figure 3e). The FE increased as the BZH concentration increased, up to 86% for a 30 mM BZH. This correlation of the FE with the BZH concentration is related to the increase in the BZH coverage and the consequent reduction of H coverage that reduces the competing HER activity. As expected, at a set voltage of -0.1 V vs RHE, the accumulated and tracked FEs decreased during the reaction as the BZH was consumed and its concentration decreased (Figure S10). Figure 3f shows the conversion and FE after 1 h reaction at different voltages at a set concentration. The FE rapidly decreases as the voltage increases, which is related to the H<sub>2</sub> bubbles generated by the stronger HER, inhibiting BZH adsorption, and thus its hydrogenation. Notice that while high FEs up to 98% were obtained at low voltages (-0.03 V vs RHE), the conversion after 1 h reaction in these conditions was moderate (just 42% at -0.03 V vs RHE).

The time-dependence transformation of BZH into BA over Pd@Ni-MOF when applying a constant voltage -0.1 V vs RHE is shown in Figure 4a. We observe that in the batch Hcell reactors, as the reaction proceeds, the concentration of BZH rapidly decreases. The related I-t curve (Figure 4b) exhibits the current density decreasing as the reaction proceeds, and BZH is consumed. These results are not fully consistent with the CV curve shown in Figure 3a due to the different reaction kinetics of BZH and H<sub>2</sub>. In contrast to the CV curve, the I-t curve reflects the indirect reduction mechanism where adsorbed BZH reacts with the reduced H<sub>ad</sub> atoms rather than accepting electrons and reacting with  $H^{+42}$  Figure S11 exhibits the I-t curves at different voltages of conversion of BZH to BA over Pd@Ni-MOF. At −0.4 V vs RHE, the current increases with time, which is related to the increasing weight of HER as BZH decreases.

To maximize the FE, we considered a progressive reduction of the applied voltage as the concentration of the substrate decreased, as shown in the I-t profile of Figure 4c. Figure 4d shows the time dependence of the conversion obtained using this step voltage function. This strategy allowed for reaching of FEs above 96% with a total conversion of 89% after 1 h reaction (Figure 4e, Table S5). Such high FEs could be maintained over five 60 min cycles, as shown in Figure 4f,g. It should be noted that the FE sharply decreased when applying a higher step voltage process due to the competing HER (Figure S12). While this strategy allows for optimizing the process, its practical implementation is not straightforward and requires optimizing challenges related to the monitoring of the best combination of substrate concentrations and voltages.

The XRD patterns (Figure S13) of the powders obtained from the sonication of the electrode after five cycles for a total of 300 min of reaction show that the Ni-MOF fingerprint has disappeared. This result shows a partial amorphization of the MOF during the reaction but without a major morphology and elemental distribution change according to SEM and HAADF-

EDS analysis (Figure S14). Compared with the fresh Pd@Ni-MOF electrocatalyst (Table S2), energy-dispersive X-ray (EDX) analysis (Table S7) of the catalyst powder after cycling shows the amount of Ni to have decreased from 10.3 to 5.4%, while the relative amount of Pd has significantly increased from 2.9% up to 7.4%. XPS spectra of the Pd@Ni-MOF after cycling (Figure S15) display no major change in the Pd 3d XPS spectrum after cycling, with the main peaks being associated with Pd<sup>0</sup> (3d<sub>5/2</sub> 335.1 eV and 3d<sub>3/2</sub> 341.9 eV), which indicate that in the operating reduction condition, some of the Pd<sup>2+</sup> was reduced to Pd<sup>0</sup>. The Ni/Pd ratio obtained by XPS significantly decreased with the reaction, consistent with EDX data. We associate this decrease with the partial leaching of Ni ions in the acid electrolyte. Notice that according to the stability test data shown in Figure 4g, this leaching had a minor effect on the performance. However, as an oxygen-rich surface material, maintaining stability under reduced voltage conditions remains

Adsorption Configuration of BZH on Pd@Ni-MOF. It is essential that the catalyst surface offers sites for the simultaneous adsorption of the organic molecules BZH and H. On a pure Pd surface, the BZH tends to be adsorbed through the phenyl ring with a vertical configuration.<sup>22</sup> To understand the high activity of Pd@Ni-MOF, the adsorption process was simulated using Materials Studio (MS) calculations. As shown in Figure S16a,b, when Pd nanoparticles are dispersed on a graphitic carbon support, the phenyl ring structure drives the adsorption of BZH with a horizontal or vertical configuration. On the other hand, within the Pd@Ni-MOF system, Pd nanoparticles bind to the oxygen-rich Ni-MOF through surface oxygen (Pd-O-Ni), accepting electrons provided by the oxygen in the MOF structure. In this scenario, Pd becomes an electron acceptor, and the reduced electron cloud density around Pd enables BZH adsorb on its surface through the carbonyl group rather than the phenyl ring; thus, the titled adsorption configuration becomes the most favorable (Figure S16c). In this configuration, the total average energy of BZH adsorbed on Pd@Ni-MOF is -64.11 kcal/mol, well above (in absolute value) that of BZH adsorbed on Pd@C, at -50.47 kcal/mol. As for H adsorption, our calculations (Figure S17) show that the adsorption energy of H on a pure Pd surface (-1.61 kcal/mol) is lower than that on the Ni-MOF (-3.64 kcal/mol), indicating that the Ni-MOF is the main H adsorber, enriching H in the Pd@Ni-MOF interphase.

Based on the initial simulation results showing the tilted adsorption configuration of BZH on the material Pd@Ni-MOF, DFT calculations were carried out to determine the adsorption energies of the substrate, intermediates, and product on the surface of Pd (Figure S18) and Pd@Ni-MOF (Figure S19). Taking into account recent literature showing that both mechanisms, LH and PCET, may be involved simultaneously, with the first electron and H proton following PCET, while the second electron and H proton follow the LH process. 47,48 Thus, we considered the overall ECH reaction 47

$$phCHO + 2H^{+} + 2e^{-} \rightarrow phCH_{2}OH$$
 (3)

involving the following elementary steps (Figure 5a)

$$phCHO + * \stackrel{1}{\rightarrow} phCHO^*$$
 (4)

$$phCHO^* + H_3O^+ + e^- \xrightarrow{2} phCHOH_3O^*$$
 (5)

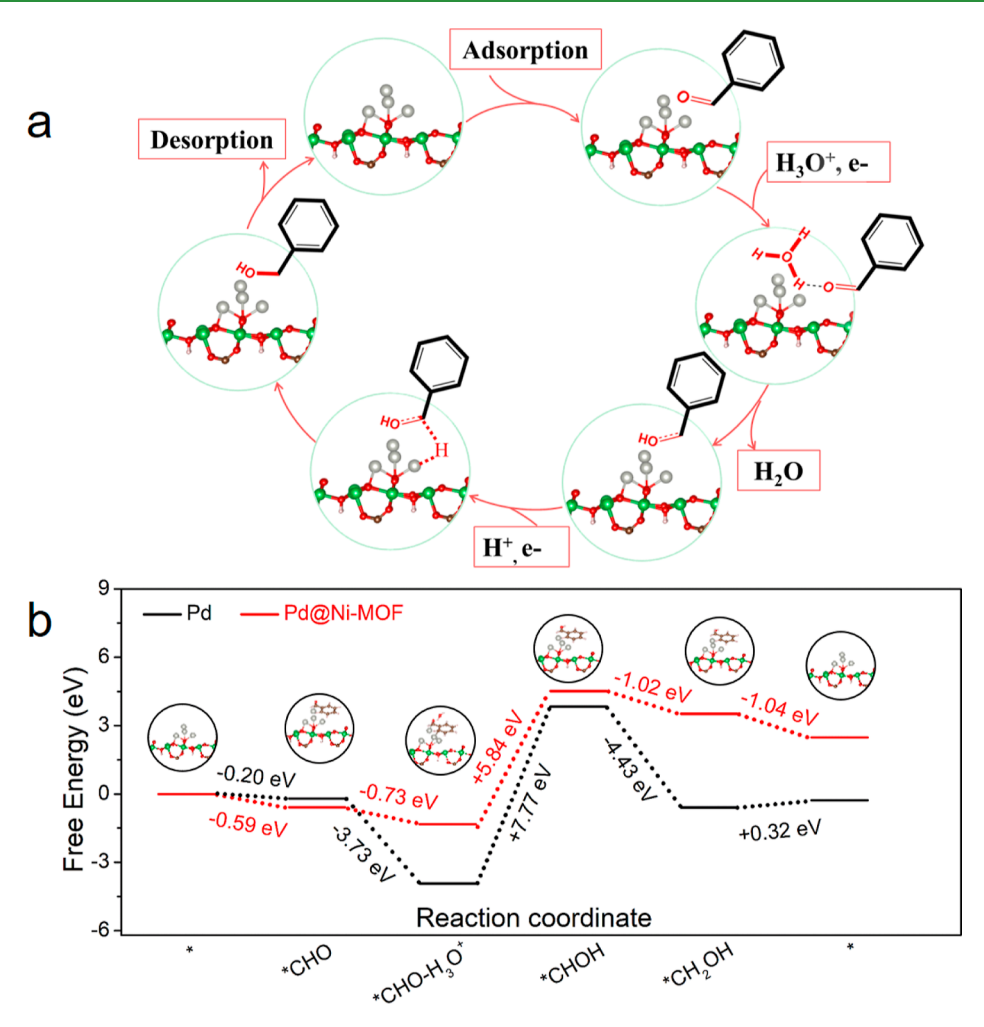


Figure 5. (a) Mechanism of the ECH of BZH to BA. Gray ball refers to Pd, green ball refers to Ni, red ball refers to O, and wine-colored ball refers to C. (b) Free energy profiles for the BZH-to-BA process on Pd and Pd@Ni-MOF.

$$phCHOH3O* \xrightarrow{3} phCHOH* + H2O$$
 (6)

$$H^{+} + e^{-} + {}^{*} \stackrel{4}{\rightarrow} H_{Ads}$$
 (7)

$$phCHOH^* + H_{Ads} \xrightarrow{5} phCH_2OH^*$$
 (8)

$$phCH2OH* \xrightarrow{6} phCH2OH + *$$
 (9)

Figure 5b displays the free energy change from the substrate phCHO, intermediate species phCHO-H<sub>3</sub>O, phCHOH, and the product phCH<sub>2</sub>OH on unsupported Pd and Pd@Ni-MOF. The substrate adsorption step indicates a stronger BZH energy on the surface of Pd@Ni-MOF (-0.59 eV) than that on Pd (-0.20 eV). The most prominent advantage of the Pd@Ni-MOF is the lower free energy change associated with the H<sub>2</sub>O molecule removal step, which is the rate-limiting step. The free energy change associated with this step in Pd@Ni-MOF is +5.84 eV, well above the value obtained for unsupported Pd, +7.77 eV. This lower energy change is related to the formation of Pd-O-Ni bonds on the Ni-MOF surface that changes Pd from an electron donor to an electron acceptor, thus facilitating the removal of H<sub>2</sub>O molecules. The free energy of the second hydrogen atom added to the species phCHOH (6) is higher on Pd@Ni-MOF (-1.02 eV) than that on the Pd

surface (-4.43 eV), which decreases the kinetic energy barrier significantly.

## CONCLUSIONS

A Pd@Ni-MOF electrocatalyst containing a uniform dispersion of Pd particles on the surface of a Ni-MOF was produced and characterized. This electrocatalyst showed excellent activity toward the BZH ECH to BA in an aqueous phase with an outstanding ECH rate of up to 283  $\mu$ mol cm<sup>-2</sup> h<sup>-1</sup> with a FE of 76%. This excellent performance is related to the important role played by the Ni-MOF in increasing the adsorbed hydrogen coverage, enabling the tilted adsorption of BZH through its carbonyl group and facilitating H<sub>2</sub>O desorption. Besides, we demonstrate that the reaction FE can be increased up to 96% by modulating the applied voltage while the total conversion is improved to close to 90%. In this strategy, relatively high voltages are applied at high substrate concentrations and are decreased as the concentration decreases to maintain a high selectivity. This work provides new insight into the selective hydrogenation of BZH into monomer-alcohol products and other carbonyl functional group organics.

### ■ EXPERIMENTAL SECTIONS

Materials. Palladium(II) acetate [Pd(OAc)<sub>2</sub> 98%, Sigma-Aldrich], terephthalic acid (BDC, 98%, Sigma-Aldrich 98%, Sigma-Aldrich),

nickel(II) chloride hexahydrates (NiCl<sub>2</sub>·6H<sub>2</sub>O, 99.9%, Sigma-Aldrich),  $N_i$ N-dimethylformamide (DMF,  $\geq$ 99.8%, Sigma-Aldrich), triethanolamine (TEOA, 97%, Thermo Scientific), ethanol (CH<sub>3</sub>CH<sub>2</sub>OH, 96%, Letslab), benzaldehyde (C<sub>7</sub>H<sub>6</sub>O, 98%, Sigma-Aldrich), acetone [(CH<sub>3</sub>)<sub>2</sub>CO, Letslab], hydrochloric acid (HCl, 37%, Thermo Scientific), and NF (99.9%, Kejing) were used aspurchased, without further purification.

Synthesis of Pd@Ni-MOF. One mmol of NiCl<sub>2</sub>·6H<sub>2</sub>O, 1 mmol of BDC, 0.2 mmol of Pd(OAc)2, and 1 mmol of TEOA were dissolved in 22 mL of a mixture solution of DMF and Milli-Q (MQ) water (20:2). After continuously stirring for 30 min, the solution was transferred into a 30 mL Teflon-lined autoclave, and a piece of NF (3 × 2 cm<sup>2</sup>), previously cleaned with 3 M HCl for 10 min and washed 3 times with MQ water, was placed into the solution leaning against the autoclave wall. The autoclave was sealed and heated to 120 °C for 12 h. After cooling to room temperature, the sample was thoroughly washed with DMF, MQ water, and ethanol and then dried at 60 °C overnight. The final mass loading was 1.2 mg cm<sup>-2</sup>. This sample was named Pd@Ni-MOF. In addition, reference samples containing no TEOA (TEOA-free Pd@Ni-MOF), no Pd (Ni-MOF), and no TEOA, and no Pd (TEOA-free Ni-MOF) were also produced. An additional reference material electrode was produced by loading a commercial 20% Pd supported on active carbon on NF (20% Pd@C).

### ASSOCIATED CONTENT

## **Solution** Supporting Information

The Supporting Information is available free of charge at https://pubs.acs.org/doi/10.1021/acsami.3c13920.

Additional experimental details, including experimental setups, XRD, SEM, FT-IR, BET, and electrochemical data (PDF)

## AUTHOR INFORMATION

## **Corresponding Authors**

Chao Yue Zhang — Catalonia Institute for Energy Research—IREC Sant Adrià de Besòs, Barcelona 08930, Spain; Key Laboratory for Magnetism and Magnetic Materials of the Ministry of Education & School of Physical Science & Technology, Lanzhou University, Lanzhou 730000, China; Email: zhangchy2020@lzu.edu.cn

Paulina R. Martínez-Alanis — Catalonia Institute for Energy Research—IREC Sant Adrià de Besòs, Barcelona 08930, Spain; Email: pmartinez@irec.cat

Andreu Cabot — Catalonia Institute for Energy Research— IREC Sant Adrià de Besòs, Barcelona 08930, Spain; Catalan Institution for Research and Advanced Studies—ICREA, Barcelona 08010, Spain; orcid.org/0000-0002-7533-3251; Email: acabot@irec.cat

## Authors

Li Gong — Catalonia Institute for Energy Research—IREC Sant Adrià de Besòs, Barcelona 08930, Spain; University of Barcelona, Barcelona 08028, Spain

Junshan Li – Institute for Advanced Study, Chengdu University, Chengdu 610106, China; ⊚ orcid.org/0000-0002-1482-1972

Guillem Montaña-Mora — Catalonia Institute for Energy Research—IREC Sant Adrià de Besòs, Barcelona 08930, Spain: University of Barcelona, Barcelona 08028, Spain

Marc Botifoll – Catalan Institute of Nanoscience and Nanotechnology (ICN2), CSIC and BIST, Bellaterra 08193 Barcelona, Spain; orcid.org/0000-0002-4876-6393

**Tiezhu Guo** – Key Laboratory of Multifunctional Materials and Structures, Ministry of Education, School of Electronic

Science and Engineering, Xi'an Jiaotong University, Xi'an 710049 Shaanxi, China

Jordi Arbiol — Catalan Institute of Nanoscience and Nanotechnology (ICN2), CSIC and BIST, Bellaterra 08193 Barcelona, Spain; Catalan Institution for Research and Advanced Studies—ICREA, Barcelona 08010, Spain; orcid.org/0000-0002-0695-1726

Jin Yuan Zhou — Key Laboratory for Magnetism and Magnetic Materials of the Ministry of Education & School of Physical Science & Technology, Lanzhou University, Lanzhou 730000, China; orcid.org/0000-0003-0284-105X

Tanja Kallio — Department of Chemistry and Materials Science, Aalto University School of Chemical Engineering, Aalto FI-00076, Finland; orcid.org/0000-0001-6671-8582

Complete contact information is available at: https://pubs.acs.org/10.1021/acsami.3c13920

### **Notes**

The authors declare no competing financial interest.

### ACKNOWLEDGMENTS

L.G. and C.Y.Z. thank the China Scholarship Council for the scholarship support. This work was financially supported by the SyDECat project from the Spanish MCIN/AEI/FEDER (PID2022-136883OB-C22). This work was supported by the Innovation Fund for Small and Medium-Sized Enterprises in Gansu Province (no. 22CX3JA006) and Lanzhou Talent Innovation and Entrepreneurship Project (no. 2022-2-81) and partially by the Fundamental Research Funds for the Central Universities (grant nos. lzujbky-2021-it33). The authors greatly acknowledge the support of the Supercomputing Center of Lanzhou University, China. J.L. is grateful for the project supported by the Natural Science Foundation of Sichuan Province (2022NSFSC1229). The authors also greatly thank for the generous help from Liming Deng and Professor Dr. Shengjie Peng (College of Materials Science and Technology Nanjing University of Aeronautics and Astronautics Nanjing 210016, China). The project on which these results are based has received funding from the European Union's Horizon 2020 research and innovation programme under Marie Skłodowska-Curie grant agreement no. 801342 (Tecniospring INDUSTRY) and the Government of Catalonia's Agency for Business Competitiveness (ACCIÓ). The authors acknowledge funding from Generalitat de Catalunya 2021SGR00457 and 2021SGR01581. ICN2 acknowledges funding from project PID2020-116093RB-C43, funded by MCIN/AEI/10.13039/501100011033/and by "ERDF A way of making Europe", by the "European Union". This study was supported by MCIN with funding from European Union NextGenerationEU (PRTR-C17.I1) and Generalitat de Catalunya. ICN2 is supported by the Severo Ochoa program from Spanish MCIN/AEI (grant no. CEX2021-001214-S). ICN2 and IREC are funded by the CERCA Programme/ Generalitat de Catalunya. Part of the present work has been performed in the framework of Universitat Autónoma de Barcelona Materials Science PhD program. M.B. acknowledges support from SUR Generalitat de Catalunya and the EU Social Fund; project ref 2020 FI 00103.

### REFERENCES

- (1) Talebi Amiri, M.; Dick, G. R.; Questell-Santiago, Y. M.; Luterbacher, J. S. Fractionation of lignocellulosic biomass to produce uncondensed aldehyde-stabilized lignin. *Nat. Protoc.* **2019**, *14* (3), 921–954
- (2) Pandey, M. P.; Kim, C. S. Lignin Depolymerization and Conversion: A Review of Thermochemical Methods. *Chem. Eng. Technol.* **2011**, 34 (1), 29–41.
- (3) Cantu, D. C.; Padmaperuma, A. B.; Nguyen, M.-T.; Akhade, S. A.; Yoon, Y.; Wang, Y.-G.; Lee, M.-S.; Glezakou, V.-A.; Rousseau, R.; Lilga, M. A. A Combined Experimental and Theoretical Study on the Activity and Selectivity of the Electrocatalytic Hydrogenation of Aldehydes. *ACS Catal.* **2018**, *8* (8), 7645–7658.
- (4) Sanyal, U.; Koh, K.; Meyer, L. C.; Karkamkar, A.; Gutiérrez, O. Y. Simultaneous electrocatalytic hydrogenation of aldehydes and phenol over carbon-supported metals. *J. Appl. Electrochem.* **2021**, *51* (1), 27–36.
- (5) Wijaya, Y. P.; Smith, K. J.; Kim, C. S.; Gyenge, E. L. Electrocatalytic hydrogenation and depolymerization pathways for lignin valorization: toward mild synthesis of chemicals and fuels from biomass. *Green Chem.* **2020**, *22* (21), 7233–7264.
- (6) Akhade, S. A.; Singh, N.; Gutiérrez, O. Y.; Lopez-Ruiz, J.; Wang, H.; Holladay, J. D.; Liu, Y.; Karkamkar, A.; Weber, R. S.; Padmaperuma, A. B.; Lee, M.-S.; Whyatt, G. A.; Elliott, M.; Holladay, J. E.; Male, J. L.; Lercher, J. A.; Rousseau, R.; Glezakou, V.-A. Electrocatalytic Hydrogenation of Biomass-Derived Organics: A Review. *Chem. Rev.* **2020**, 120 (20), 11370–11419.
- (7) Li, K.; Sun, Y. Electrocatalytic Upgrading of Biomass-Derived Intermediate Compounds to Value-Added Products. *Chem.—Eur. J.* **2018**, 24 (69), 18258–18270.
- (8) Li, J.; Li, L.; Ma, X.; Han, X.; Xing, C.; Qi, X.; He, R.; Arbiol, J.; Pan, H.; Zhao, J.; Deng, J.; Zhang, Y.; Yang, Y.; Cabot, A. Selective Ethylene Glycol Oxidation to Formate on Nickel Selenide with Simultaneous Evolution of Hydrogen. *Adv. Sci.* **2023**, *10* (15), 2300841.
- (9) Li, J.; Tian, X.; Wang, X.; Zhang, T.; Spadaro, M. C.; Arbiol, J.; Li, L.; Zuo, Y.; Cabot, A. Electrochemical Conversion of Alcohols into Acidic Commodities on Nickel Sulfide Nanoparticles. *Inorg. Chem.* **2022**, *61* (34), 13433–13441.
- (10) Zhang, Z.; Bian, L.; Tian, H.; Liu, Y.; Bando, Y.; Yamauchi, Y.; Wang, Z.-L. Tailoring the Surface and Interface Structures of Copper-Based Catalysts for Electrochemical Reduction of CO<sub>2</sub> to Ethylene and Ethanol. *Small* **2022**, *18* (18), 2107450.
- (11) Luo, M.; Yang, J.; Li, X.; Eguchi, M.; Yamauchi, Y.; Wang, Z.-L. Insights into alloy/oxide or hydroxide interfaces in Ni-Mo-based electrocatalysts for hydrogen evolution under alkaline conditions. *Chem. Sci.* **2023**, *14* (13), 3400–3414.
- (12) Zhang, Z.-Y.; Tian, H.; Bian, L.; Liu, S.-Z.; Liu, Y.; Wang, Z.-L. Cu-Zn-based alloy/oxide interfaces for enhanced electroreduction of CO<sub>2</sub> to C2+ products. *J. Energy Chem.* **2023**, *83*, 90–97.
- (13) Bhanushali, J. T.; Kainthla, I.; Keri, R. S.; Nagaraja, B. M. Catalytic Hydrogenation of Benzaldehyde for Selective Synthesis of Benzyl Alcohol: A Review. *ChemistrySelect* **2016**, *1* (13), 3839–3853.
- (14) Rodrigues, C. J. C.; de Carvalho, C. C. C. R. Process Development for Benzyl Alcohol Production by Whole-Cell Biocatalysis in Stirred and Packed Bed Reactors. *Microorganisms* **2022**, *10* (5), 966.
- (15) Yang, Y.; Song, W.-Y.; Hur, H.-G.; Kim, T.-Y.; Ghatge, S. Thermoalkaliphilic laccase treatment for enhanced production of high-value benzaldehyde chemicals from lignin. *Int. J. Biol. Macromol.* **2019**, *124*, 200–208.
- (16) Gong, L.; Zhang, C. Y.; Mu, X.; Han, X.; Li, J.; Arbiol, J.; Zhou, J. Y.; Kallio, T.; Martínez-Alanis, P. R.; Cabot, A. Semiconductor nanosheets for electrocatalytic self-coupling of benzaldehyde to hydrobenzoin. *Chem. Eng. J.* **2024**, *479*, 147612.
- (17) Vimont, A.; Goupil, J.-M.; Lavalley, J.-C.; Daturi, M.; Surblé, S.; Serre, C.; Millange, F.; Férey, G.; Audebrand, N. Investigation of Acid Sites in a Zeotypic Giant Pores Chromium(III) Carboxylate. *J. Am. Chem. Soc.* **2006**, *128* (10), 3218–3227.

- (18) Sanyal, U.; Yuk, S. F.; Koh, K.; Lee, M.-S.; Stoerzinger, K.; Zhang, D.; Meyer, L. C.; Lopez-Ruiz, J. A.; Karkamkar, A.; Holladay, J. D.; Camaioni, D. M.; Nguyen, M.-T.; Glezakou, V.-A.; Rousseau, R.; Gutiérrez, O. Y.; Lercher, J. A. Hydrogen Bonding Enhances the Electrochemical Hydrogenation of Benzaldehyde in the Aqueous Phase. *Angew. Chem., Int. Ed. Engl.* **2021**, *60* (1), 290–296.
- (19) Cheng, G.; Zhai, Z.; Sun, J.; Ran, Y.; Yang, W.; Tan, F.; Zhang, Z. Elucidating role of alloying in electrocatalytic hydrogenation of benzaldehyde over nanoporous NiPd catalysts. *Chem. Eng. J.* **2023**, 474, 145631.
- (20) Song, Y.; Sanyal, U.; Pangotra, D.; Holladay, J. D.; Camaioni, D. M.; Gutiérrez, O. Y.; Lercher, J. A. Hydrogenation of benzaldehyde via electrocatalysis and thermal catalysis on carbon-supported metals. *J. Catal.* **2018**, *359*, 68–75.
- (21) Singh, N.; Sanyal, U.; Ruehl, G.; Stoerzinger, K. A.; Gutiérrez, O. Y.; Camaioni, D. M.; Fulton, J. L.; Lercher, J. A.; Campbell, C. T. Aqueous phase catalytic and electrocatalytic hydrogenation of phenol and benzaldehyde over platinum group metals. *J. Catal.* **2020**, *382*, 372–384.
- (22) Lopez-Ruiz, J. A.; Andrews, E.; Akhade, S. A.; Lee, M.-S.; Koh, K.; Sanyal, U.; Yuk, S. F.; Karkamkar, A. J.; Derewinski, M. A.; Holladay, J.; Glezakou, V.-A.; Rousseau, R.; Gutiérrez, O. Y.; Holladay, J. D. Understanding the Role of Metal and Molecular Structure on the Electrocatalytic Hydrogenation of Oxygenated Organic Compounds. *ACS Catal.* **2019**, *9* (11), 9964–9972.
- (23) Bondue, C. J.; Koper, M. T. M. Electrochemical Reduction of the Carbonyl Functional Group: The Importance of Adsorption Geometry, Molecular Structure, and Electrode Surface Structure. *J. Am. Chem. Soc.* **2019**, *141* (30), 12071–12078.
- (24) Gao, G.; Chen, X.; Han, L.; Zhu, G.; Jia, J.; Cabot, A.; Sun, Z. Advances in MOFs and their derivatives for non-noble metal electrocatalysts in water splitting. *Coord. Chem. Rev.* **2024**, 503, 215639.
- (25) Wang, X.; Yang, L.; Xing, C.; Han, X.; Du, R.; He, R.; Guardia, P.; Arbiol, J.; Cabot, A. MOF-Derived Ultrathin Cobalt Molybdenum Phosphide Nanosheets for Efficient Electrochemical Overall Water Splitting. *Nanomaterials* **2022**, *12* (7), 1098.
- (26) Yang, D.; Liang, Z.; Tang, P.; Zhang, C.; Tang, M.; Li, Q.; Biendicho, J. J.; Li, J.; Heggen, M.; Dunin-Borkowski, R. E.; Xu, M.; Llorca, J.; Arbiol, J.; Morante, J. R.; Chou, S.-L.; Cabot, A. A High Conductivity 1D  $\pi$ -d Conjugated Metal-Organic Framework with Efficient Polysulfide Trapping-Diffusion-Catalysis in Lithium-Sulfur Batteries. *Adv. Mater.* **2022**, 34 (10), 2108835.
- (27) Wang, X.; Li, J.; Xue, Q.; Han, X.; Xing, C.; Liang, Z.; Guardia, P.; Zuo, Y.; Du, R.; Balcells, L.; Arbiol, J.; Llorca, J.; Qi, X.; Cabot, A. Sulfate-Decorated Amorphous-Crystalline Cobalt-Iron Oxide Nanosheets to Enhance O-O Coupling in the Oxygen Evolution Reaction. *ACS Nano* **2023**, *17* (1), 825–836.
- (28) Wang, X.; Han, X.; Du, R.; Liang, Z.; Zuo, Y.; Guardia, P.; Li, J.; Llorca, J.; Arbiol, J.; Zheng, R.; Cabot, A. Unveiling the role of counter-anions in amorphous transition metal-based oxygen evolution electrocatalysts. *Appl. Catal., B* **2023**, 320, 121988.
- (29) Yang, Q.; Yao, F.; Zhong, Y.; Chen, F.; Shu, X.; Sun, J.; He, L.; Wu, B.; Hou, K.; Wang, D.; Li, X. Metal-Organic Framework Supported Palladium Nanoparticles: Applications and Mechanisms. *Part. Part. Syst. Char.* **2019**, *36* (6), 1800557.
- (30) Mukhopadhyay, S.; Basu, O.; Nasani, R.; Das, S. K. Evolution of metal organic frameworks as electrocatalysts for water oxidation. *Chem. Commun.* **2020**, *56* (79), 11735–11748.
- (31) Dhakshinamoorthy, A.; Asiri, A. M.; Garcia, H. 2D Metal-Organic Frameworks as Multifunctional Materials in Heterogeneous Catalysis and Electro/Photocatalysis. *Adv. Mater.* **2019**, *31* (41), 1900617.
- (32) Deng, Y.; Yuan, P.; Yuan, X.; Wu, J.; Luo, H.-A. Preparation of Hydrophobic Cosalen/SBA-15 and Its Application in the Selective Oxidation of Toluene. *Chem. J. Chin. Univ.* **2013**, 34 (11), 2617–2622.
- (33) Wu, Y.; Guo, Z.; Sun, C.; Ren, X.; Li, Q. High-efficiency electrochemical hydrogenation of biomass-derived benzaldehyde

- compounds via a durable and versatile dendritic-like Pd/Cu-CF electrocatalyst. Fuel Process. Technol. 2022, 237, 107436.
- (34) Vasiliou, A. K.; Kim, J. H.; Ormond, T. K.; Piech, K. M.; Urness, K. N.; Scheer, A. M.; Robichaud, D. J.; Mukarakate, C.; Nimlos, M. R.; Daily, J. W.; Guan, Q.; Carstensen, H.-H.; Ellison, G. B. Biomass pyrolysis: Thermal decomposition mechanisms of furfural and benzaldehyde. *J. Chem. Phys.* **2013**, *139* (10), 104310.
- (35) Yu, I. K. M.; Deng, F.; Chen, X.; Cheng, G.; Liu, Y.; Zhang, W.; Lercher, J. A. Impact of hydronium ions on the Pd-catalyzed furfural hydrogenation. *Nat. Commun.* **2022**, *13* (1), 7154.
- (36) Wu, J.; Liang, D.; Song, X.; Liu, T.; Xu, T.; Wang, S.; Zou, Y. Sulfonic Groups Functionalized Zr-metal Organic Framework for Highly Catalytic Transfer Hydrogenation of Furfural to Furfuryl Alcohol. *J. Energy Chem.* **2022**, *71*, 411–417.
- (37) Koh, K.; Sanyal, U.; Lee, M.-S.; Cheng, G.; Song, M.; Glezakou, V.-A.; Liu, Y.; Li, D.; Rousseau, R.; Gutiérrez, O. Y.; Karkamkar, A.; Derewinski, M.; Lercher, J. A. Electrochemically Tunable Proton-Coupled Electron Transfer in Pd-Catalyzed Benzaldehyde Hydrogenation. *Angew. Chem., Int. Ed. Engl.* **2020**, 59 (4), 1501–1505.
- (38) Deng, L.; Hu, F.; Ma, M.; Huang, S.-C.; Xiong, Y.; Chen, H.-Y.; Li, L.; Peng, S. Electronic Modulation Caused by Interfacial Ni-O-M (M = Ru, Ir, Pd) Bonding for Accelerating Hydrogen Evolution Kinetics. *Angew. Chem., Int. Ed. Engl.* **2021**, *60* (41), 22276–22282.
- (39) Gao, Z.; Lai, Y.; Zhang, L.; Lin, Y.; Xiao, L.; Luo, Y.; Luo, F. Synthesis, Characterization, and Electrocatalytic Activity Exploration of MOF-74: A Research-Style Laboratory Experiment. *J. Chem. Educ.* **2021**, *98* (10), 3341–3347.
- (40) Jiang, H.; Wang, Q.; Wang, H.; Chen, Y.; Zhang, M. MOF-74 as an Efficient Catalyst for the Low-Temperature Selective Catalytic Reduction of  $NO_x$  with  $NH_3$ . ACS Appl. Mater. Interfaces **2016**, 8 (40), 26817–26826.
- (41) Li, J.; Li, L.; Ma, X.; Wang, J.; Zhao, J.; Zhang, Y.; He, R.; Yang, Y.; Cabot, A.; Zhu, Y. Unraveling the role of iron on Ni-Fe alloy nanoparticles during the electrocatalytic ethanol-to-acetate process. *Nano Res.* 2023.
- (42) Singh, N.; Sanyal, U.; Fulton, J. L.; Gutiérrez, O. Y.; Lercher, J. A.; Campbell, C. T. Quantifying Adsorption of Organic Molecules on Platinum in Aqueous Phase by Hydrogen Site Blocking and in Situ X-ray Absorption Spectroscopy. ACS Catal. 2019, 9 (8), 6869–6881.
- (43) Akinola, J.; Barth, I.; Goldsmith, B. R.; Singh, N. Adsorption Energies of Oxygenated Aromatics and Organics on Rhodium and Platinum in Aqueous Phase. *ACS Catal.* **2020**, *10* (9), 4929–4941.
- (44) Villalba, M. A.; Koper, M. T. M. Structure Sensitivity of Acetophenone Reduction on Palladium-Modified Platinum Single-Crystal Electrodes. *J. Phys. Chem. C* **2020**, *124* (47), 25884–25891.
- (45) Stevens, D. A.; Dahn, J. R. Electrochemical Characterization of the Active Surface in Carbon-Supported Platinum Electrocatalysts for PEM Fuel Cells. *J. Electrochem. Soc.* **2003**, *150* (6), A770.
- (46) Wang, X.; Jiao, Y.; Li, L.; Zheng, Y.; Qiao, S.-Z. Local Environment Determined Reactant Adsorption Configuration for Enhanced Electrocatalytic Acetone Hydrogenation to Propane. *Angew. Chem., Int. Ed.* **2022**, *61* (5), No. e202114253.
- (47) Liu, H.; Patel, D. M.; Chen, Y.; Lee, J.; Lee, T.-H.; Cady, S. D.; Cochran, E. W.; Roling, L. T.; Li, W. Unraveling Electroreductive Mechanisms of Biomass-Derived Aldehydes via Tailoring Interfacial Environments. *ACS Catal.* **2022**, *12* (22), 14072–14085.
- (48) Chadderdon, X. H.; Chadderdon, D. J.; Matthiesen, J. E.; Qiu, Y.; Carraher, J. M.; Tessonnier, J.-P.; Li, W. Mechanisms of Furfural Reduction on Metal Electrodes: Distinguishing Pathways for Selective Hydrogenation of Bioderived Oxygenates. *J. Am. Chem. Soc.* **2017**, 139 (40), 14120–14128.

## **Supporting Information**

## Enhanced Electrochemical Hydrogenation of Benzaldehyde to Benzyl Alcohol on Pd@Ni-MOF by Modifying the Adsorption Configuration

Li Gong <sup>1,2</sup>, Chaoyue Zhang <sup>1,3\*</sup>, Junshan Li <sup>4</sup>, Guillem Montaña-Mora <sup>1,2</sup>, Marc Botifoll <sup>5</sup>,

Jordi Arbiol <sup>5</sup>, Jinyuan Zhou <sup>3</sup>, Tanja Kallio <sup>7</sup>, Paulina R. Martínez-Alanis <sup>1\*</sup>, Andreu Cabot

1,6\*

- Catalonia Institute for Energy Research IREC Sant Adrià de Besòs, Barcelona 08930,
   Spain E-mail: pmartinez@irec.cat, acabot@irec.cat
- 2. University of Barcelona, Barcelona 08028, Spain.
- 3. Key Laboratory for Magnetism and Magnetic Materials of the Ministry of Education & School of Physical Science & Technology, Lanzhou University, Lanzhou, 730000, China.
- 4. Institute for Advanced Study, Chengdu University, Chengdu, 610106, China
- 5. Catalan Institute of Nanoscience and Nanotechnology (ICN2), CSIC and BIST, Campus UAB, Bellaterra, 08193, Barcelona, Spain.
- Catalan Institution for Research and Advanced Studies ICREA Pg. Lluís Companys 23, 08010, Barcelona, Spain
- 7. Department of Chemistry and Materials Science, Aalto University School of Chemical Engineering, P.O. Box 16100, FI-00076 Aalto, Finland.

## **Experimental sections**

Materials. All the chemicals were used as purchased, without further purification. Palladium(II) acetate (Pd(OAc)<sub>2</sub> 98%, Sigma Aldrich), terephthalic acid (BDC, 98%, Sigma Aldrich 98%, Sigma Aldrich), nickel(II) chloride hexahydrates (NiCl<sub>2</sub>·6H<sub>2</sub>O, 99.9%, Sigma Aldrich), N,N-dimethylformamide (DMF, ≥99.8%, Sigma Aldrich), triethanolamine (TEOA, 97%, Thermo Scientific<sup>TM</sup>), ethanol (CH<sub>3</sub>CH<sub>2</sub>OH, 96%, Letslab), benzaldehyde (C<sub>7</sub>H<sub>6</sub>O, 98%, Sigma Aldrich) acetone ((CH<sub>3</sub>)<sub>2</sub>CO, Letslab), hydrochloric acid (HCl, 37%, Thermo Scientific<sup>TM</sup>), and nickel foam (NF, 99.9%, Kejing).

Synthesis of Pd@Ni-MOF. 1 mmol NiCl<sub>2</sub>·6 H<sub>2</sub>O, 1 mmol BDC, 0.2 mmol Pd (Oac)<sub>2</sub>, and 1 mmol TEOA were dissolved in 22 mL of a mixture solution of DMF and milli-Q (MQ) water (20:2). After continuously stirring for 30 min, the solution was transferred into a 30 mL Teflon-lined autoclave and a piece of NF (3x2 cm<sup>2</sup>), previously cleaned with 3 M HCl for 10 min and washed 3 times with MQ water, was placed into the solution leaning against the autoclave wall. The autoclave was sealed and heated at 120 °C for 12 h. After cooling to room temperature, the sample was thoroughly washed with DMF, MQ water, and ethanol and then dried at 60 °C overnight (mass loading: 1.2 mg cm<sup>-2</sup>). This sample was named Pd@Ni-MOF. Besides, reference samples containing no TEOA (TEOA-free Pd@Ni-MOF), no Pd (Ni-MOF), and no TEOA and no Pd (TEOA-free Ni-MOF) were also produced. An additional reference material electrode was produced by loading a commercial 20% Pd supported on active carbon on NF (20% Pd@C).

**Materials Characterization.** The morphology of the samples (supported on the NF) was characterized by scanning electron microscopy (SEM) analysis on a Zeiss Auriga microscope

(Carl Zeiss, Jena, Germany) with an energy-dispersive X-ray spectroscopy (EDX) detector at 15 kV to analyze composition. Transmission electron microscopy (TEM) analysis was carried out on unsupported samples (sonicated from NF) using a ZEISS LIBRA 120, operating at 120 kV. Scanning TEM (STEM) and high-resolution TEM (HRTEM) were carried out under a 200 keV Tecnai F20 field emission microscope. Electron energy loss spectroscopy (EELS) and high-angle annular dark-field (HAADF) STEM were carried out using a Gatan Quantum image filter embedded in the F20 (S) TEM. Powder X-ray diffraction (XRD) patterns of unsupported samples (sonicated from NF) were collected at 40 kV and 40 mA with Cu K $\alpha$  radiation ( $\lambda$  = 1.5406 Å). Characterization of the surface of the NF-supported samples was done by X-ray photoelectron spectroscopy (XPS) on a Thermo Scientific K-Alpha+ with Mono Al Ka radiation. The pressure in the analysis chamber was at around 5\*10<sup>-9</sup> mbar and the energy, voltage and beam current were 1486.6 eV, 12 kV and 6 mA, respectively. The specific surface area and pore size distribution of the unsupported samples (collected precipitation with centrifugation after hydrothermal reaction) were obtained from N2 adsorption/desorption isotherms on a Tristar II 3020 Micromeritics system. Fourier-transformed infrared (FT-IR) spectra of the unsupported samples (collected precipitation with centrifugation after hydrothermal reaction)were recorded on an Alpha Bruker spectrometer. H2-temperatureprogrammed reduction (H2-TPR) profiles were conducted on the Autochem HP system (Micromeritics Instrument Corp.) of the powder Pd@Ni-MOF collected from solvothermal and commercial 20% Pd@C.

**Product quantification and calculation.** To quantify the organic products, high-performance liquid chromatography (HPLC) was performed on an Agilent 1200 series at 30 °C. The HPLC

was equipped with an ultraviolet-visible detector and Synergi 4u Polar-RP 80A 00G-4336-EO 250x4.60 mm column. The eluting solvents of A: 5% methanol, 0.4% phosphoric acid aqueous solution; and B: acetonitrile were utilized. The program was 15% solution B for 16 min, 25% solution B for 20 min and then 15% solution B for 16 min. The volume of injection was 5 μL. The flow rate was 0.5 mL s<sup>-1</sup>. The calibration curves of standard chemicals were employed to determine and quantify the products. The quantification of the products by percentage conversion (Conv. %) of benzaldehyde (BZH) (1), average reaction rate (ARR) (2) and faraday efficiency (FE%) (3) without hydrogen evolution reaction consideration was carried out according to equations 1-3.

Conv. 
$$[\%] = \frac{moles\ of\ Benzaldehyde\ consumed}{initial\ moles\ of\ Benzaldehyde}$$
 (1)

ARR [
$$\mu$$
mol cm<sup>-2</sup> h<sup>-1</sup>] =  $\frac{moles\ of\ Benzaldehyde\ consumed}{area\ of\ working\ electrode\ *\ time}$  (2)

FE (%) = 
$$\frac{nZF}{Q} = \frac{electrons\ consumed\ by\ hydrogenation\ of\ organics}{Total\ electrons\ flowed\ through\ the\ system}$$
 (3)

where n represents the number of moles of the target product, z the required electrons of this reaction z=2, and F the Faraday constant  $96500 \text{ C} \cdot \text{mol}^{-1}$ .

Computational theoretical calculation. Inspired by the reported model of Ru@Ni-MOF¹, the analog structure of Pd@Ni-MOF was theoretically constructed, and the geometric optimization of the "Forcite" module was used to determine the structure and cell size of Pd and Ni-MOF. The adsorption energies for BZH with Pd@Ni-MOF were obtained by the "Sorption" and "Adsorption Locator" modules (the force field was COMPASS and the charge equilibrium was QEq). All density functional theory (DFT) calculations were performed using the Vienna ab initio simulation package (VASP), employing the projected augmented wave revising Perdew—

Burke–Ernzerhof function (PAW–PBE). The cutoff energy was set at 500 eV for all the geometry optimizations. A  $2 \times 2 \times 1$  Monkhorst–Pack grid and A  $4 \times 3 \times 2$  Monkhorst–Pack grid were used to obtain the surface calculations on the Pd system and the Pd@Ni-MOF system, respectively. At least a 20 Å vacuum layer was applied in the z–direction of the slab models, preventing vertical interactions between slabs. The adsorption energy ( $E_{ads}$ ) is described by equation 4 where  $E_{(substrate/product\ and\ Pd)}$ ,  $E_{(substrate/product)}$  and  $E_{(Pd)}$  are the energies of the system involving the Pd (111) surface connecting the substrate/product, the only substrate/product, and the Pd surface, respectively. All structures were completely relaxed until the force on each atom was less than 0.01 eV Å<sup>-1</sup>.

$$E_{ads} = E_{(substrate/product \ and \ Pd)} - E_{(substrate/product)} - E_{(Pd)}$$

$$\tag{4}$$

The Free energy ( $E_{free}$ ) was calculated using equation 5,  $\Delta E$ ,  $\Delta ZPE$ , and  $T\Delta S$  are the changes in the internal energy E, zero-point energy ZPE, and entropic energy TS, respectively. As an example, The Free energy ( $E_{free}$ ) of elemental step \*CHO-+\*CHO-H<sub>3</sub>O shown in equation 6.<sup>2</sup>

$$\Delta G = \Delta E + \Delta Z P E - T \Delta S \tag{5}$$

$$E_{\text{free *CHO}\rightarrow\text{*CHO}-H_3O} = E_{free \text{*CHOH}} - E_{free \text{*CHO}-H_3O} + E_{free \text{*}H_2O}$$
(6)

Electrocatalytic hydrogenation tests. The electrochemical performance of the electrocatalyst was evaluated on a Corrtest CS2350 EIS Bipotentiostat (2-channel, Wuhan Corrtest Instrument Corp., Ltd) using an H-cell reactor divided by a Nafion 117 proton exchange membrane. The electrolyte was kept with pH=5.2 sodium acetate-acetic acid buffer solution. The prepared self-supported electrodes (cut into 3x1 cm<sup>2</sup> and keep 2x1 cm<sup>2</sup> immersed in the electrolyte) were used as the working electrode, a platinum mesh as the counter electrode, and an Ag/AgCl (KCl

saturated) as the reference electrode. Cyclic voltammetry (CV) was performed in the range -0.9 V  $\sim$  0.9 V vs. RHE. Electrochemical impedance spectroscopy (EIS) was conducted at -0.1 V vs. RHE. I-t curves were obtained by applying -0.1 V vs. RHE as a constant voltage for 1 h or the following voltage sequence: -0.2 V vs. RHE for 5 min, -0.15 V vs. RHE for 5 min, -0.1 V vs. RHE for 20 min, -0.05 V vs. RHE for 20 min, and +0.00 V vs. RHE for 10 min. Experiments were performed under constant  $N_2$  flow. All tested results were calibrated with Nernst equation to reversible hydrogen standard electrode followed:

$$E_{RHE} = E + 0.0591 * pH + E_{Ag/AgCl}^{\theta} = E + 0.5$$

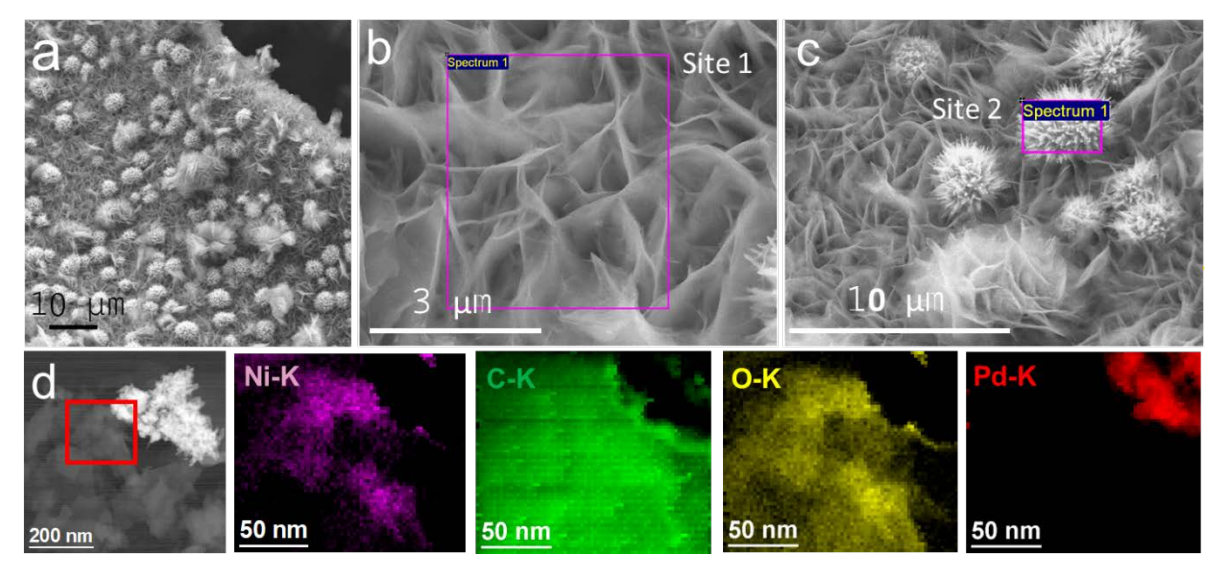


**Figure S1.** (a-c) SEM images of TEOA-free Pd@Ni-MOF; (d) EELS chemical composition maps obtained from the red squared area of the STEM micrograph of the sample produced without TEOA. Ni (purple), C (green), O (yellow) and Pd (red).

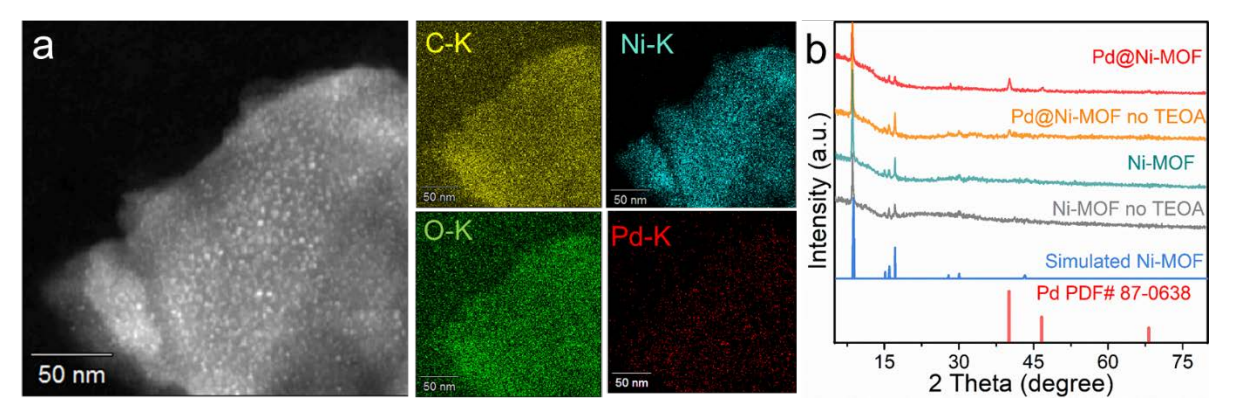


**Figure S2.** (a); STEM-HAADF image and compositional maps of Pd@Ni-MOF: yellow = C; green = O; blue = Ni; red = Pd (b) XRD patterns of Pd@Ni-MOF, TEOA-free Pd@Ni-MOF, TEOA-free Ni-MOF and Ni-MOF.

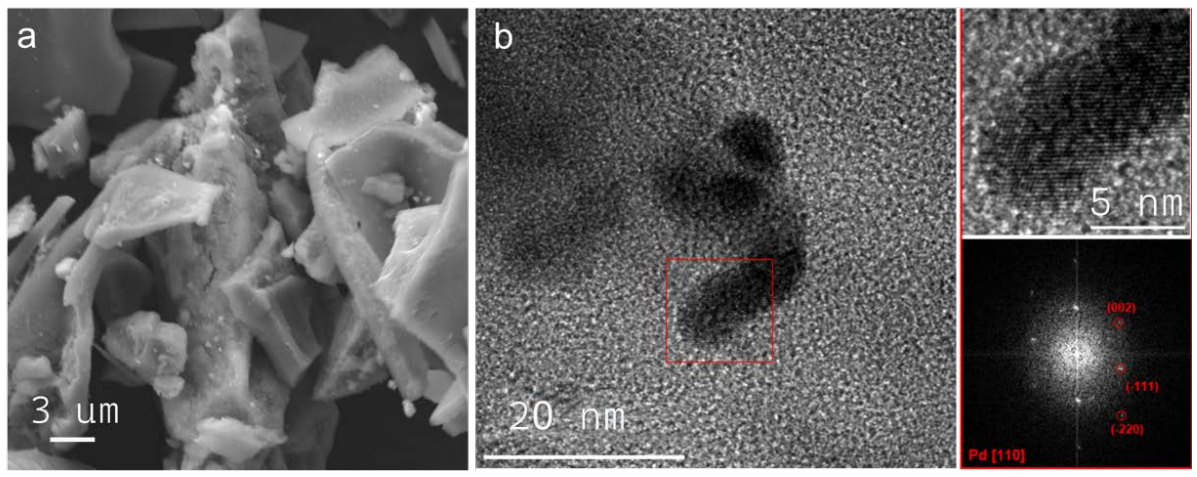


Figure S3. (a) SEM; (b) TEM images and HRTEM images of Pd@C.

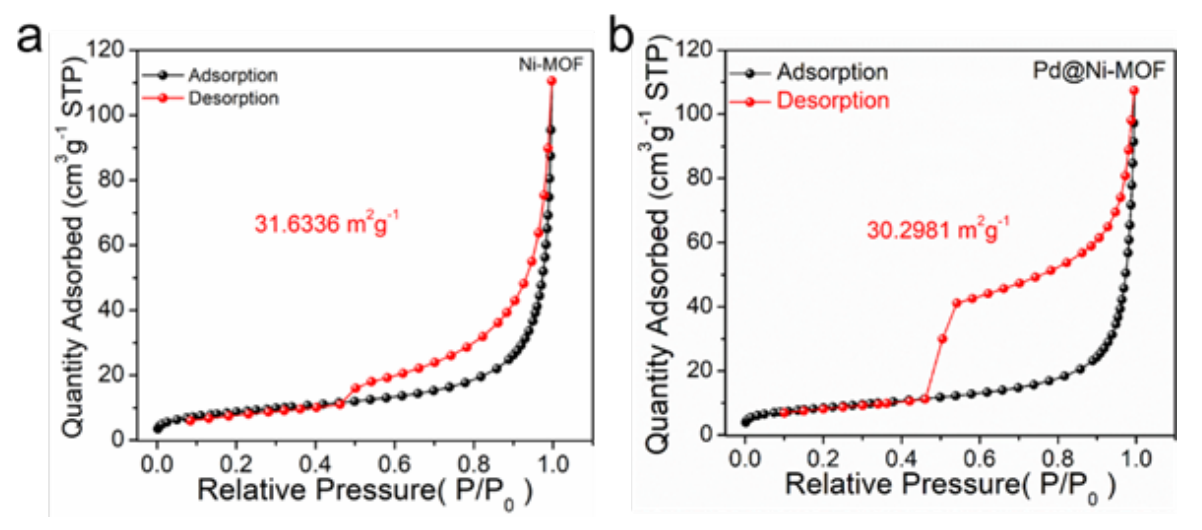
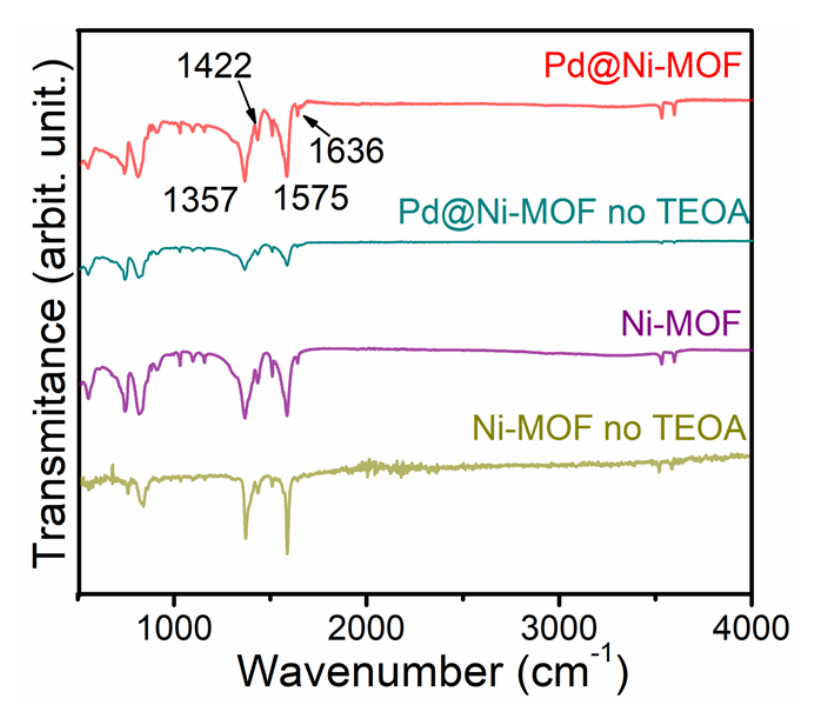
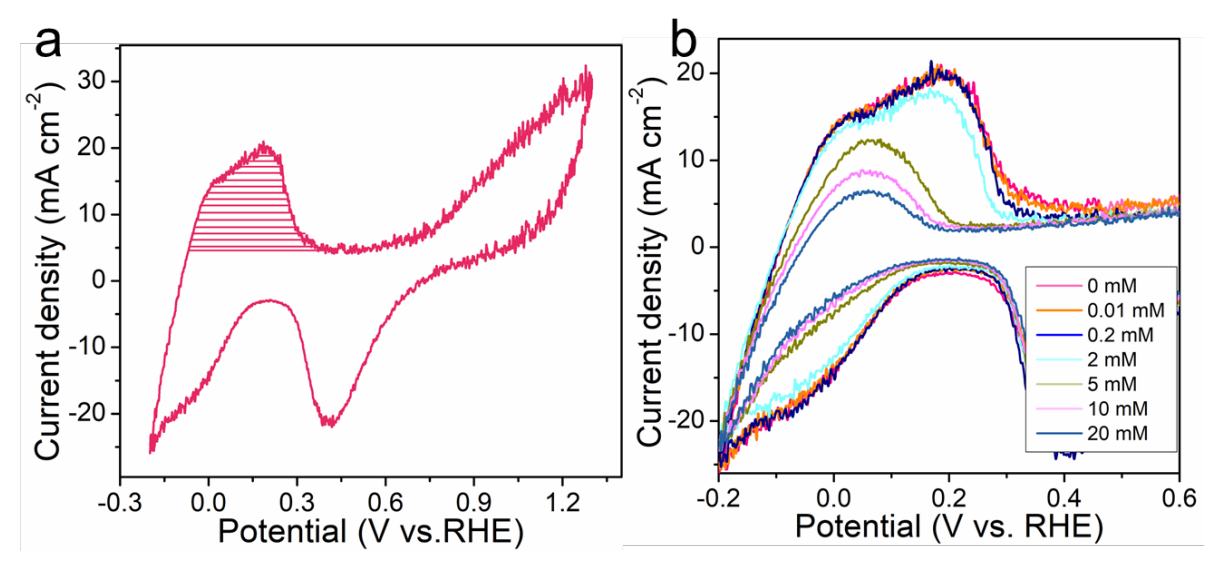


Figure S4. Nitrogen adsorption and desorption isotherms of (a) Pd@Ni-MOF and (b) Ni-MOF.



**Figure S5.** FT-IR spectra of Pd@Ni-MOF, TEOA-free Pd@Ni-MOF, Ni-MOF and TEOA-free Ni-MOF.



**Figure S6.** (a). Cyclic voltammograms measured in the presence of different concentrations of BZH (scan rate:  $50 \text{ mV s}^{-1}$ ). (Reaction conditions: Sodium acetate-acetic acid (3 M) buffer (pH 5.2) electrolyte, room temperature, 1 bar  $N_2$  flow.); (b) The shaded region was integrated to estimate the species coverage corresponding to the  $H_{UPD}$ .

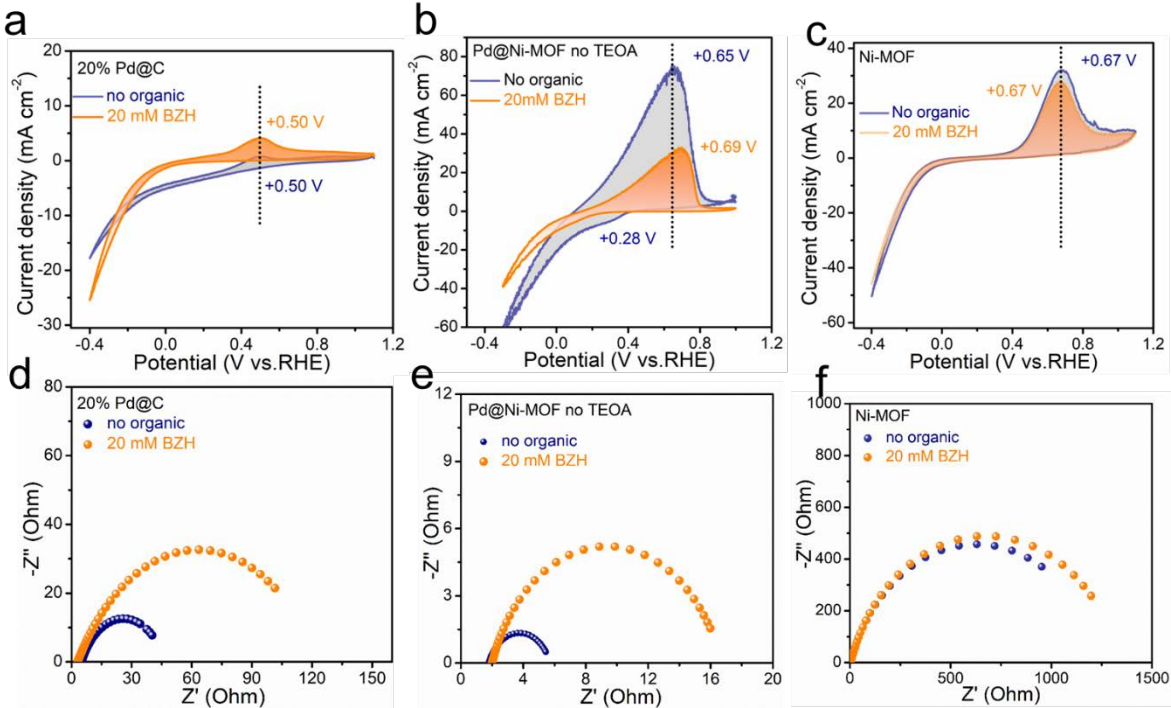


**Figure S7.** Cyclic voltammetry curves (a-c) and EIS (d-f) of 20% Pd@C (a,d); Pd@Ni-MOF (no TEOA) (b,e) and Ni-MOF (c,f) in the presence and absence of 20 mM BZH. Reaction conditions: Sodium acetate-acetic acid (3 M) buffer (pH 5.2) electrolyte, room temperature, 1 bar  $N_2$  flow.

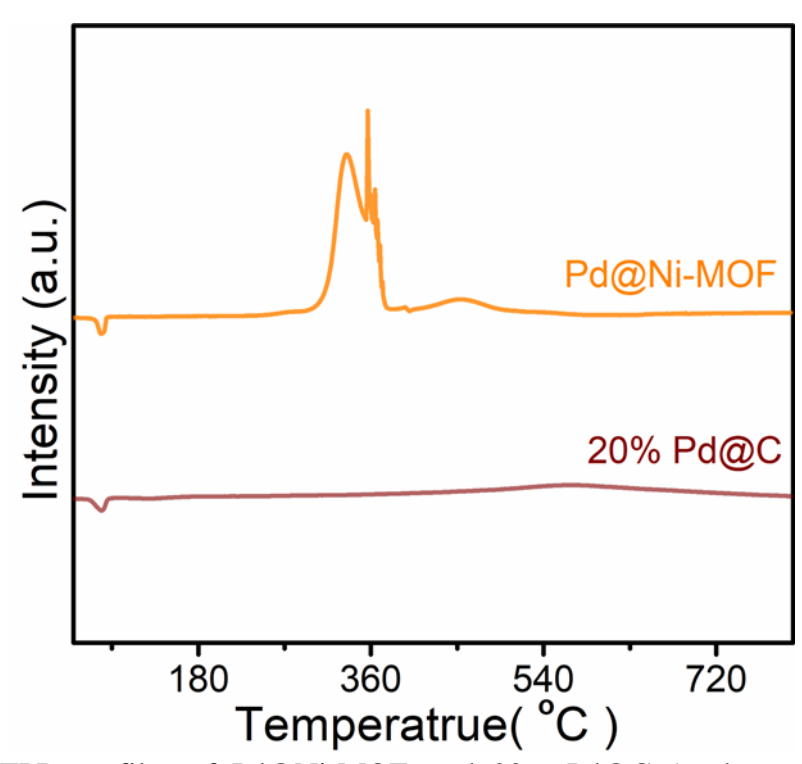


**Figure S8.** H<sub>2</sub>-TPR profiles of Pd@Ni-MOF, and 20% Pd@C (peaks area results were demonstrated at Table S4).

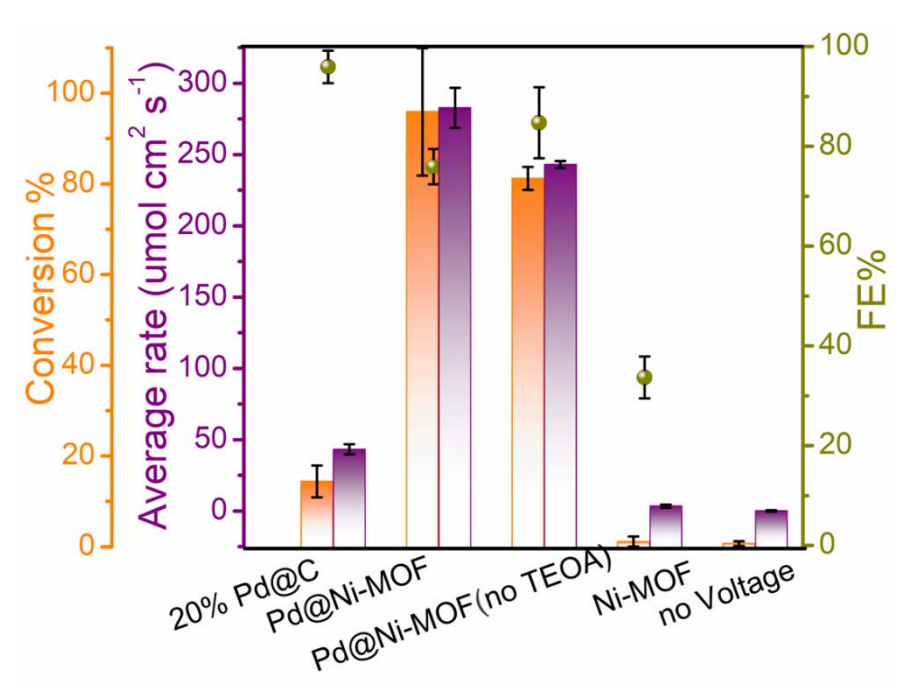


**Figure S9.** Comparison of the results of the electrochemical ECH of BZH to BA test over different materials with constant I-t (-0.1 V vs. RHE) or no voltage within 1 h in sodium acetate-acetic acid (3 M) buffer (pH 5.2) electrolyte, room temperature, 1 bar N<sub>2</sub> flow, results were summarized in Table S4.

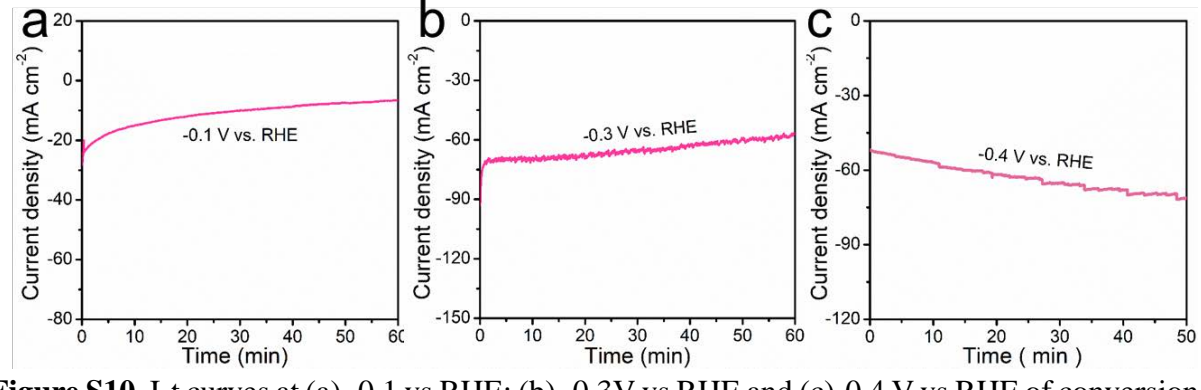


**Figure S10.** I-t curves at (a) -0.1 vs RHE; (b) -0.3V vs RHE and (c)-0.4 V vs RHE of conversion of BZH to BA over Pd@Ni-MOF.

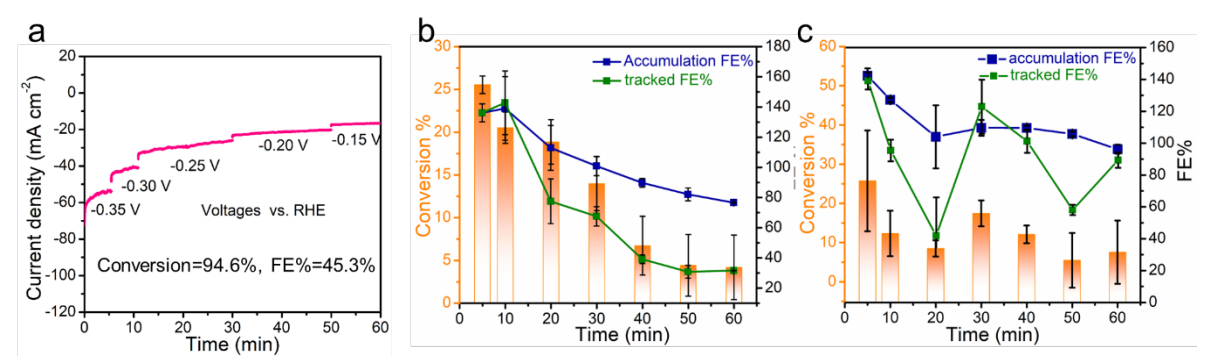


**Figure S11.** (a) I-t profile under a progressively decreasing voltage -0.35 V vs. RHE for 5 min, -0.3 V vs. RHE for 5 min, -0.25 V vs. RHE for 20 min, -0.20 V vs. RHE for 20 min, and -0.15 V vs. RHE for 10 min; (b) FE% calculation through constant voltage of -0.1 V vs. RHE for 60 min. (c) FE% calculation through whole step voltage of -0.20 V vs. RHE for 5 min, -0.15 V vs. RHE for 5 min, -0.10V vs. RHE for 20 min, -0.05 V vs. RHE for 20 min, and -0.00 V vs. RHE for 10 min within 1 h in sodium acetate-acetic acid (3 M) buffer (pH 5.2) electrolyte, room temperature, 1 bar  $N_2$  flow.

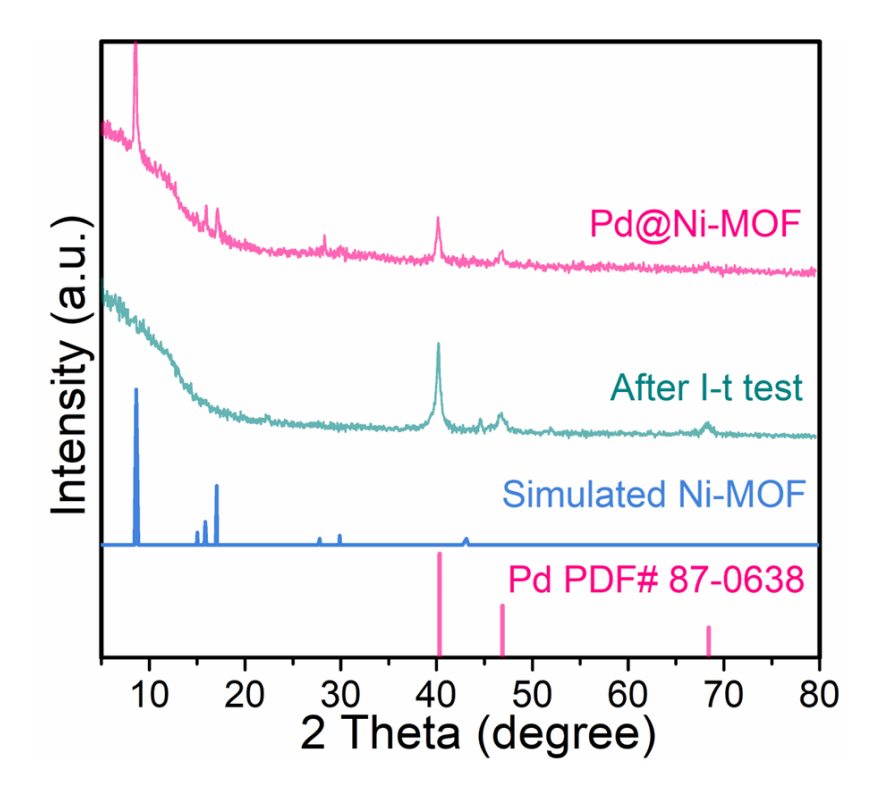


**Figure S12.** XRD pattern after 5 reaction cycles (60 min each) in sodium acetate-acetic acid (3 M) buffer (pH 5.2) electrolyte, room temperature, 1 bar N<sub>2</sub> flow..

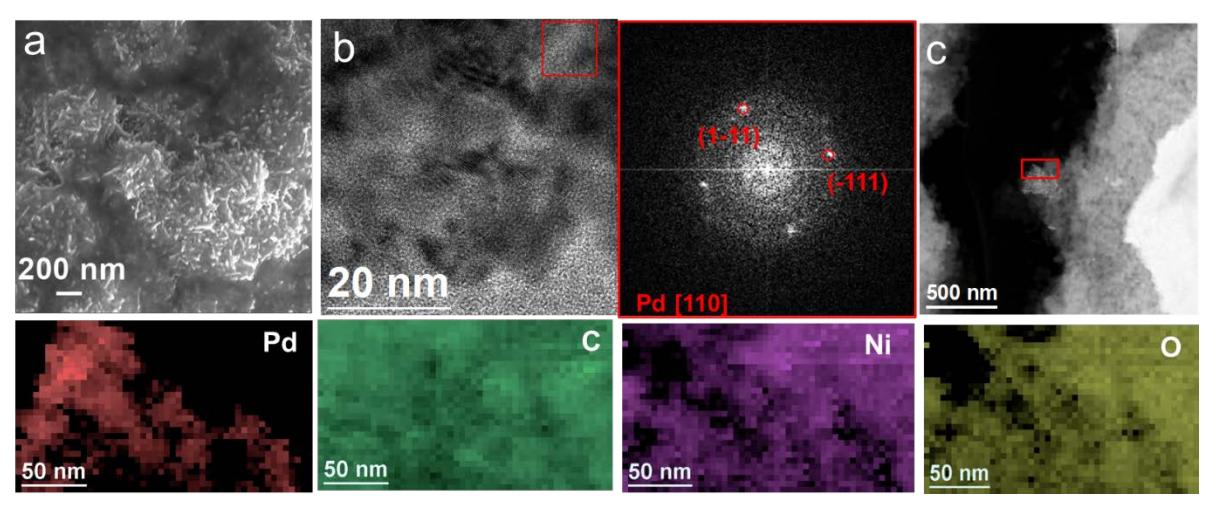


**Figure S13.** (a) SEM image, (b) HRTEM image and FFT analysis, (c) HAADF and EDS compositional maps of Pd@Ni-MOF after 5 reaction cycles (60 min each).

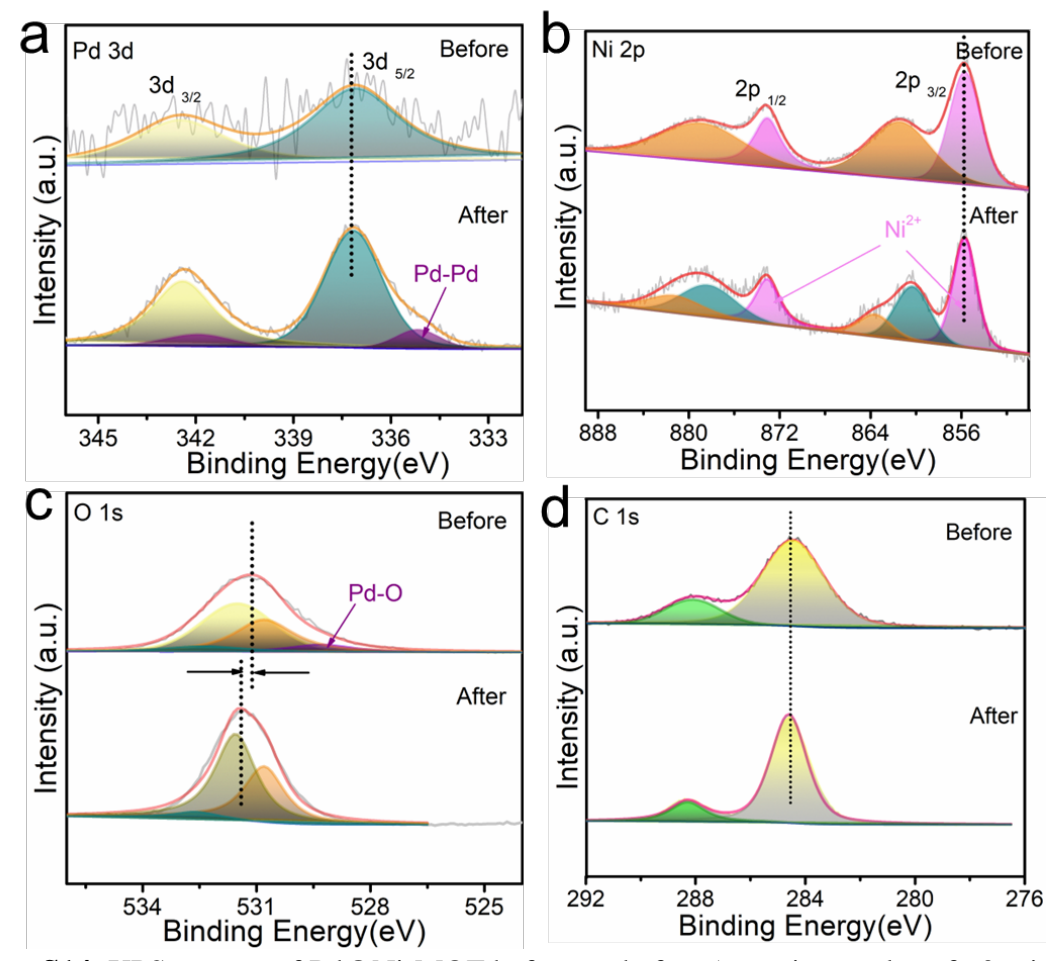


**Figure S14.** XPS spectra of Pd@Ni-MOF before and after 5 reaction cycles of 60 min each at the stepped voltages (a) Pd 3d; (b) Ni 2p; (c) O 1s; and (d) C 1s.

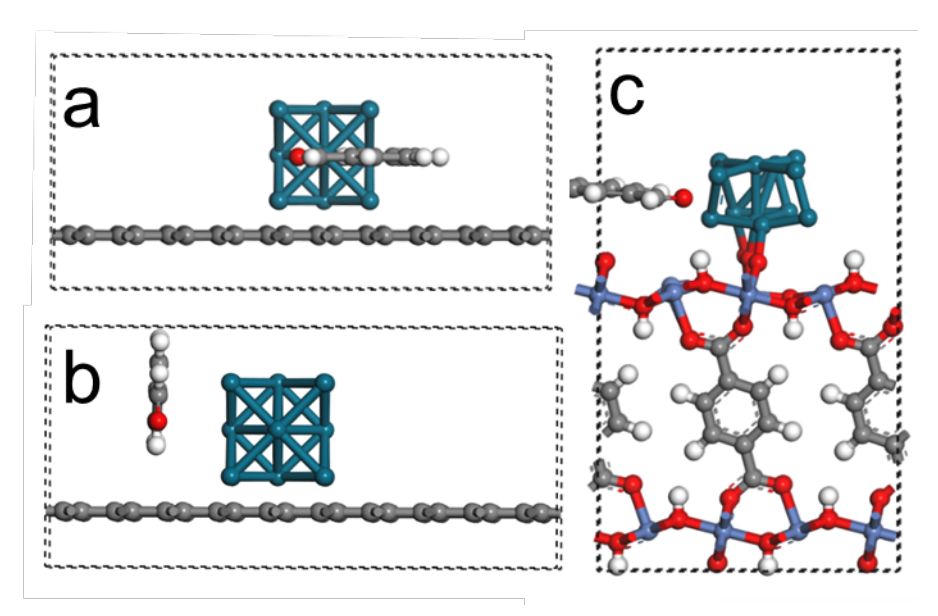


**Figure S15.** Schematic of adsorption configuration of BZH on (a-b) Pd@C. and (c) Pd@Ni-MOF, gray = C; green=Pd; red=O; blue=Ni.

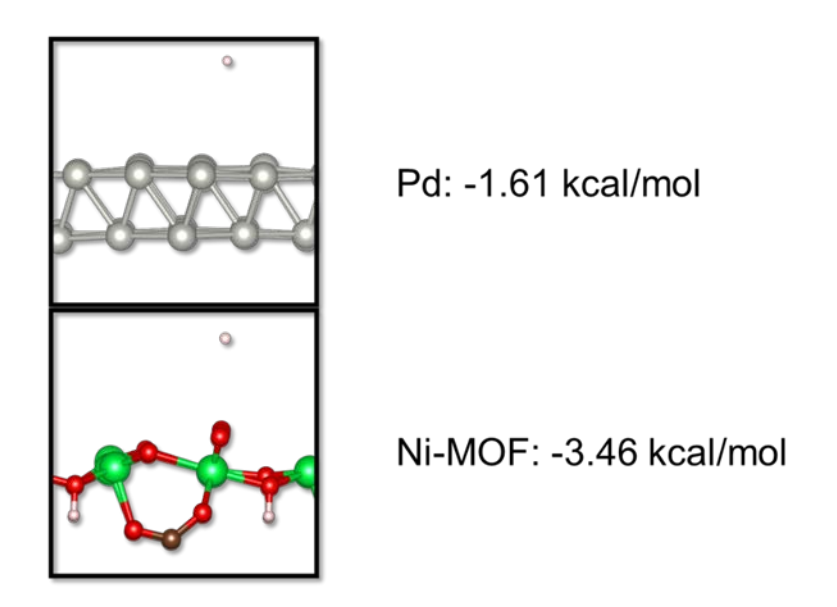


**Figure S16.** Schematic of H adsorption on Pd and Ni-MOF, gray = C; green=Pd; red=O; blue=Ni, pink=H.

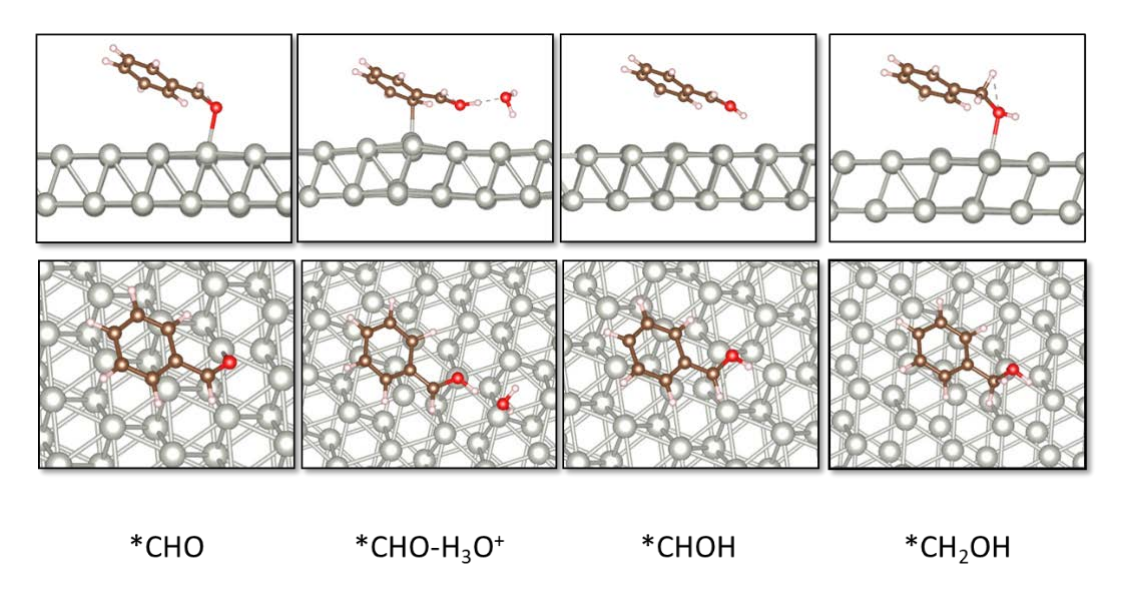
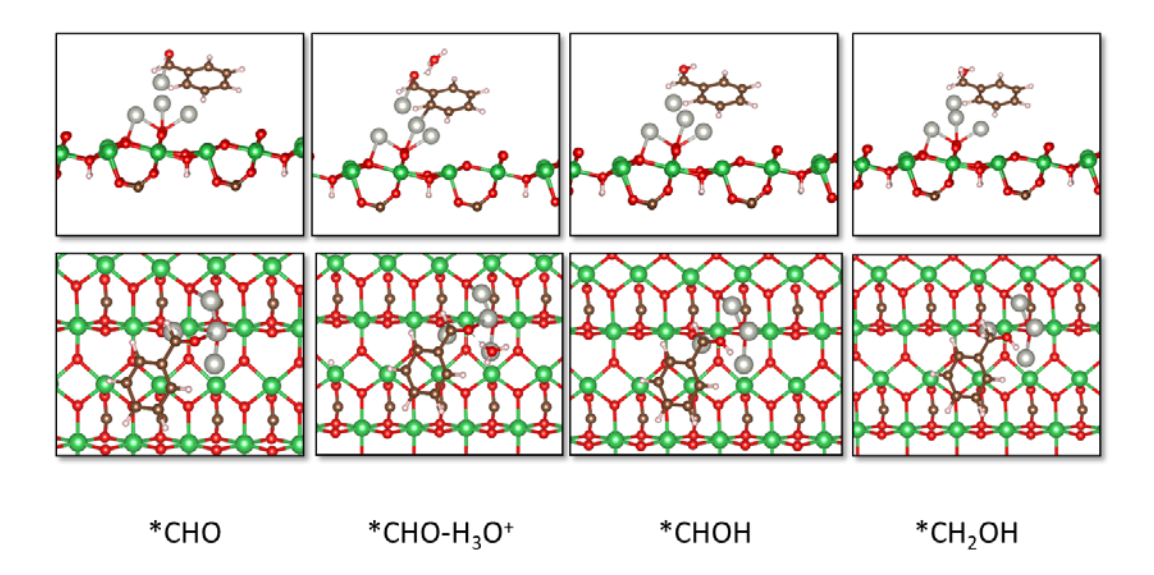


Figure S17. Structures of different species on the Pd surface



**Figure S18.** Structures of species on Pd@Ni-MOF surface, full model as depicted in Figure S15c.

**Table S1.** EDX results of TEOA-free Pd@Ni-MOF(Figure S1c)

Element	Site 1		Site 2	
Element	Weight %	Atomic %	Weight %	Atomic %
C K	28	44	9.0	26
ΟK	40	47	20	45
Ni k	29	9.0	19	11
Pd K	2.8	0.5	52	17

**Table S2.** EDX results of Pd@Ni-MOF

Element	Weight%	Atomic%
C K	31	54
ОК	25	33
Ni K	29	10
Pd L	15	2.9

**Table S3**.  $S_H$  integration in the absence and presence of BZH and the  $\theta_H$  results of Pd@Ni-MOF, Pd@Ni-MOF( no TEOA), 20% Pd@C and Ni-MOF.

	$S_{HBZHfree}(mA\!\cdot\!V)$	S <sub>H BZH presence</sub> ( mA·V)	$\theta_{\mathrm{Hydrogen}}$
Pd@Ni-MOF	18.7	7.0	0.38
Pd@Ni-MOF(no TEOA)	17.9	7.6	0.42
20% Pd@C	0.20	0.22	1
Ni-MOF	5.0	3.5	0.72

Table S4. H<sub>2</sub> chemisorption isotherm curves results of Pd@Ni-MOF and 20% Pd@C.

Samples	Peaks Tempreture (°C)	Peaks area (cm³ g-¹ STP)
DJ@N: MOE	334.8	110.5
Pd@Ni-MOF	456.7	60.6
20% Pd@C	564.5	54.5

**Table S5**. comparation results of different materials and i-t stratagies towards ECH of BZH to BA within 1 h in pH 5.2 actate buffer solution.

	Conversion	Average rate (μm cm <sup>-2</sup> h <sup>-1</sup> )	Faradic efficiency %
20% Pd@C	14.4	43.27	95.88
Pd@Ni-MOF constant E	94.27	282.82	75.92
Pd@Ni-MOF step E	89.16	243	96.05

**Table S6**. comparation results of different materials towards ECH of BZH to BA within 1 h in pH 5.2 NaAc buffer solution.

	Conversion	Average rate (μm cm <sup>-2</sup> h <sup>-1</sup> )	Faradic efficiency %
20% Pd@C	14.4	43.27	95.88
Pd@Ni-MOF	94.27	282.82	75.92
Pd@Ni-MOF ( no TEOA)	81.16	243	94.68
Ni-MOF	1.14	3.43	33.72
OCV	0.7	0.01	-

**Table S7.** EDX results of Pd@Ni-MOF after 5 reaction cycles (60 min each).

Element	Weight%	Atomic%
C K	13	26
O K	41	61
Ni K	13	5.4
Pd L	33	7.4

**Table S8**. Comparation of our results with closely related literatures.

Catalyst	Reaction rate	Reaction condition	Ref.
Pd@Ni-MOF	236 $\mu$ mol· $g_{cat}$ <sup>-1</sup> ·s <sup>-1</sup> (1573 $\mu$ mol· $g_{Pd}$ <sup>-1</sup> ·s <sup>-1</sup> )	-0.1 V vs.RHE (pH 5.2 3M acetate buffer)	This work
Pd@Ni-MOF(no TEOA)	203 $\mu$ mol· $g_{cat}$ <sup>-1</sup> · $s$ <sup>-1</sup> (1066 $\mu$ mol· $g_{Pd}$ <sup>-1</sup> · $s$ <sup>-1</sup> )	-0.1V vs.RHE (pH 5.2 3M acetate buffer)	This work
Pd/HNO <sub>3</sub> CF	558 μmol·g <sub>Pd</sub> <sup>-1</sup> ·s <sup>-1</sup>	-0.1 V vs.RHE (pH 5.2 3M acetate buffer)	3

Pd/O <sub>2</sub> Plasma CF	1441 μmol·g <sub>Pd</sub> <sup>-1</sup> ·s <sup>-1</sup>	-0.1 V vs.RHE (pH 5.2 3M acetate buffer)	3
Pd/C	1142 $\mu$ mol·s <sup>-1</sup> ·g <sub>Pd</sub> <sup>-1</sup>	-0.5 V vs.Ag/AgCl (pH 5.0 3M acetate buffer)	4
Pd/C	2112 μmol·s <sup>-1</sup> ·g <sub>Pd</sub> <sup>-1</sup>	-0.6 V vs.Ag/AgCl (pH 5.0 3M acetate buffer)	4

#### References

- 1. Deng, L.; Hu, F.; Ma, M.; Huang, S. C.; Xiong, Y.; Chen, H. Y.; Li, L.; Peng, S., Electronic Modulation Caused by Interfacial Ni-O-M (M=Ru, Ir, Pd) Bonding for Accelerating Hydrogen Evolution Kinetics. *Angew Chem Int Ed Engl* **2021**, *60* (41), 22276-22282.
- 2. Nguyen, M. T.; Seriani, N.; Gebauer, R., Nitrogen electrochemically reduced to ammonia with hematite: density-functional insights. *Phys Chem Chem Phys* **2015**, *17* (22), 14317-22.
- 3. Koh, K.; Sanyal, U.; Lee, M.-S.; Cheng, G.; Song, M.; Glezakou, V.-A.; Liu, Y.; Li, D.; Rousseau, R.; Gutiérrez, O. Y.; Karkamkar, A.; Derewinski, M.; Lercher, J. A., Electrochemically Tunable Proton-Coupled Electron Transfer in Pd-Catalyzed Benzaldehyde Hydrogenation. *Angew. Chem. Int. Ed. Engl.* **2020**, *59* (4), 1501-1505.
- 4. Song, Y.; Sanyal, U.; Pangotra, D.; Holladay, J. D.; Camaioni, D. M.; Gutiérrez, O. Y.; Lercher, J. A., Hydrogenation of benzaldehyde via electrocatalysis and thermal catalysis on carbon-supported metals. *J. Catal.* **2018**, *359*, 68-75.

# Chapter 5

# Electrochemical Reduction of benzaldehyde into Hydrobenzoin on Semiconductor Materials

# 5. Electrochemical Reduction of benzaldehyde into Hydrobenzoin on Semiconductor Materials

The study presented in "Semiconductor nanosheets for electrocatalytic self-coupling of benzaldehyde to hydrobenzoin" aims to explore the potential of semiconductor materials with nanosheet morphology as electrocatalysts for the self-coupling reaction of benzaldehyde (BZH) to hydrobenzoin (HDB). This research focuses on optimizing the reaction conditions, understanding the mechanistic pathways, and establishing the correlation between semiconductor properties and their catalytic performance. The ultimate goal is to enhance the efficiency and selectivity of electrochemical processes for converting biomass-derived products into valuable chemical commodities and biofuels.

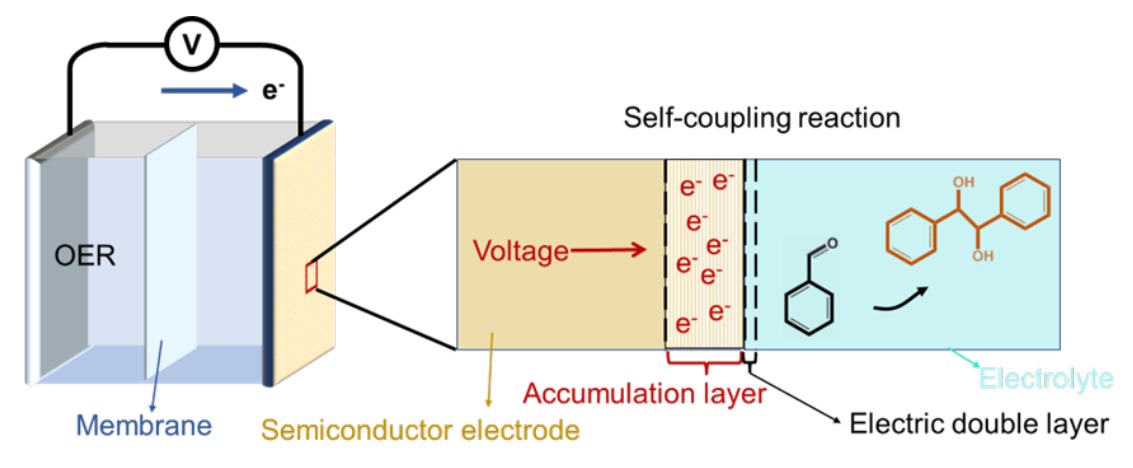


Figure 5-1. Graphic abstract.

The findings of the study indicate a strong correlation between the band gap of semiconductor materials and the electrochemical potential required to maximize selectivity towards HDB in an alkaline medium. Among the tested materials, n-type CuInS<sub>2</sub> (CIS) exhibited the highest conversion rate and selectivity, achieving a 98.5% selectivity at a conversion rate of 0.3 mmol cm<sup>-2</sup>h<sup>-1</sup> under the applied potential of -1.3 V vs. Hg/HgO. Additionally, density functional theory (DFT) calculations revealed a lower kinetic energy barrier for the BZH self-coupling reaction on CIS compared to graphitic carbon, underscoring the superior catalytic role of CIS in this reaction.

The study concludes that the semiconductor properties, particularly the band gap and the flat band potential (E<sub>fb</sub>), significantly influence the electrochemical reduction

process. Applying a negative potential lower than E<sub>fb</sub> on n-type semiconductors leads to electron accumulation on the surface, optimizing the conditions for the BZH-to-HDB electro-reductive reaction. This research advances the understanding of the relationship between semiconductor properties and catalytic performance, contributing to the rational design of more efficient electrocatalysts for biomass conversion.

After completing the first work, I discovered that another product of BZH reduction, HDB had higher value, so I shifted my focus to this reaction. Upon reviewing the literature, I found that semimetal elements with a high ηHER performed better for this reaction (As shown in Figure 5-2). Additionally, alkaline conditions resulted in higher selectivity for HDB. Besides, they are mainly the composition elements for semiconductors. There are also photocatalysis proved that the Nickel doped Zinc Indium sulfide can catalyze the c-c coupling reaction (Chinese Journal of Catalysis 43 (2022) 1084–1091). All those drives us to consider the concept: semiconductor electroccatalysis. Usually semiconductor not be considered as good electrode materials cause it has low intrinsic carriers concentration. But there is essential difference of semiconductor, space charge layer. It can be flexibly tunable by applied voltage. Which metallic electrodes doesn't have. Thus I consider to use several semiconductor materials to explore the possibility of electrocatalyze the self-coupling of BZH. Thus the start of this work.

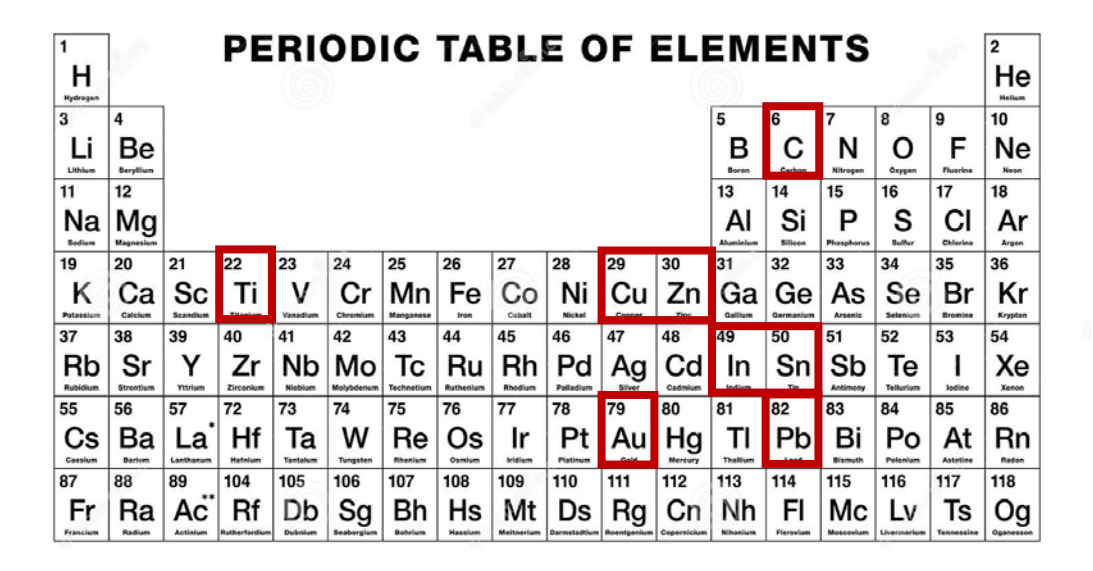


**Figure 5-2.** Schematic diagram of favorable elements towards C-C coupling reaction.

In this work, I prepared the materials, performed XRD, SEM, and solid Uv-vis characterization, and processed the corresponding data. Additionally, I handled the XPS data processing, conducted the electrochemical tests, and identified the products using HPLC along with processing the resulting data. The initial draft of the paper was written by me under the guidance and supervision of Pro. Dr. Andreu Cabot and Dr. Paulina R. Martínez-Alanis. Some characterizations and the DFT calculations were completed by other collaborators.

ELSEVIER

Contents lists available at ScienceDirect

#### Chemical Engineering Journal

journal homepage: www.elsevier.com/locate/cej





### Semiconductor nanosheets for electrocatalytic self-coupling of benzaldehyde to hydrobenzoin

Li Gong <sup>a,b</sup>, Chao Yue Zhang <sup>a,c,\*</sup>, Xiao Mu <sup>d</sup>, Xu Han <sup>e</sup>, Junshan Li <sup>f</sup>, Jordi Arbiol <sup>e,h</sup>, Jin Yuan Zhou <sup>c</sup>, Tanja Kallio <sup>g</sup>, Paulina R. Martínez-Alanis <sup>a,\*</sup>, Andreu Cabot <sup>a,h,\*</sup>

- <sup>a</sup> Catalonia Institute for Energy Research IREC Sant Adrià de Besòs, Barcelona 08930, Spain
- <sup>b</sup> Faculty of Chemistry, University of Barcelona, Barcelona 08028, Spain
- <sup>c</sup> Key Laboratory for Magnetism and Magnetic Materials of the Ministry of Education & School of Physical Science & Technology, Lanzhou University, Lanzhou 730000, China
- <sup>d</sup> Faculty of Chemistry, Fudan University, Shanghai 200438, China
- e Catalan Institute of Nanoscience and Nanotechnology (ICN2), CSIC and BIST, Campus UAB, Bellaterra 08193, Barcelona, Spain
- f Institute of Advanced Study, Chengdu University, Chengdu, 610106, China
- g Department of Chemistry and Materials Science, Aalto University School of Chemical Engineering, P.O. Box 16100 FI-00076 Aalto, Finland
- h ICREA, Pg. Lluís Companys 23 08010, Barcelona, Spain

#### ARTICLE INFO

# Keywords: Electrochemical reduction Self-coupling Semiconductor Benzaldehyde Hydrobenzoin Electrocatalysis GuinSo

#### ABSTRACT

The electrochemical reduction of biomass-derived feedstocks provides a sustainable platform for the synthesis of a wide range of chemical commodities and biofuels. Despite their interest, the optimization of reaction conditions, the screening of electrode materials, and the mechanistic understanding of these processes lag well behind other chemical routes. Here, we focus on the electrochemical self-coupling of benzaldehyde (BZH) to hydrobenzoin (HDB) using semiconductor electrocatalysts with nanosheet morphologies. By testing several semiconductor materials, a correlation is observed between their band gap and the electrochemical potential necessary to maximize selectivity towards HDB in alkaline medium, which we associate with the charge accumulation at the semiconductor surface. N-type CuInS $_2$  provides the highest conversion rate at 0.3 mmol cm $^{-2}h^{-1}$  with a selectivity of 98.5 % at -1.3 V vs. Hg/HgO. Additional density functional theory calculations demonstrate a lower kinetic energy barrier at the CuInS $_2$  surface compared with graphitic carbon, proving its catalytic role in the self-coupling reaction of BZH.

#### 1. Introduction

Biomass has huge potential as a sustainable platform for producing a wide variety of chemicals and biofuels. Through decomposition, separation, and transformation processes, biomass can be converted into its constituent molecules including polyols, carboxylic acids, furans, oxygenated aromatics, glycerol, and furfural. The addition or removal of functional groups through processes such as dehydration, deoxydehydration, hydrodeoxygenation, hydrogenolysis, or decarboxylation can upgrade the product, increasing its value [6–8].

The conversion of biomass-derived products into chemical commodities through electrochemical routes offers numerous advantages over alternative strategies. Electrocatalytic reactions can make efficient use of renewable energies such as solar and wind to drive the chemical

reaction under ambient pressures and temperatures, often without the need for additional reductive or oxidative reagents [1–5]. Besides, the combination of renewable electricity sources with biomass-derived precursors instead of fossil fuels allows processes with net zero carbon emissions.

While significant progress has been made in recent years in the development of electrocatalysts and processes for several small molecule reactions, such as hydrogen, carbon dioxide, nitrogen, and oxygen reactions [9–12], the enormous potential of electrochemical processes to produce a wide range of other chemicals has yet to be realized.

Some efforts have been dedicated to exploring the electrochemical reduction of biomass-derived carbonyls, including furfural, 5-hydroxymethylfurfural, and benzaldehyde (BZH) to monomer alcohol [13,14]. For example, the BZH hydrogenation product, benzyl alcohol (BA), is a

<sup>\*</sup> Corresponding authors at: Catalonia Institute for Energy Research – IREC Sant Adrià de Besòs, Barcelona 08930, Spain (C.Y. Zhang and A. Cabot). E-mail addresses: chzhang@irec.cat (C.Y. Zhang), pmartinez@irec.cat (P.R. Martínez-Alanis), acabot@irec.cat (A. Cabot).

chemical commodity used as a solvent in the fields of printing and coating, and as an additive in the fragrance industry [15]. Another important carbonyl electroreduction process is dimerization, which shows potential for the production of fuels [16], such as hydrofuroin (HDF) and hydrobenzoin (HDB). HDB is also an important industrial chemical as a structural motif in antiepileptic drugs and photo-initiators [17]

As shown in scheme 1, it is generally accepted that the electrochemical hydrogenation of carbonyl to monomer alcohols takes place through a proton-coupled electron transfer path (PCET) [17–19]. Li's group has shown the rate-limiting step of carbonyl electrochemical hydrogenation follows a Langmuir-Hinshelwood (L-H) mechanism, while dimer formation of pinacol from carbonyl groups occurs via radical—radical self-coupling [20–22]. Schröder's work also suggested that pinacol is formed through radical self-coupling via electro-tunneling without reactant adsorbed [23]. These two pathways compete with the hydrogen evolution reaction (HER).

In terms of electrode materials, Zhang's group screened a series of electrocatalysts towards self-coupling reactions, finding that, aside from carbon, Ti, In, and Au provide the best coupling selectivities, while also blocking the HER [24]. Other reported elements showing activity for the electroreductive carbonyl coupling reaction are Pb, Zn, Cu, and Sn [25]. One common characteristic among these elements is their limited capacity for hydrogen adsorption [16]. Besides, these elements form stable semiconductor sulfide compounds that are used in a range of applications. Thus, we considered exploring their performance as electrocatalysts for the self-coupling reaction of BZH.

In recent years, some two-dimensional (2D) metal chalcogenide semiconductors have demonstrated excellent potential for several applications, including electro- and photo-catalysis, in part related to their distinctive crystal phases and morphologies [26,27]. While compared to metals, semiconductor materials are generally considered less ideal electrocatalysts because of their low carrier densities [28,29], their tunable space charge layer (SCL) and the self-gating effect recently reported for nanosheet[30] semiconductors can overcome these limitations. Lam's group explored the use of MoS<sub>2</sub> in the electrocatalytic hydrogenation and dimerization of furfural [18]. They found that the octahedral MoS<sub>2</sub> structure (1 T phase), exhibiting metallic properties, promotes the production of mono-alcohols, while the semiconducting

hexagonal  ${\rm MoS}_2$  structure (2H phase) showed higher selectivity towards dimer formation.

Herein, we explore the use of 2D semiconductor electrocatalysts to drive the BZH coupling reaction to HDB. Different metal chalcogenide semiconductors (CuInS $_2$ , Cu $_{1.8}$ S, In $_{2.77}$ S $_4$ , ZnIn $_2$ S $_4$ , and Zn $_{0.5}$ Cd $_{0.5}$ S) with nanosheet morphology are synthesized and the effect of pH and voltage on their BZH self-coupling performance is analyzed. We further correlate the process selectivity with the applied voltage and space charge layer formed in the different semiconductor materials. Besides experimentally characterizing the charge transport properties, Density functional theory (DFT) calculations are also employed to determine the reaction steps free energy on graphitic carbon and the best performance semiconductor material CuInS $_2$ .

#### 2. Experimental sections

#### 2.1. Materials synthesis

#### 2.1.1. Chemicals

Copper(I) chloride (CuCl, Sigma Aldrich), indium(III) chloride (InCl<sub>3</sub>, Sigma Aldrich), zinc acetate (Zn(CH<sub>3</sub>COO)<sub>2</sub>, Sigma Aldrich), thiourea (CH<sub>4</sub>N<sub>2</sub>S, Sigma Aldrich), ethylene glycol (Thermo Scientific<sup>TM</sup>), cadmium acetate (Cd(CH<sub>3</sub>COO)<sub>2</sub>, Sigma Aldrich), ammonia solution (NH<sub>3</sub>·H<sub>2</sub>O 25 % ~ 28 %, Sigma Aldrich), ethanol, benzaldehyde (BZH, Sigma Aldrich), benzyl alcohol (BA, Sigma Aldrich), benzoic acid (BZA, Sigma Aldrich), and hydrobenzoin (HDB, Sigma Aldrich) were used as purchased, without further purification

#### 2.1.2. Synthesis of CuInS<sub>2</sub>

0.4 mmol CuCl, 0.4 mmol InCl $_3$ , and 1.6 mmol thiourea were dissolved into 40 mL ethylene glycol, the mixture was then transferred into a 50 mL Teflon-lined reactor, which was put in an oven and heated at 200  $^{\circ}\text{C}$  for 12 h. The black precipitate was collected by centrifugation, washed with water and ethanol several times, and dried at 60  $^{\circ}\text{C}$  overnight in an oven.

#### 2.1.3. Synthesis of Cu<sub>1.8</sub>S

 $\text{Cu}_{1.8}\text{S}$  was prepared using a similar method as the one used to produce  $\text{CuInS}_2$  but using only 0.4 mmol of CuCl as the metal precursor.

Scheme 1. (a) Proposed pathways of electrochemical reduction of carbonyls and the competing HER; (b) Proposed mechanism of two different pathways for monomer alcohol and pinacol products.

Synthesis of  $In_{2.77}S_4$ :  $In_{2.77}S_4$  was prepared using a similar method as the one used to produce  $CuInS_2$  but using only 0.4 mmol of  $InCl_3$  as the metal precursor.

#### 2.1.4. Synthesis of ZnIn<sub>2</sub>S<sub>4</sub>

1 mmol Zn (CH<sub>3</sub>COO)<sub>2</sub>, 1 mmol InCl<sub>3</sub> and 6 mmol thiourea were uniformly dissolved into 40 mL H<sub>2</sub>O. The mixture was then transferred into a 50 mL Teflon-lined reactor, which was put in an oven and heated at 200 °C for 20 h. The light-yellow precipitate was collected by centrifugation, washed with water and ethanol several times, and dried at 60 °C overnight in an oven.

#### 2.1.5. Synthesis of Zn<sub>0.5</sub>Cd<sub>0.5</sub>S

2~mmol Zn  $(\text{CH}_3\text{COO})_2$  and 2~mmol Cd  $(\text{CH}_3\text{COO})_2$  were put into a three-necked round-bottom flask. Then 14 mL MQ-water was added. After heating to 80 °C and maintaining 0.5 h with stirring, 2 mL NH $_3$ ·H $_2$ O and 500 mg thiourea were added into. keeping reflowing and stirring for 6 h. The yellow precipitate was collected by centrifugation, washed with water and ethanol several times, and dried at 60 °C overnight in an oven.

#### 2.2. Materials characterization

The morphology of the samples was characterized by scanning electron microscopy (SEM) in a Zeiss Auriga microscope (Carl Zeiss, Jena, Germany) with an energy-dispersive X-ray spectroscopy (EDS) detector at 20 kV to analyze the composition of the sample. Transmission electron microscopy (TEM) was carried out using a ZEISS LIBRA 120, operating at 120 kV. Scanning TEM (STEM) and high-resolution TEM (HRTEM) were carried out under the 200 keV Tecnai F20 field emission microscope. Electron energy loss spectroscopy (EELS) and high-angle annular dark-field (HAADF) STEM were carried out using a Gatan Quantum image filter embedded in the F20 (S)TEM. Powder X-ray diffraction (XRD) patterns were collected at 40 kV and 40 mA with Cu Kα radiation ( $\lambda = 1.5406 \text{ Å}$ ). Characterization of the surface composition and the valence of elements was done by X-ray photoelectron spectroscopy (XPS) conducted on a Thermo Scientific K-Alpha + with Mono Al Kα radiation. The energy, voltage, and beam current were 1486.6 eV, 12 KV, and 6 mA, respectively. Inductively coupled plasma mass spectroscopy (ICP-MS) was tested on 7800 ICP-MS from Agilent Technologies. The solid ultraviolet-visible (UV-Vis) spectroscopy absorbance characterization was carried out on Perkin Elmer Lambda 950 UV/vis/ MR.

#### 2.3. Product quantification and calculation

High-performance liquid chromatography (HPLC) on an Agilent 1200 series at 25  $^{\circ}\text{C}$  was used to analyze the organics. The HPLC was equipped with an ultraviolet–visible detector and 4.6 mm  $\times$  150 mm Shim-pack GWS 5  $\mu m$  C18 column. The eluting solvents of A: 5 mM ammonium formate aqueous solution; solution B: acetonitrile was utilized. The program is 60 % solution B and 40 % solution A for 11 min. The flow rate is 0.5 mL s $^{-1}$ . The injection amount is 1  $\mu L$ . The calibration curves of standard chemicals were employed to determine and quantify the products. The total conversion and selectivities were calculated using the following equations. It should be mentioned that  $\sim$  0.5 mM per 20 mM BZH was oxidized to BZA, which was deducted when calculating the results.

$$Conv = \frac{moles\ of\ BZH\ consumed}{initial\ moles\ of\ BZH} \times 100\% \tag{1}$$

$$Sel_{BA} = \frac{ratio \ of \ BA}{conversion \ ratio \ amount \ of \ BZH} \times 100\%$$
 (2)

$$Sel_{HDB} = \frac{2*ratio \ of \ HDB}{conversion \ ratio \ amount \ of \ BZH} \times 100\%$$
 (3)

$$Sel_{BZA} = \frac{ratio \ of \ BZA}{conversion \ ratio \ amount \ of \ BZH} \times 100\%$$
 (4)

$$Sel_{others} = 100\% \times (1 - \frac{ratio\ of\ BZA\ +\ 2*ratio\ of\ HDB\ +\ ratio\ of\ BZA}{conversion\ ratio\ amount\ of\ BZH})$$
(5)

#### 2.4. Density functional theory (DFT) calculation of free energy

All DFT calculations were performed using the Vienna ab initio simulation package (VASP), employing the projected augmented wave revising Perdew–Burke–Ernzerhof function (PAW–PBE). The cutoff energy was set at 500 eV for all the geometry optimizations. A  $2\times2\times1$  Monkhorst–Pack grid and A  $4\times3\times2$  Monkhorst–Pack grid were used to obtain the surface calculations on the Graphite carbon system and the CuInS $_2$  system, respectively. At least a 20 Å vacuum layer was applied in the z–direction of the slab models, preventing vertical interactions between slabs. The adsorption energy ( $E_{ads}$ ) is described by equation 4 where  $E_{(substrate/product\ and\ graphite\ carbon)}$ ,  $E_{(substrate/product\ and\ graphite\ carbon)}$  are the energies of the system involving the Graphite carbon surface connecting the substrate/product, the only substrate/product, and the Graphite carbon surface, respectively. All structures were completely relaxed until the force on each atom was less than 0.01 eV Å $^{-1}$ .

$$E_{ads} = E_{(substrate/product and graphite carbon)} - E_{(substrate/product)} - E_{(graphite carbon)}$$
 (4)

The free energy  $(E_{free})$  was calculated using equation 5,6 where the free energy phase of each adsorbent is calculated taking \*phCHO $\rightarrow$ \*phCHOH spices.

$$E_{\text{free*phCHO} \to \text{*phCHOH}} = E_{\text{free*phCHOH}} - E_{\text{free*phCHO}} - E_{\text{free*H}}$$
 (5)

$$E_{\text{free*2phCHOH} \to \text{*HDB}} = E_{\text{free*phCHOH}} - 2E_{\text{free*phCHOH}}$$
 (6)

#### 2.5. Electrocatalytic tests

The electrochemical performance of the electrocatalyst was evaluated on Corrtest CS2350 EIS Bipotentiostat (2-channel, Wuhan Corrtest Instrument Corp., Ltd) using a 3-electrodes system in an H-cell reactor divided by Nafion 117 proton exchange membrane. The working electrode was prepared as follows: 6 mg powder was dispersed into 500  $\mu L$  H<sub>2</sub>0, 480  $\mu L$  ethanol, and 80  $\mu L$  5 % Nafion solution. The solution was dropped on a 2  $\times$  2 cm² carbon cloth (~1.5 mg·cm²) that was then cut into 2  $\times$  1 cm²² pieces. Platinum mesh and Ag/AgCl (KCl saturated) or Hg/HgO as counter electrode and reference electrode, respectively.

#### 2.5.1. Sodium acetate-acetic acid solution (pH = 5.3)

Cyclic voltammetry was tested in the range 0.2 V  $\sim$  -0.9 V (vs. Ag/AgCl.) For the I-t curve, -1.1 V (vs. Ag/AgCl) was applied as a constant voltage.

#### 2.5.2. Potassium carbonate-potassium bicarbonate solution (pH = 9.0)

Cyclic Voltammetry was tested in the range  $-0.8 \text{ V} \sim -1.3 \text{ V}$  (vs. Hg/HgO). For the I-t curve, we applied -1.2 V (vs. Hg/HgO) as the constant voltage.

2.5.2.1. *M KOH solution (pH = 14)*. Cyclic Voltammetry was tested  $-0.8~V\sim -1.3~V$  (vs. Hg/HgO). EIS was conducted at -1.2~V (vs. Hg/HgO). For the I-t curve, applied -1.2~V or  $-1.0~V\sim -1.6~V$  (vs. Hg/HgO) as constant voltage and conducted 2 h. The impedance-potential (IMPE) tests were applied among open circle potential  $\pm 0.5~V$  with different frequencies.

#### 3. Results and discussion

### 3.1. Structural, crystalline, and chemical properties of semiconductor materials

Several different metal sulfide semiconductors (CuInS $_2$ , Cu $_{1.8}$ S, In $_{2.77}$ S $_4$ , ZnIn $_2$ S $_4$ , and Zn $_{0.5}$ Cd $_{0.5}$ S) were produced from the reaction of metal chlorides (copper(I) chloride and indium (III) chloride) or acetates (zinc acetate and cadmium acetate) with thiourea under solvothermal reaction at 200  $^{\circ}$ C or ambient pressure at 80  $^{\circ}$ C.

CuInS $_2$  (CIS) is an n-type semiconductor with a direct bandgap of 1.5 eV [31]. The CIS obtained by a solvothermal method displayed a nanosheet morphology with a thickness of  $\sim 50$  nm (Fig. 1a-b). Its X-ray diffraction (XRD) pattern displayed a peak at 28.03° corresponding to the (2 1 1 2) phase of CuInS $_2$  (Fig. S1b). From the crystalline domain in Fig. 1c, the CuInS $_2$  lattice fringe distances were measured to be 0.335 nm, 0.333 nm, and 0.334 nm, at 59.49° and 119.88° which could be interpreted as the hexagonal CuInS $_2$  phase, visualized along its [0001] zone axis. Electron energy loss spectroscopy (EELS) chemical composition maps show Cu, In, and S to be homogeneously dispersed throughout

the whole material (Fig. 1d and S1c-f). The elemental ratio was Cu:In:S = 1:1.3:2.5 according to energy-dispersive X-ray spectroscopy (EDS) results (Table S1), Cu:In:S = 1:0.57:1.77 according to X-ray photoelectron spectroscopy (XPS) data, and Cu:In:S = 1:1.36:2.18 as tested by ICP-MS (Tables S1-3). These results point at a copper-rich surface.

Cu<sub>1.8</sub>S (CS) is a p-type semiconductor with a bandgap of 1.29 eV [32]. CS synthesized using a solvothermal method showed a nanosheet-based architecture with 50 nm-thick plates (Fig. S2a-b). XRD analysis confirmed its rhombohedral digenite structure PDF# 047-1748 (Fig. S2c). The Cu/S elemental ratio was Cu/S = 1.8 when determined by EDS analysis, matching well the digenite phase (Table S1), Cu/S = 1.7 according to XPS data (Fig. S2d-f, Table S2), and Cu/S = 1.35 according to ICP-MS data (Table S3), denoting a sulfur-rich surface.

 $In_{2.77}S_4$  (IS) is a p-type semiconductor with a direct bandgap of  $2.0 \sim 2.3$  eV [33]. IS particles resembling a nanoflower composed of multiple nanosheets were synthesized using a solvothermal method (Fig. S3a-b). Their thickness was estimated at 50 nm and their XRD pattern matched that of the cubic  $In_{2.77}S_4$  phase (PDF# 088-2495). EDS analysis showed their elemental composition to be In/S = 0.59 (Table S1), In/S = 0.82 according to XPS (Fig. S3d-f, Table S2), which matched with ICP-MS

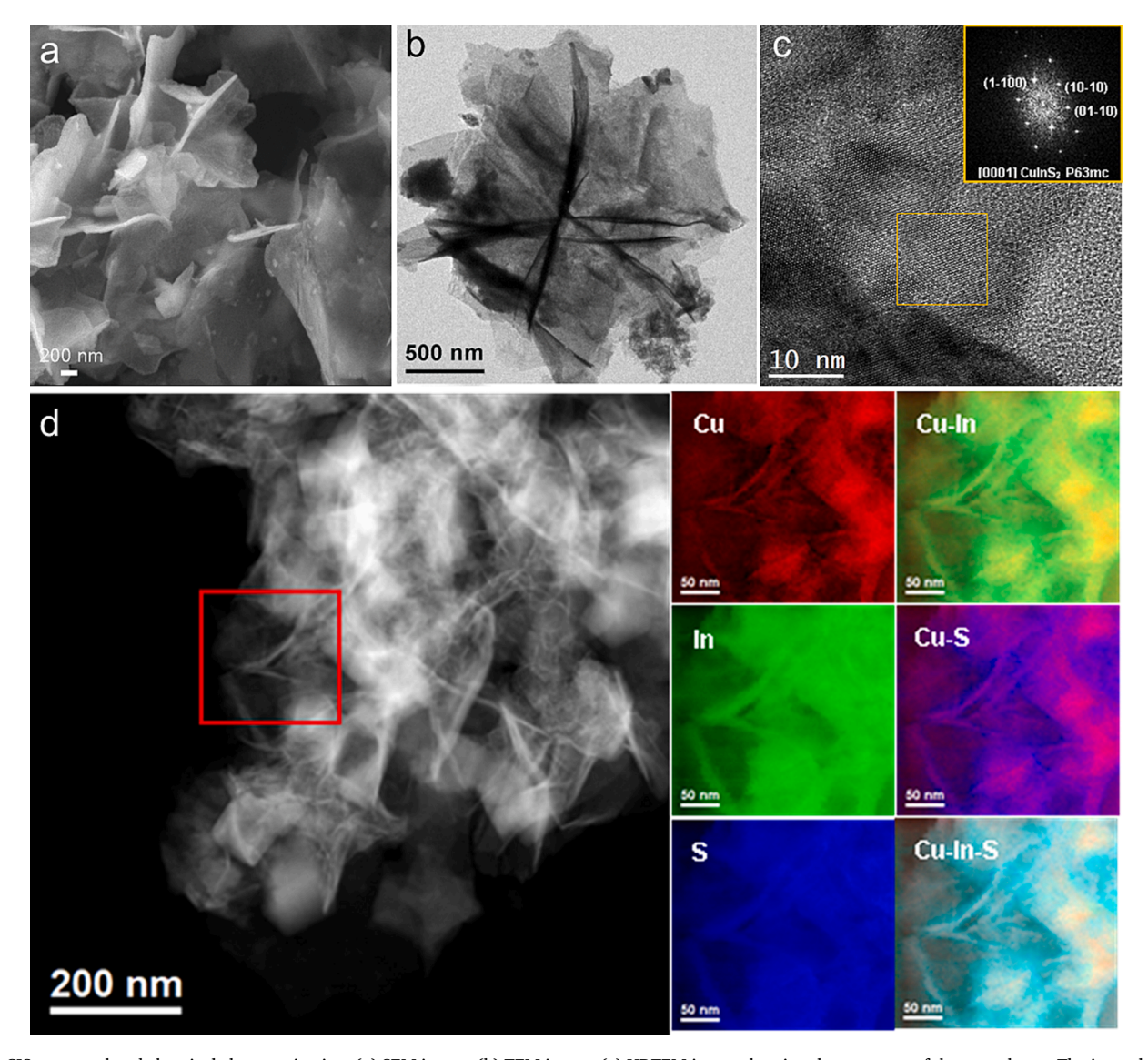


**Fig. 1.** CIS structural and chemical characterization: (a) SEM image. (b) TEM image. (c) HRTEM image showing the structure of the nanosheets. The inset shows the indexed power spectrum (FFT) obtained at the orange squared area in the HRTEM image. (d) EELS chemical composition maps from the red squared area of the STEM micrograph. Individual Cu L<sub>2,3</sub>-edges at 931 eV (red), In M<sub>4,5</sub>-edges at 443 (green), S L<sub>2,3</sub>-edges at 165 eV (blue), and composites of Cu-In, Cu-S, and Cu-In-S. (For interpretation of the references to colour in this figure legend, the reader is referred to the web version of this article.)

data at In/S = 0.56 (Table S3).

 $ZnIn_2S_4$  (ZIS) is a n-type semiconductor with a direct bandgap of 2.5 eV for the hexagonal phase [34]. ZIS obtained by a solvothermal method displayed a cross-linked nanosheet-based architecture with a nanosheet thickness of ~50 nm (Fig. S4a). XRD analysis confirmed its hexagonal  $ZnIn_2S_4$  phase (PDF# 03-065-2023, Fig. S4b). EDS analysis showed their elemental ratio to be Zn:In:S=1:1.4:3.2 (Table S1), Zn:In:S=1:1.9:2.3 according to XPS data (Fig. S4c-f, Table S2), while ICP-MS quantified their composition at Zn:In:S=1:1:2.2 (Table S3).

Finally, Zn $_{0.5}$ Cd $_{0.5}$ S (ZCS), which is a solid solution of CdS and ZnS, is a n-type semiconductor with a direct bandgap of 2.51 eV [35]. ZCS was obtained at ambient pressure and 80 °C and it was characterized by a nanosheet-based morphology with a sheet thickness of ~30 nm (Fig. S5a). The XRD pattern matched that of cubic CdS PDF# 089-0440 and cubic ZnS PDF# 05–0566 phases (Fig. S5b). The composition was Zn:Cd:S = 1:1.2:2.4 as determined by EDS analysis (Table S1) and Zn:Cd: S = 1:0.45:2.4 as determined by XPS (Fig. S5d-f, Table S2), Zn:Cd:S = 1:1:2.4 determined by ICP-MS analysis (Table S3) and thus showing a Zn-rich surface.

#### 3.2. Electrocatalytic performance

All catalysts were supported on graphitic carbon cloth (CC) with a working electrode area of  $2 \times 1~{\rm cm}^2$  and a loading of  $\sim 1.5~{\rm mg~cm}^{-2}$ . The electrochemical performance of the different semiconductors towards the reduction of 20 mM BZH was initially tested under different pH aqueous solutions at a working potential of  $-0.6~{\rm V}$  vs. RHE for 2 h (Fig. 2).

In sodium acetate buffer solution (pH 5.2), the BZH conversion was relatively low for all the semiconductors, being BZA the main product. Only CS produced a slight amount of BA (Fig. 2a). When comparing the cyclic voltammetry (CV) curves obtained in the presence and absence of 20 mM BZH at pH 5.2 (Figure S6), we observe moderate differences for all the catalysts, which points to low catalytic performance in these reaction conditions.

When increasing the pH to 9.0 with a potassium carbonate-bicarbonate buffer solution, the BZH conversion slightly increased and the selectivity to HDB sharply improved (Fig. 2b). From the comparison of the CV curves in the presence and absence of 20 mM BZH at pH 9.0  $\,$ 

(Figure S7), we observe the presence of BZH to strongly increase the current density and reduce the reaction overpotential for all the materials.

The use of a 1 M KOH electrolyte, i.e. increasing the pH to 14, significantly improved the conversion. The selectivity towards HDB also increased for some of the materials, reaching values above 95 % for all the catalysts (Fig. 2c). Besides, when comparing the CV curves in the presence and absence of BZH, the onset potential for all catalysts further decreased in absolute value and the semicircle in the Nyquist plot of the EIS greatly shrunk, which correlates with an improved charge transport at the electrode/electrolyte interphase (Figure S8).

Among the different catalysts tested, CIS showed the best performance toward HDB production from BZH, with a BZH conversion of 99.83 % and an HDB selectivity of 98.46 %. Notice that in 1 M KOH electrolyte, BZH spontaneously transforms to BZA and BA with 100 % selectivity (50 % selectivity to BZA and 50 % to BA) when no potential is applied (Figure S9). The application of a voltage speeds up the reaction and shifts its selectivity toward HDB in an alkaline environment.

Fig. 3a and S10-S14 show the conversion and product selectivity after a 2 h reaction at different potentials for all the different catalysts. For CIS, when increasing the absolute value of the applied potential, the selectivity towards HDB initially increased and later decreased at too high negative potentials (Fig. 3a and Table S4). The selectivity toward HDB reached a maximum of 98.46 % at -1.3 V vs. Hg/HgO. The other catalysts showed a similar trend, except for CS which showed no maximum selectivity toward HDB. Notably, graphitic carbon showed notable performance, with selectivities up to 98 % for the coupling reaction and conversion just below 95 %, consistent with previous reports that associated this characteristic with the ability of graphite to promote radical generation [24,36].

Fig. 3b shows the time-dependent conversion/selectivity at -1.3~V vs. Hg/HgO on CIS. The BZH concentration gradually decreases and the concentration of HDB gradually increases. The reaction rate on CIS was estimated at 0.3 mmol cm $^{-2}h^{-1}$ , well above that of CC (0.13 mmol cm $^{-2}h^{-1}$ , Figure S15).

The CIS stability upon cycling was also tested. Figures S16 and S17 show the performance obtained in 5 consecutive 2 h I-t curve cycles, using the same electrode but replacing the electrolyte at each cycle. Within each cycle, the current slightly decreases as the reactants are

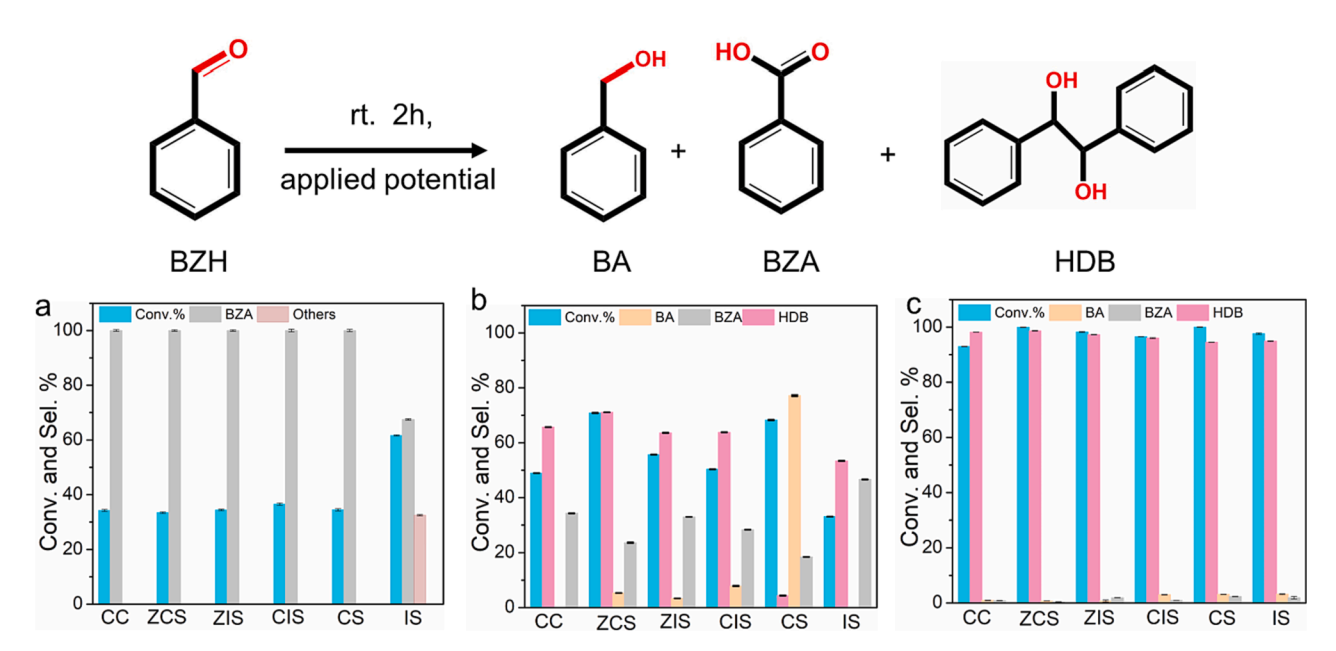


Fig. 2. Products of the electroreduction of BZH after 2 h reaction on the different catalysts tested. Electrolyte compositions: 1 M sodium acetate buffer solution (pH 5.3) (a); 1 M potassium carbonate bicarbonate buffer solution (pH 9) (b) and 1 M KOH aqueous solution (pH 14) (c) at working potentials -1.1 V vs. Ag/AgCl; -1.2 V vs. Hg/HgO -1.4 V vs. Hg/HgO; (~-0.6 V vs. RHE), respectively.

5

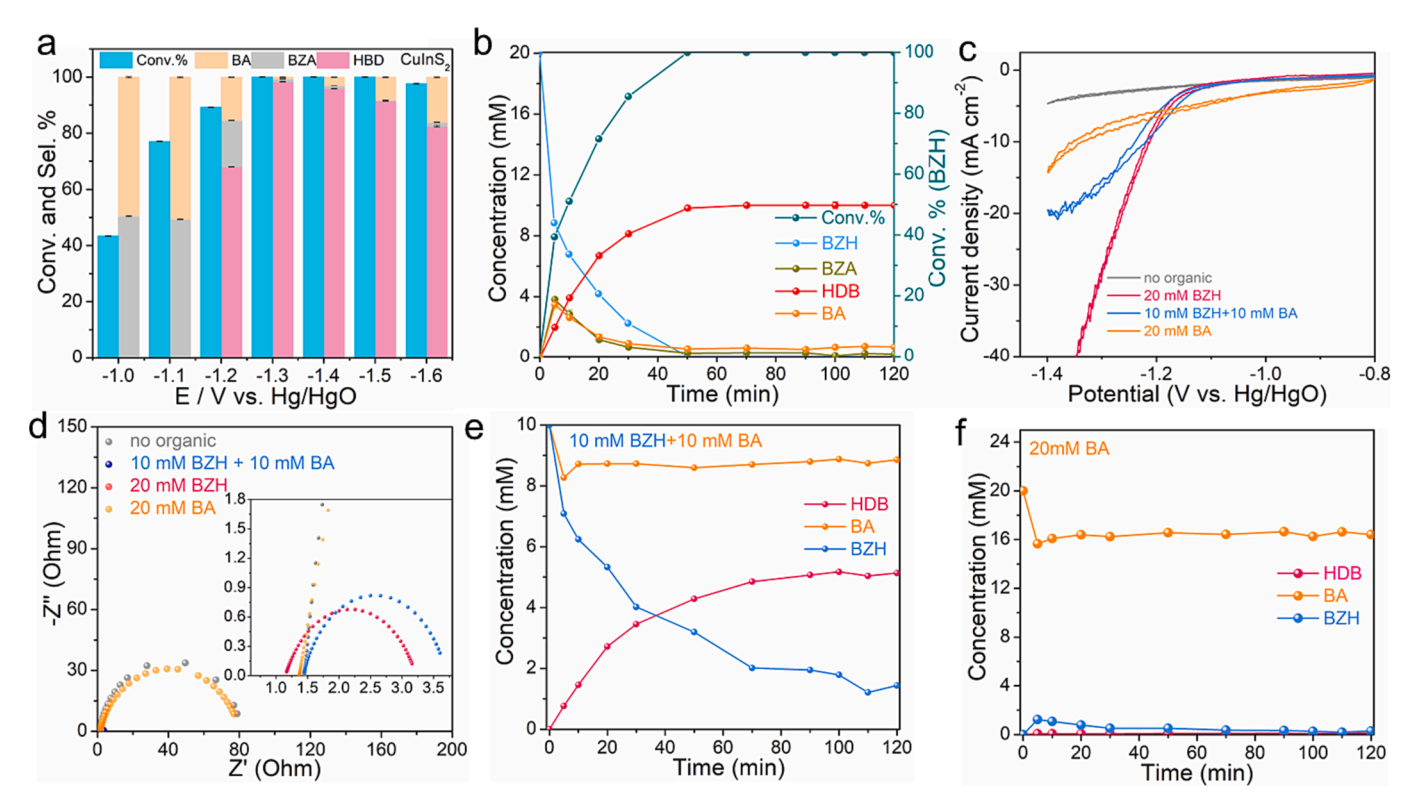


Fig. 3. (a) Potential-dependent conversion (conv.%) and selectivity (sel.%) over CIS in pH 14 (1 M KOH); (b) Time-dependent transformation of 20 mM BZH over CIS at -1.3 V vs. Hg/HgO. (c,d) CV curves (c) and Nyquist plots (d) of the CIS electrode with and without organics; (e) Time-dependent transformation of 10 mM BZH and 10 mM BA over CIS in pH 14 and at -1.3 V vs. Hg/HgO; (f) Time-dependent transformation of 20 mM BA over CIS in pH 14 at -1.3 V vs. Hg/HgO.

consumed. However, when refreshing the electrolyte, the conversion and selectivity towards HDB are recovered in the five cycles. Besides, SEM characterization of the sample after cycling (Figure S18) shows the nanosheet structure to be partially transformed into smaller particles with a fine nanostructured surface.

To better determine the role of BA, CV curves of CIS with different substrates were measured. As shown in Fig. 3c, when adding 10 mM BZH + 10 mM BA into the electrolyte, the current density decreased over that obtained with 20 mM BZH. This decrease was more accentuated when adding just 20 mM BA. EIS data (Fig. 3d) also showed the charge transfer resistance in the presence of 20 mM BZH ( $\sim\!3.0~\Omega$ ) to be lower than that obtained with a combination of 10 mM BZH + 10 mM BA ( $\sim\!3.2~\Omega$ ), although both showed a relatively fast charge transfer rate compared with a pure 1 M KOH electrolyte ( $\sim\!75~\Omega$ ) and an electrolyte containing 20 mM BA ( $\sim\!75~\Omega$ ). Besides, the time-dependent transformation of 10 mM BZH + 10 mM BA and 20 mM BA over CIS in pH 14 at -1.3~V vs. Hg/HgO was measured and displayed in Fig. 3f. We observe a minor conversion of BA in both cases. From these experimental results, we conclude that BA could not be activated into a radical to yield HDB, and the presence of BZH was required to yield HDB.

## 3.3. Relationships between semiconductor materials properties with performance

Upon immersing a semiconductor into an electrolyte, the interphase reaches equilibrium when the Fermi level  $(E_F)$  at the semiconductor surface matches the chemical potential of the redox couple  $(E_R)$  in the solution. Thus, a space charge layer (SCL) with a modified carrier concentration and bent electronic bands is formed at the semiconductor side of the interphase. In thin enough semiconductors, this SCL extends over the whole material. The flat band potential  $(E_{fb})$  is the potential that needs to be applied to the semiconductor to equilibrate the interface  $E_F$  so there is no SCL at the junction between the semiconductor and the

electrolyte. Thus,  $E_{fb}$  depends not only on the semiconductor properties but also on the electrolyte composition.

The E<sub>F</sub> of an n-type semiconductor is generally higher than E<sub>R</sub> (for this self-coupling reaction, normally E<sub>R</sub> is located at 0 V vs. RHE [37,38]). Thus, when immersing an n-type semiconductor into an electrolyte, to reach an equilibrium, free electrons are transferred to the solution and an upward band bending at the surface of a bulk semiconductor or a downshift of the Fermi level for a thin semiconductor layer is obtained (Fig. 4). In this case, the generated SCL is depleted of electrons and provides a barrier for electrons to be transferred from the semiconductor into the electrolyte. When applying a negative voltage, that is shifting upwards the potential at the semiconductor surface in contact with the CC electrode, the band bending decreases (E<sub>F</sub> increases) up to a point when the E<sub>fb</sub> is reached. At even more negative potentials, the bands bend downwards (EF shifts upwards) generating an accumulation layer and eventually forming a degenerated layer with a metallic character [28,39,40]. Liu et al. observed the electronic conductivity of thin enough semiconductors to strongly increase with the applied electrochemical potential and described this phenomenon as a self-gating effect [30].

In the case of a p-type semiconductor, when immersed into the electrolyte, if the  $E_F$  is below the  $E_R$ , holes are injected into the solution and a hole depletion layer is formed at the interface. To reach the  $E_{fb}$ , a positive potential needs to be applied at the CC/semiconductor interface. If applying a negative potential, an increased band bending reinforces the hole depletion layer near the surface of the semiconductor. This depletion layer becomes wider and impedes the flow of holes into the electrolyte. At highly negative potentials, the bands may bend to a point where the valence band edge aligns with the  $E_R$  of the electrolyte. This alignment creates a condition known as inversion, where the surface region of the p-type semiconductor becomes n-type in nature. In this case, the surface can become conductive.

Ultraviolet-visible (UV-vis) spectroscopy (Figure S19a-e) and Mott-

6

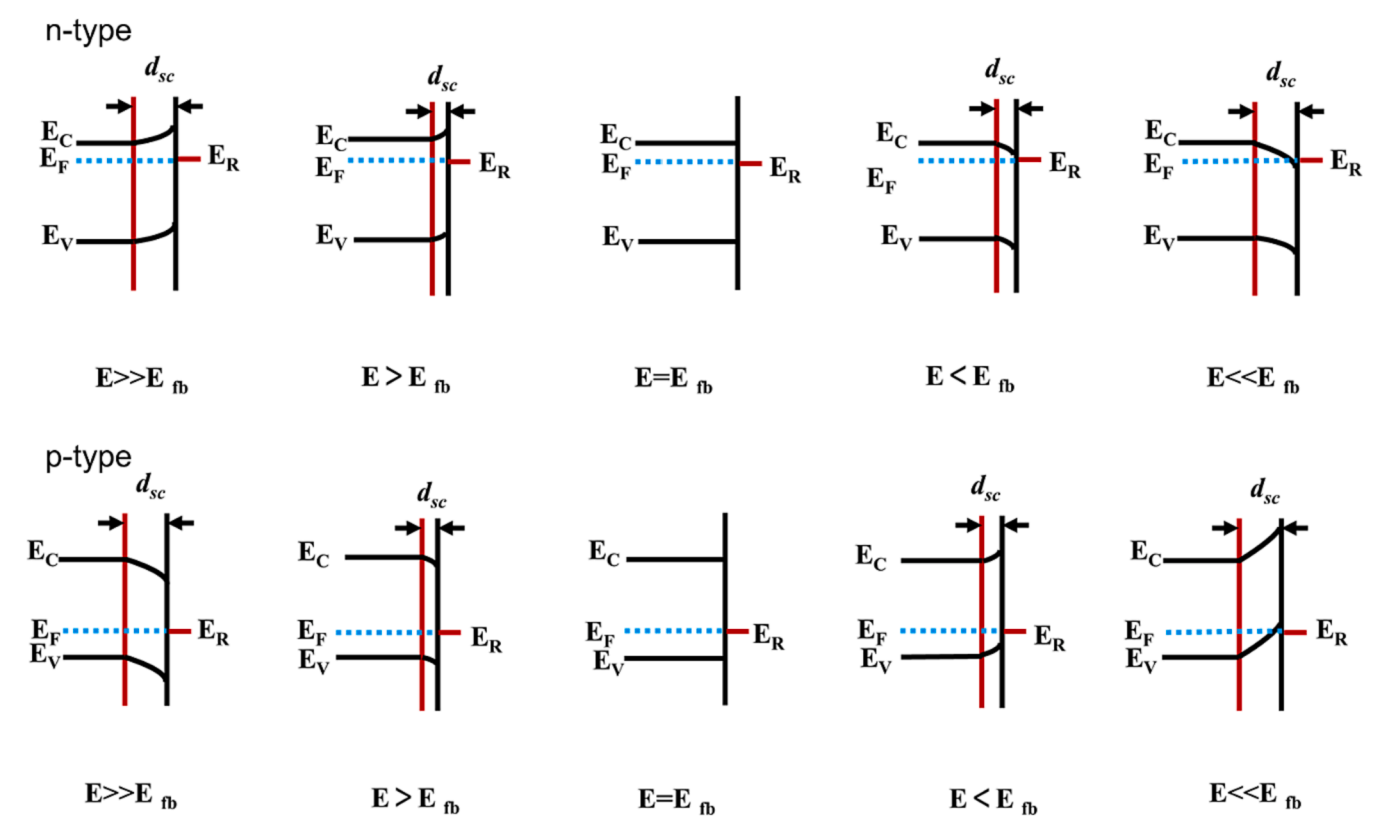


Fig. 4. Effect of varying the applied potential on the band bending.  $E_F$  and  $d_{sc}$  are the Fermi energy and thickness of the space charge layer formed in the semi-conductor, respectively.

Schottky analyses (Figure S20a-e) were used to determine the band gap and  $E_{fb}$  of the different electrodes after immersion in pH 14 solution. The obtained results are summarized and related to the potential of maximum BZH-to-HDB selectivity in Fig. 5 and Table S5. For n-type ZCS, showing the largest band gap and the largest absolute value of  $E_{fb}$  among the tested materials, the BZH-to-HDB conversion at all the potentials applied is the lowest, ZCS required –1.5 V vs. Hg/HgO to reach its peak performance. In contrast, n-type CIS required just –1.3 V vs. Hg/HgO to reach its peak performance. Notably, when applying –1.6 V vs. Hg/HgO on CIS, both the selectivity and conversion of BZH-to-HDB decreased, which we associated with an HER increase. For p-type CS, when applying a negative potential of –1.3 V vs. Hg/HgO the conversion was lower than that of CIS. Overall, we observed the potential of the maximum BZH-to-HDB selectivity to increase with  $E_{fb}$  and to decrease with the semiconductor band gap. We associate this experimental result

with the applied potential having to be lower than  $E_{\rm fb}$  for a proper concentration of electrons to accumulate on the space charge layer and reach an optimal thickness for the formation of HDB. When applying a too high negative potential, a too large excess of electrons at the semi-conductor surface induces a buildup of the amount of adsorbed hydrogen and substrate that results in the favored formation of monomer alcohols over dimers as the reaction product.

The electroreduction of BZH in acidic conditions might take place as follows (\* = active site) [41]:

$$phCHO + * \rightarrow *phCHO \tag{1}$$

$$phCHO^* + H_3O^+ + e^- \rightarrow phCHOH(H_2O)$$
 (2)

$$*phCHOH(H_2O) \rightarrow *phCHOH + H_2O$$
 (3)

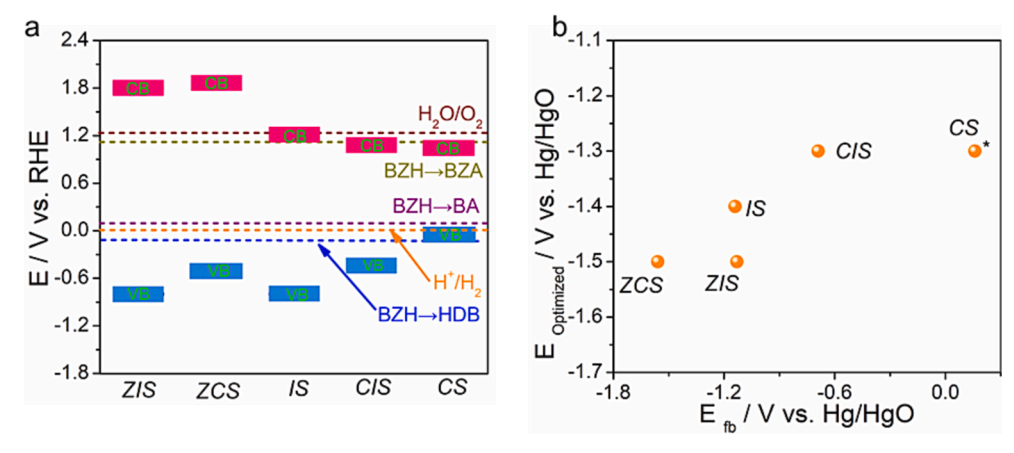


Fig. 5. Illustration of band edges, E fb. and the applied potential providing the highest sel.% for each of the semiconductor materials, ZCS, ZIS, IS, CIS, and CS.

$$H^+ + e^- + *\rightarrow *H \tag{4}$$

$$*phCHOH + *H \rightarrow *phCH_2OH + *$$
 (5)

$$*phCH2OH \rightarrow phCH2OH + *$$
 (6)

\*
$$phCHOH + phCHOH \rightarrow ph(HO)CH - CH(HO)ph + 2*$$
 (7)

Equations (1)-(6) correspond to the formation of BZH, while equations (1)-(5) and (7) correspond to the formation of HDB.

On the other hand, the electroreduction of BZH in alkaline media most likely follows ( $\cdot$ = radical specie): [24]

$$phCHO + * \rightarrow * phCHO \tag{1}$$

$$*phCHO + e^- + H_2O \rightarrow *phCHO(H_2O)$$
(8)

$$*phCHO(H_2O) + e^- \rightarrow *ph(OH)HC \bullet + OH^-$$
(9)

$$H_2O + e^- + * \rightarrow *H + OH^-$$
 (9)

$$*ph(OH)HC \bullet + *H \rightarrow *phCH_2OH + *$$
 (10)

$$*phCH_2OH \rightarrow phCH_2OH + *$$
 (6)

$$2 ph(OH)HC \bullet * \rightarrow ph(HO)CH - CH(HO)ph* + *$$
 (11)

$$ph(HO)CH - CH(HO)ph^* \rightarrow ph(HO)CH - CH(HO)ph + *$$
 (12)

Equations (1), (8)-(10) and (6) correspond to the formation of BZH, while equations (1), (8)-(12) correspond to the formation of BZH.

To obtain monomer alcohol, the adsorption of hydrogen and substrate, a low pH electrolyte and a high H adsorption ability of the anode material are required [21,42], and at least one electron needs transfer to H. On the other hand, coupling products are more easily obtained at higher pH and on materials having poor H adsorption abilities, where the electron directly transfers to the substrate.

Previous in situ Raman spectroscopy measurements by C. Liu et al. show that the in-plane aromatic C–H bending peaks of BZH change upon adsorption on carbon fiber paper, while the peak assigned to the C-O stretching vibration in carbonyl group C=O remains unchanged [24]. When applying a relatively low voltage, the C-O peak disappears, which is explained by considering that upon increasing the electronic concentration at the electrode surface, C=O with higher electron cloud density tends to move away, while the phenyl ring center with low electron density tends to adsorb more strongly. Therefore, according to previous investigations, to explain the excellent performance of CuInS<sub>2</sub>, we considered the BZH adsorption through the phenyl ring.

While graphitic carbon has a notable BZH electroreduction performance, the CIS-based electrode displays significantly higher conversion rates. To investigate the favorable effect of CIS at the atomic surface level, we explored the free energy changes from the substrate BZH, to the ketyl intermediate BZH-H<sub>2</sub>O, BZH-H, and the product HDB using DFT calculations (Figures. S21-22). Fig. 6 displays the free energy profiles for CIS and graphite, assuming the BZH adsorption through the phenyl ring. DFT results demonstrate that while the proton transfer and the coupling steps show little difference, the substrate BZH shows a much higher affinity for CIS (-4.98 eV) than for graphite carbon (-0.03 eV), and the splitting of H<sub>2</sub>O into H (3rd step in Fig. 6) is much favored on CIS (+1.87 eV) than on C (+4.71 eV). The significant difference between carbon and CIS in adsorption energy of the phenyl group of BZH is related to the stronger d- $\pi$  interactions between d-orbitals of transition metal of Cu with  $\pi$  electrons of phenyl ring than  $\pi$ - $\pi$  stacking interactions between phenyl rings [43]. This improved adsorption is essential to promote the BZH conversion on CIS. On the other hand, the adsorption enhancement might also facilitate the splitting of H2O into H attached to O=C of BZH converted into the ph(OH)CH radical. To

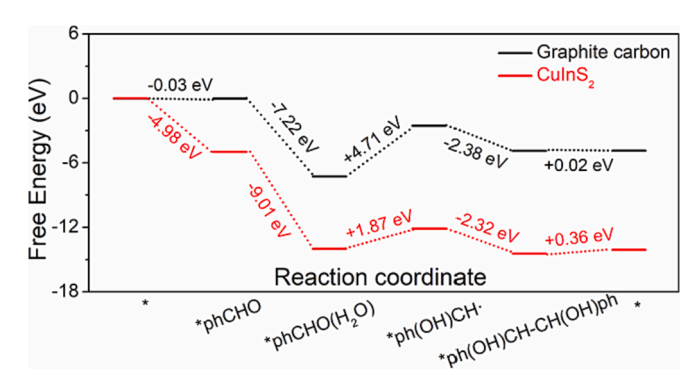


**Fig. 6.** Free energy profiles for the self-coupling reaction process from BZH to HDB on CIS and graphic carbon. \* Represents an adsorption site.

further clarify the active site toward the BZH to HDB reaction, we computed the BZH adsorption energy on Cu and In sites within their sulfides (Figure S23), showing Cu to provide a stronger binding, consistently with previous literature [43].

#### 4. Conclusion

A series of semiconductor materials with nanosheet morphology were explored as electrocatalysts for the BZH self-coupling reaction to HDB. While the conversion rate strongly increased with pH, the selectivity towards HDB was strongly related to the applied potential. Conversions up to 99.83 % and HDB selectivity of 98.46 % were obtained using CIS at  $-1.3~\rm V$  vs. Hg/HgO. We further analyzed the relationship between the semiconductor band gap and  $E_{fb}$  and the potential required to maximize selectivity. Applying negative potential lower than  $E_{fb}$  on n-type semiconductors, the electrons accumulate on the surface to reach the optimized condition towards the electro-reductive reaction BZH-to-HDB. Meanwhile, DFT-based computational simulations further indicated that the kinetic energy barrier of the BZH self-coupling reaction on CIS is lower than on graphitic carbon, which is associated with the much higher affinity of BZH for CIS and the favored splitting of  $\rm H_2O$  into H on CIS when compared to C.

#### **Declaration of competing interest**

The authors declare that they have no known competing financial interests or personal relationships that could have appeared to influence the work reported in this paper.

#### Data availability

Data will be made available on request.

#### Acknowledgements

L. Gong and C.Y. Zhang thank the China Scholarship Council for the scholarship support. The authors greatly acknowledge the computational simulation support from the Supercomputing Center of Lanzhou University, China. J. Li is grateful for the project funded by the Natural Science Foundation of Sichuan Province (No. 2022NSFSC1229) and the China Postdoctoral Science Foundation (No.2023MD734228). The project on which these results are based has received funding from the European Union's Horizon 2020 research and innovation program under Marie Skłodowska-Curie grant agreement No. 801342 (Tecniospring INDUSTRY) and the Government of Catalonia's Agency for Business Competitiveness (ACCIO). ICN2 acknowledges funding from Generalitat de Catalunya 2021SGR00457. This study was supported by MCIN with funding from the European Union NextGenerationEU (PRTR-C17.11) and Generalitat de Catalunya. This research is part of the CSIC

program for the Spanish Recovery, Transformation, and Resilience Plan funded by the Recovery and Resilience Facility of the European Union, established by the Regulation (EU) 2020/2094. The authors thank the support from the project NANOGEN (PID2020-116093RB-C43), funded by MCIN/AEI/10.13039/501100011033/ and by "ERDF A way of making Europe", by the "European Union". ICN2 is supported by the Severo Ochoa program from Spanish MCIN /AEI (Grant No.: CEX2021-001214-S) and is funded by the CERCA Programme / Generalitat de Catalunya.

#### Appendix A. Supplementary data

Supplementary data to this article can be found online at https://doi.org/10.1016/j.cej.2023.147612.

#### References

- [1] P. Ramakrishnan, H. Im, S.-H. Baek, J.I. Sohn, Recent Studies on Bifunctional Perovskite Electrocatalysts in Oxygen Evolution, Oxygen Reduction, and Hydrogen Evolution Reactions under Alkaline Electrolyte, Isr. J. Chem 59 (2019) 708–719.
- [2] J. Li, X. Wang, C. Xing, L. Li, S. Mu, X. Han, R. He, Z. Liang, P. Martinez, Y. Yi, Q. Wu, H. Pan, J. Arbiol, C. Cui, Y. Zhang, A. Cabot, Electrochemical reforming of ethanol with acetate Co-Production on nickel cobalt selenide nanoparticles, Chem. Eng. J. 440 (2022), 135817.
- [3] J. Li, C. Xing, Y. Zhang, T. Zhang, M.C. Spadaro, Q. Wu, Y. Yi, S. He, J. Llorca, J. Arbiol, A. Cabot, C. Cui, Nickel Iron Diselenide for Highly Efficient and Selective Electrocatalytic Conversion of Methanol to Formate, Small 17 (2021) 2006623.
- [4] Z. Li, Y. Yan, S.-M. Xu, H. Zhou, M. Xu, L. Ma, M. Shao, X. Kong, B. Wang, L. Zheng, H. Duan, Alcohols electrooxidation coupled with H2 production at high current densities promoted by a cooperative catalyst, Nat. Commun. 13 (2022) 147.
- [5] M. Garedew, D. Young-Farhat, J.E. Jackson, C.M. Saffron, Electrocatalytic Upgrading of Phenolic Compounds Observed after Lignin Pyrolysis, ACS Sustain. Chem. Eng. 7 (2019) 8375–8386.
- [6] F.W.S. Lucas, R.G. Grim, S.A. Tacey, C.A. Downes, J. Hasse, A.M. Roman, C. A. Farberow, J.A. Schaidle, A. Holewinski, Electrochemical Routes for the Valorization of Biomass-Derived Feedstocks: From Chemistry to Application, ACS Energy Lett. 6 (2021) 1205–1270.
- [7] R. Matthessen, J. Fransaer, K. Binnemans, D.E. De Vos, Electrocarboxylation: towards sustainable and efficient synthesis of valuable carboxylic acids, Beilstein J. Org. Chem. 10 (2014) 2484–2500.
- [8] Y. Liu, G. Li, Y. Hu, A. Wang, F. Lu, J.-J. Zou, Y. Cong, N. Li, T. Zhang, Integrated Conversion of Cellulose to High-Density Aviation Fuel, Joule 3 (2019) 1028–1036.
- [9] C.-K. Ran, L.-L. Liao, T.-Y. Gao, Y.-Y. Gui, D.-G. Yu, Recent progress and challenges in carboxylation with CO<sub>2</sub>, Curr. Opin. Green Sustain. Chem. 32 (2021), 100525.
- [10] Y.Y. Birdja, E. Pérez-Gallent, M.C. Figueiredo, A.J. Göttle, F. Calle-Vallejo, M.T. M. Koper, Advances and challenges in understanding the electrocatalytic conversion of carbon dioxide to fuels, Nat. Energy 4 (2019) 732–745.
- [11] J. Li, L. Li, X. Ma, J. Wang, J. Zhao, Y. Zhang, R. He, Y. Yang, A. Cabot, Y. Zhu, Unraveling the Role of Iron on Ni-Fe Alloy Nanoparticles during the Electrocatalytic Ethanol-to-Acetate Process, Nano Research (2023).
- [12] J. Li, L. Li, X. Ma, X. Han, C. Xing, X. Qi, R. He, J. Arbiol, H. Pan, J. Zhao, J. Deng, Y. Zhang, Y. Yang, A. Cabot, Selective Ethylene Glycol Oxidation to Formate on Nickel Selenide with Simultaneous Evolution of Hydrogen, Adv. Sci. 10 (2023) 2300841.
- [13] D.C. Cantu, A.B. Padmaperuma, M.-T. Nguyen, S.A. Akhade, Y. Yoon, Y.-G. Wang, M.-S. Lee, V.-A. Glezakou, R. Rousseau, M.A. Lilga, A Combined Experimental and Theoretical Study on the Activity and Selectivity of the Electrocatalytic Hydrogenation of Aldehydes, ACS Catal. 8 (2018) 7645–7658.
- [14] C. Xu, E. Paone, D. Rodríguez-Padrón, R. Luque, F. Mauriello, Recent catalytic routes for the preparation and the upgrading of biomass derived furfural and 5hydroxymethylfurfural, Chem. Soc. Rev. 49 (2020) 4273–4306.
- [15] J.T. Bhanushali, I. Kainthla, R.S. Keri, B.M. Nagaraja, Catalytic Hydrogenation of Benzaldehyde for Selective Synthesis of Benzyl Alcohol: A Review, ChemistrySelect 1 (2016) 3839–3853.
- [16] M.T. Bender, X. Yuan, M.K. Goetz, K.-S. Choi, Electrochemical Hydrogenation, Hydrogenolysis, and Dehydrogenation for Reductive and Oxidative Biomass Upgrading Using 5-Hydroxymethylfurfural as a Model System, ACS Catal. 12 (2022) 12349–12368.
- [17] J. Yu, P. Zhang, L. Li, K. Li, G. Zhang, J. Liu, T. Wang, Z.-J. Zhao, J. Gong, Electroreductive coupling of benzaldehyde by balancing the formation and dimerization of the ketyl intermediate, Nat. Commun. 13 (2022) 7909.
- [18] S. Huang, B. Gong, Y. Jin, P.H.L. Sit, J.-C.-H. Lam, The Structural Phase Effect of MoS<sub>2</sub> in Controlling the Reaction Selectivity between Electrocatalytic Hydrogenation and Dimerization of Furfural, ACS Catal. 12 (2022) 11340–11354.

- [19] L.C. Meyer, U. Sanyal, K.A. Stoerzinger, K. Koh, J.L. Fulton, D.M. Camaioni, O. Y. Gutiérrez, J.A. Lercher, Influence of the Molecular Structure on the Electrocatalytic Hydrogenation of Carbonyl Groups and H<sub>2</sub> Evolution on Pd, ACS Catal. 12 (2022) 11910–11917.
- [20] X.H. Chadderdon, D.J. Chadderdon, J.E. Matthiesen, Y. Qiu, J.M. Carraher, J.-P. Tessonnier, W. Li, Mechanisms of Furfural Reduction on Metal Electrodes: Distinguishing Pathways for Selective Hydrogenation of Bioderived Oxygenates, J. Am. Chem. Soc. 139 (2017) 14120–14128.
- [21] H. Liu, D.M. Patel, Y. Chen, J. Lee, T.-H. Lee, S.D. Cady, E.W. Cochran, L.T. Roling, W. Li, Unraveling Electroreductive Mechanisms of Biomass-Derived Aldehydes via Tailoring Interfacial Environments, ACS Catal. 12 (2022) 14072–14085.
- [22] J. Anibal, B. Xu, Electroreductive C-C Coupling of Furfural and Benzaldehyde on Cu and Pb Surfaces, ACS Catal. 10 (2020) 11643–11653.
- [23] P. Nilges, U. Schröder, Electrochemistry for biofuel generation: production of furans by electrocatalytic hydrogenation of furfurals, Energy Environ. Sci. 6 (2013) 2925–2931.
- [24] C. Liu, R. Li, W. Zhou, Y. Liang, Y. Shi, R.-L. Li, Y. Ling, Y. Yu, J. Li, B. Zhang, Selectivity Origin of Organic Electrosynthesis Controlled by Electrode Materials: A Case Study on Pinacols, ACS Catal. 11 (2021) 8958–8967.
- [25] J. Anibal, A. Malkani, B. Xu, Stability of the ketyl radical as a descriptor in the electrochemical coupling of benzaldehyde, Catal, Sci. Technol. 10 (2020) 3181–3194.
- [26] Y. Wang, B. Ren, J. Zhen Ou, K. Xu, C. Yang, Y. Li, H. Zhang, Engineering twodimensional metal oxides and chalcogenides for enhanced electro- and photocatalysis, Sci. Bull. 66 (2021) 1228–1252.
- [27] T. Eisa, M.A. Abdelkareem, D.A. Jadhav, H.O. Mohamed, E.T. Sayed, A.G. Olabi, P. Castaño, K.-J. Chae, Critical review on the synthesis, characterization, and application of highly efficient metal chalcogenide catalysts for fuel cells, Progress in Energy and Combustion Science 94 (2023), 101044.
- [28] R. Memming, Semiconductor Electrochemistry, Wiley, 2015.
- [29] R. Krishnan, Fundamentals of Semiconductor Electrochemistry and Photoelectrochemistry, Encyclopedia of Electrochemistry, 2007.
- [30] Y. He, Q. He, L. Wang, C. Zhu, P. Golani, A.D. Handoko, X. Yu, C. Gao, M. Ding, X. Wang, F. Liu, Q. Zeng, P. Yu, S. Guo, B.I. Yakobson, L. Wang, Z.W. Seh, Z. Zhang, M. Wu, Q.J. Wang, H. Zhang, Z. Liu, Self-gating in semiconductor electrocatalysis, Nat. Mater. 18 (2019) 1098–1104.
- [31] K. Sulawan, C. Nawapong, Solvothermal Synthesis of CuInS<sub>2</sub> Nanoparticles in Ethylene Glycol-Water Medium and Their Photovoltaic Properties, Russ. J. Inorg. Chem. 64 (2019) 1469–1474.
- [32] J. Zhang, J. Li, Q. Zhang, D. Guo, Constructing a novel CuS/Cu<sub>2</sub>S Z-scheme heterojunction for highly-efficiency NIR light-driven antibacterial activity, Applied Surface Science 624 (2023), 156848.
- [33] B. Zhou, X. Zhang, P. Jin, X. Li, X. Yuan, J. Wang, L. Liu, Synthesis of In2.77S4 nanoflakes/graphene composites and their application as counter electrode in dyesensitized solar cells, Electrochim. Acta 281 (2018) 746–752.
- [34] Y. Chen, R. Huang, D. Chen, Y. Wang, W. Liu, X. Li, Z. Li, Exploring the Different Photocatalytic Performance for Dye Degradations over Hexagonal Znln<sub>2</sub>S<sub>4</sub> Microspheres and Cubic Znln<sub>2</sub>S<sub>4</sub> Nanoparticles, ACS Appl. Mater. Interfaces. 4 (2012) 2273–2279.
- [35] W. Liu, L. Lu, Q. Li, B. Wu, R. Zhang, W. Shi, P. Cheng, An Efficient and Stable MoS<sub>2</sub>/Zn<sub>0.5</sub>Cd<sub>0.5</sub>S Nanocatalyst for Photocatalytic Hydrogen Evolution, Chem. Eur. J. 26 (2020) 12206–12211.
- [36] M.S. Ahmad, H. He, Y. Nishina, Selective Hydrogenation by Carbocatalyst: The Role of Radicals, Org. Lett. 21 (2019) 8164–8168.
- [37] C.P. Andrieux, J. Pinson, The Standard Redox Potential of the Phenyl Radical/ Anion Couple, J. Am. Chem. Soc. 125 (2003) 14801–14806.
- [38] S.A. Akhade, N. Singh, O.Y. Gutiérrez, J. Lopez-Ruiz, H. Wang, J.D. Holladay, Y. Liu, A. Karkamkar, R.S. Weber, A.B. Padmaperuma, M.-S. Lee, G.A. Whyatt, M. Elliott, J.E. Holladay, J.L. Male, J.A. Lercher, R. Rousseau, V.-A. Glezakou, Electrocatalytic Hydrogenation of Biomass-Derived Organics: A Review, Chem. Rev. 120 (2020) 11370–11419.
- [39] L. Giorgi, E. Salernitano, T. Dikonimos Makris, R. Giorgi, E. Leoni, M.L. Grilli, N. Lisi, Titania nanotubes self-assembled by electrochemical anodization: Semiconducting and electrochemical properties, Thin Solid Films 601 (2016) 28–34
- [40] A. Hankin, F.E. Bedoya-Lora, J.C. Alexander, A. Regoutz, G.H. Kelsall, Flat band potential determination: avoiding the pitfalls, J. Mater. Chem. A 7 (2019) 26162–26176.
- [41] K. Koh, U. Sanyal, M.-S. Lee, G. Cheng, M. Song, V.-A. Glezakou, Y. Liu, D. Li, R. Rousseau, O.Y. Gutiérrez, A. Karkamkar, M. Derewinski, J.A. Lercher, Electrochemically Tunable Proton-Coupled Electron Transfer in Pd-Catalyzed Benzaldehyde Hydrogenation, Angew. Chem., Int. Ed. Engl. 59 (2020) 1501–1505.
- [42] I.K.M. Yu, F. Deng, X. Chen, G. Cheng, Y. Liu, W. Zhang, J.A. Lercher, Impact of hydronium ions on the Pd-catalyzed furfural hydrogenation, Nat. Commun. 13 (2022) 7154.
- [43] A. Takahashi, F.H. Yang, R.T. Yang, Aromatics/Aliphatics Separation by Adsorption: New Sorbents for Selective Aromatics Adsorption by π-Complexation, Ind. Eng. Chem. Res. 39 (2000) 3856–3867.

Semiconductor Nanosheets for Electrocatalytic Self-coupling of Benzaldehyde to Hydrobenzoin

Li Gong<sup>a,b</sup>, Chao Yue Zhang<sup>a,c\*</sup>, Xiao Mu<sup>d</sup>, Xu Han<sup>e</sup>, Junshan Li<sup>f</sup>, Jordi Arbiol<sup>e,h</sup>, Jin Yuan Zhou<sup>c</sup>, Tanja Kallio<sup>g</sup>, Paulina R. Martínez-Alanis<sup>a\*</sup>, Andreu Cabot<sup>a,h\*</sup>

- a\*. Catalonia Institute for Energy Research IREC Sant Adrià de Besòs, Barcelona 08930, Spain E-mail: chzhang@irec.cat, pmartinez@irec.cat, acabot@irec.cat
- b\*. Faculty of Chemistry, University of Barcelona, Barcelona 08028, Spain.
- c\*. Key Laboratory for Magnetism and Magnetic Materials of the Ministry of Education & School of Physical Science & Technology, Lanzhou University, Lanzhou 730000, China.
- d. Faculty of Chemistry, Fudan University, Shanghai 200438, China.
- e. Catalan Institute of Nanoscience and Nanotechnology (ICN2), CSIC and BIST, Campus UAB, Bellaterra,08193, Barcelona, Spain.
- f. Institute of Advanced Study, Chengdu University, Chengdu, 610106, China
- g. Department of Chemistry and Materials Science, Aalto University School of Chemical Engineering, P.O.Box 16100, FI-00076 Aalto, Finland.
- h. ICREA, Pg. Lluís Companys 23, 08010, Barcelona, Spain

E-mail addresses: chzhang@irec.cat (C.Y. Zhang); pmartinez@irec.cat (P. R. Martínez-Alanis), acabot@irec.cat (Andreu Cabot)

<sup>\*</sup>Corresponding authors.

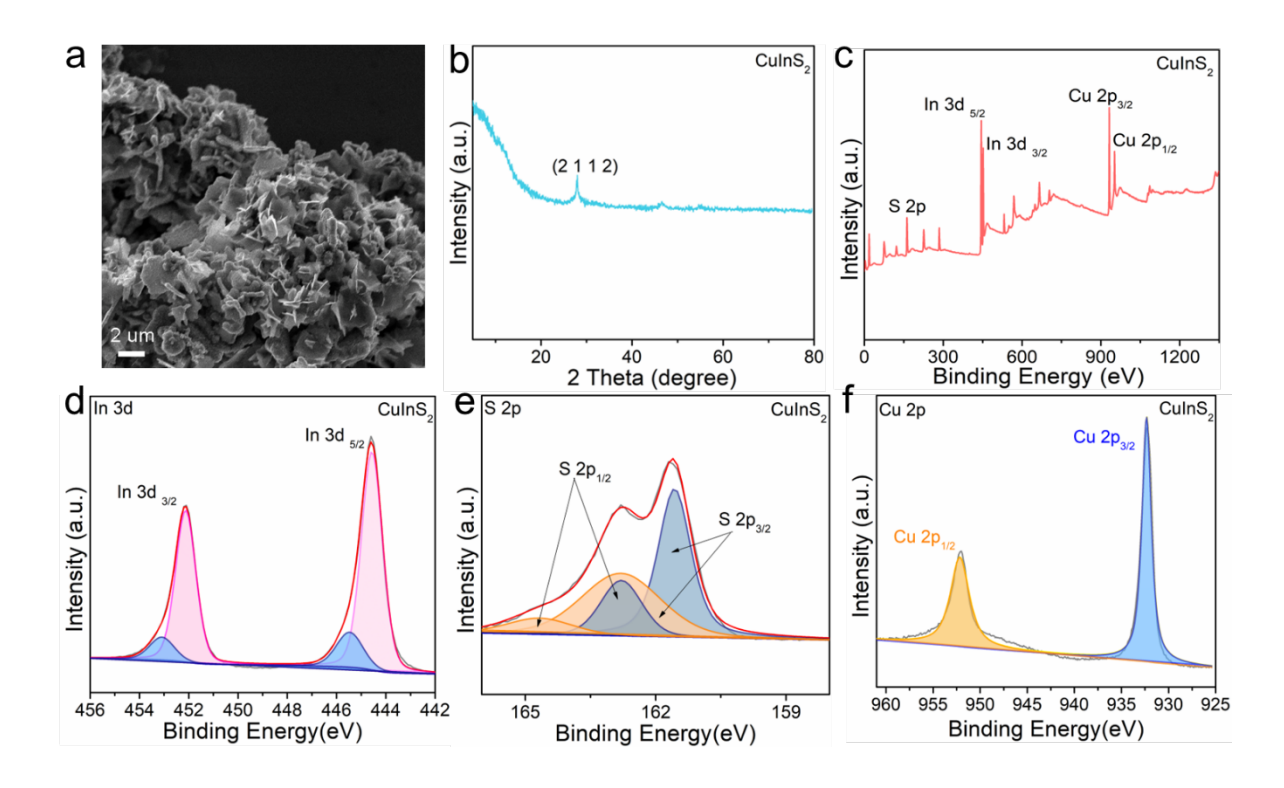


**Figure S1**. (a) SEM images; (b) XRD pattern; XPS spectra of (c) full-scan; (d) In 3d; (e) S 2p and (f) Cu 2p of semiconductor CuInS<sub>2</sub>

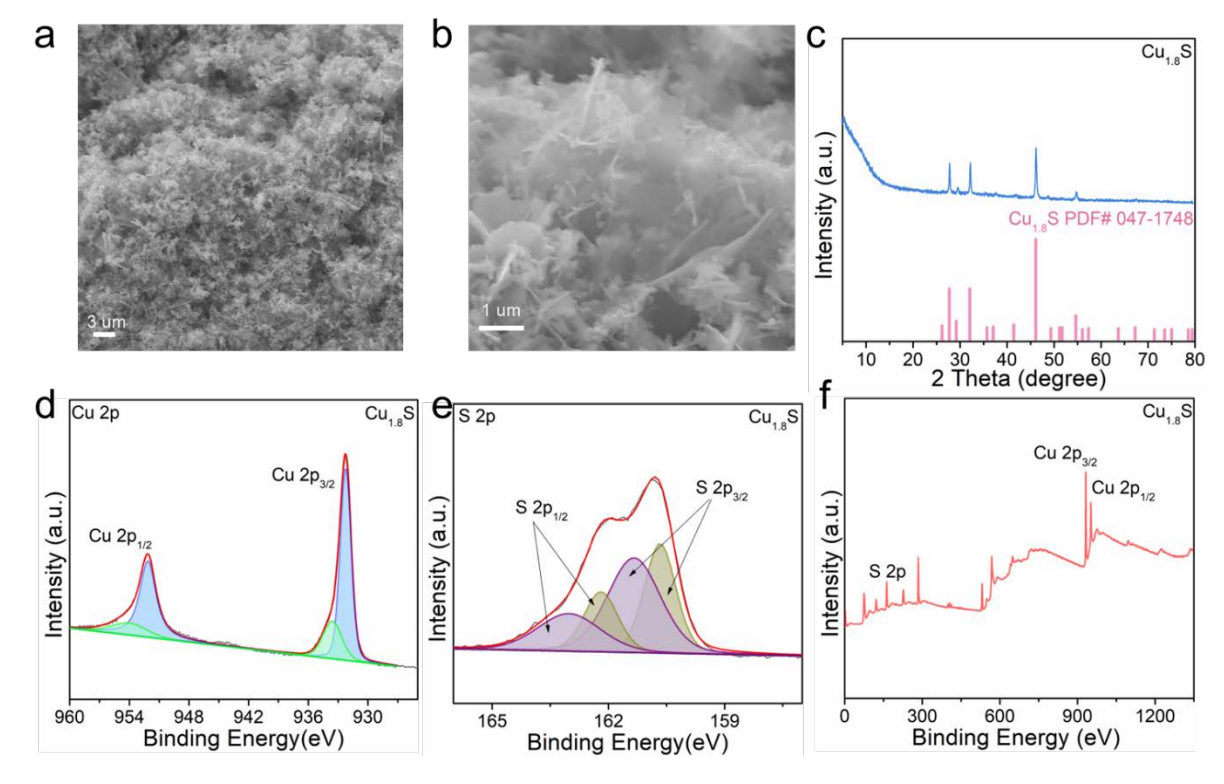


**Figure S2**. (a-b) SEM images; (c) XRD pattern; XPS spectra of (d) Cu 2p; (e) S 2p and (f) full-scan of semiconductor Cu<sub>1.8</sub>S.

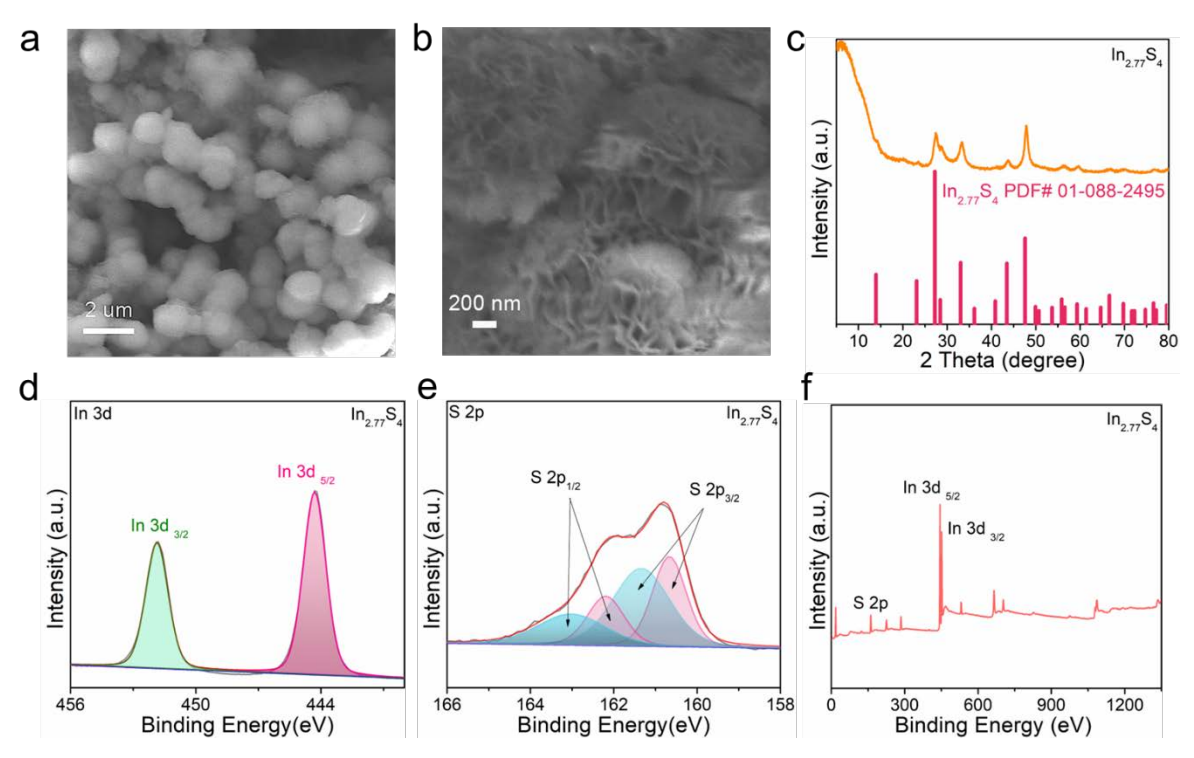


**Figure S3**. (a-b) SEM images; (c) XRD pattern; XPS spectra of (d) In 3d; (e) S 2p and (f) full-scan of semiconductor In<sub>2.77</sub>S<sub>4</sub>.

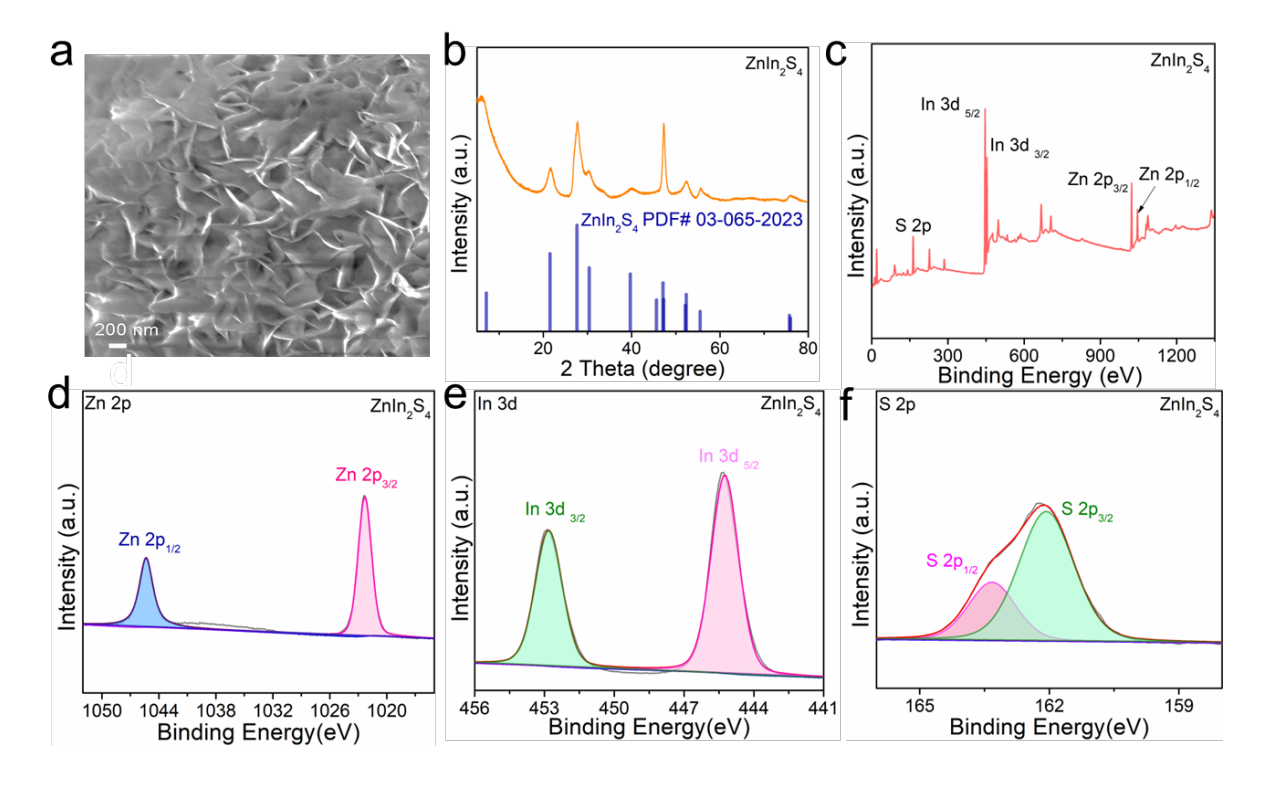


**Figure S4**. (a) SEM image; (b) XRD pattern; XPS spectra of (c) full-scan; (d) Zn 2p; (e) In 3d and (f) S 2p and of semiconductor ZnIn<sub>2</sub>S<sub>4</sub>

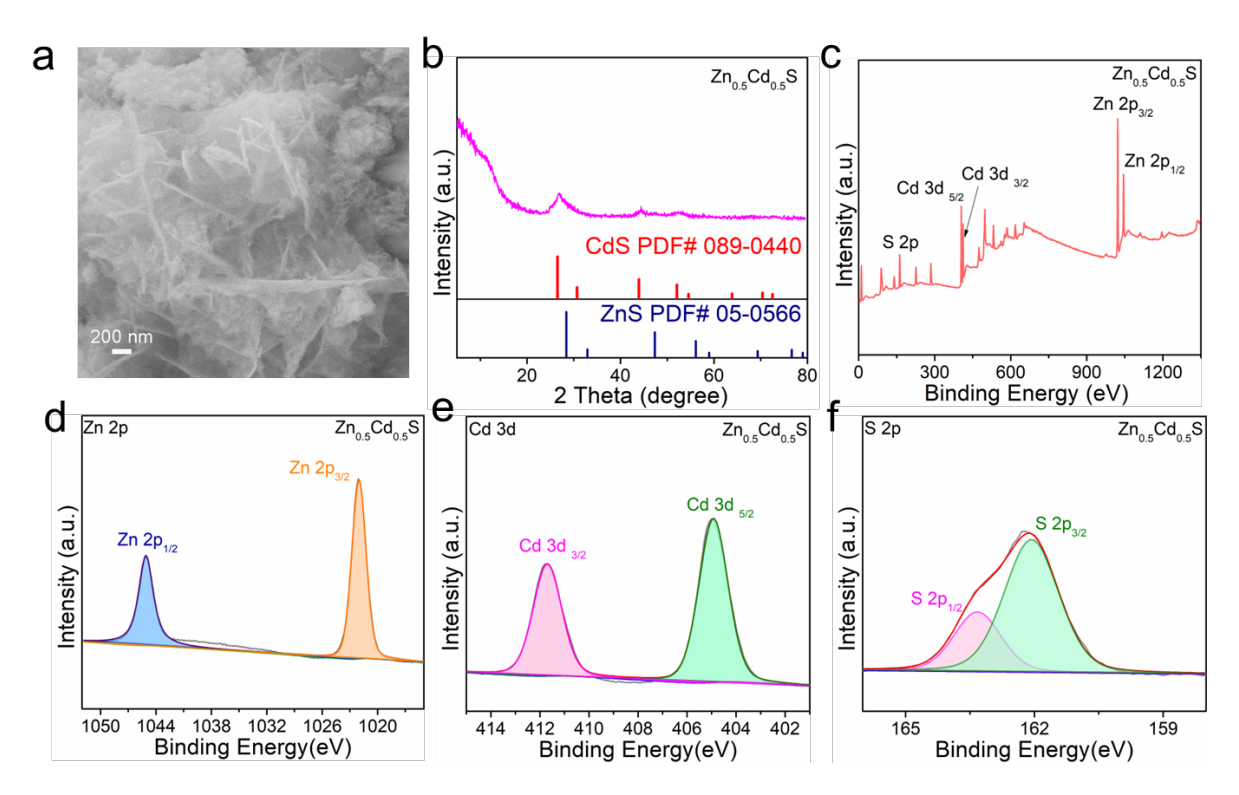


**Figure S5**. (a) SEM image; (b) XRD pattern; XPS spectra of (c) full-scan; (d) Zn 2p; (e)Cd 3d and (f) S 2p and of semiconductor  $Zn_{0.5}Cd_{0.5}S$ 

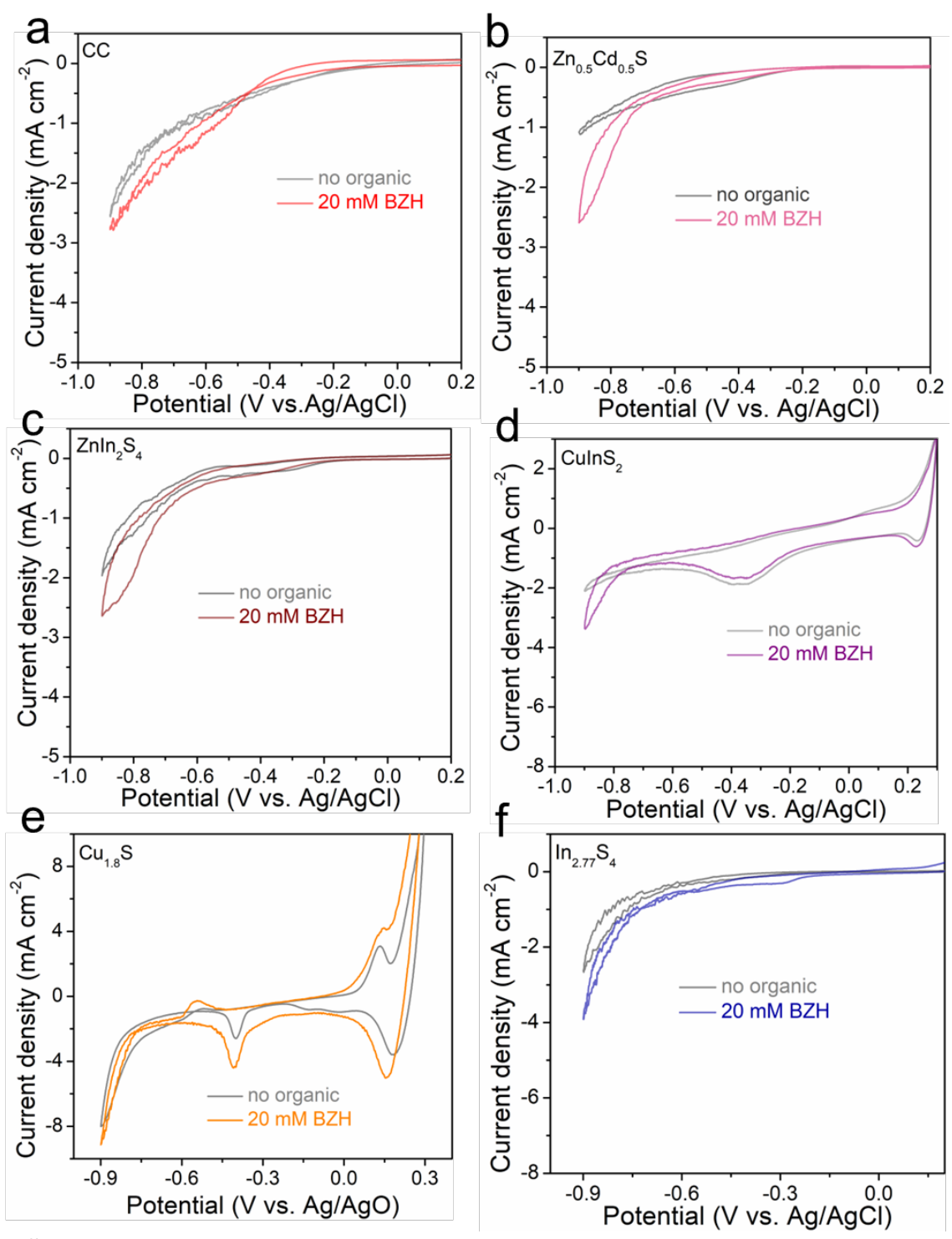


**Figure S6.** CV curves over different cathodic materials with no organic or with 20 mM benzaldehyde in 1 M sodium acetate-acetic acid solution, pH 5.3.

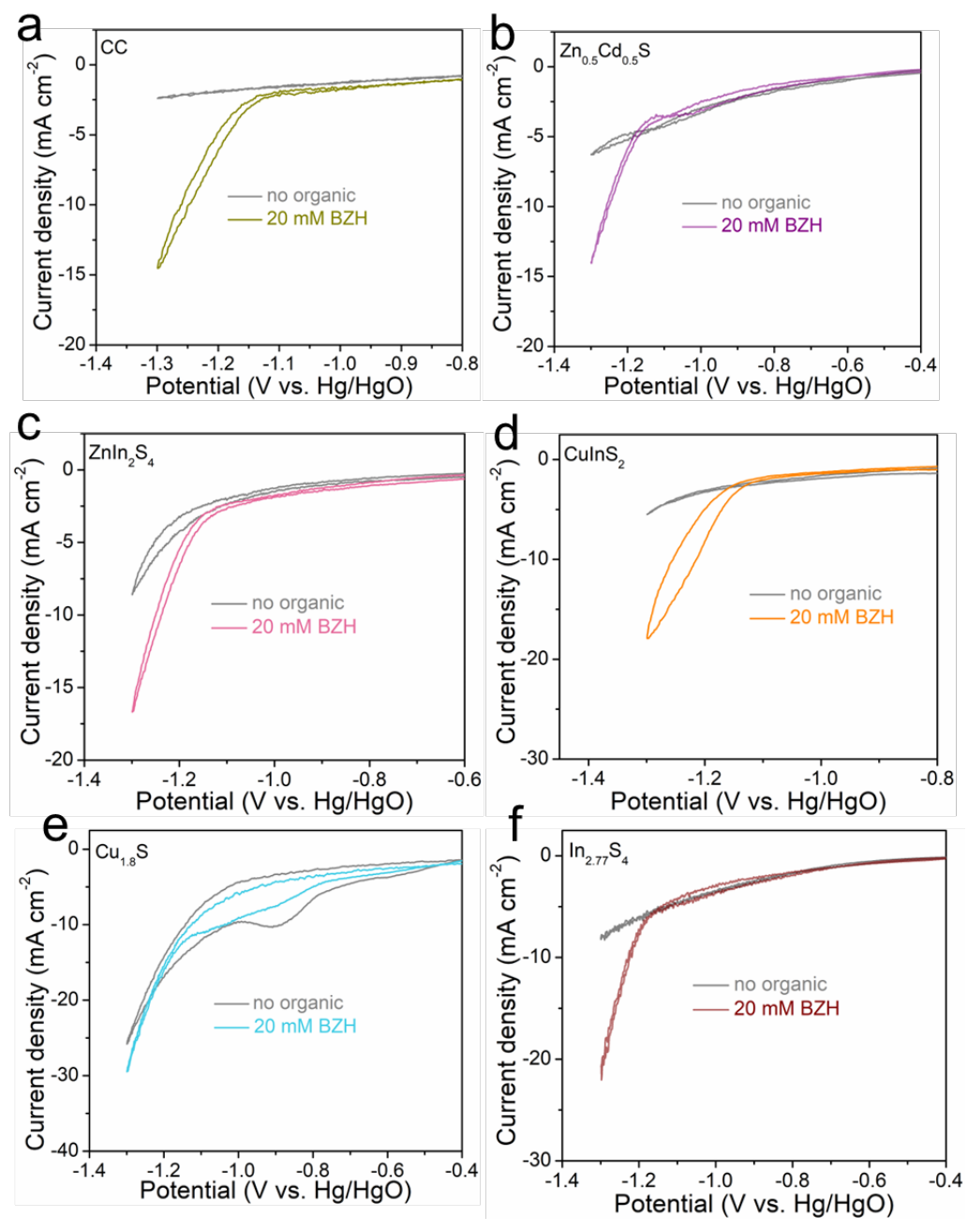


**Figure S7.** CV curves over different cathodic materials with no organic or with 20 mM benzaldehyde in 1 M potassium carbonate-potassium bicarbonate solution, pH 9.0.

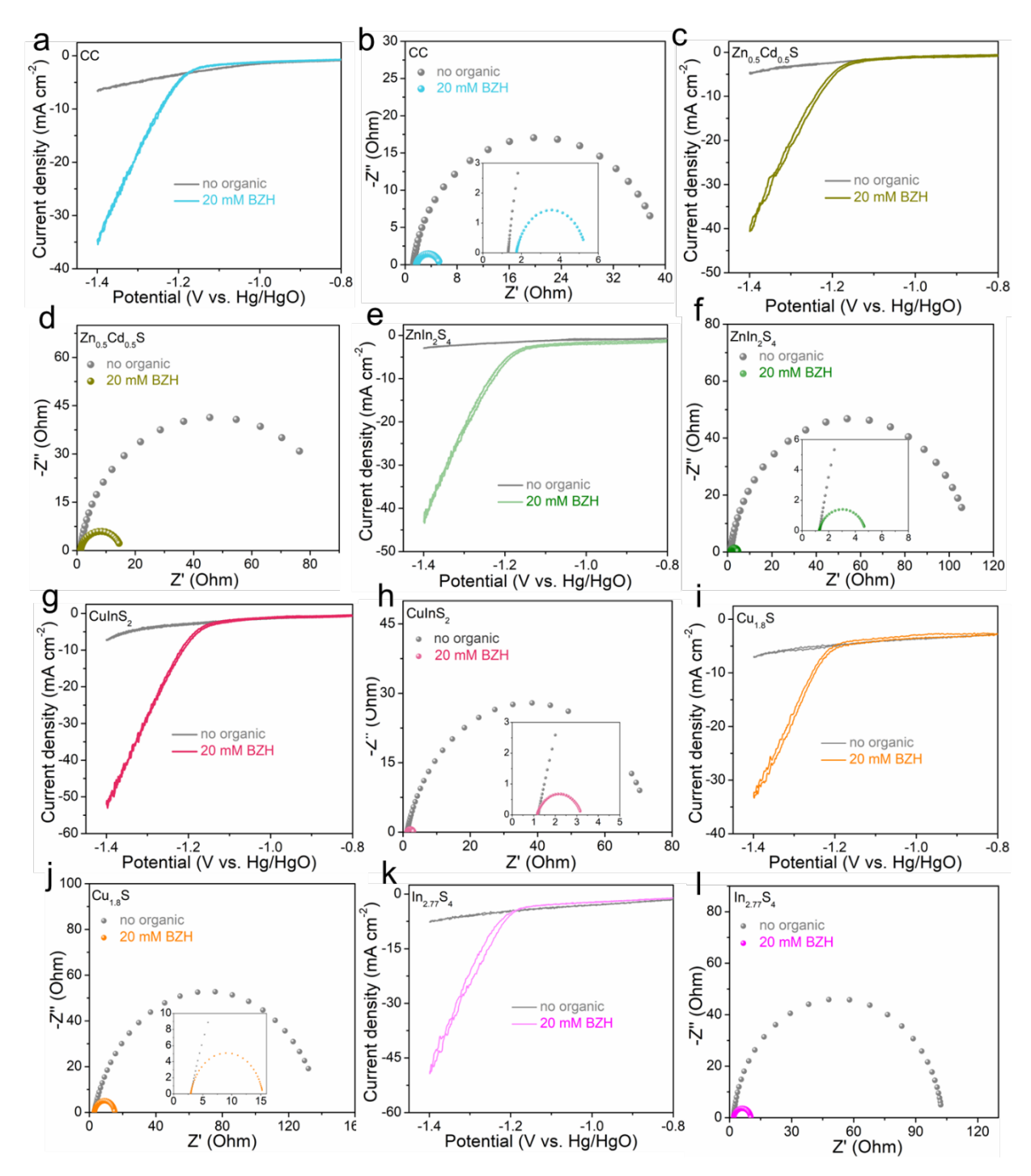


**Figure S8.** CV curves and Nyquist plots over different cathodic materials with no organic or with 20 mM benzaldehyde in 1 M KOH, pH 14.

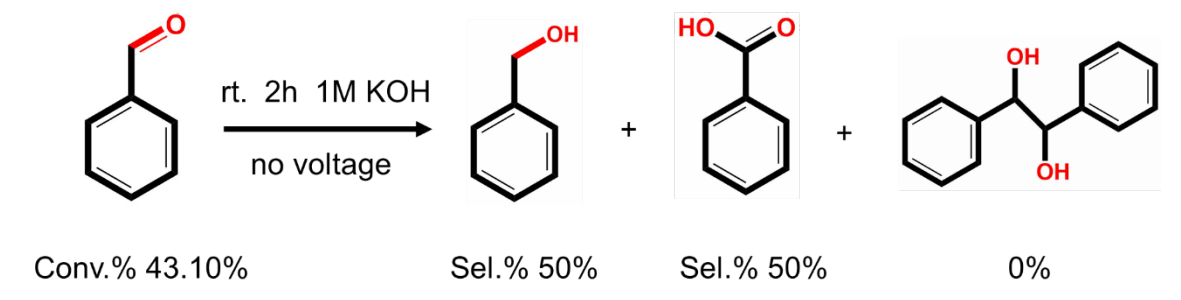


**Figure S9.** Conv.% and sel.% of benzaldehyde when using CIS as a catalyst with no applied potential.

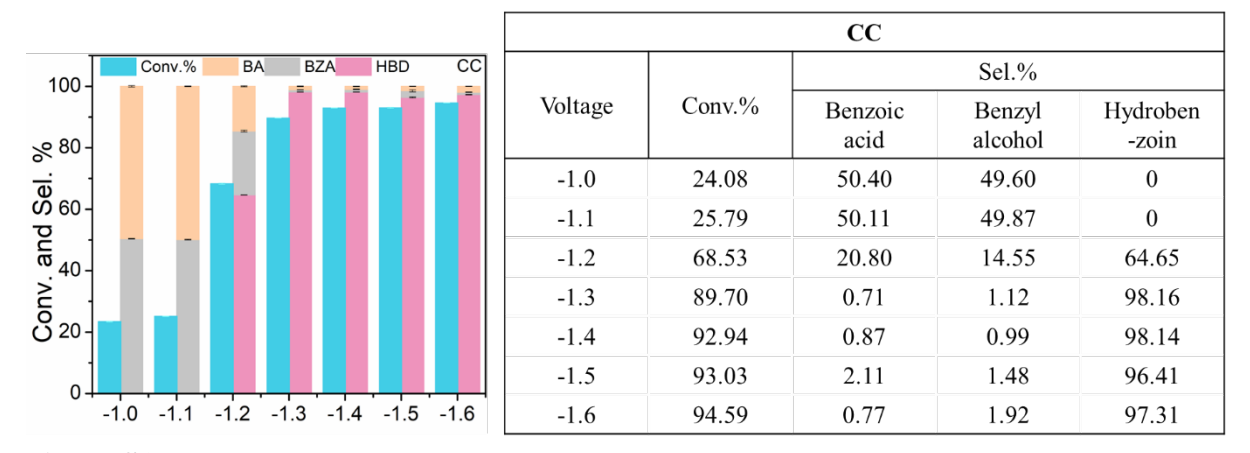


**Figure S10.** potential-dependent conversion yield (conv. %) and selectivity (sel.%) over carbon cloth for 2 h.

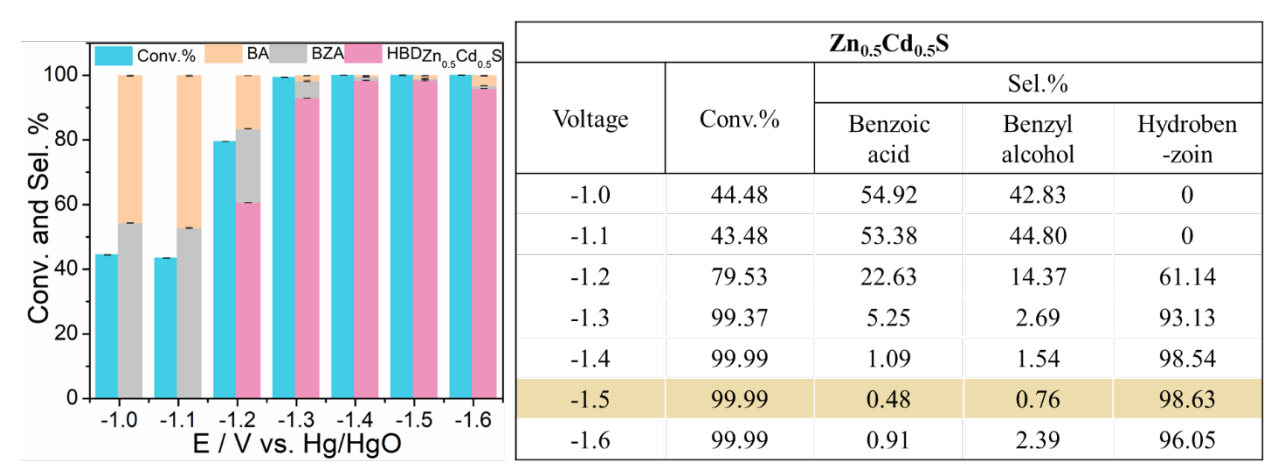


**Figure S11.** Potential-dependent conversion yield (conv. %) and selectivity (sel.%) over Zn<sub>0.5</sub>Cd<sub>0.5</sub>S for 2 h.

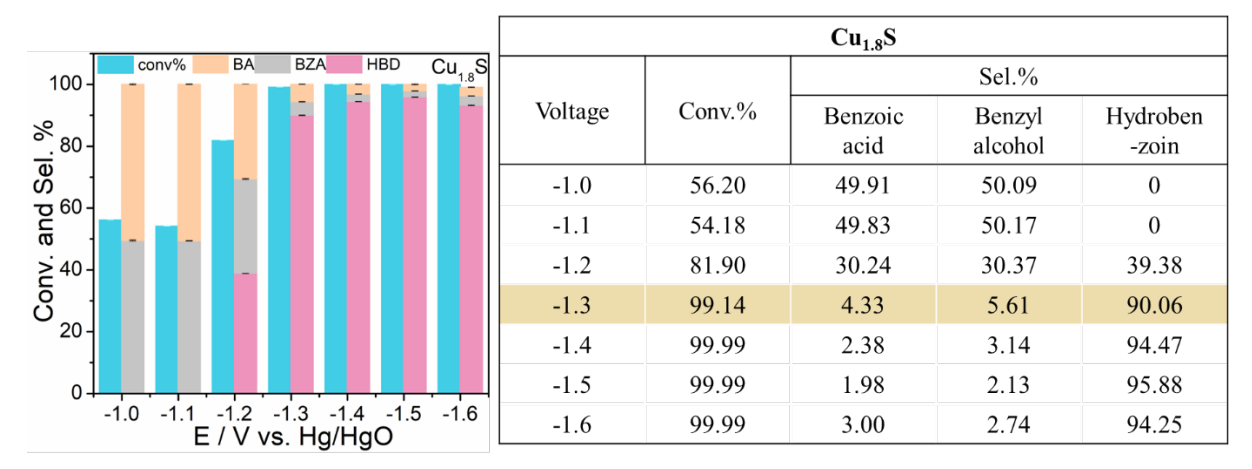


**Figure S12.** Potential-dependent conversion yield (conv. %) and selectivity (sel.%) over Cu<sub>1.8</sub>S for 2 h.

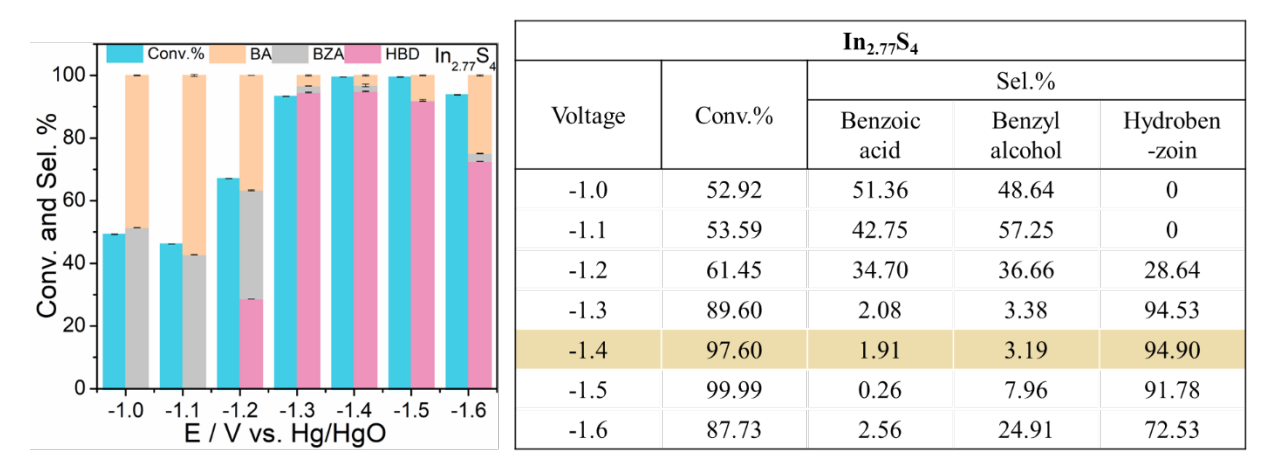


**Figure S13.** Potential-dependent conversion yield (conv. %) and selectivity (sel.%) over In<sub>2.77</sub>S<sub>4</sub> for 2 h.

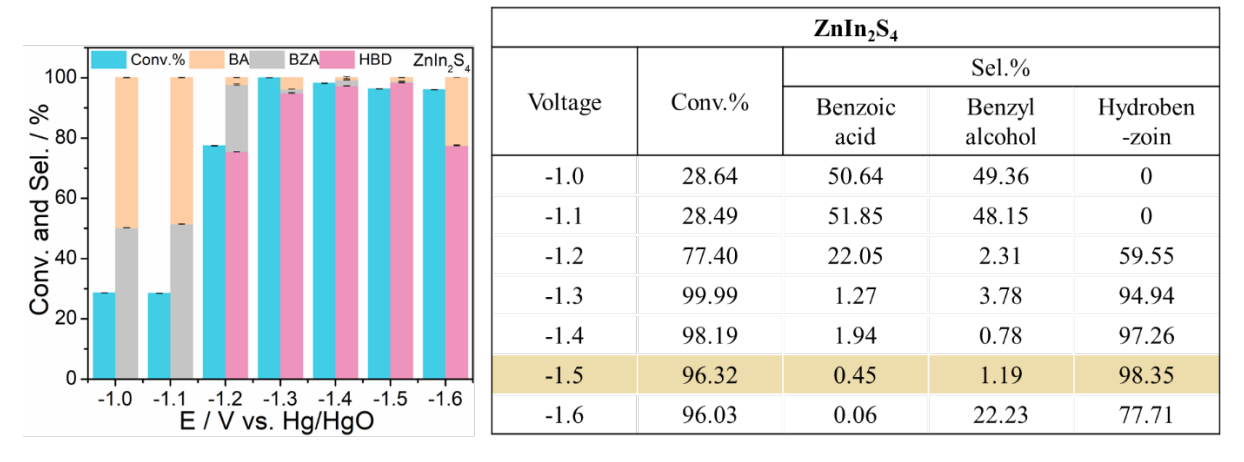


**Figure S14.** Potential-dependent conversion yield (conv. %) and selectivity (sel.%) over ZnIn<sub>2</sub>S<sub>4</sub> for 2 h.

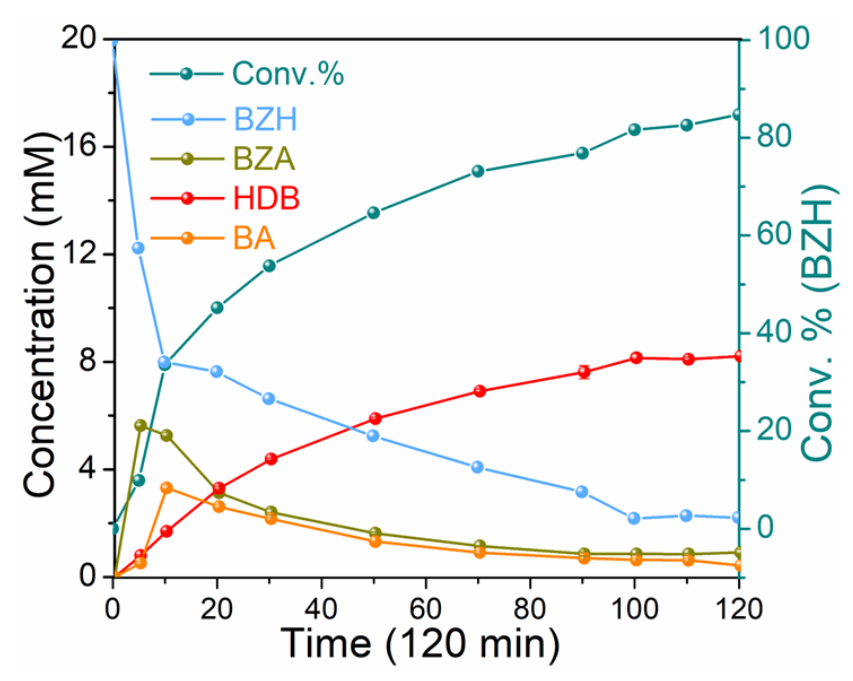


**Figure S15.** Time-dependent transformation of 20 mM benzaldehyde over CC at -1.3~V vs. Hg/HgO.

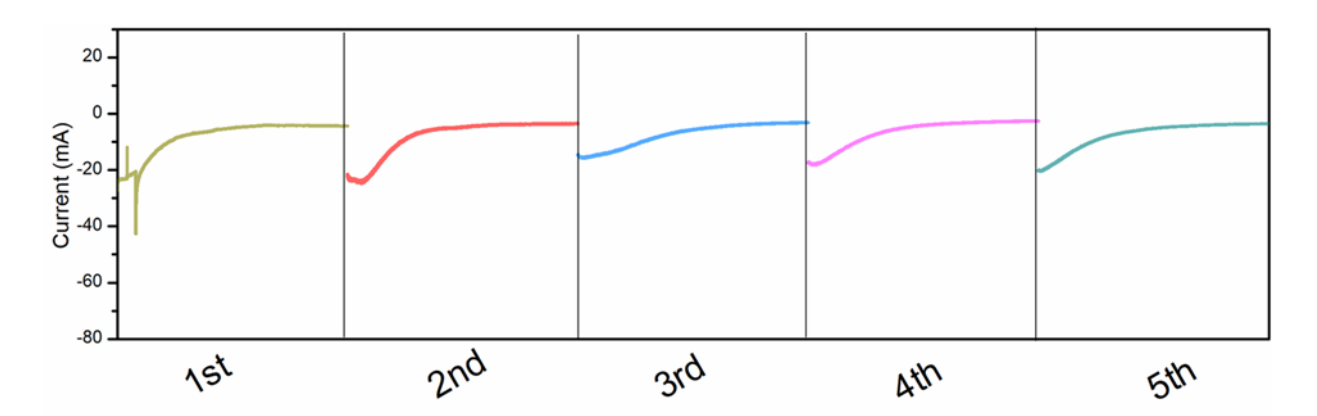


Figure S16. I-t curves for 5 times over CIS at -1.3 V vs. Hg/HgO in pH 14 condition.



**Figure S17.** BZH to HDB conversion and selectivity for 5 times over CIS at -1.3 V vs. Hg/HgO in pH 14 condition.

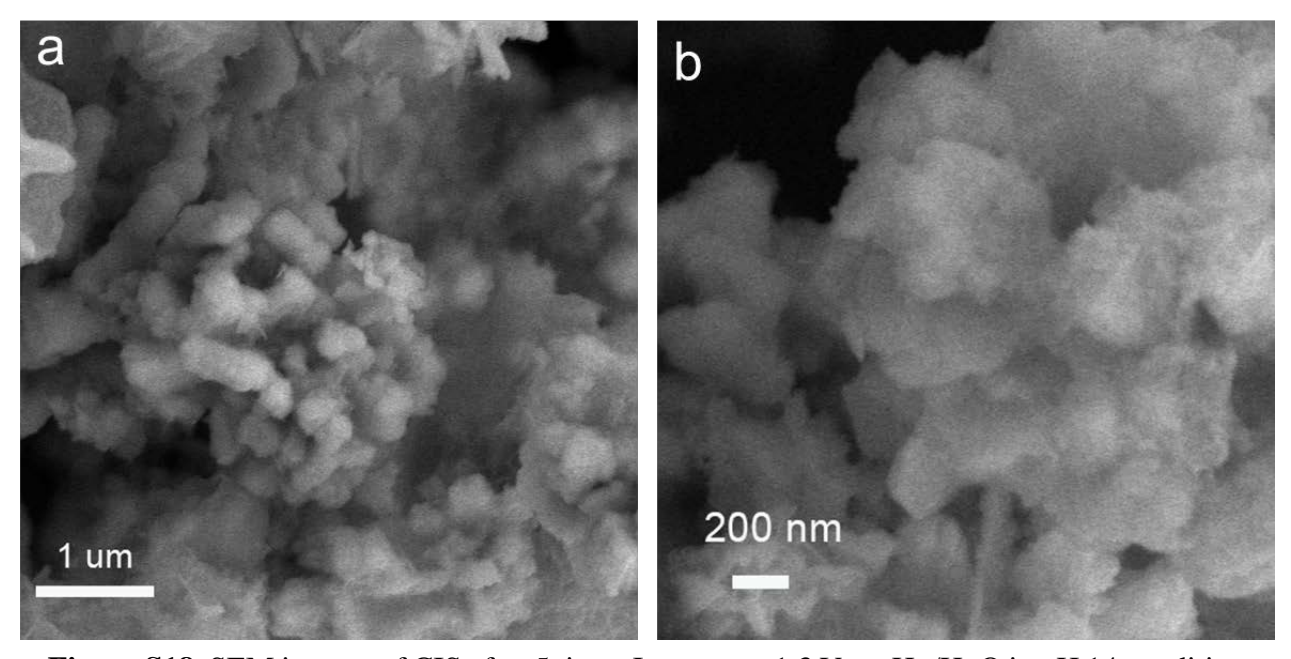
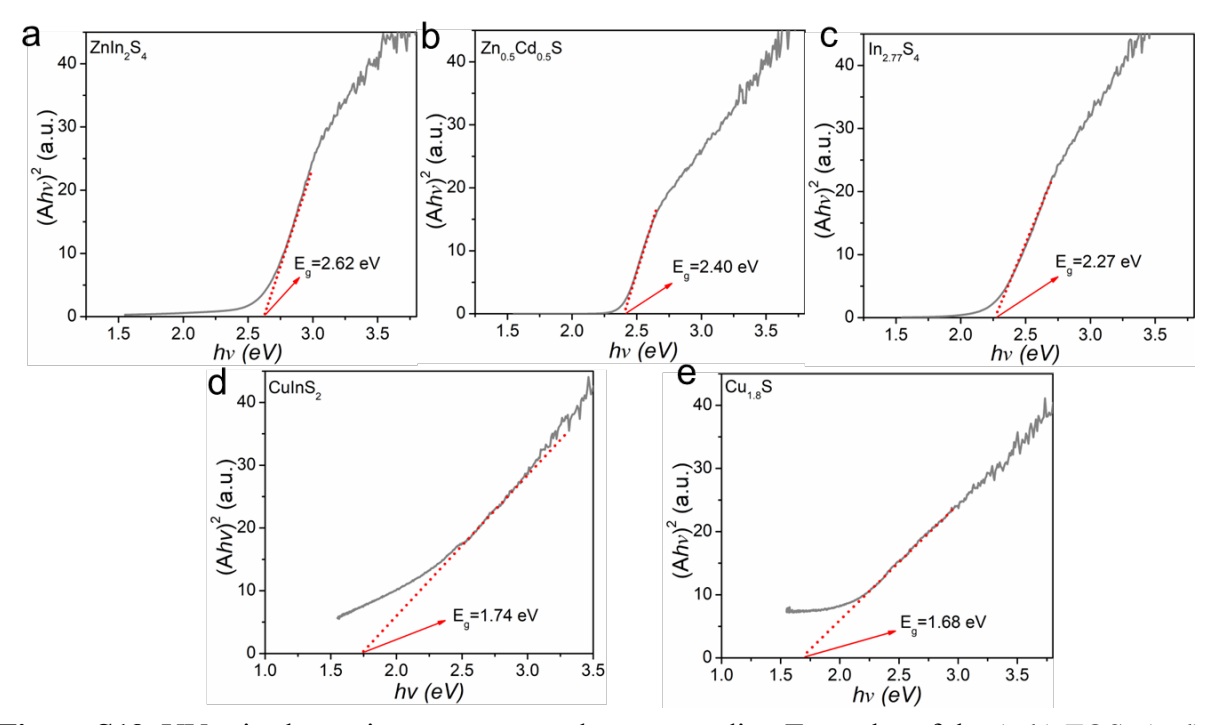


Figure S18. SEM images of CIS after 5 times I-t tests at -1.3 V vs. Hg/HgO in pH 14 condition.



**Figure S19.** UV—vis absorption spectrum and corresponding Tauc plot of the (a-b) ZOS; (c-d) ZCS; (e-f) IS; (g-h) CIS and (i-j) CS.

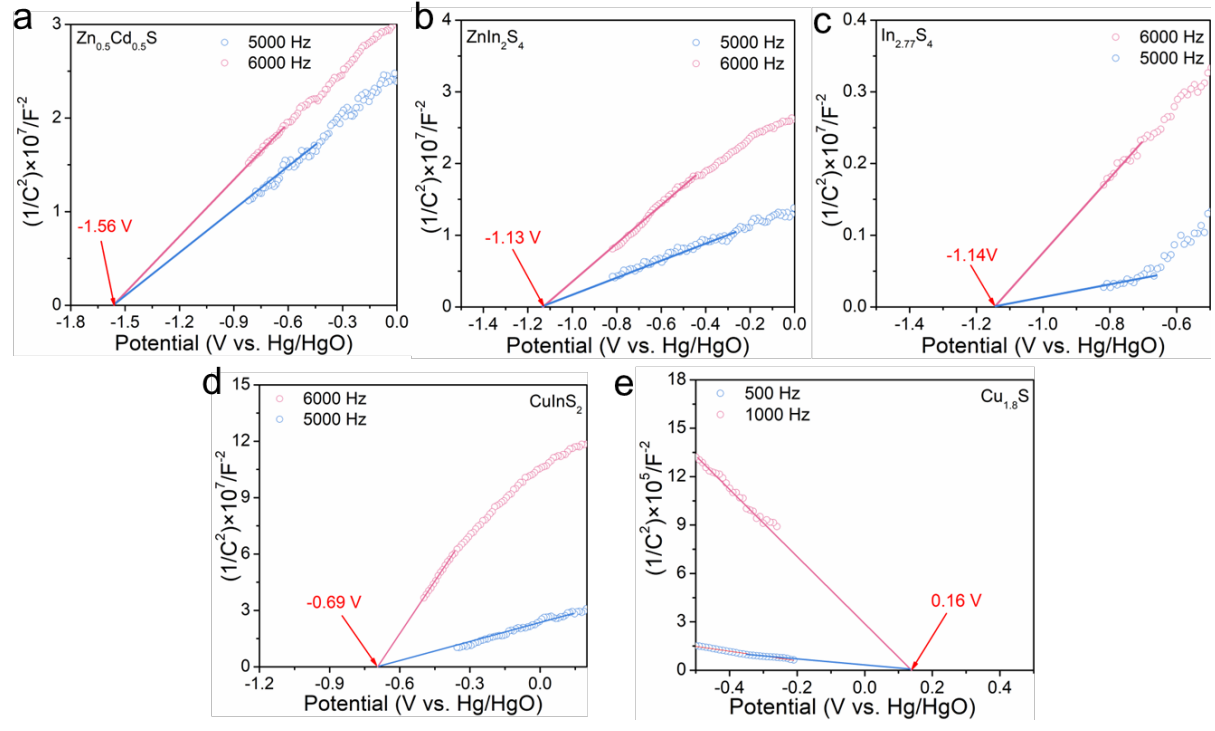
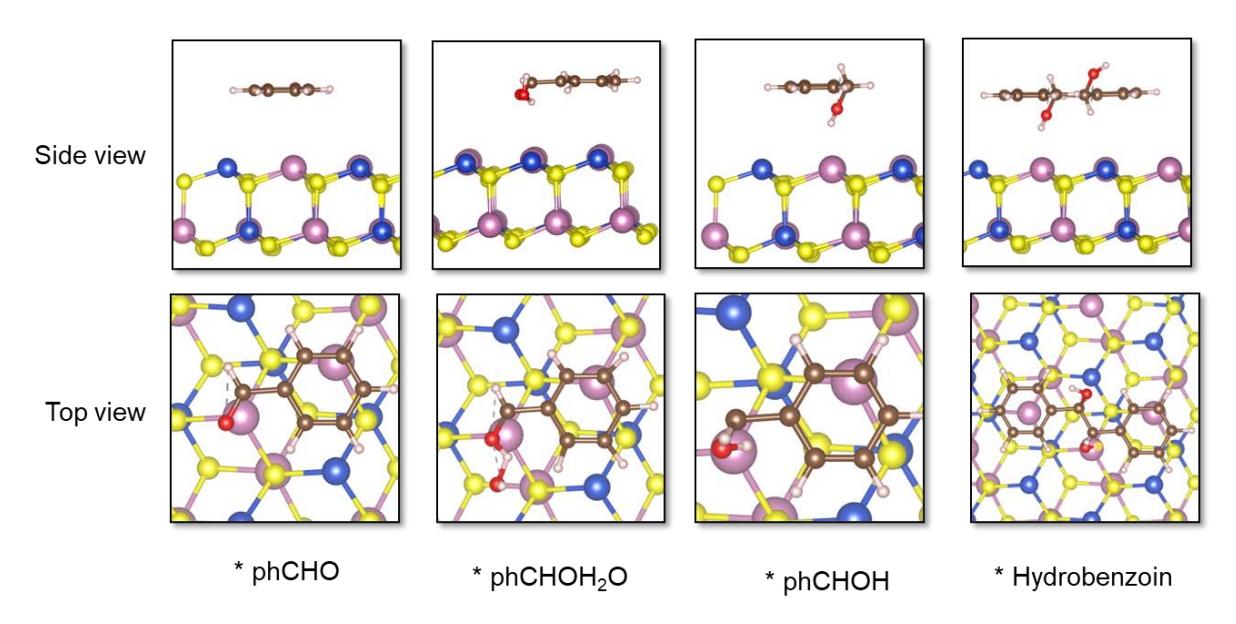
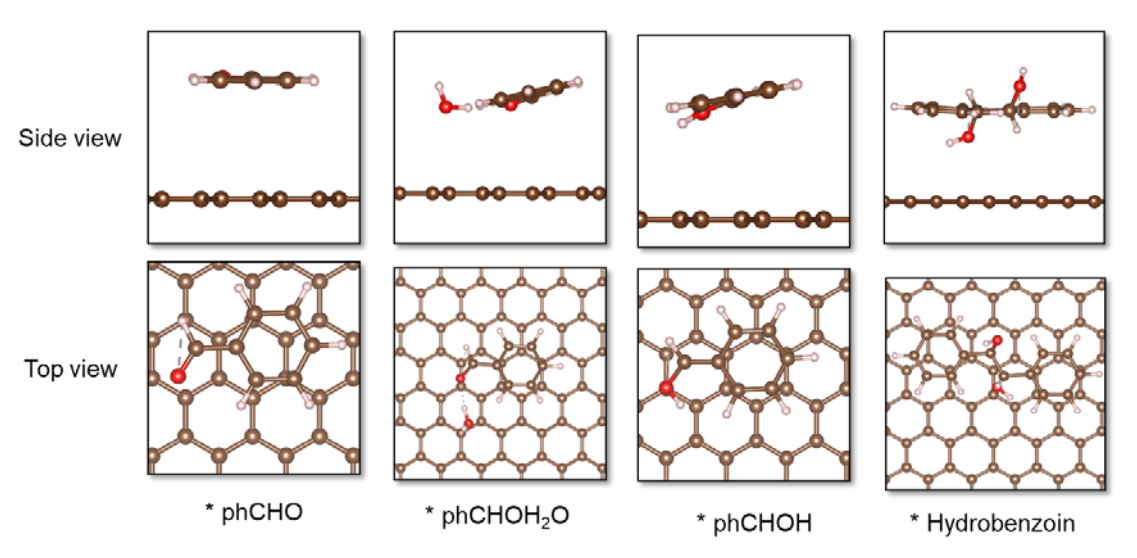


Figure S20. Mott-Schottky curves of (a) ZCS; (b) ZIS; (c) IS; (d) CIS and (e) CS.



**Figure S21**. Structures of the phCHO, phCHOH and hydrobenzoin on CuInS<sub>2</sub>, the atoms are represented such as spheres, in the following color code, In =purple, S=yellow, Cu=blue, H=white, C=grey, and O=red



**Figure S22.** Structures of the phCHO, phCHOH and hydrobenzoin on graphic carbon. the atoms are represented such as spheres, in the following color code, H=white, C=grey, and O=red.

**Table S1.** Elements weight percentage (wt.%) and atomic percentage (at.%) of materials ZCS, ZIS, CIS, IS and CS as obtained by EDS.

	ZCS		ZIS		CIS		IS		CS	
	wt %	at %								
S K	28	36	30	56	29	52	32	62	23	36
Cu K	-	-	-	-	30	27	-	-	77	64
In K	-	-	50	26	41	21	68	37	-	-
Zn K	24	16	20	18	-	-	-	-	-	-
Cd K	48	48	-	-	-	-	-	-	-	-

**Table S2.** Elements weight percentage (wt.%) and atomic percentage (at.%) of materials ZCS, ZIS, CIS, IS and CS as obtained by XPS.

	ZCS		ZIS		CIS		IS		CS	
	wt %	at %								
S K	19	36	20	44	24	48	25	55	23	37
Cu K	-	-	-	-	22	22	-	-	77	63
In K	-	-	62	37	54	30	75	45	-	-
Zn K	46	44	18	19	-	-	-	-	-	-
Cd K	35	20	-	-	-	-	-	-	-	-

**Table S3.** Elements weight percentage (wt.%) and atomic percentage (at.%) of materials ZCS, ZIS, CIS, IS and CS as obtained by ICP-MS.

	ZCS		ZIS		CIS		IS		CS	
	wt %	at %								
S K	31	55	28	52	25	47	34	65	27	43
Cu K	-	-	-	-	32	30	-	-	73	57
In K	-	-	46	24	43	23	66	35	-	-
Zn K	26	23	26	24	-	-	-	-	-	-
Cd K	43	22	-	-	-	-	-	-	-	-

**Table S4.** Potential-dependent conversion (conv. %) and selectivity (sel.%) over CIS for 2 h.

CuInS <sub>2</sub>								
		Sel.%						
Voltage	Conv.%	Benzoic acid	Benzyl alcohol	Hydroben -zoin				
-1.0	60.37	51.03	48.97	0				
-1.1	56.48	49.93	50.07	0				
-1.2	83.10	16.38	15.22	68.10				
-1.3	99.83	0.95	3.15	98.46				
-1.4	99.99	0.98	3.01	96.01				
-1.5	99.99	0.25	8.13	91.62				
-1.6	97.61	1.42	15.88	82.70				

**Table S5.** Results Band gap, E <sub>fb</sub> in the 1M KOH at room temperature and the experimental optimal applied voltages (E <sub>optimized</sub>) towards self-coupling of benzaldehyde on different semiconductor electrodes ZCS, ZIS, CIS, IS, and CS.

	ZIS	ZCS	IS	CIS	CS
Band gap (eV)	2.62	2.40	2.27	1.74	1.68
E <sub>fb</sub> (V vs. Hg/HgO)	-1.13	-1.56	-1.14	-0.69	0.16
E optimization (V vs. Hg/HgO)	-1.5	-1.5	-1.4	-1.3	-1.3*

## Chapter 6

# Electrochemical Reduction of benzaldehyde into Hydrobenzoin on OAm-capped Cu<sub>2</sub>S

## 6. Electrochemical Reduction of benzaldehyde into Hydrobenzoin on OAm-capped Cu<sub>2</sub>S

The purpose of this study was to investigate the electrocatalytic reduction of biomass-derived BZH using Cu<sub>2</sub>S nanoparticles with capped ligands as catalysts. Specifically, the study aimed to understand the influence of surface chemistry modifications, particularly with oleylamine (OAm), on the selective production of BA and HDB. The research focused on optimizing reaction conditions, including pH, temperature, and electrode potential, to enhance the selectivity towards either BA or HDB, thus providing insights for designing efficient and selective electrocatalysts for sustainable chemical synthesis.

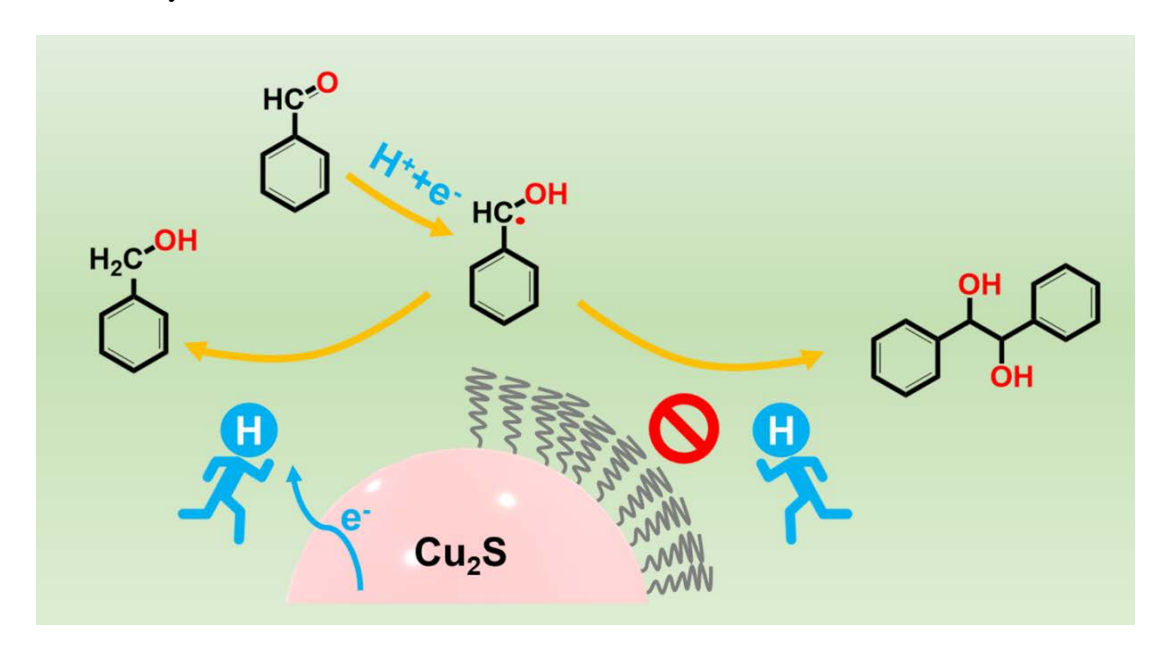


Figure 6-1. Graphic abstract.

#### The study found that:

- 1. Modifying the surface of Cu<sub>2</sub>S nanoparticles with OAm significantly influenced the selectivity of the BZH reduction reaction. Bare Cu<sub>2</sub>S favored the production of BA, while OAm-capped Cu<sub>2</sub>S promoted HDB formation.
- 2. The selectivity towards BA or HDB was highly dependent on the reaction conditions. High HER overpotential elements improved the selectivity towards HDB.

- 3. Alkaline conditions (pH 9.0) resulted in higher selectivity for HDB compared to acidic conditions (pH 5.2).
- 4. The presence of OAm inhibited hydrogen adsorption on the catalyst surface, reducing the formation of high-energy state Had and favoring the formation of HDB through an outer-sphere reaction mechanism. Conversely, in the absence of OAm, BA production was favored due to the L-H mechanism involving adsorbed hydrogen.

These findings highlight the importance of catalyst surface modifications and reaction environment in controlling product selectivity in the electrocatalytic reduction of biomass-derived compounds.

As previously said, the reaction for obtaining HDB is an outer-sphere reaction with ketyl radical self-coupling. The radical formation steps in different pH:

In acid media: 
$$ph - HC = O - H_3O^+ + e^- \rightarrow ph(OH)HC^{\bullet} + H_2O$$

In alkaline media: 
$$ph - HC = 0 - H_2O + e^- \rightarrow ph(OH)HC + OH^-$$

The common point is obtaining an electron from the electrode. Different point is that in acidic condition, H proton comes from a hydronium ion splitting. in alkaline condition, H proton comes from the H<sub>2</sub>O molecule splitting. Obviously, in acidic condition, the energy is lower, but in practice, the selectivity for HDB is higher under alkaline conditions. Another thing is for the element's choices, semimetals are commemly employed since they have high overpotential towards HER. Even though, when use semimetals, the reaction still need conduct at low voltage, when applied higher negative voltage, selectivity towards hydrobenzoin decreased. These experimental phenomena can all be explained by the structure of the EDL. Even when using semimetal materials, as the negative voltage increases, electrons accumulate on the electrode. To reach equilibrium, positive ions, specifically hydrogen ions in the aqueous solution, will approach and gain electrons, combining with free radicals to form alcohol products. At this point, the selectivity for the coupling product decreases. Our goal is to solve the question: How selectivity for HDB can be independent on pH and voltages?

The solution lies in the modification of the EDL. Given our research group's extensive experience with colloidal synthesis methods, I propose leveraging this expertise to

prepare the materials for our study. Colloidal synthesis offers precise control over the size, shape, and surface chemistry of nanoparticles, which can be crucial for optimizing their catalytic properties.

In fact, the initial design of this work aimed to be more comprehensive and complex. We hoped that the ligands be various as hydrophilic/hydrophobic, with different chain lengths, or aromatic ring modifications on the catalyst surface. However, after a considerable amount of exploration, I was unsuccessful in achieving ligand exchange. Consequently, we retained only the most conclusive and reasonable parts of the study.

In this work, I prepared the materials, performed XRD, SEM, and FTIR characterization, and processed the corresponding data. Additionally, I handled the XPS data processing, conducted the electrochemical tests, and identified the products using HPLC along with processing the resulting data. The initial draft of the paper was written by me under the guidance and supervision of Pro. Dr. Andreu Cabot and Dr. Paulina R. Martínez-Alanis. Some tests and characterizations were completed by other collaborators.

## Influence of the catalyst surface chemistry on the electrochemical self-coupling of biomass-derived benzaldehyde into hydrobenzoin

Received 00th January 20xx, Accepted 00th January 20xx

DOI: 10.1039/x0xx00000x

Li Gong<sup>a,b</sup>, Shiling Zhao<sup>c</sup> Jing Yu<sup>a,d</sup>, Junshan Li<sup>e</sup>, Jordi Arbiol<sup>d,h</sup>, Tanja Kallio<sup>f</sup>, Mariano Calcabrini<sup>g</sup>, Paulina R. Martínez-Alanis<sup>a</sup>\*, Maria Ibáñez<sup>g</sup>, Andreu Cabot<sup>a,h</sup>\*

The electroreduction of biomass-derived benzaldehyde (BZH) provides a potentially cost-effective route to produce benzyl alcohol (BA). This reaction competes with the electrochemical self-coupling of BZH to hydrobenzoin (HDB), which holds significance as a biofuel. Herein, we demonstrate the selectivity towards one or the other product strongly depends on the surface chemistry of the catalyst, specifically on its ability to adsorb hydrogen, as showcased with Cu<sub>2</sub>S electrocatalysts. We particularly analyze the effect of surface ligands, oleylamine (OAm), on the selective conversion of BZH to BA or HDB. The effect of the electrode potential, electrolyte pH, and temperature are studied. Results indicate that bare Cu<sub>2</sub>S exhibits higher selectivity towards BA, while OAm-capped Cu<sub>2</sub>S promotes HDB formation. This difference is explained by the competing adsorption of protons and BZH. During the BZH electrochemical conversion, electrons first transfer to the C in the C=O group to form a ketyl radical. Then the radical either couples with surrounding H<sup>+</sup> to form BA or self-couple to produce HDB, depending on the H<sup>+</sup> availability that is affected by the electrocatalyst surface properties. The presence of OAm inhibits the H adsorption on the electrode surface therefore reducing the formation of high-energy state H<sub>ad</sub> and its combination with ketyl radicals to form BA. Instead, the presence of OAm promotes the outer sphere reaction for obtaining HDB.

#### 1. Introduction

Addressing the environmental crisis requires transitioning toward clean and zero-carbon energies on both the supply and consumption fronts, alongside the adoption of sustainable and efficient chemical synthesis methods. <sup>1,2</sup> Electrocatalysis enables precise control over reaction conditions and facilitates the use of mild, sustainable, and energy-efficient processes. <sup>3-10</sup> This enables fine-tuning reaction products through easily modifiable parameters, such as the electrode potential and current density, for the eco-friendly synthesis of complex molecules with unprecedented efficiency. <sup>11-13</sup> In particular, the electrocatalytic reduction of organic compounds is a field of significant interest and broad application potential.

Despite their high economic potential, the industrialization of electrocatalytic organic reduction processes for the valorization of biomass-derived feedstocks is not widely extended. This is due to their notable complexity and challenging optimization, which arises from the intricate nature of organic compounds and the involvement of multi-step electron transfer mechanisms and

various intermediates. As an example in this direction, the electroreduction of biomass-derived benzaldehyde (BZH) provides a fascinating route for the selective production of benzyl alcohol (BA), a versatile compound widely utilized in the pharmaceutical and fine chemical industries. <sup>14-16</sup> Moreover, the electrochemical self-coupling of BZH to hydrobenzoin (HDB) holds significance as a potential biofuel production route. <sup>17,18</sup> Both processes, the production of BA and HDB, compete with the hydrogen evolution reaction (HER). As shown in Scheme 1, the first elementary step in both reactions involves the protonation of C=O in BZH, which facilitates the posterior acquisition of one electron from the electrode to form a radical intermediate. <sup>18-20</sup>

In acid media:

$$phCHO + H_3O^+ \to ph - HC = O - H_3O^+$$
  
 $ph - HC = O - H_3O^+ + e^- \to ph(OH)HC \cdot + H_2O$ 

In alkaline media:

$$phCHO + H_2O \rightarrow ph - HC = O - H_2O$$
  
$$ph - HC = O - H_2O + e^- \rightarrow ph(OH)HC \cdot + OH^-$$

After the protonation and electron transfer steps, either the dimerization of two radicals in solution to produce HDB or the combination of the radical with an adsorbed hydrogen ( $H_{ad}$ ) in a Langmuir-Hinshelwood (L-H) scheme to obtain BA takes place. While the electroreduction of BZH to HDB is an outer-sphere reaction, i.e. does not involve surface adsorption,  $^{21\text{-}25}$  BA production depends on the  $H_{ad}$  availability on the catalyst surface:

In acid media:  $H_3O^+ + e^- + * \rightarrow *H + H_2O$ 

In alkaline media:  $H_2O + e^- + * \rightarrow *H + OH^-$ 

a\*. Catalonia Institute for Energy Research – IREC Sant Adrià de Besòs, Barcelona 08930, Spain E-mail: pmartinez@irec.cat, acabot@irec.cat

b. University of Barcelona, Barcelona 08028, Spain.

c. School of Petrochemical Engineering, Lanzhou University of Technology, Lanzhou, 730050, China.

d. Catalan Institute of Nanoscience and Nanotechnology (ICN2), CSIC and BIST, Campus UAB, Bellaterra, 08193, Barcelona, Spain.

e. Institute of Advanced Study, Chengdu University, Chengdu, 610106, China

f. Department of Chemistry and Materials Science, Aalto University School of Chemical Engineering, P.O. Box 16100, FI-00076 Aalto, Finland.

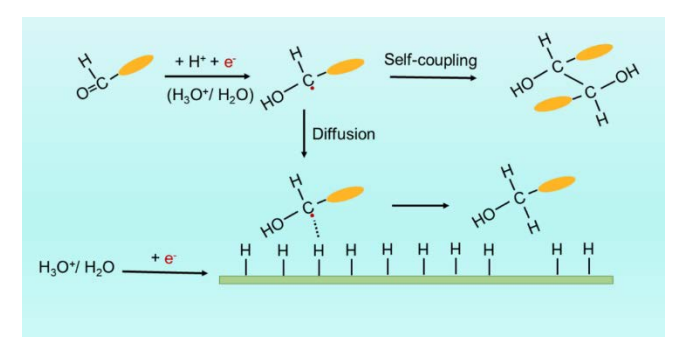
g. IST Austria, Am Campus 1, Klosterneuburg, 3400 Austria

h. ICREA, Pg. Lluís Companys 23, 08010, Barcelona, Spain

Supplementary Information available: See DOI: 10.1039/x0xx00000x

where  $\ast$  represents an adsorption site. Both in acid and basic conditions, the selective production of HDB requires reducing the amount of  $H_{ad}$  to reduce the formation of BA.

To maximize HDB selectivity, current catalyst design strategies primarily focus on materials characterized by high HER overpotentials such as Hg, Pb, In, and Cd among others. <sup>22, 26-29</sup> However, beyond metal toxicity and cost issues, this strategy is intrinsically limited by the increase of the Fermi level on the catalyst surface when increasing the negative voltage or the temperature to accelerate the reaction, which results in more adsorbed hydrogen protons concentrating on the solution side of the electrical double layer (EDL). This promotes the hydrogenation of the ketyl radicals to yield BA.



Scheme 1. Two pathways for the BZH electroreduction, to BA or HDB. The orange ellipsoid represents the benzene ring. Red spots represent electrons provided by the electrode that is represented here by a green bar.

Beyond material selection, the rational design and engineering of the catalyst surface chemistry is a powerful strategy to promote selectivity. More specifically, the modification of the electronic energy levels of the catalyst surface using functional groups such as -OH and -SOOH, 30, 31 as well as larger organic groups such as aromatic thiols, have been shown to favor specific reaction mechanisms. 32-34 Besides modifying the electronic energy levels, the presence of surface species can also adjust selectivity by tailoring the surface adsorption properties. As an example, lipophilic species can enhance the gathering of organic substances at the catalyst surface. In this direction, Baik's group demonstrated an increase in selectivity by promoting the Suzuki-Miyaura cross-coupling reaction with organic monolayers selfassembled at the electrode surface.<sup>35</sup> Besides, Li's group tailored the interfacial environments of Pb electrodes using quaternary alkyl ammonium cations to control the selectivity of BZH to BA or HDB. They showed that the longer the chain length and the higher the cation concentration, the higher the selectivity towards HDB. 26

Herein, we modify the surface of  $Cu_2S$  nanoparticles (NPs) by adding a monolayer of unsaturated fatty amines, specifically oleylamine (OAm), and explore its effect on the electrocatalytic conversion of BZH to either BA or HDB. Cu was used taking into account its exceptional ability for radical generation.<sup>27</sup> We investigate the effect of voltage and temperature on the reaction selectivity at pH 5.2 and pH 9.0. We further explore the involved electroreduction reaction pathways aiming to unveil the rate-determining steps and gain insight into the parameters determining the reaction selectivity. Our final goal is to enable a more rational design of electrocatalyst for the selective electroreduction of biomass-derived BZH.

#### 2. Experimental

#### 2.1 Materials.

Copper(II) acetylacetonate (Cu(acac)<sub>2</sub>, Sigma Aldrich, 97%), oleylamine (OAm, Aladdin Reagent, 70%), dodecanethiol (DDT, Sigma Aldrich, 98%), N,N-dimethylformamide (DMF, Sigma Aldrich, anhydrous, 99.8%), methanol (CH<sub>3</sub>OH, 96%, Letslab), ethanol (CH<sub>3</sub>CH<sub>2</sub>OH, 96%, Letslab), benzaldehyde (BZH, Sigma Aldrich), benzyl alcohol (BA, Sigma Aldrich), benzoic acid (BZA, Sigma Aldrich), and hydrobenzoin (HDB, Sigma Aldrich) were used as purchased, without further purification.

#### 2.2. Cu<sub>2</sub>S preparation.

Cu<sub>2</sub>S NPs were produced following a modified version of a previously reported procedure.<sup>35</sup> Briefly, in a three-neck flask equipped with a reflux condenser, a mixture of Cu(acac)2 (1.56 g, 0.6 mmol), DDT (20 mL), and OAm (40 mL) was deaerated with nitrogen at 120 °C for 20 min. After the nitrogen purging step, the mixture exhibited a light brownish-yellow color. Then, the solution was heated to 200 °C at a constant heating rate of 8 °C min-1 and kept at this temperature for 60 min. During this time, the solution becomes turbid, and the color deepens to a brown-black indicating the occurrence of the chemical reaction. Then, the mixture was cooled down to room temperature. The material was washed with hexane/methanol, separated by centrifugation (9000 rpm, 10 min), and finally dispersed in hexane.

#### 2.3 Ligands removal.

The ligands used to control the Cu<sub>2</sub>S NP growth were removed using an annealing step.<sup>36</sup> The dried Cu<sub>2</sub>S NP powder was annealed for 2 h under an Ar flow inside a tube furnace at 400 °C, reached using a heating rate of 10 °C min<sup>-1</sup>.

#### 2.4 Materials Characterization.

High-resolution transmission electron microscopy (HRTEM) and high-angle annular dark field (HAADF) images were acquired in a Tecnai F20 microscope operated at 200 kV. Energy dispersive spectroscopy (EDS) spectra were obtained in a double-corrected and monochromated Thermo Fisher Spectra 300 microscope operated at 200 kV. Powder X-ray diffraction (XRD) patterns were collected at 40 kV and 40 mA with Cu K $\alpha$  radiation ( $\lambda=1.5406$  Å). Fourier-transformed infrared (FT-IR) spectra of the unsupported samples were recorded on an Alpha Bruker spectrometer. X-ray photoelectron spectroscopy (XPS) was conducted on a ThermoFisher (ESCALAB 250Xi) system with Mono Al K $\alpha$  radiation. The vacuum of the analysis chamber was approximately 2\*10-9 mbar. The energy, voltage, and beam current were 1486.6 eV, 16 kV, and 15 mA, respectively. XPS spectra were corrected to the position of the C 1s peak at 284.6 eV.

#### 2.5 Product identification and conversion and selectivity quantification.

High-performance liquid chromatography (HPLC) analysis of the organics was carried out on an Agilent 1200 series apparatus at 25 °C. The HPLC was equipped with an ultraviolet-visible detector and a 4.6 mm×150 mm Shim-pack GWS 5  $\mu m$  C18 column. The eluting solvents of A: 5 mM ammonium formate aqueous solution; and solution B: acetonitrile were used. The program used was 60% solution B and 40% solution A for 11

min. The flow rate was  $0.5~\text{mL}~\text{s}^{-1}$ . The injection amount was 1  $\mu l$ . Calibration curves of standard chemicals were employed to determine and quantify the products. The total conversion and selectivities were calculated using the following equations:

Conv. % = 
$$\frac{moles\ of\ BZH\ consumed}{initial\ moles\ of\ BZH} \times 100\%$$
 (1)

SelBA % = 
$$\frac{\text{ratio of BA}}{\text{conversion ratio amount of BZH}} \times 100\%$$
 (2)

SelHDB %= 
$$\frac{2*ratio\ of\ HDB}{conversion\ ratio\ amount\ of\ BZH} \times 100\%$$
 (3)

#### 2.6 Electrocatalytic tests.

The electrochemical performance of the electrocatalyst was evaluated on a Corrtest CS2350 EIS bipotentiostat (2-channel, Wuhan Corrtest Instrument Corp. Ltd) using a 3-electrode system in an H-cell reactor divided by a Nafion 117 proton exchange membrane. The working electrode was prepared as follows: 9 mg powder was dispersed into 500 μL H<sub>2</sub>0, 420 μL methanol, and 80 µL 5% Nafion solution. For activity, conversion, and selectivity determination, the catalyst was supported on a carbon cloth used as working electrodes. 1000 µL ink solution was dropped on 2×3 cm<sup>2</sup> carbon cloth (~1.5 mg cm<sup>-1</sup> 2) that was then cut into 1.5×1 cm<sup>2</sup> pieces. When testing, an electrode area of 1×1 cm<sup>2</sup> was immersed into the solution. To determine activation energies, 6 µL ink solution was dropped on a glassy carbon working electrode (d=0.15 cm, ~0.7 mg cm<sup>-2</sup>) and let dry. Platinum mesh and Ag/AgCl (KCl saturated) were used as counter and reference electrodes, respectively. Cyclic voltammetry (CV) and linear sweep voltammetry (LSV) results were calibrated with Nernst equation (4) to the reference hydrogen electrode (RHE) without iR correction. The temperature effects were neglected when setting the parameters for I-t curves.

$$E_{RHE} = E + 0.0591 * pH + E_{Aa/AaCl}^{\theta}$$
 (4)

where T represents temperature in °C, and

$$E_{Ag/AgCl(KCl \, saturated)}^{\theta} = [0.197 - 0.0007 \, (T - 25)] \, V(5)$$

Two electrolytes were tested to explore the influence of the pH. A sodium acetate-acetic acid solution (pH=5.2), and a potassium carbonate-potassium bicarbonate solution (pH=9.0). LSV was tested in the range 0.5 V  $\sim$  -1.0 V (vs. RHE). Electrochemical impedance spectroscopy (EIS) was tested at -0.7 V vs. RHE. For the I-t curve, -0.4 V, -0.8 V, -1.0 V (vs. RHE) was applied as a constant voltage.

#### Results and discussion

 $Cu_2S$  and  $Cu_2S$ -OAm electrocatalysts were prepared at 200 °C using a one-pot synthetic reaction followed by post-treatment (see details in the Experimental section, Figure 1a). DDT was employed as the source of S and solvent and OAm was used as an additional solvent and surface ligand. After 1 h reaction at 200 °C,  $Cu_2S$ -OAm was obtained by centrifugation.  $Cu_2S$  was obtained by annealing the  $Cu_2S$ -OAm powder at 400 °C under an Ar atmosphere.

Figure 1b shows the Cu<sub>2</sub>S-OAm NPs to have spherical geometry and an average size of  $10 \pm 2$  nm. HRTEM micrographs of Cu<sub>2</sub>S-OAm reveal their hexagonal crystal phase, space group P63mmC, with a=b=3.95 Å and c=6.75 Å (Figure 1c), which was consistent with XRD analysis results (PDF#00-02-1294, Figure 1d). HAADF intensity profiles and TEM-EDS chemical composition maps show a homogeneous dispersion of Cu and S within the Cu<sub>2</sub>S-OAm particles that are surrounded by a carbon-based shell (Figures 1e and S1). The carbon shell is discerned by the stronger carbon signal detected at the border of the particle and it is associated with the presence of OAm at the NP surface.

To remove OAm ligands from the NP surface, the material was annealed at 400 °C under an Ar atmosphere. The removal of the stabilizing ligands resulted in increased surface energy that, combined with the relatively high processing temperature, led to NP aggregation and additional growth into Cu<sub>2</sub>S particles with irregular morphologies (Figure S2a). Yet, the hexagonal crystal phase of Cu<sub>2</sub>S was maintained as shown by XRD characterization (Figure 1d). EDS analysis confirmed the Cu<sub>2</sub>S composition to be close to the stoichiometric Cu:S = 2:1 (Figure S2e). Besides, HAADF intensity profiles and STEM-EDS elemental maps showed no evidence of an organic layer surrounding the Cu2S particles, confirming the surface ligand removal (Figure S2). The complete ligand removal was further verified using FT-IR analysis (Figure 1f). The FT-IR spectrum of Cu<sub>2</sub>S-OAm displays the signal corresponding to the -NH bending vibration at 1619 cm<sup>-1</sup> and–NH<sub>2</sub> wagging vibration at 721 cm <sup>-1</sup>, which indicates the presence of OAm molecules on the Cu<sub>2</sub>S surface. Besides, the FT-IR spectrum of Cu<sub>2</sub>S-OAm does not show the band at 2577 cm<sup>-1</sup> associated with the stretching vibration of S–H. This result indicates the lack of free alkylthiol and Cu thiolate complexes, i.e. the absence of DDT on the surface of the Cu<sub>2</sub>S-OAm NPs.<sup>35, 37</sup> Peak signals at around 3000 cm<sup>-1</sup> corresponds to the stretching vibration of both saturated and unsaturated C-H. On the other hand, the FT-IR spectrum of Cu<sub>2</sub>S displayed no fingerprint associated with the presence of OAm or DDT, proving the successful ligand removal during the annealing process.

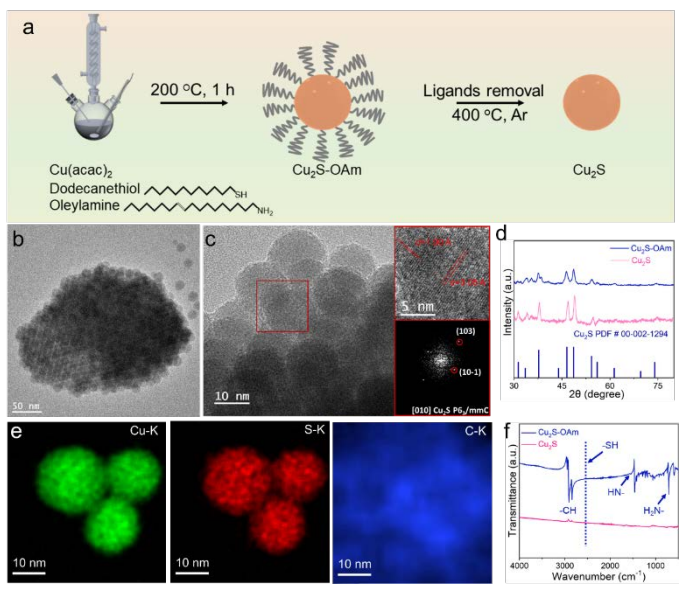


Figure 1. (a) Scheme of the procedure used to prepare  $Cu_2S$ -OAm and  $Cu_2S$ . (b) TEM and (c) HRTEM images and indexed power spectrum of  $Cu_2S$ -OAm NPs. From the crystalline domain, the  $Cu_2S$  lattice fringe distances were measured to be 0.1902 nm, 0.3057 nm, at 80.46° which is interpreted as the hexagonal  $Cu_2S$  phase, visualized along its [101] zone axis. (d) STEM-EDS chemical composition maps of  $Cu_2S$ -OAm NPs; (e) XRD patterns of  $Cu_2S$  and  $Cu_2S$ -OAm. (f) FT-IR spectra of  $Cu_2S$ -OAm.

The survey and high-resolution XPS spectra are displayed in Figures S3 and 2, respectively. The Cu 2p XPS spectrum of Cu<sub>2</sub>S-OAm displays a unique doublet, at 932.1 eV (Cu 2p3/2), associated with Cu(I) within the Cu<sub>2</sub>S lattice.<sup>35</sup> In contrast, the Cu<sub>2</sub>P XPS spectrum of Cu<sub>2</sub>S displays two doublets and additional satellite peaks. The first doublet, at 932.1 eV (Cu 2p<sub>3/2</sub>), is associated with Cu(I) within the Cu<sub>2</sub>S lattice. The second doublet, at 934.3 eV (Cu 2p<sub>3/2</sub>), and the satellites are related to the presence of a significant amount of Cu(II) at the Cu2S surface. This second component is associated with the oxidation of Cu(I) after ligand removal. The S 2p XPS spectrum of Cu<sub>2</sub>S-OAm shows one doublet at 161.5 eV (S 2p<sub>3/2</sub>) which is assigned to S ions coordinated to Cu within the Cu2S lattice. A second minor component is observed at lower binding energies, 160.9 eV (S 2p<sub>3/2</sub>), which we associate with sulfur next to OAm-bond metal ions. After the ligand removal, the S 2p XPS spectrum of Cu<sub>2</sub>S shows just one doublet associated with S ons within the Cu<sub>2</sub>S lattice. This component is redshifted by around 0.4 eV, which indicates a higher electron concentration around the surface S within the Cu<sub>2</sub>S sample.

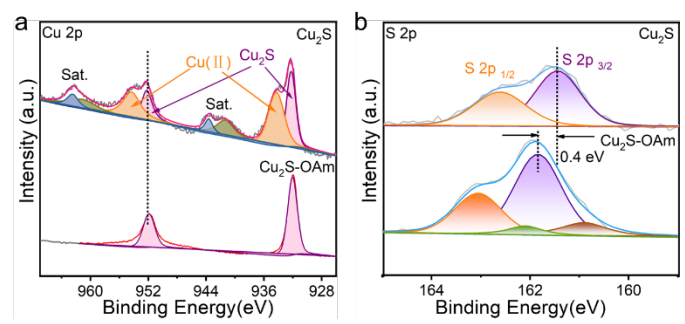


Figure 2. High-resolution Cu 2p (a) and S 2p (b) XPS spectra of  $\text{Cu}_2\text{S}$  and  $\text{Cu}_2\text{S}\text{-OAm}$ .

The electrochemical properties of Cu<sub>2</sub>S and Cu<sub>2</sub>S-OAm particles supported on glassy carbon were initially tested in acidic conditions, within a 1M sodium acetate-acetic acid electrolyte (pH=5.2) with and without 20 mM BZH. Lower pH values were not considered as pH values below 5.2 might cause C=O cleavage of BZH to toluene or other side products. Figure 3a displays the LSV curves obtained in a three-electrodes H-cell reactor. In acidic conditions, without BZH, electrons are only transferred to H+ to form Had, thus the measured current densities in the absence of BZH correspond to the HER. We observe that the Cu<sub>2</sub>S-OAm electrode displays a significantly lower HER activity, with a higher overpotential and lower current densities at all applied voltages than the Cu<sub>2</sub>S electrode. This result is consistent with the presence of OAm partially inhibiting H<sub>ad</sub> formation and HER. In the presence of BZH, electrons can be also transferred to C in ph-HC=O-H<sub>3</sub>O<sup>+</sup> to form a ketyl radical. The subsequent step, after the electron transfer process, involves the combination of the ketyl radical and Had into BA or the combination of ketyl radicals into BZH, involving no additional charge transfer. For both electrodes, the addition of BZH in the electrolyte results in a current increase at low negative potentials, below the HER onset potential. This implies that ketyl radicals are readily formed at lower negative voltages than Had and H<sub>2</sub>, at ca. -0.3 V vs. RHE in both electrodes. For the Cu<sub>2</sub>S-OAm electrode, the current density in the presence of BZH is systematically higher than in its absence, at all potentials tested, which reflects a promoted ketyl radical generation over the partially inhibited Had formation and H2 evolution. As for the Cu2S electrode, while at low negative potentials, the current density is higher in the presence of BZH, as the applied potential increases, the HER-related current in the absence of BZH overcomes the combination of the current density associated with the BZH reaction and the HER in the presence of BZH. Thus the presence of BZH partially inhibits the HER in this material, potentially as a result of the ketyl radical reaction with Had, reducing its concentration, or through the adsorption of ph-HC=O-H<sub>3</sub>O<sup>+</sup> or the ketyl radical on the Cu<sub>2</sub>S surface thus ocuppying H<sub>ad</sub> adsorption sites.

LSV curves depend on charge transfer frequency. They are influenced by mass transport in the electrode and solution, the intrinsic catalytic properties and the number of available adsorption and reaction sites. Thus processes that do not involve charge transfer but potentially blocking/releasing reaction sites such as the ketyl radical conversion to BA through reaction with a  $H_{ad}$  play also an important role. EIS spectra were used for a more precise characterization of the charge transfer mechanisms, without the involvement of site density and occupancy.

EIS spectra of the two electrodes at -0.7 V vs. RHE in the presence and absence of BZH show one semicircle associated with the impedance of the charge transfer from the electrode surface to the electrolyte species (Rct). The Rct of Cu<sub>2</sub>S-OAm in the absence of BZH is significantly larger than that of Cu<sub>2</sub>S, which is consistent with the inhibition of the H<sup>+</sup> adsorption and H<sub>2</sub> evolution being related not to a lower site density but to a larger barrier for electron transfer to H+ in solution probably related to the long OAm chains. We observe the series resistance (Rs) to slightly decrease in the presence of BZH, which is related to an increase of the electrolyte conductivity in the presence of the generated ph-HC=O-H<sub>3</sub>O<sup>+</sup> and ketyl radicals. Besides, both, Cu<sub>2</sub>S and especially Cu<sub>2</sub>S-OAm electrodes show much smaller Rct values in the presence of BZH. This is consistent with LSV data for Cu<sub>2</sub>S-OAm but it is in contrast with LSV data for Cu<sub>2</sub>S. The smaller Rct is associated with the easier electron transfer from the electrode to BZH and formation of ketyl radical than to H+ to form Had. This result, combined with LSV data, shows the slower kinetics detected in the presence of BZH to be related to the BZH radical conversion to BA instead of the ketyl radical formation. The charge transfer resistance of Cu<sub>2</sub>S-OAm in the presence of BZH is slightly smaller than that of Cu<sub>2</sub>S, which is surprising taking into account the presence of OAm hindering charge transfer to species in solution. We associate these results with the hydrophobic surface of Cu<sub>2</sub>S-OAm that leads to an enrichment of BZH, facilitating electron transfer to ph-HC=O-H<sub>3</sub>O<sup>+</sup>. Also, the possibility of partial electron transfer to OAm in Cu<sub>2</sub>S-OAm cannot be ruled out.

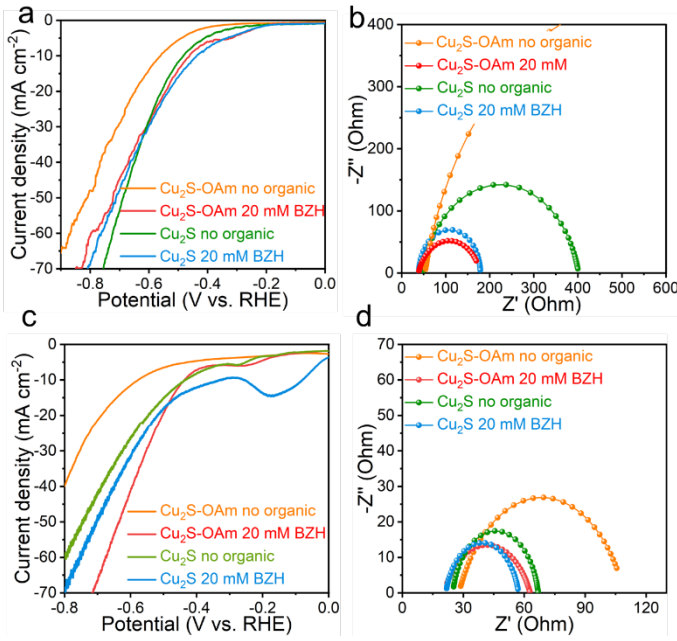


Figure 3. (a) LSV curves; (b) Nyquist plots at -0.7 V vs. RHE of  $Cu_2S$ -OAm and  $Cu_2S$  in 1M sodium acetate-acetic acid electrolyte (pH=5.2) with and without BZH at room temperature; (c) LSV curves; (d) Nyquist plot at -0.7 V vs. RHE of  $Cu_2S$ -OAm and  $Cu_2S$  in 1 M potassium carbonate-potassium bicarbonate electrolyte (pH=9) with or without BZH at room temperature.

In an acidic solution, under an applied voltage, the OAm of the  $Cu_2S$ -OAm surface may accept electrons and could be also replaced by  $H^{+,38}$  Therefore, the stability of the  $Cu_2S$ -OAm electrode in 1M

sodium acetate-acetic acid electrolyte (pH=5.2) was further analyzed (Figure S4). The repetitive CV curves showed Cu<sub>2</sub>S to have good stability both with and without BZH. In contrast, the current density obtained from the Cu<sub>2</sub>S-OAm electrode was not constant. It increased in an electrolyte containing 20 mM BZH and decreased in the pure electrolyte. These results indicate that the OAm ligand undergoes slight reaction/substitution. Still, after more than 20 cycles, the effect of OAm on the Cu<sub>2</sub>S-OAm electrode is clearly noticed (Figure S5).

Results obtained in alkaline conditions, using glassy carbon with 1M potassium carbonate-potassium bicarbonate electrolyte (pH=9.0), are displayed in Figure 3d-f. In these conditions, due to the significant suppression of HER, the concentration of ketyl radicals is expected to increase, resulting in an enhancement of their self-coupling. Indeed, in the absence of BZH, a clear decrease in the HER-related current densities is observed for both electrode materials. LSV curves show the current densities to significantly increase when adding BZH into the system for Cu<sub>2</sub>S-OAm (Figure 3d), displaying a similar onset potential as in acidic conditions, but providing overall lower current densities at higher negative voltages due to the lower HER contribution. For Cu<sub>2</sub>S, current densities show a much slighter variation in the presence of BZH, as in the acidic case.

EIS spectra of the two electrodes in basic conditions at -0.7 V vs. RHE are displayed in Figure 3f. A notable decrease of  $R_{ct}$  is noticed in alkaline conditions compared with acidic ones in the absence of BZH, associated with the enhancement of radical-radical coupling. At low pH, the hydrogen binding strength is lower due to the surrounding hydronium ions, <sup>39</sup> which facilitates the formation of  $H_{ad}$  that combines with the ketyl radicals to produce benzyl alcohol. As the pH increases, the formation of  $H_{ad}$  requires overcoming a higher energy barrier. Thus radicals are more inclined to undergo self-coupling, which further accelerates the charge transfer and radical formation. With the introduction of BZH, both electrodes display similar tendencies as in acidic conditions, with a notable decrease of the  $R_{ct}$  attributed to the formation of ketyl radicals.

As observed from the CV curves (Figure S6), the performance of the  $\text{Cu}_2\text{S}$  electrode was stable both with and without BZH (Figure S6a-b). In contrast, the current density increased for  $\text{Cu}_2\text{S}\text{-OAm}$  electrodes in the pure electrolyte, indicating moderate stability in these conditions, potentially due to ligand displacement with -OH. This instability was not observed in the presence of BZH (Figure S7), which indicates a smooth and efficient transfer of charge to BZH.

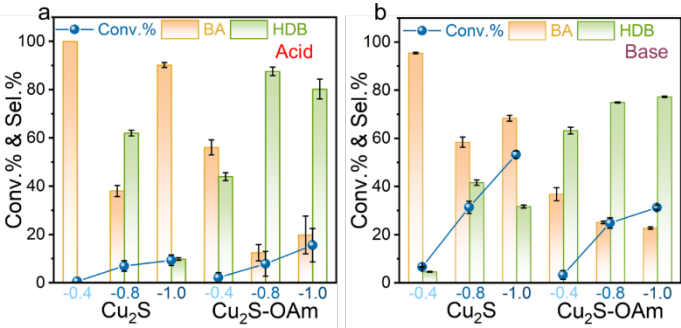


Figure 4. BZH conversion and selectivity toward BA and HDB after 20 min reaction on  $Cu_2S$  and  $Cu_2S$ -OAm electrodes at 0.4, -0.8, -1.0 V vs. RHE, 25 °C in (a) 1 M sodium acetate-acetic acid solution (pH=5.2) with 20 mM BZH; (b) 1 M potassium carbonate-potassium bicarbonate solution (pH=9.0) with 20 mM BZH.

To quantify the reaction products, additional electrocatalytic measurements were carried out with the materials supported on CC using a constant reaction time of 20 min. Different pH, voltage, and temperature conditions were tested to evaluate the effect of these parameters on the BZH conversion and product selectivity.

Figure 4 shows the effect of the applied potential on the BZH conversion and selectivity. Under acidic conditions (Figure 4a), at a low voltage of -0.4 V vs. RHE, both Cu<sub>2</sub>S and Cu<sub>2</sub>S-OAm catalysts exhibit relatively low BZH conversion (~ 5%), and notable selectivity towards BA, especially Cu<sub>2</sub>S. This result is attributed to the hydrogen bonding to the catalyst surface, forming Cu-H bonds at low negative voltages. Then, this H is combined with ketyl radical. 40 As the negative voltage increases, the conversion increases. Additionally, as increasing the voltage, the selectivity of the two electrodes towards the conversion of BZH into BA first decreases and then increases again. The voltage increase elevates the electrochemical potential at the electrode-solution interface, augmenting the formation of Had, thereby bolstering BA selectivity. As expected, Cu<sub>2</sub>S-OAm exhibited higher selectivity to HDB at all voltages due to the inhibited formation of Had. The slight decrease in HDB selectivity obtained for Cu2S-OAm at high voltage may be related to the partial OAm reaction/replacement from the Cu<sub>2</sub>S surface.

Under basic conditions (Figure 4b), a substantial increase in BZH conversion is measured, but the selectivity trends with the applied voltage remain unchanged. Notably, the selectivity of Cu<sub>2</sub>S-OAm towards the conversion of BZH into HDB increases with the voltage, which is consistent with good catalyst stability.

A temperature increase also results in an elevation of the material surface Fermi level thus leading to a decrease of the charge transfer resistance and the formation of additional  $H_{ad}$ . Therefore, a similar dependence to that obtained for the voltage is expected. The difference lies in that the temperature also accelerates the mass transfer efficiency in the solution. At -0.8 V vs. RHE, the  $Cu_2S$  selectivity towards BA increased with temperature both in acid and alkaline conditions owing to the higher  $H_{ad}$  formed. The  $Cu_2S$  selectivity towards BA is higher under acidic conditions compared to alkaline in the whole temperature range tested. For  $Cu_2S$ -OAm, the selectivity towards HDB decreased with temperature in acidic conditions, owing to the  $H_{ad}$  increase. However, the HDB selectivity increased with temperature under alkaline conditions.

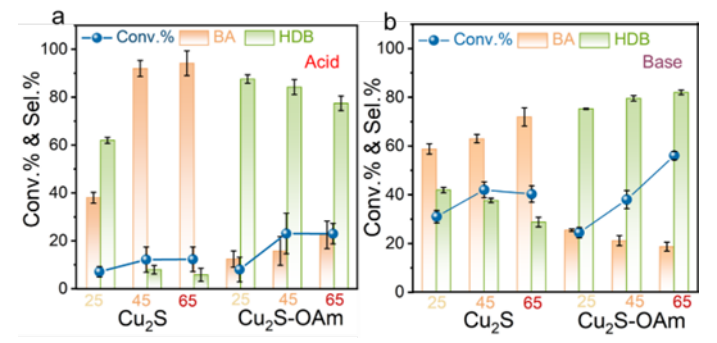


Figure 5. BZH conversion and selectivity toward BA and HDB after 20 min reaction on  $Cu_2S$  and  $Cu_2S$ -OAm electrodes at -0.8 vs. RHE, 25 °C, 45 °C or 65 °C in (a) 1 M sodium acetate-acetic acid solution (pH=5.2); (b) 1 M potassium carbonate-potassium bicarbonate solution (pH=9.0).

To further understand the effect of temperature on mass transfer and the acceleration of the reaction rate, EIS measurements at different temperatures were carried out on the catalysts supported on glassy carbon. From these results, the corresponding activation energy barriers were calculated (Figures 6 and S8). As pH increased, the reaction energy barrier in Cu<sub>2</sub>S decreased from 70 kJ/mol to 44 kJ/mol. In contrast, the energy barrier in Cu<sub>2</sub>S-OAm increased from 46 kJ/mol to 61 kJ/mol. These results imply the higher sterical barriers for the formation of  $H_{ad}$  to combine with the hydroxyl carbon of the intermediate ketyl radical in alkaline than in acidic conditions, while BZH can combine with  $H^+$  in acidic conditions to form ketyl radical more easily than in alkaline.

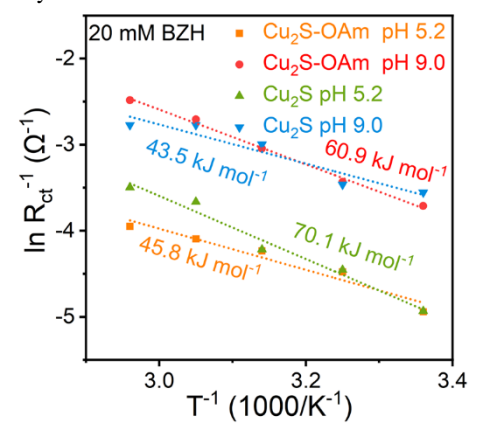


Figure 6. Activation energies calculated from the Nyquist plot.

Based on the above results, it is clear that a high selectivity for obtaining HDB by BZH electrochemical reduction can be achieved by adjusting the pH, applied voltages, catalyst components and catalyst surface properties. The energy barrier for the formation of the high-energy intermediate species  $H_{ad}$  increases as the pH increases, leading to a decrease in the concentration of  $H_{ad}$  on the catalyst surface, thereby increasing the chances of radical dimerization for the formation of HDB. For catalysts with exposed active sites, applying a higher voltage leads to surface electron accumulation, causing enrichment of  $H^+$  on the EDL solution side, and increasing the possibility of forming  $H_{ad}$  and BA. Thus, blocking the active sites of the catalyst surface with organic ligands to prevent the formation of  $H_{ad}$  can improve the selectivity of HDB independently of pH.

#### **Conclusions**

In summary,  $Cu_2S$ -OAm and  $Cu_2S$  have been synthesized using a one-pot synthetic approach and a post-treatment. By comparing their electrocatalytic performance towards the electrochemical reduction of BZH, we conclude that OAm prevents the organic substrate and the H proton from reaching the  $Cu_2S$  active sites. Therefore hydrogen cannot become an activated intermediate species and combine with ketyl radicals to form BA. At the same time, the organic BZH and its ketyl radicals concentrate near the OAm ligands of the catalyst surface based on the miscibility for their similar polarity, thus promoting the selectivity and conversion of forming HDB.

#### **Author contributions**

Li Gong: Conceptualization and Writing – original draft; Shiling Zhao and Tanja Kallio: Investigation; Jing Yu, Jordi Arbiol and Junshan Li: Formal Analysis; Paulina R. Martínez-Alanis: Supervision and Funding acquisition; Mariano Calcabrini and Maria Ibáñez: Methodology; Andreu Cabot: Supervision and Writing – review & editing.

#### **Conflicts of interest**

There are no conflicts to declare.

#### Data availability

No data were used for the research described in this article.

#### **Acknowledgements**

L. Gong and J. Yu thank the China Scholarship Council for the scholarship support. ICN2 acknowledges funding from Generalitat de Catalunya 2021SGR00457. This study is part of the Advanced Materials programme and was supported by MCIN with funding from European Union NextGenerationEU (PRTR-C17.I1) and by Generalitat de Catalunya. The authors thank support from the project NANOGEN (PID2020-116093RB-C43), funded by AEI/10.13039/501100011033/ and by "ERDF A way of making Europe", by the "European Union". ICN2 is supported by the Severo Ochoa program from Spanish MCIN / AEI (Grant No.: CEX2021-001214-S) and is funded by the CERCA Programme / Generalitat de Catalunya. Part of the present work has been performed in the framework of Universitat Autònoma de Barcelona Materials Science PhD program. Authors acknowledge the use of instrumentation as well as the technical advice provided by the Joint Electron Microscopy Center at ALBA (JEMCA). ICN2 acknowledges funding from Grant IU16-014206 (METCAM-FIB) funded by the European Union through the European Regional Development Fund (ERDF), with the support of the Ministry of Research and Universities, Generalitat de Catalunya. ICN2 is founding member of e-DREAM.41

#### **Notes and references**

- G. Zeng, Q. Sun, S. Horta, S. Wang, X. Lu, C. Y. Zhang, J. Li, J. Li, L. Ci, Y. Tian, M. Ibáñez and A. Cabot, *Adv. Mater.*, 2024, 36, 2305128.
- C. Huang, J. Yu, C. Li, Z. Cui, C. Zhang, C. Zhang, B. Nan, J. Li, J. Arbiol and A. Cabot, *Adv. Funct. Mater.*, 2023, 33, 2305624.
- 3. U. Sanyal, K. Koh, L. C. Meyer, A. Karkamkar and O. Y. Gutiérrez, *J. Appl. Electrochem.*, 2021, **51**, 27-36.
- Y. P. Wijaya, K. J. Smith, C. S. Kim and E. L. Gyenge, Green Chem., 2020, 22, 7233-7264.
- S. A. Akhade, N. Singh, O. Y. Gutiérrez, J. Lopez-Ruiz, H. Wang, J. D. Holladay, Y. Liu, A. Karkamkar, R. S. Weber, A. B. Padmaperuma, M.-S. Lee, G. A. Whyatt, M. Elliott, J. E. Holladay, J. L. Male, J. A. Lercher, R. Rousseau and V.-A. Glezakou, *Chem. Rev.*, 2020, 120, 11370-11419.
- K. Li and Y. Sun, Chemistry A European Journal, 2018, 24, 18258-18270.
- J. Li, L. Li, X. Ma, X. Han, C. Xing, X. Qi, R. He, J. Arbiol, H. Pan, J. Zhao, J. Deng, Y. Zhang, Y. Yang and A. Cabot, Adv. Sci., 2023, 10, 2300841.
- J. Li, X. Tian, X. Wang, T. Zhang, M. C. Spadaro, J. Arbiol, L. Li, Y. Zuo and A. Cabot, *Inorg. Chem.*, 2022, 61, 13433-13441.
- 9. Z. Zhang, L. Bian, H. Tian, Y. Liu, Y. Bando, Y. Yamauchi and Z.-L. Wang, *Small*, 2022, **18**, 2107450.
- M. Luo, J. Yang, X. Li, M. Eguchi, Y. Yamauchi and Z.-L. Wang, *Chem. Sci.*, 2023, 14, 3400-3414.
- J. Li, L. Li, X. Ma, J. Wang, J. Zhao, Y. Zhang, R. He, Y. Yang, A. Cabot and Y. Zhu, *Nano Res.*, 2023, DOI: 10.1007/s12274-023-6049-4.
- J. Li, L. Li, X. Ma, X. Han, C. Xing, X. Qi, R. He, J. Arbiol, H. Pan, J. Zhao, J. Deng, Y. Zhang, Y. Yang and A. Cabot, Adv. Sci., 2023, 10, 2300841.
- 13. Z. J. Schiffer and K. Manthiram, *Joule*, 2017, **1**, 10-14.
- J. T. Bhanushali, I. Kainthla, R. S. Keri and B. M. Nagaraja, ChemistrySelect, 2016, 1, 3839-3853.
- D. C. Cantu, A. B. Padmaperuma, M.-T. Nguyen, S. A. Akhade, Y. Yoon, Y.-G. Wang, M.-S. Lee, V.-A. Glezakou, R. Rousseau and M. A. Lilga, ACS Catal., 2018, 8, 7645-7658.
- C. Xu, E. Paone, D. Rodríguez-Padrón, R. Luque and F. Mauriello, *Chem. Soc. Rev.*, 2020, 49, 4273-4306.
- M. T. Bender, X. Yuan, M. K. Goetz and K.-S. Choi, ACS Catal., 2022, 12, 12349-12368.
- J. Yu, P. Zhang, L. Li, K. Li, G. Zhang, J. Liu, T. Wang, Z.-J. Zhao and J. Gong, *Nat. Commun.*, 2022, 13, 7909.
- S. Huang, B. Gong, Y. Jin, P. H. L. Sit and J. C.-H. Lam, ACS Catal., 2022, 12, 11340-11354.
- L. C. Meyer, U. Sanyal, K. A. Stoerzinger, K. Koh, J. L. Fulton, D. M. Camaioni, O. Y. Gutiérrez and J. A. Lercher, ACS Catal., 2022, 12, 11910-11917.
- 21. X. H. Chadderdon, D. J. Chadderdon, J. E. Matthiesen, Y. Qiu, J. M. Carraher, J.-P. Tessonnier and W. Li, *J. Am. Chem. Soc.*, 2017, **139**, 14120-14128.
- H. Liu, D. M. Patel, Y. Chen, J. Lee, T.-H. Lee, S. D. Cady,
   E. W. Cochran, L. T. Roling and W. Li, *ACS Catal.*, 2022,
   12, 14072-14085.
- 23. J. Anibal and B. Xu, ACS Catal., 2020, 10, 11643-11653.
- P. Nilges and U. Schröder, Energy Environ. Sci., 2013, 6, 2925-2931.
- 25. T. Guena and D. J. A. C. S. Pletcher, 1998, **52**, 23-31.
- X. H. Chadderdon, D. J. Chadderdon, J. E. Matthiesen, Y. Qiu, J. M. Carraher, J. P. Tessonnier and W. Li, *J Am Chem Soc*, 2017, 139, 14120-14128.
- J. Anibal, A. Malkani and B. Xu, Catal. Sci. Technol., 2020, 10, 3181-3194.

- L. Gong, C. Y. Zhang, J. Li, G. Montaña-Mora, M. Botifoll, T. Guo, J. Arbiol, J. Y. Zhou, T. Kallio, P. R. Martínez-Alanis and A. Cabot, ACS Appl. Mater. Interfaces., 2024, 16, 6948-6957.
- L. Gong, C. Y. Zhang, X. Mu, X. Han, J. Li, J. Arbiol, J. Y. Zhou, T. Kallio, P. R. Mart-<sup>1</sup>nez-Alanis and A. Cabot, *J. Chem. Eng.*, 2024, 479, 147612.
- J. Wu, D. Liang, X. Song, T. Liu, T. Xu, S. Wang and Y. Zou, J. Energy Chem., 2022, 71, 411-417.
- 31. K. Koh, U. Sanyal, M.-S. Lee, G. Cheng, M. Song, V.-A. Glezakou, Y. Liu, D. Li, R. Rousseau, O. Y. Gutierrez, A. Karkamkar, M. Derewinski and J. A. Lercher, *Angew. Chem.*, 2020, **59**, 1501-1505.
- 32. F. Wang and S. S. Stahl, Acc. Chem. Res., 2020, **53**, 561-574.
- 33. R. Cheng, Y. Min, H. Li and C. Fu, *Nano Energy*, 2023, **115**, 108718.
- J. Heo, H. Ahn, J. Won, J. G. Son, H. K. Shon, T. G. Lee,
   S. W. Han and M.-H. Baik, *Science*, 2020, 370, 214-219.
- 35. A. Tang, S. Qu, K. Li, Y. Hou, F. Teng, J. Cao, Y. Wang and Z. Wang, *Nanotechnol.*, 2010, **21**, 285602.
- Y. Zhang, C. Xing, Y. Liu, M. C. Spadaro, X. Wang, M. Li,
   K. Xiao, T. Zhang, P. Guardia, K. H. Lim, A. O.
   Moghaddam, J. Llorca, J. Arbiol, M. Ibáñez and A. Cabot,
   Nano Energy, 2021, 85.
- A. Shavel, M. Ibáñez, Z. Luo, J. De Roo, A. Carrete, M. Dimitrievska, A. Genç, M. Meyns, A. Pérez-Rodríguez, M. V. Kovalenko, J. Arbiol and A. Cabot, *Chem. Mater.*, 2016, 28, 720-726.
- 38. L. Lu, B. Lou, S. Zou, H. Kobayashi, J. Liu, L. Xiao and J. Fan, *ACS Catal.*, 2018, **8**, 8484-8492.
- 39. I. K. M. Yu, F. Deng, X. Chen, G. Cheng, Y. Liu, W. Zhang and J. A. Lercher, *Nat. Commun.*, 2022, **13**, 7154.
- B. M. Tackett, D. Raciti, A. R. Hight Walker and T. P. Moffat, *The Journal of Physical Chemistry Letters*, 2021, 12, 10936-10941.
- 41. R. Ciancio, R. E. Dunin-Borkowski, E. Snoeck, M. Kociak, R. Holmestad, J. Verbeeck, A. I. Kirkland, G. Kothleitner and J. Arbiol, *Microscopy and Microanalysis*, 2022, **28**, 2900-2902.

#### **Supporting Information**

### Influence of the catalyst surface chemistry on the electrochemical selfcoupling of biomass-derived benzaldehyde into hydrobenzoin

Li Gong<sup>1,2</sup>, Shiling Zhao<sup>3</sup> Jing Yu<sup>1,4</sup>, Junshan Li<sup>5</sup>, Jordi Arbiol<sup>4,8</sup>, Tanja Kallio<sup>6</sup>, Mariano Calcabrini<sup>7</sup>, Paulina R. Martínez-Alanis<sup>1\*</sup>, Maria Ibáñez<sup>7</sup>, Andreu Cabot<sup>1,8</sup>\*

- 1\*. Catalonia Institute for Energy Research IREC Sant Adrià de Besòs, Barcelona 08930, Spain E-mail: pmartinez@irec.cat,\_acabot@irec.cat
- 2. University of Barcelona, Barcelona 08028, Spain.
- 3. School of Petrochemical Engineering, Lanzhou University of Technology, Lanzhou, 730050, China.
- 4. Catalan Institute of Nanoscience and Nanotechnology (ICN2), CSIC and BIST, Campus UAB, Bellaterra, 08193, Barcelona, Spain.
- 5. Institute of Advanced Study, Chengdu University, Chengdu, 610106, China
- 6. Department of Chemistry and Materials Science, Aalto University School of Chemical Engineering, P.O. Box 16100, FI-00076 Aalto, Finland.
- 7. IST Austria, Am Campus 1, Klosterneuburg, 3400 Austria
- 8. ICREA, Pg. Lluís Companys 23, 08010, Barcelona, Spain

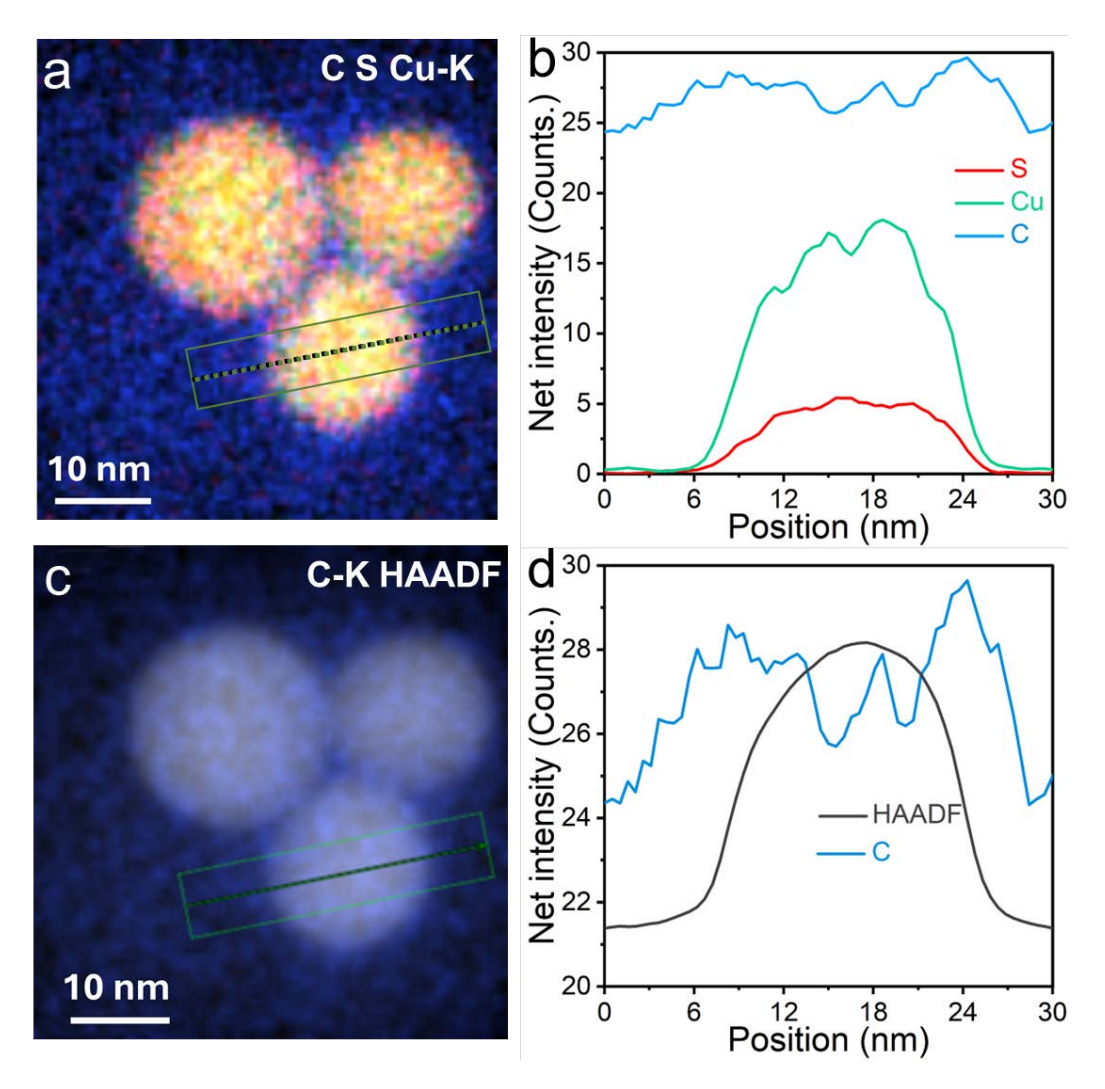


**Figure S1.** (a) STEM-EDS chemical composition map of different elements of Cu<sub>2</sub>S-OAm NPs; (b) EDS linear profile of detected elements of Cu<sub>2</sub>S-OAm NPs; (c) STEM-HAADF image of Cu<sub>2</sub>S-OAm and element C mapping and (d) its EDS linear profile.

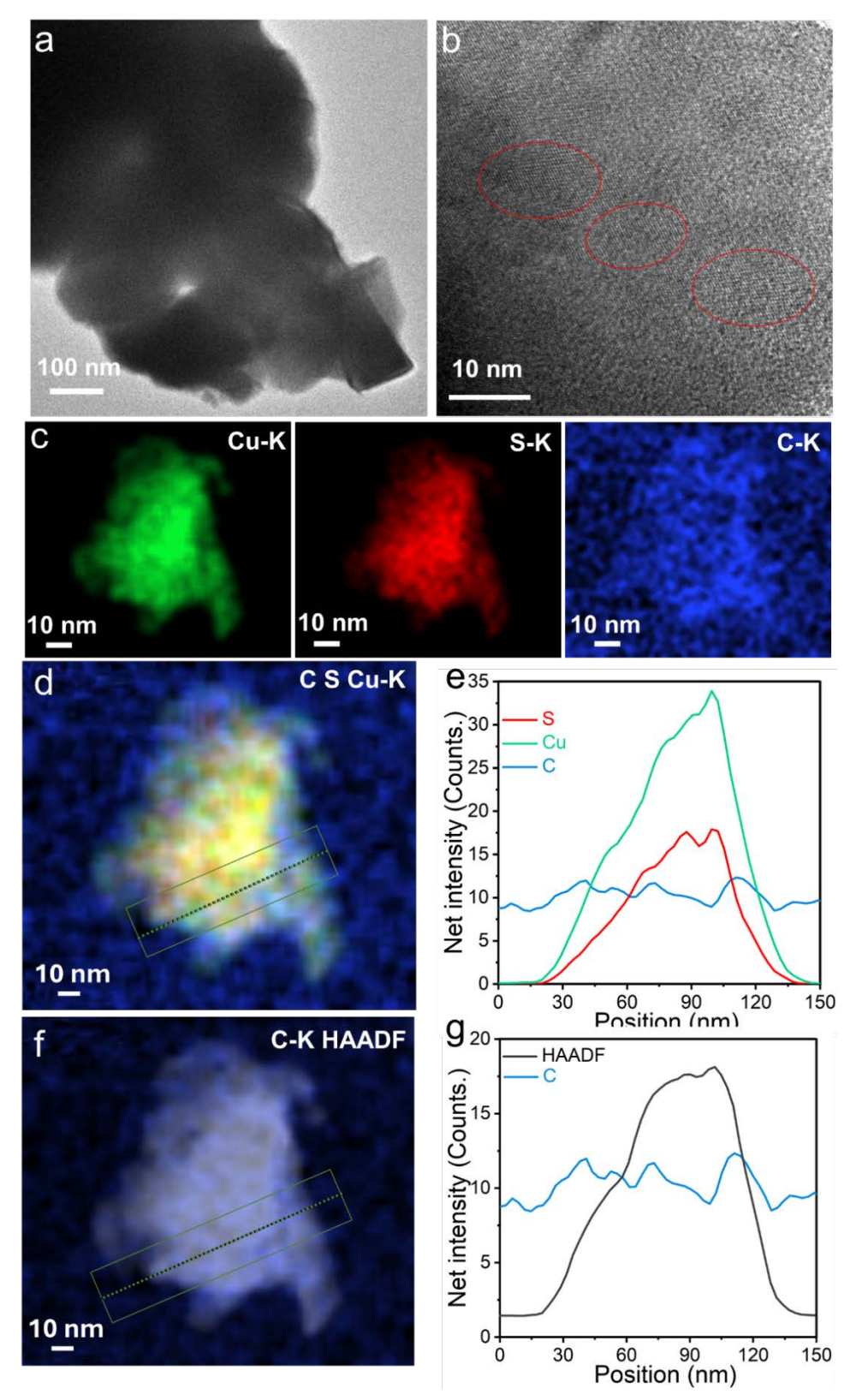


**Figure S2.** Structural and chemical characterization of Cu<sub>2</sub>S. (a) TEM image; (b) High magnification TEM image; (c) STEM-EDS chemical composition maps of Cu<sub>2</sub>S; (d) STEM-EDS chemical composition map of different elements; (e) EDS linear profile of detected elements; (f) STEM-HAADF image of Cu<sub>2</sub>S and element C mapping and (g) its EDS linear profile.

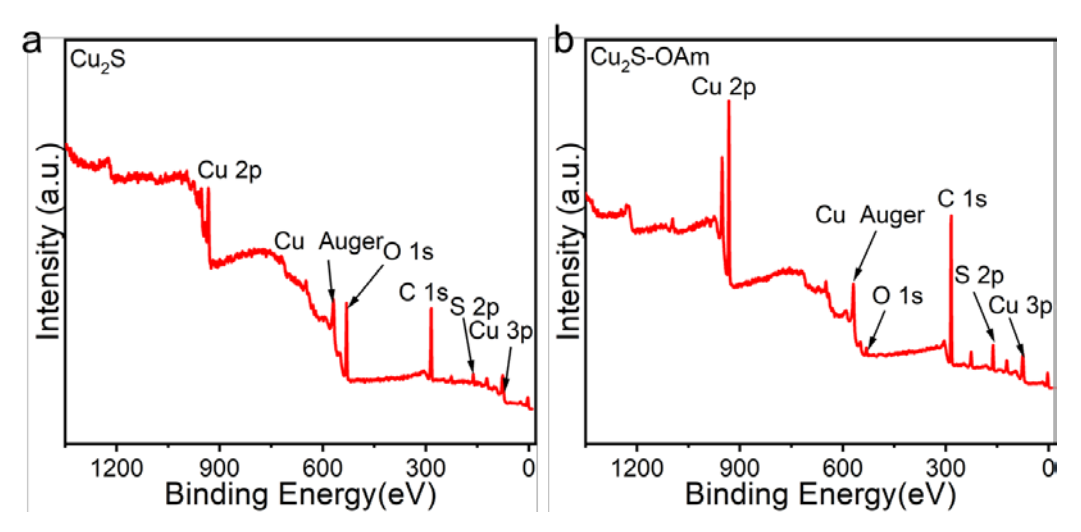
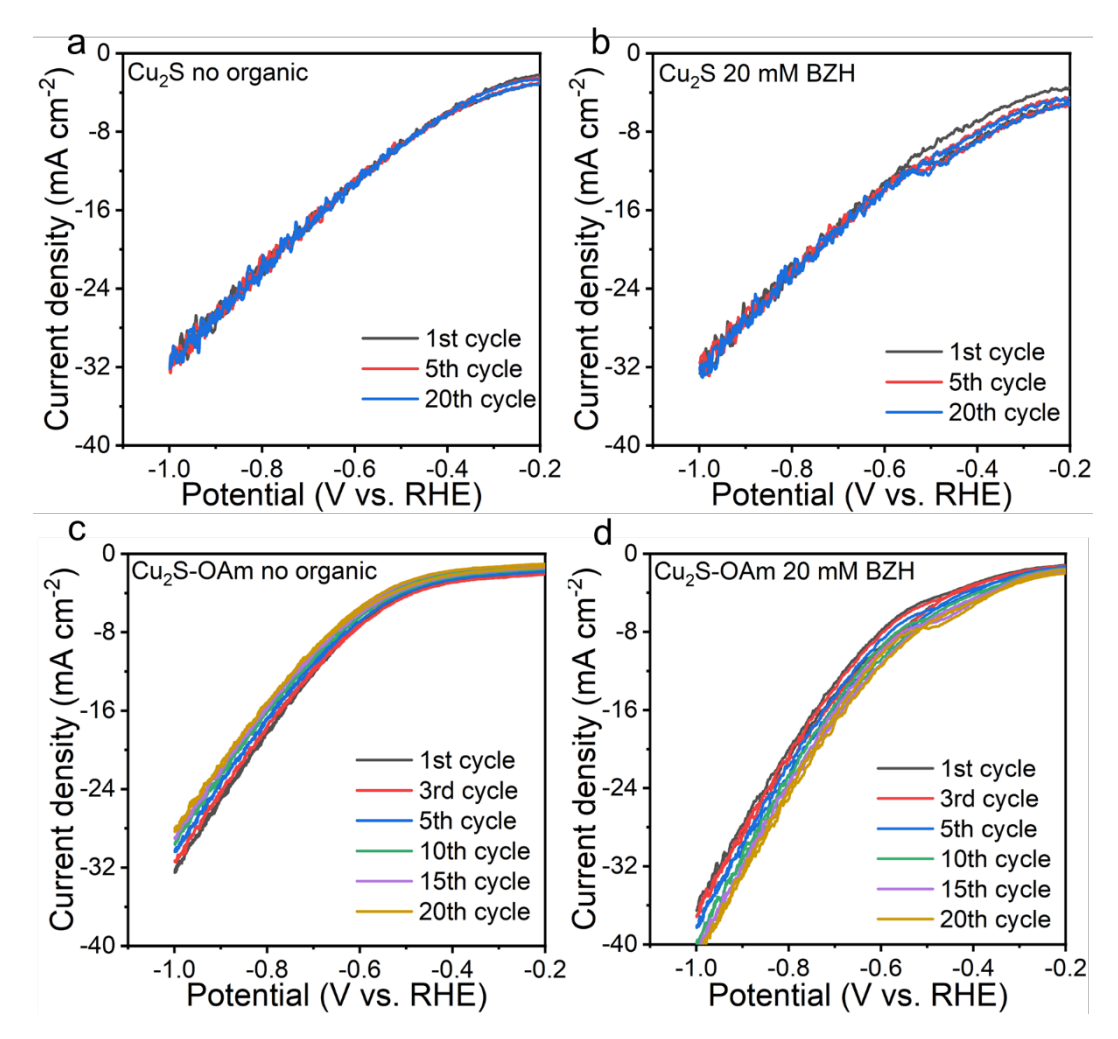
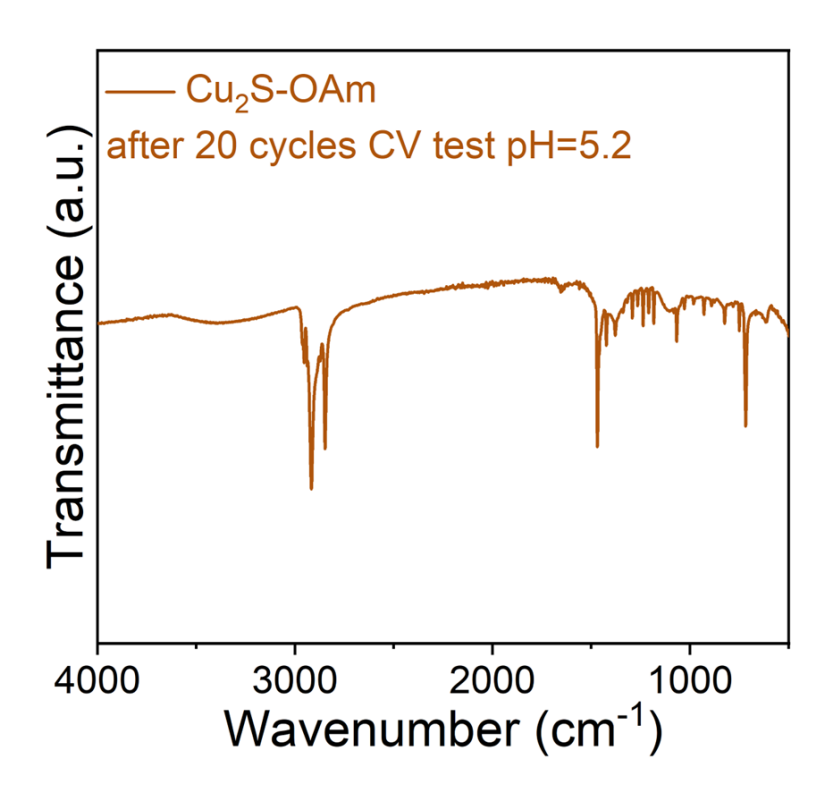


Figure S3. The XPS survey spectrum of Cu<sub>2</sub>S and Cu<sub>2</sub>S-OAm.



**Figure S4.** Stability tests using CV of (a) Cu<sub>2</sub>S in 1 M sodium acetate-acetic acid electrolyte (pH=5.2); (b) Cu<sub>2</sub>S in 1 M sodium acetate-acetic acid electrolyte (pH=5.2) and 20 mM BZH; (c) Cu<sub>2</sub>S-OAm in 1 M sodium acetate-acetic acid electrolyte (pH=5.2); (d) Cu<sub>2</sub>S-OAm in 1 M sodium acetate-acetic acid electrolyte (pH=5.2) and 20 mM BZH.



**Figure S5.** FTIR spectrum of Cu<sub>2</sub>S-OAm after 20 cycles CV tests in 1 M sodium acetate-acetic acid electrolyte (pH=5.2) and 20 mM BZH.

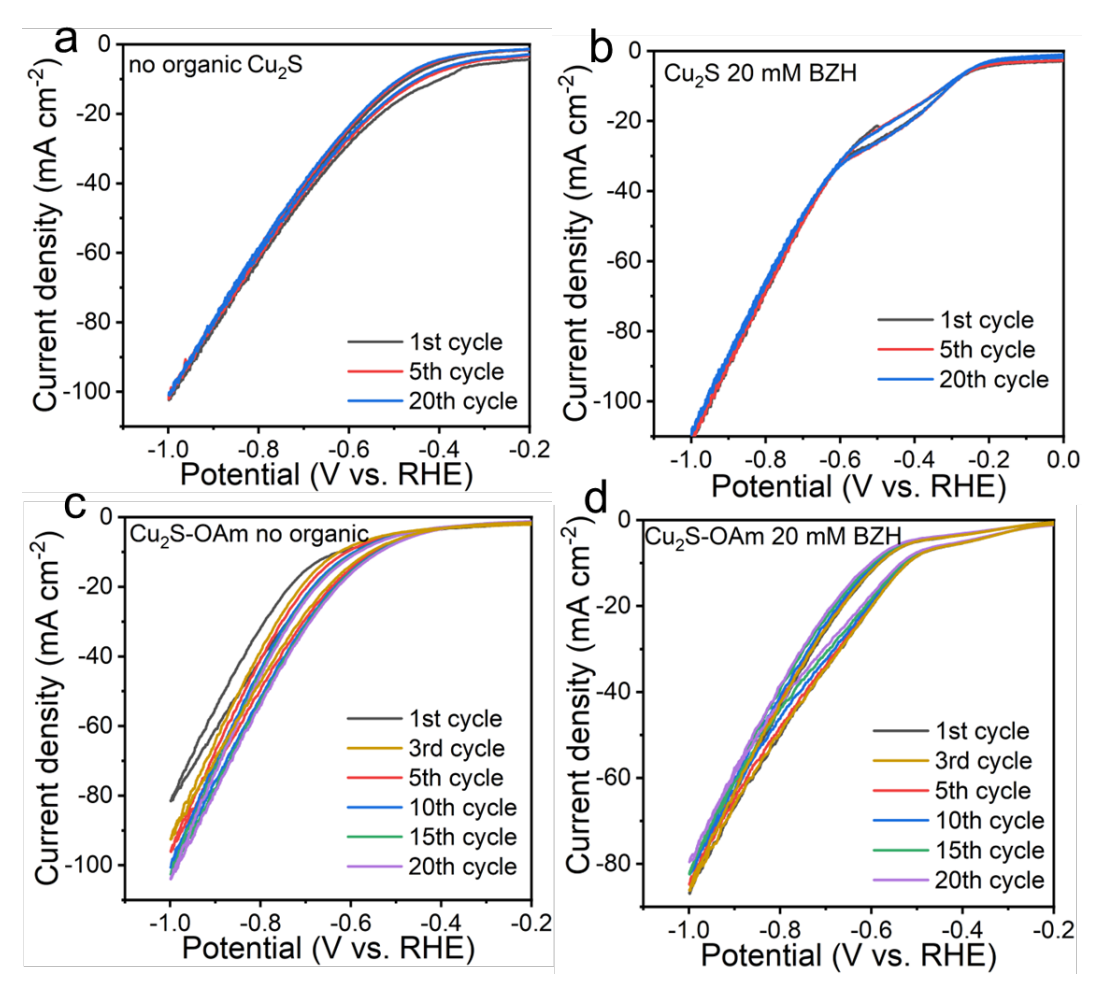


**Figure S6.** Stability tests of Cyclic voltammetry (CV) of (a) Cu<sub>2</sub>S in 1 M potassium carbonate-potassium bicarbonate electrolyte (pH=9.0); (b) Cu<sub>2</sub>S in 1 M potassium carbonate-potassium bicarbonate electrolyte (pH=9.0) and 20 mM BZH; (c) Cu<sub>2</sub>S-OAm in 1 M potassium carbonate-potassium bicarbonate electrolyte (pH=9.0); (d) Cu<sub>2</sub>S-OAm in 1 M potassium carbonate-potassium bicarbonate electrolyte (pH=9.0) and 20 mM BZH.

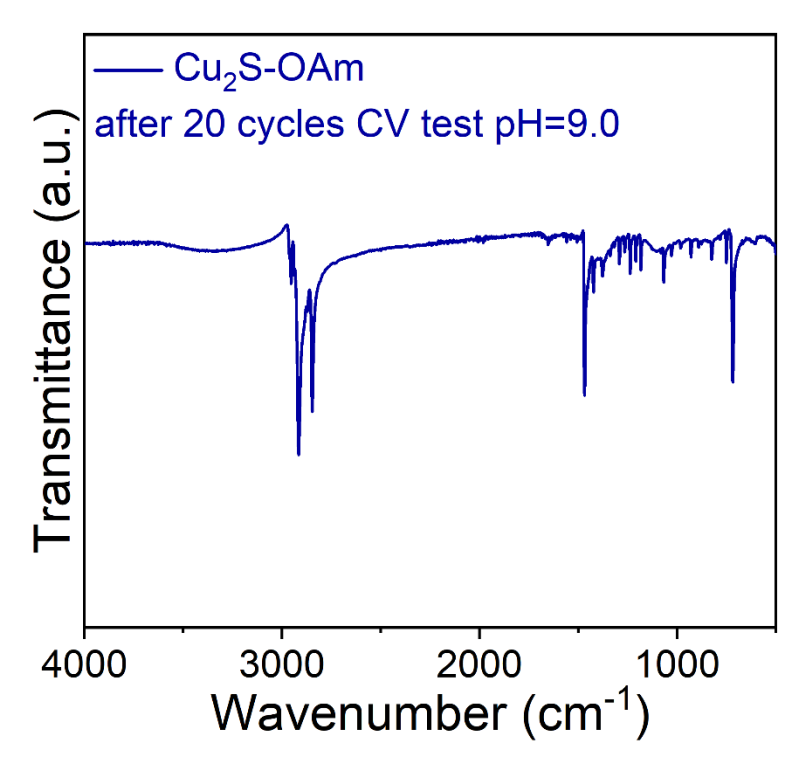


**Figure S7.** FTIR spectrum of Cu<sub>2</sub>S-OAm after 20 cycles CV tests in 1 M potassium carbonate-potassium bicarbonate electrolyte (pH=9.0) and 20 mM BZH.

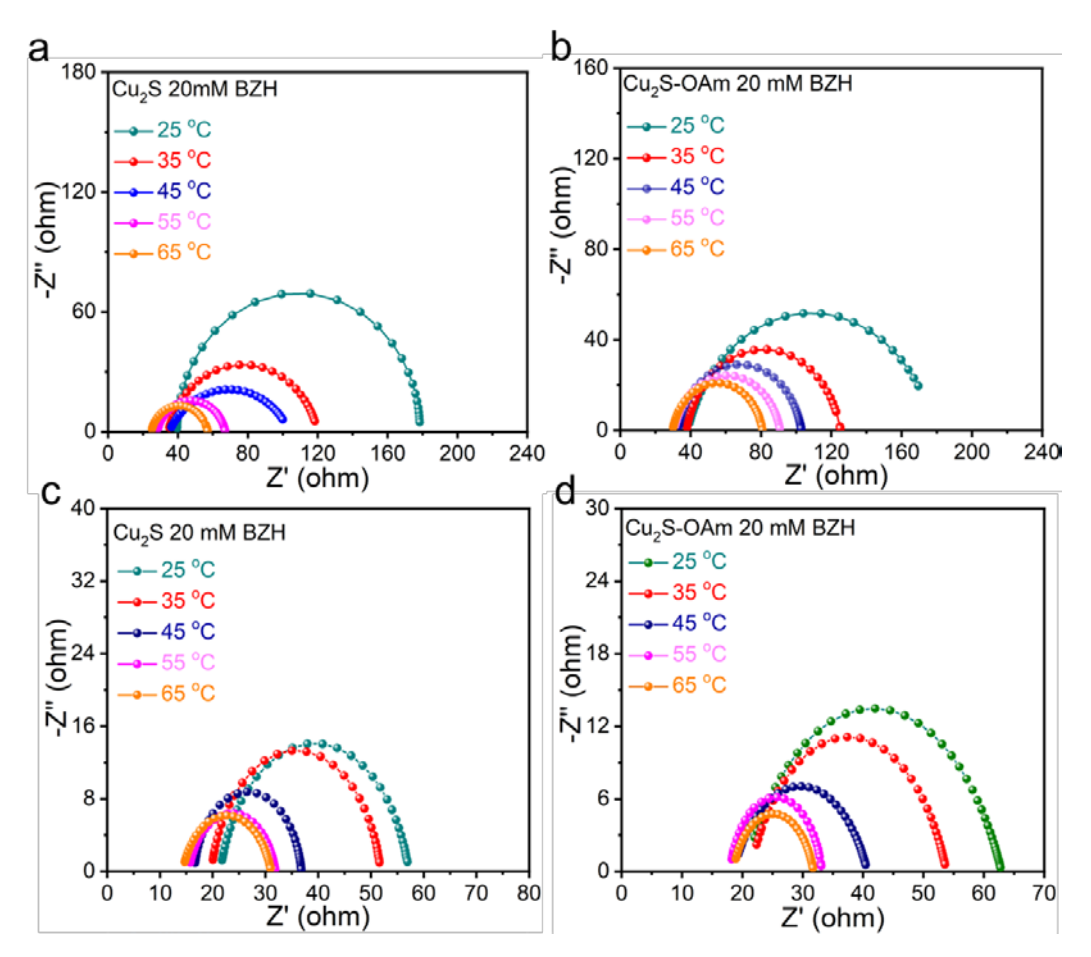


**Figure S8.** Nyquist plot of electrode material (a) Cu<sub>2</sub>S; (b) Cu<sub>2</sub>S-OAm in 1 M sodium acetate-acetic acid electrolyte (pH=5.2) and 20 mM BZH at different temperature; (c)Cu<sub>2</sub>S; (d) Cu<sub>2</sub>S-OAm in 1 M potassium carbonate-potassium bicarbonate electrolyte (pH=9.0) and 20 mM BZH.

## **Chapter 7**

# Electrochemical Oxidization of benzaldehyde into Benzoic Acid on Au-TiO<sub>2</sub>

## 7. Electrochemical Oxidization of Benzaldehyde into Benzoic Acid on Au-TiO<sub>2</sub>

The purpose of this study was to evaluate the electrochemical performance and catalytic efficiency of Au-TiO<sub>2</sub>-P25 supported on carbon cloth, specifically for OER and BZH electrooxidation reactions. This work aimed to understand the impact of different TiO<sub>2</sub> phases (anatase, rutile, and mixed) and the presence of BZH on the catalytic properties of Au-TiO<sub>2</sub> materials. Findings and results are listed as:

- 1. The three catalytic materials, Au-TiO<sub>2</sub>-P25, Au-TiO<sub>2</sub>-A, and Au-TiO<sub>2</sub>-R, were prepared using an impregnation followed by H<sub>2</sub> reduction process. XRD patterns confirmed the retention of the TiO<sub>2</sub> crystal structure with Au-loading.
- 2. XPS spectra revealed shifts in the Ti 2p and O 1s peaks, indicating changes in the electronic structure of TiO<sub>2</sub> but not in Au.
- 3. Electrochemical tests showed that Au-TiO<sub>2</sub>-P<sub>25</sub> exhibited the highest activity towards OER, with a notable decrease in overpotential in the presence of BZH.
- 4. LSV curves indicated that the current density increased with voltage and further increased with the addition of BZH.
- 5. EIS demonstrated reduced resistance in the presence of BZH, indicating improved catalytic performance.
- 6. The conversion of BZH to BZA increased with voltage, achieving a maximum of 29% at 1.8 V vs. RHE within 30 min.
- 7. The electrocatalyst displayed excellent stability over five consecutive 30-minute cyclic tests, with consistent current density and conversion rates of BZH.

The study concluded that the Au-TiO<sub>2</sub>-P25 electrocatalyst exhibits superior electrochemical performance for both OER and BZH electrooxidation. The addition of BZH significantly enhances the catalytic activity and reduces the energy consumption required for these reactions. The stability and efficiency of the catalyst make it a promising candidate for practical applications in electrochemical conversion processes.

The catalyst chosen of Au-TiO<sub>2</sub>-P25, due to its higher level of commercialization. In this work, I processed the corresponding data XRD, SEM, TEM, FTIR XPS, EPR. The initial draft of the paper was written by me under the guidance and supervision of Pro. Dr. Andreu Cabot and Dr. Paulina R. Martínez-Alanis. Some tests and characterizations were completed by other collaborators.



MDPI

Article

## Electrocatalytic Oxidation of Benzaldehyde on Gold Nanoparticles Supported on Titanium Dioxide

Li Gong <sup>1,2,†</sup>, Yu Jin <sup>3,†</sup>, Shiling Zhao <sup>4</sup>, Kaizhi Wang <sup>5,\*</sup>, Paulina R. Martínez-Alanis <sup>1,\*</sup> and Andreu Cabot <sup>1,6,\*</sup>

- <sup>1</sup> Catalonia Institute for Energy Research–IREC Sant Adrià de Besòs, 08930 Barcelona, Spain
- <sup>2</sup> Faculty of Chemistry, University of Barcelona, 08028 Barcelona, Spain
- <sup>3</sup> Key Laboratory of Applied Organic Chemistry (SKLAOC), The Key Laboratory of Catalytic Engineering of Gansu Province, College of Chemistry and Chemical Engineering, Lanzhou University, Lanzhou 730000, China; jiny21@lzu.edu.cn
- School of Petrochemical Engineering, Lanzhou University of Technology, Lanzhou 730050, China; slzhao@lut.edu.cn
- Department of Chemistry, Shanghai Key Laboratory of Molecular Catalysis and Innovative Materials, Fudan University, Shanghai 200433, China
- <sup>6</sup> ICREA, Pg. Lluís Companys 23, 08010 Barcelona, Spain
- \* Correspondence: 20110220096@fudan.edu.cn (K.W.); pmartinez@irec.cat (P.R.M.-A.); acabot@irec.cat (A.C.)
- † These authors contributed equally to this work.

**Abstract:** The electrooxidation of organic compounds offers a promising strategy for producing value-added chemicals through environmentally sustainable processes. A key challenge in this field is the development of electrocatalysts that are both effective and durable. In this study, we grow gold nanoparticles (Au NPs) on the surface of various phases of titanium dioxide (TiO<sub>2</sub>) as highly effective electrooxidation catalysts. Subsequently, the samples are tested for the oxidation of benzaldehyde (BZH) to benzoic acid (BZA) coupled with a hydrogen evolution reaction (HER). We observe the support containing a combination of rutile and anatase phases to provide the highest activity. The excellent electrooxidation performance of this Au-TiO<sub>2</sub> sample is correlated with its mixed-phase composition, large surface area, high oxygen vacancy content, and the presence of Lewis acid active sites on its surface. This catalyst demonstrates an overpotential of 0.467 V at 10 mA cm<sup>-2</sup> in a 1 M KOH solution containing 20 mM BZH, and 0.387 V in 100 mM BZH, well below the oxygen evolution reaction (OER) overpotential. The electrooxidation of BZH not only serves as OER alternative in applications such as electrochemical hydrogen evolution, enhancing energy efficiency, but simultaneously allows for the generation of high-value byproducts such as BZA.

**Keywords:** electrooxidization; benzaldehyde; titanium dioxide; oxygen vacancy; Lewis acid active sites



Citation: Gong, L.; Jin, Y.; Zhao, S.; Wang, K.; Martínez-Alanis, P.R.; Cabot, A. Electrocatalytic Oxidation of Benzaldehyde on Gold Nanoparticles Supported on Titanium Dioxide. Nanomaterials 2024, 14, 1005. https://doi.org/10.3390/nano14121005

Academic Editor: Barbara Ballarin

Received: 14 May 2024 Revised: 6 June 2024 Accepted: 7 June 2024 Published: 10 June 2024



Copyright: © 2024 by the authors. Licensee MDPI, Basel, Switzerland. This article is an open access article distributed under the terms and conditions of the Creative Commons Attribution (CC BY) license (https://creativecommons.org/licenses/by/4.0/).

#### 1. Introduction

The excessive dependence on fossil fuels exacerbates environmental pollution and contributes to geopolitical energy issues [1]. Integrating renewable energy sources such as solar, wind, and tidal power into the electricity grid can significantly reduce carbon emissions and contribute to a more uniform distribution of power. This integration also holds promise for supporting the burgeoning global clean hydrogen energy sector [2]. However, the realization of this vision hinges on the development of cost-effective energy storage technologies and particularly electrochemical technologies and materials for converting electrical energy into chemical energy [3].

One of the key processes in this field is the electrolysis of water, where the hydrogen evolution reaction (HER) at the cathode is highly regarded due to its high energy density and clean attributes [4,5]. Conversely, the oxygen evolution reaction (OER) at the anode, with a substantial thermodynamic potential (1.23 V vs. RHE), impedes multiple proton–electron transfer kinetics and consumes over 80% of the electricity used in

water electrolysis. Additionally, the OER's product, oxygen, has relatively low economic value. Given these factors, substituting the OER with the electrooxidation of some biomass-derivate that have more favorable thermodynamics offers a strategic avenue for more energy-efficient production while also enabling the simultaneous creation of high-value-added biomass-derived chemicals [6–8]. Organic electrochemical oxidation reactions, including alcohol and aldehyde oxidations [9,10], typically require much lower theoretical thermodynamic potentials than the OER, as evidenced by reactions like the urea oxidation reaction (0.37 V vs. RHE) [11], hydrazine oxidation reaction (–0.33 V vs. RHE) [12], ammonia oxidation reaction (0.06 V vs. RHE) [13,14], and glucose oxidation reaction (0.05 V vs. RHE) [15]. These reactions not only promise greater energy efficiency than OER-based water splitting but also expand the potential applications of electrolytic processes in producing economically significant chemicals derived from biomass products, i.e., having net-zero and even negative CO<sub>2</sub> emissions.

Numerous catalysts based on Co, Fe, Ni, and Cu-based materials dispersed on diverse high surface area supports such as carbon cloth (CC) or nickel foam (NF) have been employed as electrooxidation catalysts [8,11,15]. For example, Sun's group has explored  $Ni_2P/Ni/NF$  as electrocatalyst for the oxidation of furfural to 2-furoic acid coupled with  $H_2$  evolution [16]. Furthermore, Wang's group reported a bipolar hydrogen production system, which couples the low-potential anodic oxidation of biomass aldehydes with cathodic HER. In this system, a two-electrode electrolyser for bipolar hydrogen production was assembled using Cu foam as the anode and Pt/C as the cathode, with serpentine flow channels. Under an applied voltage of only ~0.1 V, both the cathode and anode can simultaneously generate  $H_2$  [17]. We have also demonstrated the viability of the oxidation of other small molecules such as ethanol, methanol, urea, formate, and ethylene glycol [18,19].

As an electrocatalyst, gold (Au) is an excellent candidate for the oxidation of alcohols and aldehydes due to the facile formation of highly active Au-O-H intermediate states with reactants [20]. Au is generally dispersed onto substrates able to modulate its properties and minimize aggregation due to its high cost and relatively low abundance. Rutile and anatase titanium dioxide (TiO<sub>2</sub>) nanoparticles (NPs) with a bandgap of 3.1–3.2 eV are widely used in organic compound degradation and catalysis for their low cost, excellent stability, significantly large surface area, and adjustable electronic properties. The rutile phase exhibits higher catalytic activity, whereas the anatase structure is more stable [21,22]. TiO<sub>2</sub>-P25 belongs to the mixed-phase type, with an approximate weight ratio of 80/20 between anatase and rutile. The mixing of the two phases increases the oxygen defect density within the TiO<sub>2</sub> lattice, enhancing the concentration of charge carriers. This leads to an increase in the number of holes, endowing it with a stronger ability to capture components, including water, oxygen, and organic compounds, on the surface.

To explore the performance of Au nanoparticles (NPs) loaded on TiO<sub>2</sub> support as a potential electrooxidation catalyst, as well as the alternative electrocatalytic anodic reaction of the OER, here, we choose the benzaldehyde (BZH) electrooxidation to benzoic acid (BZA) as an OER alternative. BZH is widely acknowledged as a versatile platform for biomass intermediates, given its capability to be transformed into numerous highly valuable chemical feedstocks. The reduction products benzyl alcohol (BA) and hydrobenzoin (HDB), and the hydrolysis product toluene are important high-value-added chemicals [23,24]. Additionally, the BZH oxidation product BZA plays a crucial role as a precursor in the biosynthesis of numerous secondary metabolites and its salts are widely employed as food preservatives due to their antimicrobial properties [25]. Moreover, BZA serves as a key building block in the industrial synthesis of various organic compounds [26]. As the catalyst, we explore the use of Au NPs supported on three types of TiO<sub>2</sub>, anatase TiO<sub>2</sub> (TiO<sub>2</sub>-A), rutile TiO<sub>2</sub> (TiO<sub>2</sub>-R), and TiO<sub>2</sub>-P25 with a phase mixture. The catalyst's physicochemical properties are thoroughly investigated and their performance toward the BZH electrooxidation to BZA is tested as a function of the support phase.

Nanomaterials **2024**, 14, 1005 3 of 12

#### 2. Materials and Methods

#### 2.1. Reagents and Chemicals

All reagents and chemicals were used as received without any further purification. Metal oxides,  $TiO_2$ -P25, anatase  $TiO_2$  ( $TiO_2$ -A), and rutile  $TiO_2$  ( $TiO_2$ -R) were supplied by Evonik. HAuCl<sub>4</sub>·4 H<sub>2</sub>O, sodium hydroxide (NaOH, 97%), and hydrochloric acid (HCl, 37%) were purchased from Sigma Aldrich.

#### 2.2. Synthesis of the Au-TiO<sub>2</sub>-P25, Au-TiO<sub>2</sub>-A, and Au-TiO<sub>2</sub>-R

Au-loaded TiO<sub>2</sub> samples were prepared by a modified impregnation method [27]. Briefly, 0.1 g powder TiO<sub>2</sub> was uniformly dispersed in 10 mL of a 0.1 mg<sub>Au</sub> mL<sup>-1</sup> aqueous HAuCl<sub>4</sub> solution (pH adjusted to 9 with 0.2 M NaOH). Following that, the mixture was heated at 80 °C for 2 h while vigorously stirred. Upon cooling to 25 °C, the suspension underwent filtration, followed by a comprehensive wash with deionized water. The material was subsequently dried in a vacuum oven at 60 °C for 12 h. Next, it underwent annealing in a 5% hydrogen/argon atmosphere (flow rate: 80 mL/min) at 350 °C for reduction with a duration of 4 h.

#### 2.3. Characterizations

Powder X-ray diffraction (XRD) patterns were collected at 40 kV and 40 mA with Cu  $K\alpha$  radiation ( $\lambda = 1.5406 \text{ Å}$ ). X-ray photoelectron spectroscopy (XPS) was conducted on a ThermoFisher (ESCALAB 250Xi) system with Mono Al K $\alpha$  radiation. The vacuum of the analysis chamber was approximately  $2 \times 10^{-9}$  mbar. The energy, voltage, and beam current were 1486.6 eV, 16 kV, and 15 mA, respectively. Accurate binding energies ( $\pm 0.1$  eV) were corrected with respect to the position of the adventitious C 1s peak at 284.6 eV. To determine the specific acid sites of Brønsted or Lewis acid sites, Fourier-transform infrared spectroscopy (FTIR) spectra of pyridine adsorption were collected on a Thermo-Fisher Nicolet iS50 spectrometer. Self-supporting pellets made of the catalysts were placed in a flow cell and evacuated under reduced pressure at 300 °C for 2 h to remove the adsorbed moisture from the material surface. Spectrum was recorded in the range of 4000–650 cm<sup>-1</sup> at 150 °C. Transmission electron microscopy (TEM) measurements were carried out on a Tecnai G<sub>2</sub> F20 S-Twin electron microscope, operating at 200 kV. H<sub>2</sub>-temperature programmed reduction (H<sub>2</sub>-TPR) profiles were conducted on the Autochem HP system (Micromeritics Instrument Corp.). The particle size distribution was determined using the software Nano Measurer developed by the Department of Chemistry at Fudan University. At least 50 particles were manually marked and measured from each sample. The chemical compositions of catalysts were analyzed on a PerkinElmer inductively coupled plasma optical emission spectrometer (ICP-OES) Optima 8300 DV.

#### 2.4. Product Identification and Conversion and Selectivity Quantification

Organic compounds were analyzed via high-performance liquid chromatography (HPLC) using an Agilent 1200 series apparatus operating at 25 °C. The HPLC setup comprised an ultraviolet–visible detector and a 4.6 mm  $\times$  150 mm Shim-pack GWS 5  $\mu m$  C18 column. Elution employed solvents A (5 mM ammonium formate aqueous solution) and B (acetonitrile), with a gradient program of 60% B and 40% A over 11 min. The flow rate was maintained at 0.5 mL/s, and the injection volume was 1  $\mu L$ . To exclude the effect of the BZH Cannizzaro reaction on the product quantification, the samples need to be injected into the HPLC system as soon as possible. Calibration curves of standard chemicals facilitated product determination and quantification. Total conversion was computed using the following formula:

Conv. 
$$\% = \frac{\text{moles of BZH consumed}}{\text{initial moles of BZH}} \times 100\%$$
 (1)

Nanomaterials **2024**, 14, 1005 4 of 12

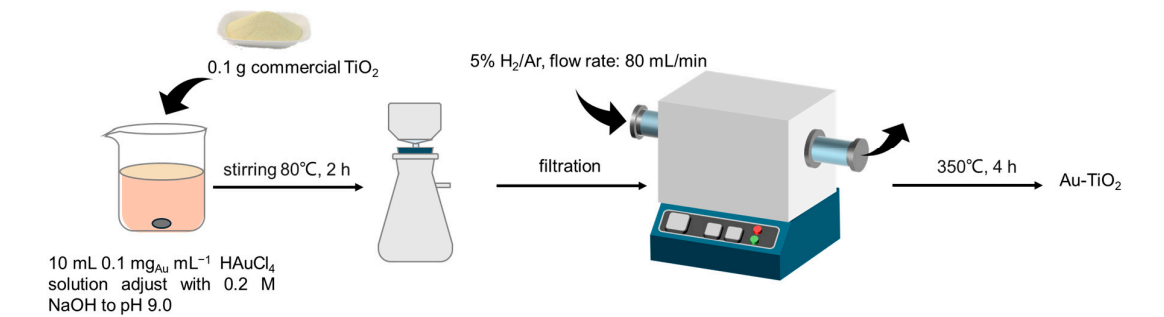
#### 2.5. Electrochemistry Tests

The electrochemical performance of the electrocatalyst was evaluated on a CHI66E (Shanghai Chenhua) workstation using a 3-electrode system in an H-cell reactor divided by a Nafion 117 proton exchange membrane. The working electrode was prepared as follows: 6 mg powder was dispersed into 500  $\mu$ L H<sub>2</sub>O, 420  $\mu$ L ethanol, and 80  $\mu$ L 5% Nafion solution. For glassy carbon working electrode preparation, 8  $\mu$ L ink solution was dropped on a glassy carbon working electrode (d = 0.15 cm, ~0.7 mg cm<sup>-2</sup>) and left to dry. Carbon cloth (4 cm<sup>2</sup>) and Ag/AgCl (KCl-saturated) were used as counter and reference electrodes, respectively. Linear sweep voltammetry (LSV) was tested with a glassy carbon working electrode and results were calibrated with the Nernst Equation (2) to the reference hydrogen electrode (RHE) without iR correction. Electrochemical impedance spectroscopy (EIS) was tested at 1.6 V vs. RHE. Dropping the ink to 1 × 2 cm<sup>2</sup> carbon cloth (keep loading mass: ~1.5 mg cm<sup>2</sup>) as working electrode for conversion and stability tests.

$$E_{RHE} = E + 0.0591 \times pH + E_{Ag/AgCl}^{\theta}$$
 (2)

#### 3. Results and Discussion

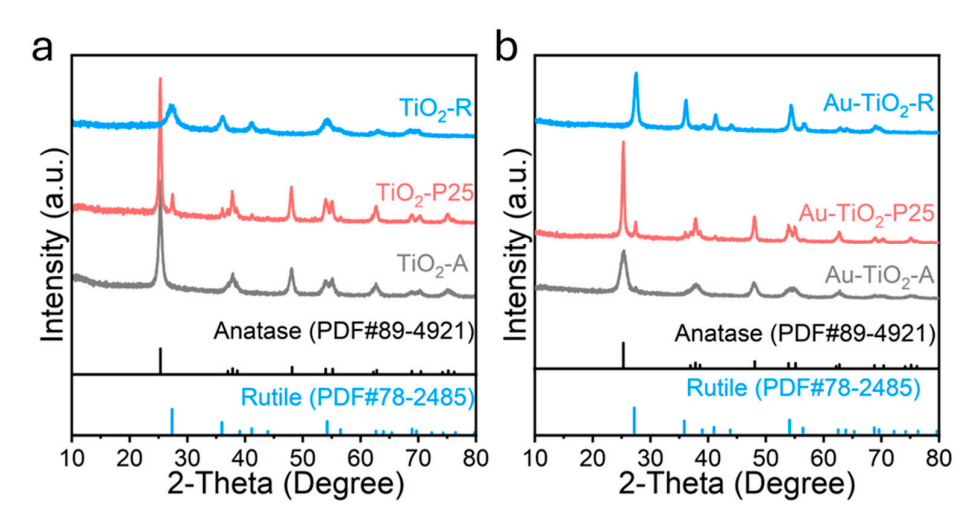
The three catalytic materials, Au-TiO $_2$ -P25, Au-TiO $_2$ -A, and Au-TiO $_2$ -R, were prepared by impregnation followed by H $_2$  reduction process (Scheme 1, see details in the Section 2). XRD patterns are displayed in Figure 1a. The peaks at 25.35°, 37.01°, 37.85°, 38.64°, 48.14°, 53.97°, and 55.18° correspond to anatase TiO $_2$  (TiO $_2$  PDF#89-4921), while peaks at 27.44°, 36.08°, 41.24°, 54.32°, 56.62°, and 69.00° are assigned to rutile TiO $_2$  (TiO $_2$  PDF#78-2485). Notice how the peaks co-exist in the mixed phase TiO $_2$ -P25. The XRD patterns of the materials after the Au loading (Figure 1b) reveal that the crystal structure of TiO $_2$  is maintained. The Au peaks are not prominently observed, potentially due to the low loading.



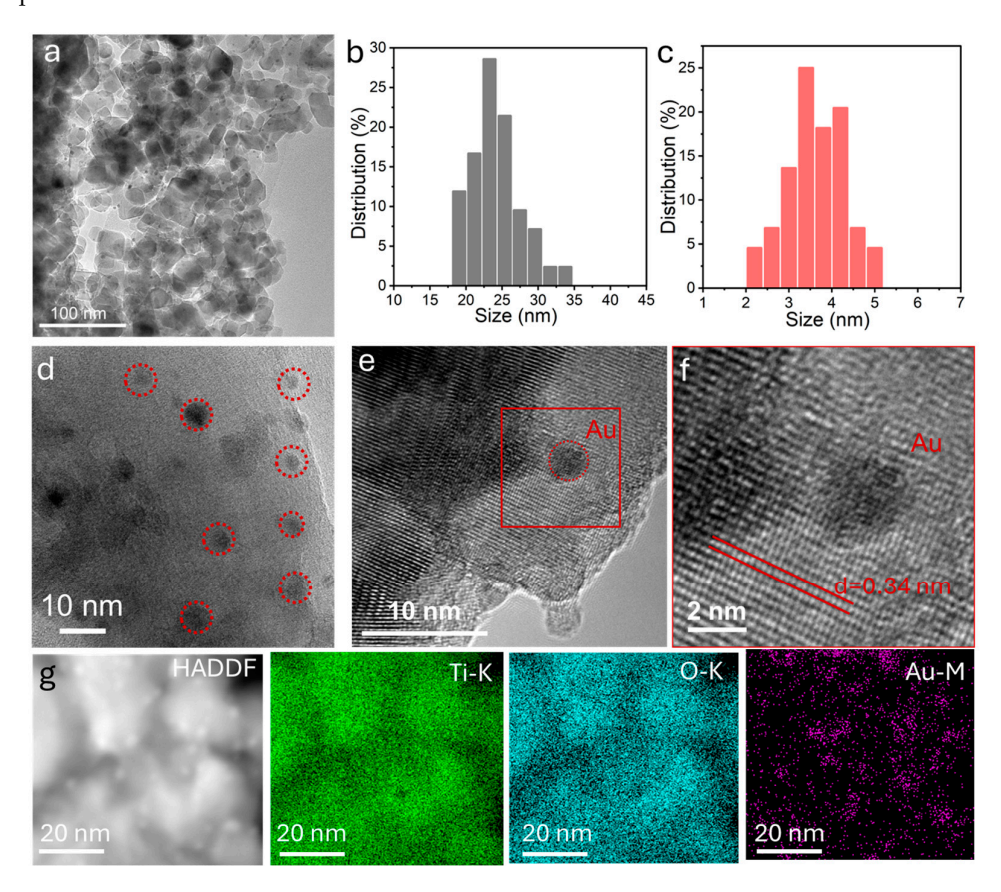
**Scheme 1.** Scheme of the preparation process of the electrocatalyst Au-TiO<sub>2</sub>.

Figure 2a shows the regular polyhedral morphologies of TiO<sub>2</sub>-P25 NPs with a uniform distribution of Au NPs. We utilized particle analysis software to perform particle size measurements on the TiO<sub>2</sub> NPs and Au NPs as displayed in Figure 2b,c, respectively. TiO<sub>2</sub>-P25 NPs had an aveage size of 24 nm (Figure 2b). Numerous Au NPs with a size of around 3.5 nm are distributed on their surface (Figure 2c,d). Both other materials, Au-TiO<sub>2</sub>-A and Au-TiO<sub>2</sub>-R, show similar morphologies and Au particle sizes (Figure S1). HRTEM images in Figure 2e confirm both the crystallographic structure of TiO<sub>2</sub> in Au-TiO<sub>2</sub>-P25 and the presence of crystalline Au NPs. From the STEM-EDS chemical composition maps of Au-TiO<sub>2</sub>-P25 (Figure 2g), it can be observed that Ti and O are uniformly distributed throughout the entire material, as well as the uniform distribution of Au particles. The amount of Au was determined by ICP and found to match the nominal 1 wt% concentration introduced.

Nanomaterials **2024**, 14, 1005 5 of 12



**Figure 1.** XRD patterns of the different catalytic materials, (**a**) TiO<sub>2</sub>, (**b**) Au-TiO<sub>2</sub>, including reference patterns for rutile and anatase.



**Figure 2.** (a) TEM image of Au-TiO<sub>2</sub>-P25. (b) TiO<sub>2</sub> particle size histogram of Au-TiO<sub>2</sub>-P25. (c) TEM image of Au-TiO<sub>2</sub>-P25. (d) Au particle size histogram of Au-TiO<sub>2</sub>-P25. (e) HRTEM image of Au-TiO<sub>2</sub>-P25. (f) Magnified red framed area of an Au NP and TiO<sub>2</sub> lattice space of 0.34 nm. (g) STEM-EDS chemical composition maps of Au-TiO<sub>2</sub>-P25.

Au-TiO<sub>2</sub> samples show a hydrophilic surface with a static water contact angle of about 35° (Figure 3a). N<sub>2</sub> adsorption–desorption isotherms of the four materials tested, TiO<sub>2</sub>-P25, Au-TiO<sub>2</sub>-P25, Au-TiO<sub>2</sub>-R, and Au-TiO<sub>2</sub>-A, show type IV with H1 hysteresis loops characteristic of mesoporous structures with a Brunauer–Emmett–Teller (BET) surface area of 49 m<sup>2</sup> g<sup>-1</sup>, 48 m<sup>2</sup> g<sup>-1</sup>, 31 m<sup>2</sup> g<sup>-1</sup>, and 41 m<sup>2</sup> g<sup>-1</sup>, respectively (Figures 4b and S2a,c,e). Au-TiO<sub>2</sub>-P25 has a significant distribution of mesopores with pore sizes around 12 nm. H<sub>2</sub>-TPR curves (Figure 3d) show one broad peak from 80 °C to 700 °C, which is assigned to

the reduction of bulk  $TiO_2$  species. The electron spin resonance (EPR) spectra of  $TiO_2$ -P25 and Au- $TiO_2$ -P25 both show noticeable signals at g = 2.004 (Figure 3e) ascribed to the existence of oxygen vacancies. The very similar spectra obtained indicate that the amount of surface oxygen vacancies is independent of the Au NP modification.

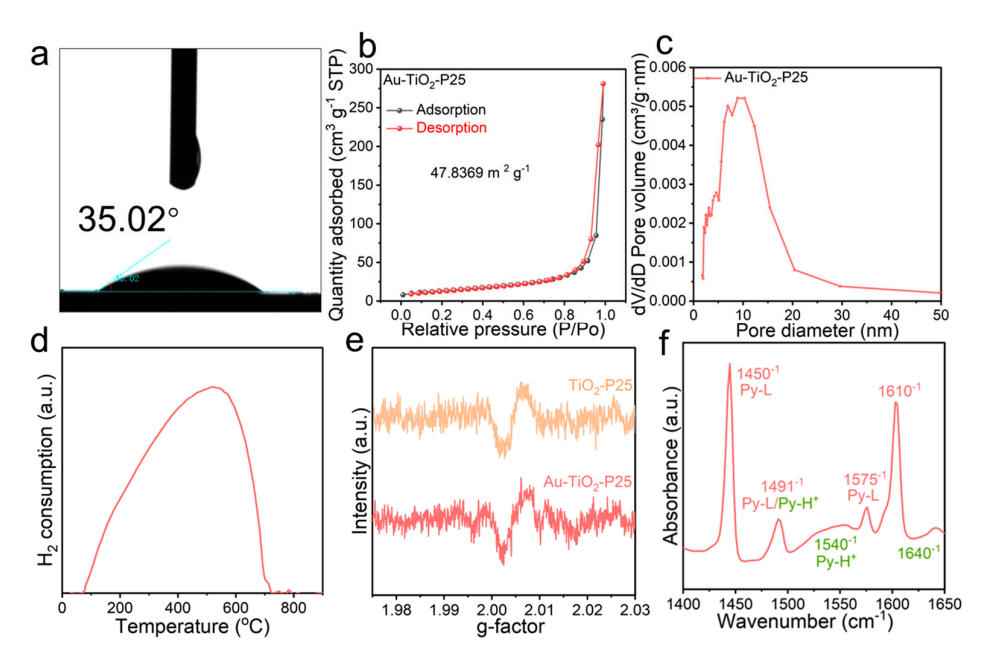


**Figure 3.** (a) A drop of water on Au-TiO<sub>2</sub>-P25; (b) nitrogen adsorption–desorption isothermal curves and (c) pore diameter distribution of Au-TiO<sub>2</sub>-P25; (d)  $H_2$ –temperature programmed reduction ( $H_2$ -TPR) profiles of Au-TiO<sub>2</sub>-P25; (e) EPR signals of TiO<sub>2</sub>-P25 and Au-TiO<sub>2</sub>-P25; (f) FTIR-Py spectrum tested at 150 °C to unravel the Brønsted/Lewis acid sites on the surface of Au-TiO<sub>2</sub>-P25.

The interaction of Brønsted/Lewis acid sites with alkaline probe molecules on the surface of Au-TiO<sub>2</sub>-P25 was investigated using pyridine-adsorbed FTIR. As shown in Figure S3, at different active sites on the material surface, pyridine exhibits varied adsorption behaviors. The infrared characteristic peaks and intensities of the probe molecule pyridine can be used to discern the types of active sites on the material surface. Brønsted acid sites and Lewis acid sites on the catalyst surface are identified at 1540 cm<sup>-1</sup> and 1450 cm<sup>-1</sup>, respectively. The signal at 1610 cm<sup>-1</sup> was also ascribed to the strong Lewisbound peak pyridine of pyridine ring vibration. The peak at 1640 cm<sup>-1</sup> was ascribed to the pyridinium ion ring vibration owing to pyridine molecules bound to Brønsted acid sites. The in-plane ring vibration absorption peak of pyridine molecules was observed at 1575 cm<sup>-1</sup>. The C-H vibration absorption peak on the pyridine molecule was observed at 1491 cm<sup>-1</sup> [28]. From the FTIR spectrum, we conclude that there is a notable density of Lewis acid sites on the catalyst surface but barely Brønsted sites. The electron-rich O in carbonyl groups tends to adsorb onto Lewis acidic sites for its electron-accepting property; therefore, accelerating the reaction rate. Several previous works have proved the efficiency of Lewis acid sites for electrooxidization reactions such as OER [29,30] and alcohol electrooxidization [31,32].

Figure 4a displays the Au 4f XPS spectra of the different materials. Peaks at 83.20 eV and 86.85 eV are assigned to Au  $4f_{7/2}$  and Au  $4f_{5/2}$  electronic states of metallic Au. The Ti  $2p_{3/2}$  XPS spectrum of Au-TiO<sub>2</sub>-P25 shows one peak at 458.36 eV. This peak is redshifted for Au-TiO<sub>2</sub>-A and blueshifted for Au-TiO<sub>2</sub>-R. The O 1s XPS spectrum exhibits similar binding energy shifts (Figure 4c). The simultaneous shift in the Ti 2p and O 1s spectra is associated with a shift in the Fermi level in the TiO<sub>2</sub>. Notice this shift is not followed by the Au spectra, denoting a relatively independent electronic structure, consistent with our previous observations on SnO<sub>2</sub> [33]. The O 1s XPS spectra can be deconvoluted in

three peaks at 529.41 eV, 529.92 eV, and 531.1 eV corresponding to lattice  $O^{2-}$ , O-containing adsorbed species, and OH groups on the material surface.

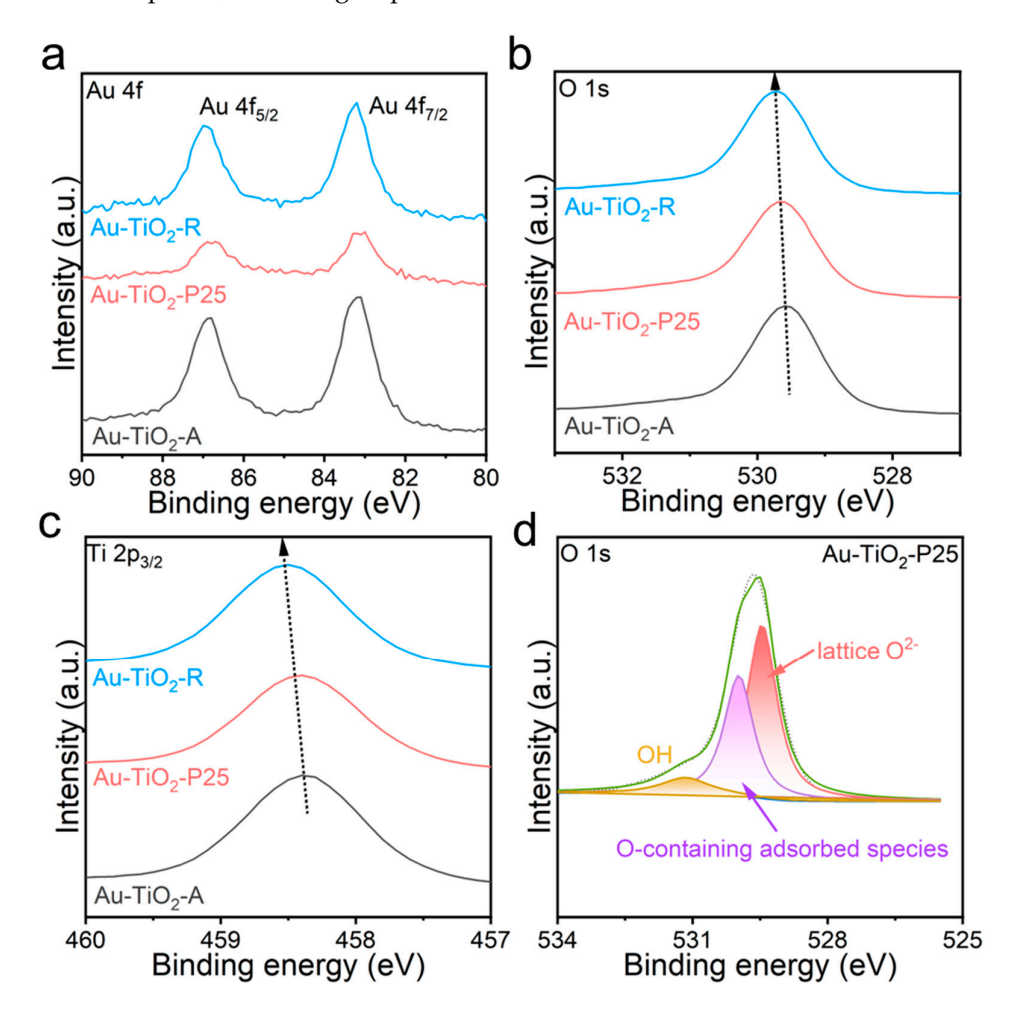


**Figure 4.** XPS spectra of (a) Au 4f; (b) Ti  $2p_{3/2}$ ; (c,d) O 1s in materials Au-TiO<sub>2</sub>-P25, Au-TiO<sub>2</sub>-A; and Au-TiO<sub>2</sub>-R.

The catalysts' electrooxidation activity towards the OER was tested using an H-cell reactor with a three-electrode system. Au-TiO<sub>2</sub> was supported on a glassy carbon as the working electrode, Ag/AgCl (KCl-saturated) as the reference electrode, and a 4 cm<sup>2</sup> carbon cloth was used as the counter electrode. The electrooxidation performance was tested in 1 M KOH solution by LSV at a scan rate of 50 mV s<sup>-1</sup>, and the results as shown in Figure 5a. Au-TiO<sub>2</sub>-P25 showed the highest activity towards OER, with an overpotential of 0.505 V at 10 mA cm<sup>-2</sup>. When adding BZH into the system, the overpotentials were significantly decreased for all materials (Figure 5b). Still, Au-TiO<sub>2</sub>-P25 showed the lowest overpotential of 0.467 V at 10 mA cm<sup>-2</sup> (Figure 5c). Moreover, the current densities at 1.70, 1.75, and 1.80 V vs. RHE in the presence of BZH were all larger than those in the absence of BZH (Figure 5d).

The Nyquist plot of the EIS spectra of Au-TiO<sub>2</sub>-P25 is shown in Figure 5e. Upon adding BZH, the semicircle diameter shrinks from 41  $\Omega$  to 18  $\Omega$ . The solution resistance also decreased from approximately 4  $\Omega$  to 2  $\Omega$ . When increasing the concentration of BZH to 100 mM, the overpotential further decreased to 0.387 V at 10 mA cm<sup>-2</sup>. The above data demonstrate both the excellent performance of catalyst Au-TiO<sub>2</sub>-P25 in the electrooxidation reaction and that the addition of BZH to the system can reduce the energy consumption of the redox electrochemical reaction that produces hydrogen at the cathode, the carbon cloth counter electrode.

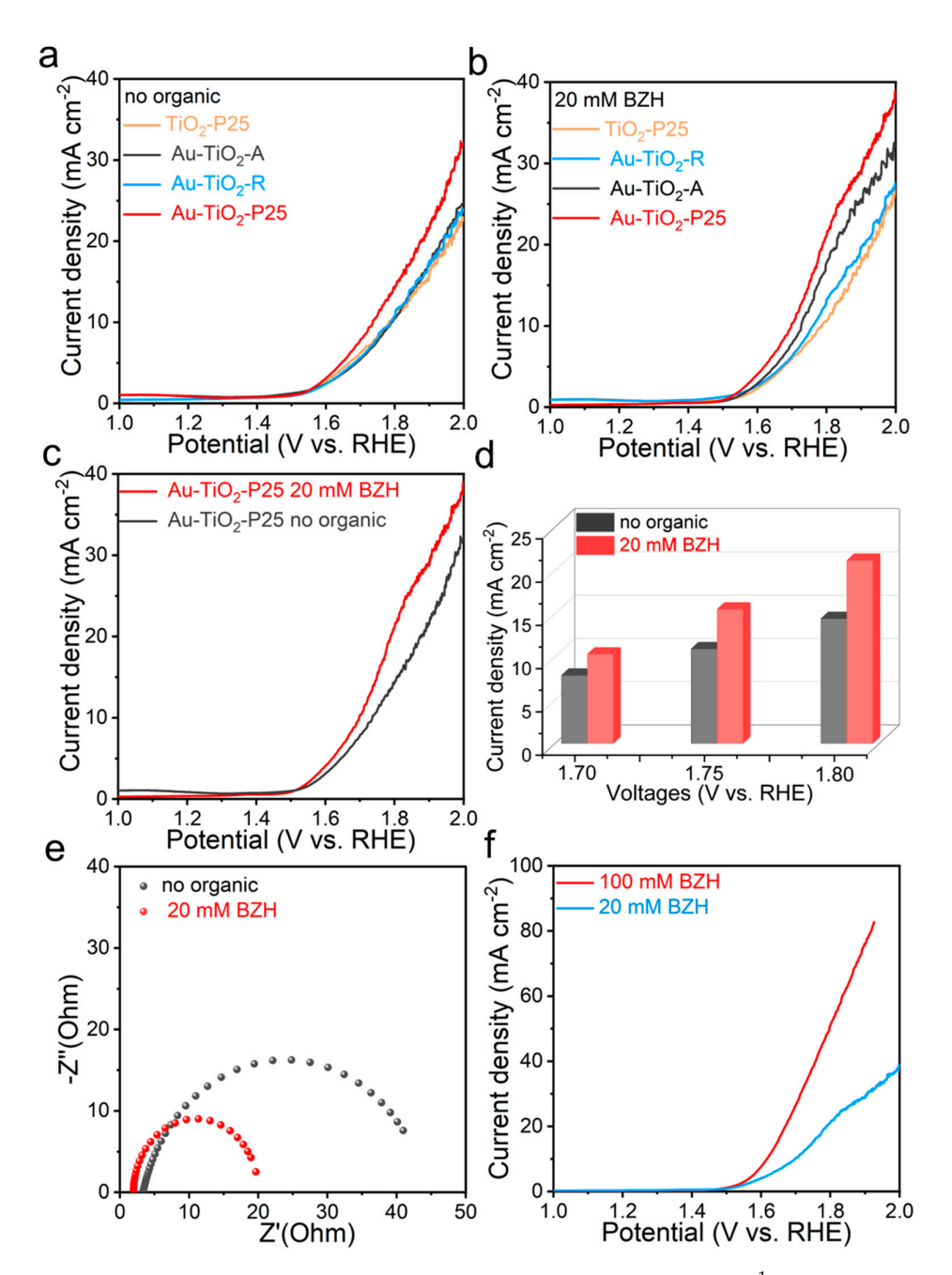


**Figure 5.** (**a**,**b**) LSV curves of different materials at a scan rate of 50 mV s $^{-1}$  in (**a**) 1 M KOH solution; (**b**) 1 M KOH solution and 20 mM BZH. (**c**) Comparison of LSV curves of Au-TiO<sub>2</sub>-P25 in 1.0 M KOH and in the presence of 20 mM BZH. (**d**) Comparison of the current density of Au-TiO<sub>2</sub>-P25 at 1.70, 1.75, and 1.80 V vs. RHE in 1.0 M KOH and in addition of 20 mM BZH. (**e**) Nyquist plots of Au-TiO<sub>2</sub>-P25 electrode in 1.0 M KOH and in addition of 20 mM BZH. (**f**) Comparison of LSV curves when adding 20 mM BZH or 100 mM BZH.

To further evaluate the catalyst performance, the electrocatalyst Au-TiO $_2$ -P25 was supported onto carbon cloth and its efficiency was assessed towards OER and BZH electrooxidation reactions. The tests were conducted using an immersion area of  $1 \times 1$  cm $^2$  in 1 M KOH electrolyte in the absence or the presence of BZH, and at various voltages within a 30-min timeframe. Fresh electrode materials were used for each experiment. Figure 6a illustrates the sustained OER performance of the electrocatalyst Au-TiO $_2$ -P25 over 30 min at voltages of 1.5 V, 1.6 V, 1.7 V, and 1.8 V vs. RHE. The current density increased with the voltage. Upon subsequent addition of 20 mM BZH to the system, the current density

further increased (Figure 6b). The change in current density, associated with the BZH electrooxidation, was determined by integrating the charge (Q) passing through the system at each voltage during BZH electrooxidation, and then subtracting the corresponding OER values (Figure 6c). The difference in Q values (DQ) shows no monotonous pattern, but it increased with voltage in the range from 1.5 V to 1.6 V and decreased with voltage at higher applied potentials. This is related to the increase in OER at voltages above 1.6 V. Still, the conversion of BZH to BZA increased with the voltage from 10% at 1.6 V vs. RHE to 29% at 1.8 V vs. RHE (Figure 6d). To assess the electrocatalyst stability, we conducted five consecutive 30-min cyclic tests. From Figure 6e, it can be observed that the catalyst exhibits excellent stability with no major variation in current density at constant voltages 1.6 V vs. RHE of five cycles with 30 min/ cycle. Furthermore, the conversion rate of BZH remained constant at 15–16% (Figure 6f).

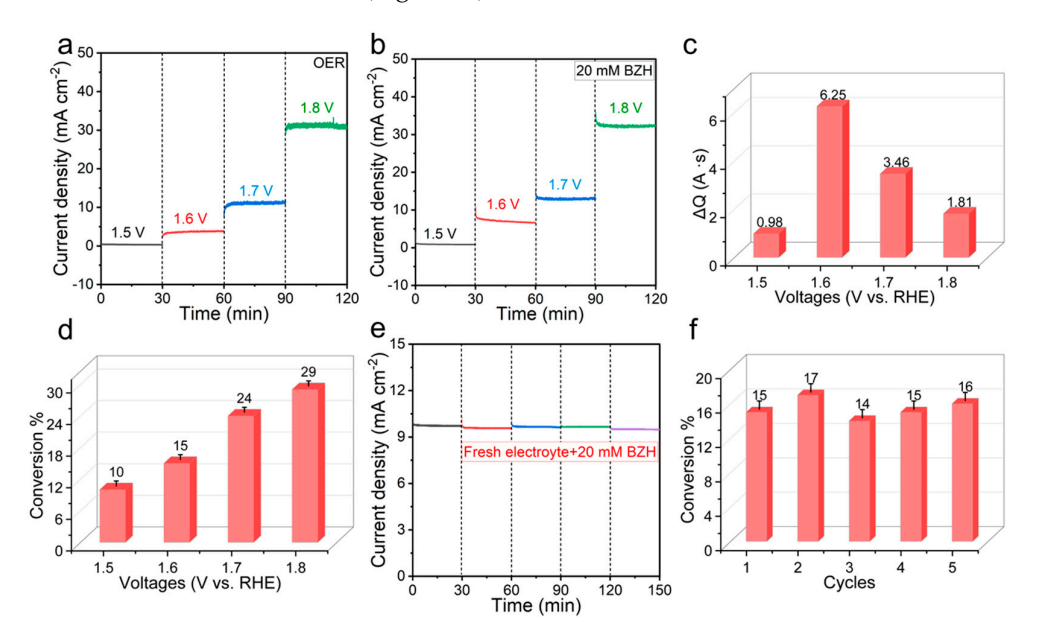


**Figure 6.** (a) ORE i-t curve in 1 M KOH at different voltages vs. RHE. (b) OER + BZH electrooxidation i-t curves in 1 M KOH with 20 mM BZH at different voltages vs. RHE. (c) Accumulated charge difference (DQ) between BZH electrooxidation and OER within 30 min at different voltages. (d) Conversion of BZH to BZA within 30 min as a function of the applied voltage. (e) Stability tests of 5 cycles i-t curves at constant voltage 1.6 V vs. RHE. (f) Conversion of BZH to BZA during 5 consecutive 30-min periods.

Under strong alkaline conditions, BZH undergoes the autoxidation-reduction reaction known as the Cannizzaro reaction. The pre-step of the BZH electrooxidation reaction shares with the Cannizzaro reaction the first rapid and crucial step of formation of an intermediate by combining BZH with hydroxide ions, as shown in Figure 7. The high OH<sup>-</sup> concentration at pH 14 strongly promotes this step (Figure S4). Following this, when applying positive voltages, there are two possible reaction pathways, both involving the intermediate product bound to gold with the oxygen atom. A possible mechanism is that both electrons transfer stepwise through the solution to Au (downside). Another possibility is that the two electrons transfer separately. One electron moves from the oxygen of the intermediate to the electrode material, while the other electron transfers from the hydroxide ion to the electrode material, forming a hydroxyl adsorption state. Subsequently, the C-H bond breaks, combining with hydroxyl to form a water molecule that is then removed [34–36]. Since TiO<sub>2</sub> itself also exhibits electrocatalytic properties towards OER and electrooxidization of BZH, the activity of the material originates from the combined effect of Au and the substrate TiO2. Therefore, we are more inclined towards a mechanism where the two electrons transfer separately. In this scenario, oxygen vacancies and Lewis basic sites effectively accept electrons transferred from hydroxide ions to form adsorbed

Nanomaterials **2024**, 14, 1005

hydroxyl groups, increasing the probability of bonding with H on intermediates, thus enhancing reaction efficiency. Due to the consistent loading amount of Au (~1%), the outstanding performance of Au-TiO<sub>2</sub>-P25 stems from the strong adsorption capability of TiO<sub>2</sub> towards substrates, its Lewis acid sites properties and the mixed anatase/rutile phase of TiO<sub>2</sub> catalysts with increased surface area and enhanced defect density.

**Figure 7.** Illustration of electrooxidization pathways of BZH on Au-TiO<sub>2</sub>-P25. Arrows represent the direction of paired electron transfer, while half-arrows represent single-electron transfer.

#### 4. Conclusions

This study demonstrates the electrooxidation of BZH into BZA in an alkaline 1.0 M KOH aqueous solution over different phase  $TiO_2$ -based catalysts loaded with Au NPs. Among the different phases of  $TiO_2$  as support catalysts, a mixture of anatase and rutile with 1 wt% Au loading showed the best OER performance due to its unique properties of mixed-phase, larger surface area, sufficient surface oxygen defects and Lewis acid sites. A decrease in overpotential at a constant current density of 10 mA cm $^{-2}$  was observed from 0.505 V to 0.476 V after the addition of 20 mM BZH into the anode chamber of the three-electrode H-cell test system. Finally, considering further energy-saving purposes, a higher concentration of 100 mM of BZH decreased the overpotential to 0.387 V consecutively. In addition, the catalyst demonstrated excellent stability.

**Supplementary Materials:** The following supporting information can be downloaded at https://www.mdpi.com/article/10.3390/nano14121005/s1. Figure S1: (a,b) TEM image of Au-TiO<sub>2</sub>-R; (c,d) TEM image of Au-TiO<sub>2</sub>-A; Figure S2: Nitrogen adsorption-desorption isothermal curves of materials and their pore sizes distributions (a,b) TiO<sub>2</sub>-P25; (c,d) Au-TiO<sub>2</sub>-R; (e,f) Au-TiO<sub>2</sub>-A; Figure S3: Diagram of pyridine adsorption on Brønsted acid sites and Lewis acid sites; Figure S4: LSV curves of material Au-TiO<sub>2</sub>-P25 at a scan rate of 50 mV s<sup>-1</sup> in 1 M KOH (pH 14) and 0.1 M KOH (pH 13).

**Author Contributions:** L.G. designed the experiment; performed XRD, SEM, and XPS data processing; and wrote the first draft of the manuscript. Y.J. conducted electrochemical measurements. L.G. and Y.J. contributed equally to this work. S.Z. methodology. K.W. prepared all the materials. P.R.M.-A. significantly contributed to the result discussion. A.C. conceived and guided the project and supervised the work. The manuscript was corrected and improved by all authors. All authors have read and agreed to the published version of the manuscript.

**Funding:** L. Gong thanks the China Scholarship Council for the scholarship support. This work was financially supported by the SyDECat project from the Spanish MCIN/AEI/FEDER (PID2022-136883OB-C22). The authors acknowledge funding from Generalitat de Catalunya 2021 SGR 01581 and European Union NextGenerationEU/PRTR.

Data Availability Statement: Data available on request from the authors.

Conflicts of Interest: The authors declare no conflicts of interest.

Nanomaterials **2024**, 14, 1005

#### References

 Zeng, G.; Sun, Q.; Horta, S.; Wang, S.; Lu, X.; Zhang, C.Y.; Li, J.; Li, J.; Ci, L.; Tian, Y.; et al. A Layered Bi<sub>2</sub>Te<sub>3</sub>@PPy Cathode for Aqueous Zinc-Ion Batteries: Mechanism and Application in Printed Flexible Batteries (Adv. Mater. 1/2024). Adv. Mater. 2024, 36, 2470004. [CrossRef]

- 2. Zhong, W.; Huang, W.; Ruan, S.; Zhang, Q.; Wang, Y.; Xie, S. Electrocatalytic Reduction of CO2 Coupled with Organic Conversion to Selectively Synthesize High-Value Chemicals. *Chem. Eur. J.* **2023**, 29, e202203228. [CrossRef] [PubMed]
- 3. Gong, M.; Cao, C.; Zhu, Q.-L. Paired electrosynthesis design strategy for sustainable CO<sub>2</sub> conversion and product upgrading. *EnergyChem* **2023**, *5*, 100111. [CrossRef]
- 4. Gao, G.; Chen, X.; Han, L.; Zhu, G.; Jia, J.; Cabot, A.; Sun, Z. Advances in MOFs and their derivatives for non-noble metal electrocatalysts in water splitting. *Coord. Chem. Rev.* **2024**, *503*, 215639. [CrossRef]
- 5. Wang, X.; Li, D.; Dai, J.; Xue, Q.; Yang, C.; Xia, L.; Qi, X.; Bao, B.; Yang, S.; Xu, Y.; et al. Blocking Metal Nanocluster Growth through Ligand Coordination and Subsequent Polymerization: The Case of Ruthenium Nanoclusters as Robust Hydrogen Evolution Electrocatalysts. *Small* **2023**, *20*, 2309176. [CrossRef] [PubMed]
- 6. Wu, X.; Wang, Y.; Wu, Z.-S. Design principle of electrocatalysts for the electrooxidation of organics. *Chem* **2022**, *8*, 2594–2629. [CrossRef]
- 7. Chen, G.; Li, X.; Feng, X. Upgrading Organic Compounds through the Coupling of Electrooxidation with Hydrogen Evolution. *Angew. Chem. Int. Ed.* **2022**, *61*, e202209014. [CrossRef] [PubMed]
- 8. Wang, T.; Cao, X.; Jiao, L. Progress in Hydrogen Production Coupled with Electrochemical Oxidation of Small Molecules. *Angew. Chem. Int. Ed.* **2022**, *61*, e202213328. [CrossRef]
- 9. Li, J.; Li, L.; Ma, X.; Wang, J.; Zhao, J.; Zhang, Y.; He, R.; Yang, Y.; Cabot, A.; Zhu, Y. Unraveling the role of iron on Ni-Fe alloy nanoparticles during the electrocatalytic ethanol-to-acetate process. *Nano Res.* **2024**, *17*, 2328–2336. [CrossRef]
- 10. Li, J.; Li, L.; Wang, J.; Cabot, A.; Zhu, Y. Boosting Hydrogen Evolution by Methanol Oxidation Reaction on Ni-Based Electrocatalysts: From Fundamental Electrochemistry to Perspectives. *ACS Energy Lett.* **2024**, *9*, 853–879. [CrossRef]
- 11. Shrestha, N.K.; Patil, S.A.; Salunke, A.S.; Inamdar, A.I.; Im, H. Unprecedented urea oxidation on Zn@Ni-MOF with an ultra-high current density: Understanding the competition between UOR and OER, catalytic activity limitation and reaction selectivity. *J. Mater. Chem. A* 2023, 11, 14870–14877. [CrossRef]
- 12. Shen, P.; Zhou, B.; Chen, Z.; Xiao, W.; Fu, Y.; Wan, J.; Wu, Z.; Wang, L. Ruthenium-doped 3D Cu<sub>2</sub>O nanochains as efficient electrocatalyst towards hydrogen evolution and hydrazine oxidation. *Appl. Catal. B* **2023**, 325, 122305. [CrossRef]
- 13. Cao, Y.; Yuan, S.; Meng, L.; Wang, Y.; Hai, Y.; Su, S.; Ding, W.; Liu, Z.; Li, X.; Luo, M. Recent Advances in Electrocatalytic Nitrate Reduction to Ammonia: Mechanism Insight and Catalyst Design. *ACS Sustain. Chem. Eng.* **2023**, *11*, 7965–7985. [CrossRef]
- 14. Zhong, C.; Hu, W.B.; Cheng, Y.F. Recent advances in electrocatalysts for electro-oxidation of ammonia. *J. Mater. Chem. A* **2013**, *1*, 3216–3238. [CrossRef]
- Howard, E.E.; Allen, J.T.; Coleman, J.L.; Small, S.D.; Karl, J.P.; O'Fallon, K.S.; Margolis, L.M. Ketone Monoester Plus Carbohydrate Supplementation Does Not Alter Exogenous and Plasma Glucose Oxidation or Metabolic Clearance Rate During Exercise in Men Compared with Carbohydrate Alone. J. Nutr. 2023, 153, 1696–1709. [CrossRef] [PubMed]
- 16. Jiang, N.; Liu, X.; Dong, J.; You, B.; Liu, X.; Sun, Y. Electrocatalysis of Furfural Oxidation Coupled with H<sub>2</sub> Evolution via Nickel-Based Electrocatalysts in Water. *ChemNanoMat* **2017**, *3*, 491–495. [CrossRef]
- 17. Wang, T.; Tao, L.; Zhu, X.; Chen, C.; Chen, W.; Du, S.; Zhou, Y.; Zhou, B.; Wang, D.; Xie, C.; et al. Combined anodic and cathodic hydrogen production from aldehyde oxidation and hydrogen evolution reaction. *Nat. Catal.* **2022**, *5*, 66–73. [CrossRef]
- 18. Liu, J.; Wang, Q.; Li, T.; Wang, Y.; Li, H.; Cabot, A. PdMoSb trimetallene as high-performance alcohol oxidation electrocatalyst. *Nano Res.* **2023**, *16*, 2041–2048. [CrossRef]
- 19. Li, T.; Wang, Q.; Wu, J.; Sui, Y.; Tang, P.; Liu, H.; Zhang, W.; Li, H.; Wang, Y.; Cabot, A.; et al. Strain and Shell Thickness Engineering in Pd3Pb@Pt Bifunctional Electrocatalyst for Ethanol Upgrading Coupled with Hydrogen Production. *Small* **2024**, 20, 2306178. [CrossRef]
- Sharma, R.K.; Bandichhor, R.; Mishra, V.; Sharma, S.; Yadav, S.; Mehta, S.; Arora, B.; Rana, P.; Dutta, S.; Solanki, K. Advanced metal oxide-based nanocatalysts for the oxidative synthesis of fine chemicals. *Mater. Adv.* 2023, 4, 1795–1830. [CrossRef]
- 21. Van Thuan, D.; Ngo, H.L.; Thi, H.P.; Chu, T.T.H. Photodegradation of hazardous organic pollutants using titanium oxides -based photocatalytic: A review. *Environ. Res.* **2023**, 229, 116000. [CrossRef] [PubMed]
- 22. Luo, C.; Ren, X.; Dai, Z.; Zhang, Y.; Qi, X.; Pan, C. Present Perspectives of Advanced Characterization Techniques in TiO<sub>2</sub>-Based Photocatalysts. *ACS Appl. Mater. Interfaces* **2017**, *9*, 23265–23286. [CrossRef] [PubMed]
- 23. Gong, L.; Zhang, C.Y.; Li, J.; Montaña-Mora, G.; Botifoll, M.; Guo, T.; Arbiol, J.; Zhou, J.Y.; Kallio, T.; Martĺnez-Alanis, P.R.; et al. Enhanced Electrochemical Hydrogenation of Benzaldehyde to Benzyl Alcohol on Pd@Ni-MOF by Modifying the Adsorption Configuration. ACS Appl. Mater. Interfaces 2024, 16, 6948–6957. [CrossRef] [PubMed]
- 24. Gong, L.; Zhang, C.Y.; Mu, X.; Han, X.; Li, J.; Arbiol, J.; Zhou, J.Y.; Kallio, T.; Martĺnez-Alanis, P.R.; Cabot, A. Semiconductor nanosheets for electrocatalytic self-coupling of benzaldehyde to hydrobenzoin. *J. Chem. Eng.* **2024**, *479*, 147612. [CrossRef]
- 25. Dong, Y.; Dong, L.; Gu, X.; Wang, Y.; Liao, Y.; Luque, R.; Chen, Z. Sustainable production of active pharmaceutical ingredients from lignin-based benzoic acid derivatives via "demand orientation". *Green Chem.* **2023**, *25*, 3791–3815. [CrossRef]

Nanomaterials **2024**, 14, 1005

26. Zhang, X.; Ma, S.; Gao, B.; Bi, F.; Liu, Q.; Zhao, Q.; Xu, J.; Lu, G.; Yang, Y.; Wu, M. Effect of benzoic acid and dopamine hydrochloride as a modulator in the water resistance of Universitetet i Oslo-67: Adsorption performance and mechanism. *J. Colloid Interface Sci.* 2023, 651, 424–435. [CrossRef] [PubMed]

- 27. Wang, K.; Sun, Z.; Guo, W.; Chen, M.; Zhu, C.; Fei, J.; Liu, Y.; He, H.; Cao, Y.; Bao, X. Upgrading Waste Polylactide via Catalyst-Controlled Tandem Hydrolysis-Oxidation. *ChemSusChem* 2023, 16, e202301128. [CrossRef] [PubMed]
- 28. Du, P.; Zheng, P.; Song, S.; Wang, X.; Zhang, M.; Chi, K.; Xu, C.; Duan, A.; Zhao, Z. Synthesis of a novel micro/mesoporous composite material Beta-FDU-12 and its hydro-upgrading performance for FCC gasoline. *RSC Adv.* **2016**, *6*, 1018–1026. [CrossRef]
- 29. Zhao, S.; Wang, Y.; Hao, Y.; Yin, L.; Kuo, C.-H.; Chen, H.-Y.; Li, L.; Peng, S. Lewis Acid Driving Asymmetric Interfacial Electron Distribution to Stabilize Active Species for Efficient Neutral Water Oxidation. *Adv. Mater.* **2024**, *36*, 2308925. [CrossRef]
- 30. Qi, J.; Shen, X.; Chen, M.; Shangguan, E.; Zhang, W.; Cao, R. Lewis acid Mg<sup>2+</sup>-doped cobalt phosphate nanosheets for enhanced electrocatalytic oxygen evolution reaction. *Chem. Commun.* **2022**, *58*, 10801–10804. [CrossRef]
- 31. Guo, J.; Wang, G.; Cui, S.; Xia, B.; Liu, Z.; Zang, S.-Q.; Wang, S. Enhanced adsorption with hydroxymethyl and aldehyde over the heterophase interface for efficient biomass electrooxidation. *Sci. China Mater.* **2023**, *66*, 2698–2707. [CrossRef]
- 32. Tian, H.; Zhang, Z.-Y.; Fang, H.; Jiao, H.; Gao, T.-T.; Yang, J.-T.; Bian, L.; Wang, Z.-L. Selective electrooxidation of methane to formic acid by atomically dispersed CuOx and its induced Lewis acid sites on V2O5 in a tubular electrode. *Appl. Catal. B* **2024**, 351, 124001. [CrossRef]
- 33. Cabot, A.; Arbiol, J.; Morante, J.R.; Weimar, U.; Bârsan, N.; Göpel, W. Analysis of the noble metal catalytic additives introduced by impregnation of as obtained SnO<sub>2</sub> sol-gel nanocrystals for gas sensors. *Sens. Actuators B Chem.* **2000**, *70*, 87–100. [CrossRef]
- 34. Tremiliosi-Filho, G.; Gonzalez, E.R.; Motheo, A.J.; Belgsir, E.M.; Léger, J.M.; Lamy, C. Electro-oxidation of ethanol on gold: Analysis of the reaction products and mechanism. *J. Electroanal. Chem.* **1998**, 444, 31–39. [CrossRef]
- 35. Suga, T.; Shida, N.; Atobe, M. Au-catalyzed electrochemical oxidation of alcohols using an electrochemical column flow cell. *Electrochem. Commun.* **2021**, 124, 106944. [CrossRef]
- 36. Bender, M.T.; Warburton, R.E.; Hammes-Schiffer, S.; Choi, K.-S. Understanding Hydrogen Atom and Hydride Transfer Processes during Electrochemical Alcohol and Aldehyde Oxidation. *ACS Catal.* **2021**, *11*, 15110–15124. [CrossRef]

**Disclaimer/Publisher's Note:** The statements, opinions and data contained in all publications are solely those of the individual author(s) and contributor(s) and not of MDPI and/or the editor(s). MDPI and/or the editor(s) disclaim responsibility for any injury to people or property resulting from any ideas, methods, instructions or products referred to in the content.

# Electrocatalytic Oxidation of Benzaldehyde on Gold Nanoparticles Supported on Titanium Dioxide

Li Gong<sup>&,1,2</sup>, Yu Jin<sup>&,3</sup>, Shiling Zhao<sup>4</sup>, Kaizhi Wang<sup>\*,5</sup>, Paulina R. Martínez-Alanis<sup>\*,1</sup>, Andreu Cabot<sup>\*,1,6</sup>

- Catalonia Institute for Energy Research IREC Sant Adrià de Besòs, Barcelona 08930, Spain E-mail: pmartinez@irec.cat, acabot@irec.cat
- 2. Faculty of Chemistry, University of Barcelona, Barcelona 08028, Spain.
- 3. Key Laboratory of Applied Organic Chemistry (SKLAOC), The Key Laboratory of Catalytic Engineering of Gansu Province, College of Chemistry and Chemical Engineering, Lanzhou University, Lanzhou, Gansu 730000, China
- 4. School of Petrochemical Engineering, Lanzhou University of Technology, Lanzhou, 730050, China.
- 5. Department of Chemistry, Shanghai Key Laboratory of Molecular Catalysis and Innovative Materials, Fudan University, Shanghai 200433, P. R. China. E-mail: 20110220096@fudan.edu.cn
- 6. ICREA, Pg. Lluís Companys 23, 08010, Barcelona, Spain

<sup>\*</sup>These authors contributed equally to this work.

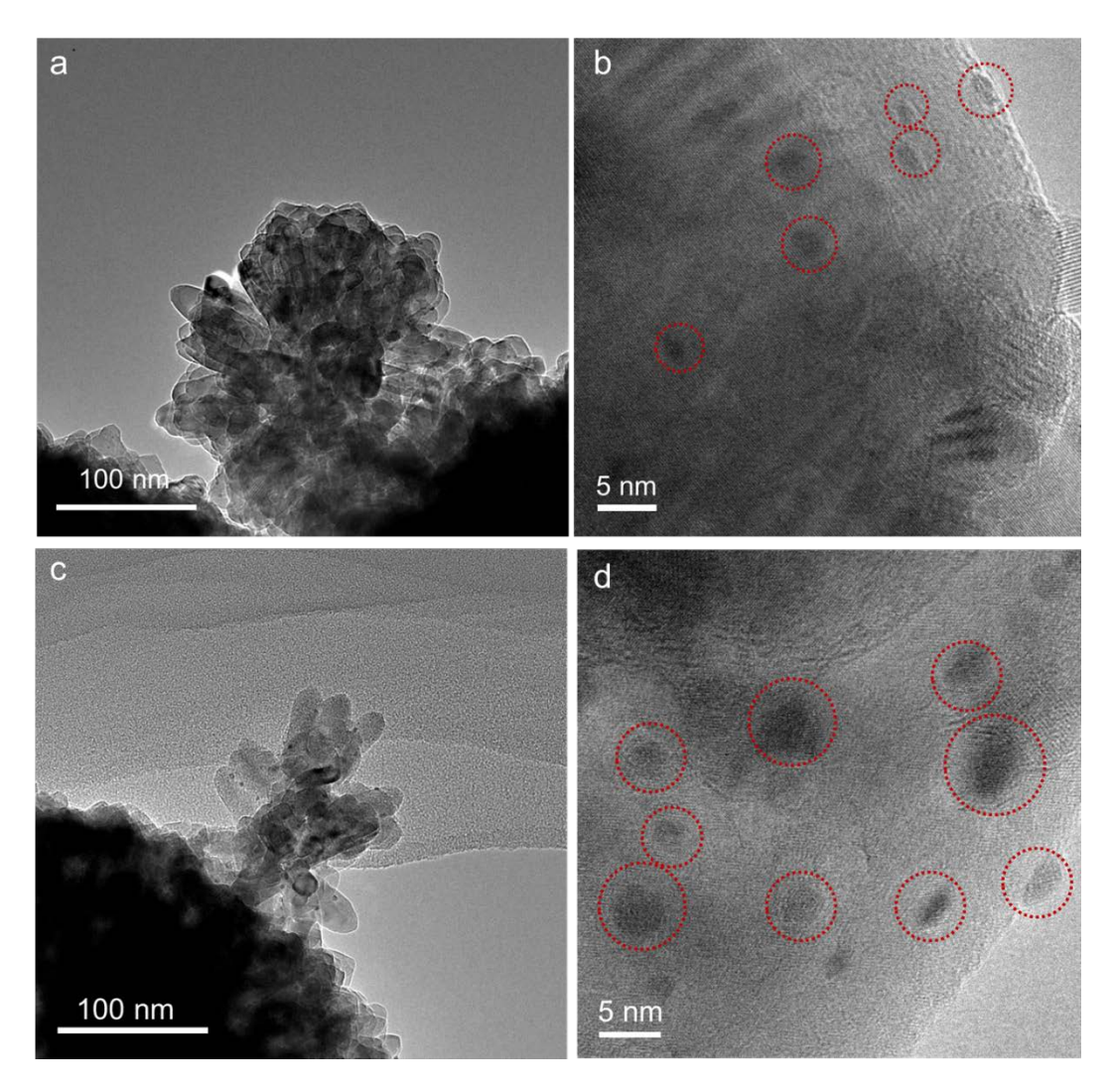
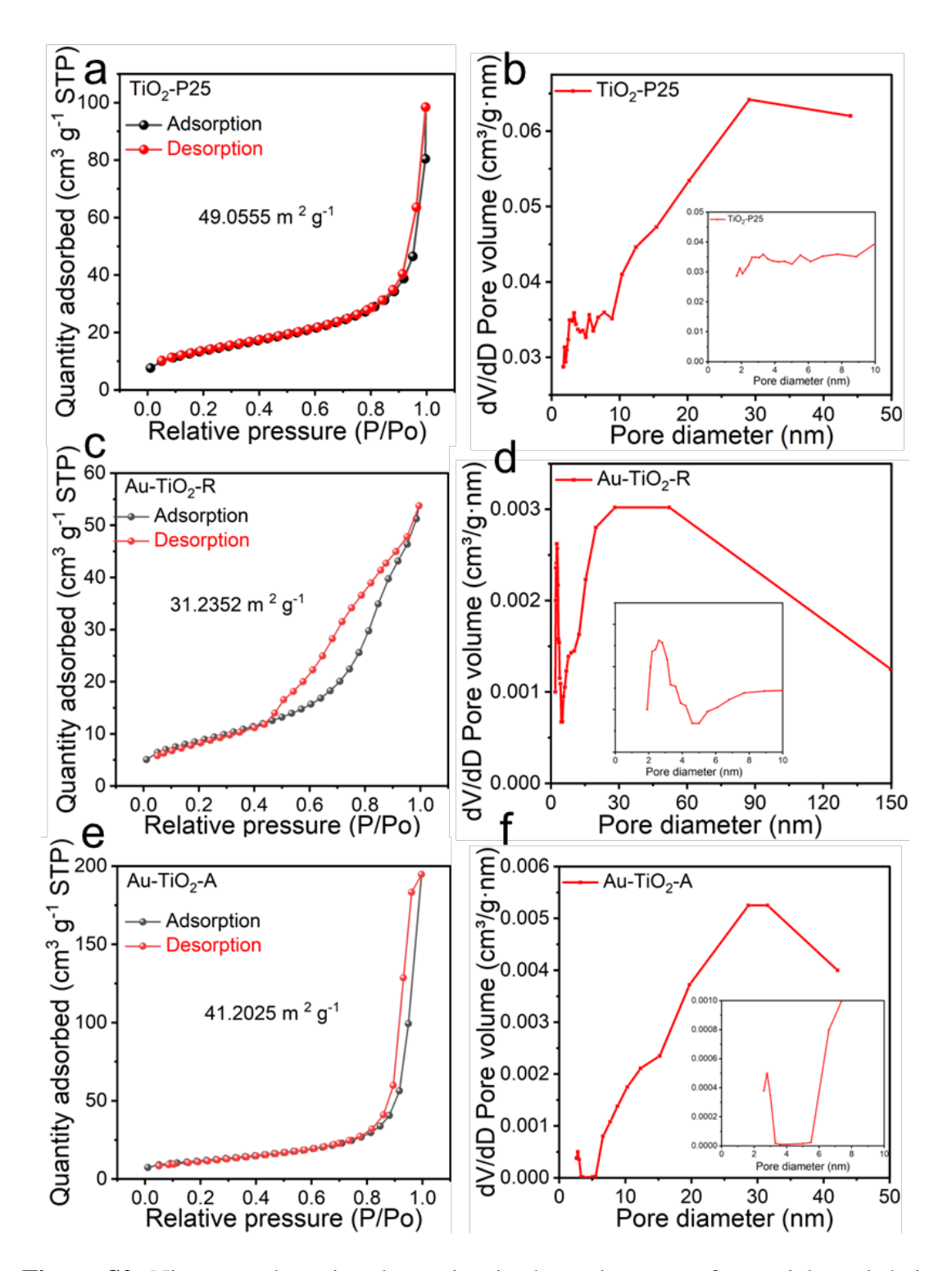


Figure S1. (a-b) TEM image of Au-TiO<sub>2</sub>-R; (c-d) TEM image of Au-TiO<sub>2</sub>-A.



**Figure S2.** Nitrogen adsorption-desorption isothermal curves of materials and their pore sizes distributions (a-b) TiO<sub>2</sub>-P25; (c-d) Au-TiO<sub>2</sub>-R; (e-f) Au-TiO<sub>2</sub>-A

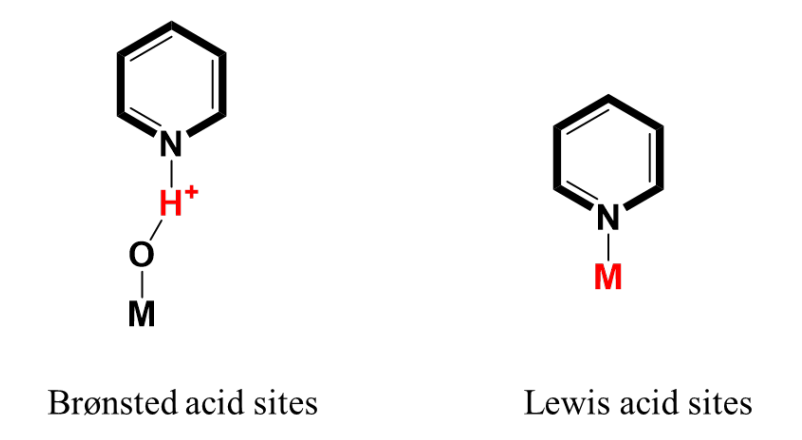
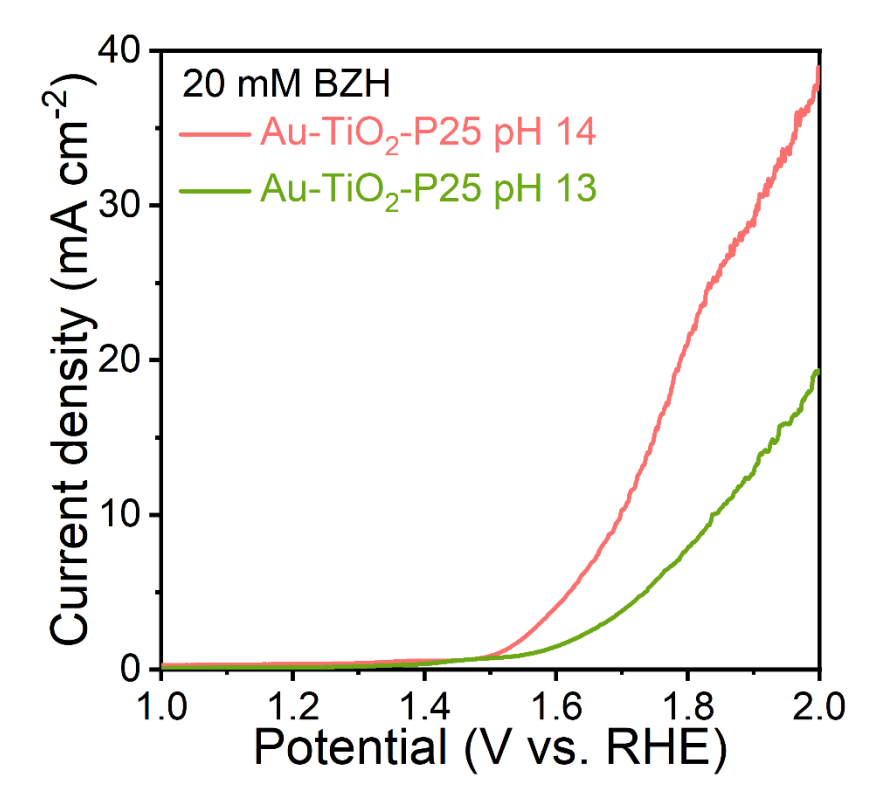


Figure S3. Diagram of pyridine adsorption on Brønsted acid sites and Lewis acid sites.



**Figure S4.** LSV curves of Au-TiO<sub>2</sub>-P25 at a scan rate of 50 mV s<sup>-1</sup> in 1 M KOH (pH 14) and 0.1 M KOH (pH 13).

# **Chapter 8**

# **Conclusion and further work**

## Chapter 8. Conclusion and further work

Excessive fossil fuel use harms the environment, prompting a shift to clean energy. Biomass energy is a promising alternative, but its unsaturated and oxygenated components lower bio-oil value and stability. Hydrogenation improves bio-oil, and electrocatalytic reduction using water as a hydrogen source offers energy-efficient, safe, and clean solutions. Understanding carbonyl reduction mechanisms is key to optimizing reaction selectivity and efficiency, despite the complexity of organic molecule adsorption and electrochemical environments on catalysts. This thesis focuses on electrocatalytic conversion pathways of BZH into BA, HDB and BZA exploration of the reaction mechanisms, adjustment of electrocatalytic environments, and rational catalyst design to achieve a high-performance biomass electrocatalytic reduction conversion system. The main conclusions of this thesis are as follows:

1) The onset potential of BZH hydrogenation is comparable with HER but the kinetics of the BZH hydrogenation reaction is slower than that of HER. In ECH processes, LH and PCET mechanisms have been proposed. Both pathways require the concentration of H proton and organic substrate on the EDL near the cathode surface. Thus, beyond selecting a proper active phase and having it highly dispersed on a high surface area support, the support composition, transport properties, and surface chemistry are fundamental parameters to be optimized to maximize the catalyst performance. In response to this fundamental theory, a Pd@Ni-MOF electrocatalyst containing a uniform dispersion of Pd particles on the surface of a Ni-MOF was produced and characterized. The oxygen-rich surface of Ni-MOF synthesized with 1,4-BDC and Ni enhances the concentration of Brønsted acid centers around the

Pd active sites, which increased the local proton concentration significantly boosts the reaction efficiency in pH 5.2 aqueous solution. This excellent performance is related to the important role played by the Ni-MOF in increasing the adsorbed hydrogen coverage, enabling the tilted adsorption of BZH through its carbonyl group, and facilitating H<sub>2</sub>O desorption.

- 2) Electrocatalytic reduction pathways of BZH into BA or HDB compete with the hydrogen evolution reaction HER. In terms of electrode materials towards self-coupling reaction of BZH into HDB, aside from carbon, Ti, In, Pb, Zn, Cu Sn and Au provide the best coupling selectivity, one common characteristic among these elements is their limited capacity for hydrogen adsorption. Besides, these elements form stable semiconductor sulfide compounds that are used in a range of applications. Thus, we considered exploring the use of different 2D metal chalcogenide semiconductor electrocatalysts to drive the BZH self-coupling reaction to HDB. The best pH condition is 1 M KOH. Properties of semiconductors tunable SCL and the self-gating effect can overcome their low carrier density limitations and function as ideal electrocatalysts towards this self-coupling reaction. The applied potential has to be lower than E<sub>fb</sub> for a proper concentration of electrons to accumulate on the space charge layer and reach an optimal thickness for the formation of HDB. When applying a too high negative potential, a too large excess of electrons at the semiconductor surface induces a buildup of the amount of adsorbed hydrogen and substrate that results in the favored formation of monomer alcohols over dimers as the reaction product.
- 3) Through the conclusions drawn from the studies above, it is not difficult for us to observe that the products BA and HDB are more easily obtained under acidic and alkaline conditions, respectively. Applying higher negative voltage could enhance HER, thereby reducing organic electrochemical reduction reaction efficiency. As for reaction selectivity, besides considering the enrichment of organic substrates on the electrode material surface, the

concentration of hydrogen proton accumulation on the electrode surface can significantly influence the selectivity of reaction pathways. Controlling solely the electrode material composition may limited by applying lower negative potential would reduce the organic reduction reaction efficiency and target products. In such cases, the strategy of surface chemistry can be employed to modify the entire electrode material with organic functional groups to enhance the selectivity of BZH to HDB. The material Cu<sub>2</sub>S-OAm with ligands and material with exposed active sites Cu<sub>2</sub>S capped were synthesized in a hot reaction system using a one-pot synthetic approach and by removing ligands, respectively. Results successfully demonstrate that the ligands OAm prevent organic substrate and the H proton from getting access to the active components Cu<sub>2</sub>S therefore hydrogen couldn't become activated intermediate species combined with ketyl radicals to form BA. At the same time, the organic BZH and its ketyl radicals concentrated near the OAm ligands of the catalyst surface based on the miscibility for their similar polarity, thus promoting the selectivity and conversion of forming HDB. This is a new strategy different from adjusting the catalyst's active components.

4) The overpotential for BZH electrooxidation decreased compared to the OER when coupled with the HER. Electrooxidation of BZH can not only replace the OER in fuel cells or water splitting, thereby reducing energy consumption but also yield high-value-added chemicals. Due to the unique properties of mixed-phase, larger surface area, high content oxygen vacancy and Lewis acid active sites on the surface, Au-TiO<sub>2</sub>-P25 shows the potential catalyzed ability towards electrooxidization of benzaldehyde (BZH).

For future research, there are other numerous strategies to design the catalysts for ECH reactions. Additionally, due to the low solubility of reactants in pure water systems, electrolyte composition adjustments are required. Consideration must also be given to issues such as product enrichment. Therefore, the industrialization path for ECH still has a long way to go. The self-coupling reaction of BZH to HDB in catalyst

design primarily hinges on the ability to strongly inhibit the accumulation of H proton on the catalyst surface. Furthermore, this reaction occurs efficiently under alkaline conditions, and the coupled product is expensive. Hence, this reaction holds significant potential for commercial applications. Moreover, it inspires the possibility of achieving more efficient self/cross-coupling reactions of organic compounds using electrocatalytic methods. Examples include the reaction involving CO<sub>2</sub> and 2-Furoic acid, producing 2,5-furandicarboxylic acid (FDCA). This reaction holds more complex conditions, involving the activation of 2-Furoic acid into an intermediate at the anode, CO<sub>2</sub> reduction on the cathode to obtain an activated intermediate, and the challenge of combining the two intermediates. The realization of this reaction is more difficult but holds substantial research significance.

## **Curriculum Vitae**

### Personal information

Li GONG

Nationality: Chinese

Phone: +86 18419702597 Date of birth: 1994.09

E-mail: <u>lgong0928@163.com</u>, <u>lgong0928@gmail.com</u>

Disciplines: Electrochemistry, Catalysis



### Education

Sep.2021-present University of Barcelona, Barcelona, Spain

PhD candidate, Electrochemistry, Science and Technology

Supervisors: Prof. Andreu Cabot and Dr. Paulina R. Martínez-Alanis

Sep. 2018-Jun. 2021 Lanzhou University, Lanzhou, Gansu, China

M.S. chemical engineering and Technology

Supervisor: Prof. Rong Li

Sep. 2014-Jun. 2018 Lanzhou University, Lanzhou, Gansu, China

B.S. Applied Chemistry

### **Research Interest**

Nanomaterials synthesis and characterization

Colloidal, solvent-thermal, annealing, electrodeposition methods for materials preparation.

Electrochemistry

Electrocatalysis (HER, OER, Organic Electro-oxidization / Electro-reduction etc.)

### **Meetings and Publications:**

# https://scholar.google.com/citations?hl=ca&user=EqETaRAAAAJ&view op=list works&sortby=p ubdate

- 1. Meeting: E-MRS 2023 FALL MEETING held at the University of Technology in Warsaw (Poland) from September 18 to 21 and presented the contribution entitled: Enhanced Electrochemical Hydrogenation (ECH) of Benzaldehyde to Benzyl Alcohol on Pd@Ni-MOF by Modifying the Adsorption Configuration.
- **2. Gong,** L; Zhao, S.; Yu, J.; Li, J.; Arbiol, J.; Kallio, T.; Martínez-Alanis, P. R.; Cabot, A., Influence of the catalyst surface chemistry on the electrochemical self-coupling of biomass-derived benzaldehyde into hydrobenzoin. (submitted to the journal)
- **3. Gong, L.**; Jin, Y.; Zhao, S.; Wang, K.; Martínez-Alanis, P.R.; Cabot, A., Electrocatalytic Oxidation of Benzaldehyde on Gold Nanopar-ticles Supported on Titanium Dioxide.(Nanomaterials accepted)
- **4. Gong,** L.; Zhang, C. Y.; Li, J.; Montaña-Mora, G.; Botifoll, M.; Guo, T.; Arbiol, J.; Zhou, J. Y.; Kallio, T.; Martínez-Alanis, P. R.; Cabot, A., Enhanced Electrochemical Hydrogenation of Benzaldehyde to Benzyl Alcohol on Pd@Ni-MOF by Modifying the Adsorption Configuration. *ACS Appl. Mater. Interfaces.* 2024, 16 (6), 6948-6957.
- **5. Gong,** L.; Zhang, C. Y.; Mu, X.; Han, X.; Li, J.; Arbiol, J.; Zhou, J. Y.; Kallio, T.; Martínez-Alanis, P. R.; Cabot, A., Semiconductor nanosheets for electrocatalytic self-coupling of benzaldehyde to hydrobenzoin. *J. Chem. Eng.* 2024, 479, 147612.
- **6.** Zhang, C. Y.; **Gong, L.**; Zhang, C.; Cheng, X.; Balcells, L. S.; Zeng, G.; Biendicho, J. J.; Li, J.; Sun, G. Z.; Zhou, J. Y.; Cabot, A., Sodium-Sulfur Batteries with Unprecedented Capacity, Cycling Stability and Operation Temperature Range Enabled by a CoFe<sub>2</sub>O<sub>4</sub> Catalytic Additive Under an External Magnetic Field. *Adv. Funct. Mater.* 2023, 33 (48), 2305908.
- 7. Mu, X.; Gong, L.; Yang, G.; Xiong, Y.; Wan, J.; Zhu, J.; Li, R., Biomass-based transition metal phosphides supported on carbon matrix as efficient and stable electrocatalyst for hydrogen evolution reaction. *Int. J. Energy Res.* 2022, 46 (3), 3502-3511.
- **8.** Gong, L.; Mu, X.; Li, Q.; Ma, L.; Xiong, Y.; Li, R., Rational design of Ni-induced NC@ Mo<sub>2</sub>C@ MoS<sub>2</sub> sphere electrocatalyst for efficient hydrogen evolution reaction in acidic and alkaline media. *Int. J. Hydrogen Energy.* 2021, 46 (7), 5250-5258.
- **9. Gong, L.**; Lan, K.; Wang, X.; Huang, X.; Jiang, P.; Wang, K.; Yang, M.; Ma, L.; Li, R., Carbon-coated Co-Mo-P nanosheets supported on carbon cloth as efficient electrocatalyst for Hydrogen Evolution Reaction. *Int. J. Hydrogen Energy.* 2020, 45 (1), 544-552.
- **10.** Huang, X.; **Gong, L.;** Xu, H.; Qin, J.; Ma, P.; Yang, M.; Wang, K.; Ma, L.; Mu, X.; Li, R., Hierarchical iron-doped CoP heterostructures self-assembled on copper foam as a bifunctional electrocatalyst for efficient overall water splitting. *J. Colloid Interface Sci.* 2020, 569, 140-149.